# Thèse

Présentée à

## L'Université de Lille – Sciences et Technologies

Par

## Batoul ALMOUSSAWI

Soutenue le 15 Décembre 2021
En vue d'obtenir le grade de
Docteur de l'Université Lille

Filière : Molécule et Matière Condensée
Discipline : Chimie des matériaux

## Semi-conducteurs innovants par ingénierie du band gap et manipulation anionique

| | | |
|---|---|---|
| **Directrice de thèse** | Mme Houria KABBOUR | Chargée de recherche HDR CNRS - UCCS - Lille |
| **Co-encadrant de thèse** | M. Angel Arevalo-Lopez | Chargé de recherche CNRS UCCS - Lille |
| **Rapportrice** | Mme Christel LABERTY-ROBERT | Professeurs des universités LCMCP - Paris |
| **Rapporteur** | M. Pierre Bonnet | Maitre de conférences HDR - ICCF - Clermont Auvergne |
| **Examinateur** | M. Pascal Roussel | Directeur de recherche CNRS UCCS - Lille |
| **Examinateur et président du jury** | M. Franck Gascoin | Professeurs des universités CRISMAT - Caen |

# Innovative semiconductors by band gap engineering and anionic manipulation

# **Acknowledgement**

*First, I express my gratitude to God, the eternal love. All words are not enough to express my gratitude to my parents, sisters, and brothers, who believed in me and always supported me. Without the trust and love of mom and dad I couldn't do it.*

*It is with emotion that I would like to thank all those who contributed directly or indirectly in this work.*

*I address all my respectful thanks to my thesis jury members, their evaluation of my work is an honor to me.*

*I would like to express my gratitude to Houria Kabbour, my thesis director for her support, foresight and skills that have been an invaluable help to me.*

*I address my warmest thanks to all the members of the UCCS lab, it is a great pleasure to be a member of such lab. I especially mention Pascal Roussel for his support and XRD data interpretation, Victor for ATG Analysis, Angel for magnetic measurements, Marielle for MET analysis, Nora for her beautiful morning smile and the EDS analysis, Laurence for XRD analysis, Philippe, Maxence for his good mood, Myriam for her efficiency and kindness, Frederic for the XRD analysis on single crystals, Edouard, Olivier, Florent.*

*I wish to express my profound gratitude to Prof. Hiroshi Kageyama, to Cédric Tassel and Satoko Nojiri for their help during my internships at Kyoto University.*

*I thank all my friends for their support: Zeinab and Fatima who heard me for hours and hours. With them I was able to go beyond the lock down and spent unforgettable happy moments. Thanks to all PhD students and colleagues who I met in the UCCS lab: Eleonora with her I enjoyed the time lab, Ana who I have always appreciated her presence next to me, Racha, thanks for Sandy who revitalizes the office with her humor, thanks for the magical presence of Maxime, Hicham,*

*Parth (the best office mate), Lama, Elias, Bastien, Anastasia, Despoina, Martin, Maeva, Soukaina, Jennifer, Florian, Mathilde, Edouard, Fatima zohra, Diane, Elena, Ayman and Guillaume.*

# **Abstract**

Mixed anions compounds may allow to reach structures and properties inaccessible in the case of single anion phases, which provide great opportunities for exploratory research of functional mixed anions compounds. One major interest of mixing anions in a phase is the band gap engineering by controlling the contribution of anionic orbitals at the top of the valence band, hence controlling the electronic structure and the properties. In addition, heteroleptic environments around a cation (directly surrounded by at least two types of anions) makes it possible to accentuate the acentric character of a structural entity, and therefore the polarity in the case of a polar arrangement comparing to a mono-anionic analogue. These two aspects combined, i.e. band gap engineering and local acentric character both reached with multiple anions, are powerful to control and exacerbate various properties. With the aim to reach such environments in innovative mixed anion phases and study their physical and chemical properties, several series of potential materials were formulated based on interesting mixed anion building blocks and their synthesis attempted. In this work, a wide variety of new systems are presented, including some unusual environments and properties: Non-linear optical properties, magnetic properties and photoelectric properties. Among these compounds, a large series of new compounds, including $Ba_5(VO_2S_2)_2(S_2)_2$, characterized by heteroleptic thiovanadates ($VO_2S_2$, $VO_3S$, $VOS_3$) and the presence of dichalcogenide pairs are described. From those building blocks, our strategy to reach polar phases was successful with one of those compounds showing interesting non-linear optical properties (SHG). Also, a series of versatile halide-thiovanadates phases (halide= F, Cl and I) could also be developed and proves the appearance of a photoelectric current under visible light. In addition, their calculated bands alignment with respect to H2 and O2 evolution reactions makes them potential candidates for photocatalysis of water-splitting under visible light. On another hand, the first Fresnoite oxysulfide (polar) with SHG properties is also presented. Finally, magnetic phases were also developed like the non-centrosymmetric $Ba_{10}Fe_{7.75}Zn_{5.25}S_{18}Si_3O_{12}$, with (Fe/Zn)$_3$O mixed anion tetrahedra involved in an original large magnetic cluster as elementary block. Those series of compounds are discussed with

combination of DFT calculations in order to deliver a comprehension of their structure-properties

relationships to help further design functional mixed anion material

# Résumé

Les composés à anions mixtes peuvent permettre d'atteindre des structures et des propriétés inaccessibles dans le cas de phases mono-anionique, ce qui offre de nombreuses opportunités pour la recherche exploratoire de composés à anions mixtes fonctionnels. Un intérêt majeur de la présence d'anions multiples au sein d'une phase est l'ingénierie du band gap via les contributions des orbitales anioniques en haut de la bande de valence, permettant ainsi le contrôle de la structure électronique et des propriétés. De plus, les environnement hétéroleptiques autour d'un cation (entouré d'au moins deux types d'anions) permettent d'accentuer le caractère acentrique d'une entité structurale, et donc la polarité dans le cas d'un arrangement polaire par rapport à un analogue mono-anionique. Ces deux aspects combinés, c'est-à-dire l'ingénierie du band gap et le caractère acentrique local tous deux modulables avec plusieurs anions, sont puissants pour contrôler et exacerber diverses propriétés. Dans le but d'atteindre de tels environnements dans des phases innovantes à anions mixtes et d'étudier leurs propriétés physiques et chimiques, plusieurs séries de composés ont été formulées sur la base d'unités structurales à anions mixtes intéressantes et leurs synthèses ont été tentées. Dans ce travail, une grande variété de nouveaux systèmes sont présentés, y compris certains environnements peu répandus et propriétés remarquables : propriétés d'optique non linéaire, propriétés magnétiques et propriétés photoélectriques. Parmi ces composés, une grande série de nouveaux composés, dont $Ba_5(VO_2S_2)_2(S_2)_2$, caractérisés par des thiovanadates hétéroleptiques ($VO_2S_2$, $VO_3S$, $VOS_3$) et la présence de paires dichalcogénures sont décrits. À partir de ces éléments constitutifs, notre stratégie pour atteindre les phases polaires a été couronnée de succès avec l'un de ces composés présentant des propriétés d'optique nonlinéaires (SHG) intéressantes. Aussi, une série de phases polyvalentes halogénure-thiovanadates (halogénure = F, Cl et I) a également pu être développée et montre l'apparition d'un courant photoélectrique sous lumière visible. De plus, l'alignement des bandes calculées par rapport aux réactions d'évolution de $H_2$ et $O_2$ en fait des candidats potentiels pour la photocatalyse de l'eau sous lumière visible. D'autre part, le premier oxysulfure de type Fresnoite (polaire) aux propriétés SHG est également présenté. Enfin, des phases magnétiques ont également été développées

comme le composé $Ba_{10}Fe_{7.75}Zn_{5.25}S_{18}Si_3O_{12}$ non centrosymétrique, avec des tétraèdres à anions mixtes $(Fe/Zn)_3O$ impliqués dans un cluster magnétique original qui forme l'unité structurale élémentaire. Ces séries de composés sont discutées en s'appuyant également sur des calculs DFT afin de fournir une compréhension de leurs relations structure-propriétés pour aider à concevoir davantage de matériaux à anions mixtes fonctionnels.

# Table of Contents

# General Introduction

# General Introduction

Anionic substitution in complex compounds and the properties which can result from it has been less explored and is attracting a growing attention since recent years. While cationic substitution leads to moderate chemical alterations (modulation of valence, chemical pressure effects or control of oxygen deficiency for instance), anionic substitution can strongly affect the chemical bonding. Beyond that, mixed anion can promote original structural edifices and allow fine control of the electronic structure around the band gap region which dictates the properties. Transition metals can, for example, form bonds with many anions in a large number of structural varieties. The example of iron illustrates this well with a rich diversity of binary compounds and properties ($FeO$, $FeF_3$, $FeCl_3$, $FeS$, $FeP$, $FeN$…). Then mixing anion around such transition metals will allow tuning the local symmetry and for instance induce or accentuate a distortion. In the meantime, the contributions of the different anions to the band gap region allow tuning the electronic structure. This opportunity to have a concomitant tuning of both the local symmetry (acentric character) and the band gap trough anionic manipulation is powerful and is the guiding strategy of this work**.** The later dual benefit appears in some remarkable examples of great enhancement or control of properties (non-linear optical properties, superconductivity…) and more advances are expected in various fields.

In view of the possibilities, anionic diversification in complex phases (especially quaternary and beyond) represents a particularly interesting prospecting field for the discovery of new phases and which remains underexploited despite the enormous potentialities. The incorporation of a second anion in complex oxides, with a radius close to $O^{2-}$ (r = 1.4 Å), i. e. $F^{-}$ (r = 1.3 Å) or $N^{3-}$ (r = 1.5 Å), should instead modify the structure locally. In contrast, with a mixture of distinct radius anions such as an oxide and a chalcogenide anion, completely different structural types may occur. In both cases, original compounds and properties can be reached.

In that context, this thesis work was developed within the MISSP (the Inorganic Materials, Structures, Systems and Properties) group. It belongs to the Solid-State Chemistry department UCCS laboratory and aims to develop new inorganic compounds mainly oriented for energetic

applications. More particular, it is motivated by the need of exploratory research of new phases and frameworks that could exhibit remarkable physical properties in many areas such as magnetism, optics, or conductivity, which can be complex and therefore require significant knowledge and diversity in characterization techniques (structure and properties). As such, the aim of this work was to explore and characterize new functional inorganic compounds by anionic manipulation which encompasses the mixed anions compounds study.

Despite the challenging topic with less studies than found for cationic manipulation, many new phases in different systems with a large range of properties are reported in this work. The UCCS equipment was in service to complete this study, starting from glove box, furnaces to the diffractometers for XRD on single crystals and on powders, the electronic scanning microscope and the transmission scanning microscope, etc..… DFT calculations were carried out using the University of Lille super-calculators in order to support the structure-properties relationships comprehension.

The strategy followed consists of target relevant structures and mixed anion building blocks and to formulate their compositions. The building blocks are selected regarding their properties and/or the unusual environments. In some cases, it consisted of applying anionic substitution to induce mixed anion around a metal cation with the aim to enhance properties.

A variety of systems were discovered during this thesis work including three polar systems. They also represent a wide variety properties and some unusual environments. In addition, the new synthesized materials can be raw materials for further future studies.

Depending on the chemical system or the type of properties studied, this thesis is presented in six chapters.

**Chapter** Ⅰ is a bibliographic study to introduce the context of mixed anion research in particular for oxychalcogenides: Generalities about mixed anion compounds with focus on oxychalcogenides and heteroleptic building blocks.

**Chapter** Ⅱ focuses on new Oxychalcogenides build from thiovanadates and dichalcogenide pairs in the systems Ba-V-S-O and Ba-V-S-Se-O. In the **first part** the original layered phase $Ba_5$

$(VO_2S_2)_2(S_2)_2$, its structure, DFT calculation, optical properties (UV-reflectance and Third Harmonic Generation (THG) properties). $Ba_7 S(VOS_3)_2(S_2)$ and its three selenide derivatives $Ba_7(S_{1-\alpha} Se_\alpha)(VOS_3)_2(S_{1-\gamma} Se_\gamma)_2$, their DFT calculations and optical measurements are presented in the **second part**. In this crystalline system the acentric tetrahedra $VOS_3$, the dichalcogenides pairs, and the isolated chalcogenide differentiate this system.

**Chapter Ⅲ :** The originality of the new **polar** oxysulfide $Ba_2SnSSi_2O_7$ is discussed in this chapter with its unusual tin oxysulfide environment and SHG properties. In the **second part,** another **polar phase** $Ba_5V_2O_{5.29} S_{2.55} Se_{4.16}$ could be reached and is presented. It shows Second Harmonic generation (SHG) properties.  The polar entities $VSO_3$ and the di-selenide pairs are arranged in an original manner for this phase.

**Chapter Ⅳ :** In this chapter all new magnetic phases obtained during the thesis are presented. In the **first part,** the new non-centrosymmetric oxysulfide $Ba_{10}Fe_{7.75}Zn_{5.25}S_{18}Si_3O_{12}$ containing $FeS_3O$ tetrahedra is presented. It is characterized by a remarkable three-dimensional framework defined by large magnetic clusters as elementary building blocks and shows spin glass behavior. The **polar** sulfide $Ba_5Fe_2ZnIn_4S_{15}$ designed from Fe incorporation in a polar sulfide matrix is also presented. In the third part, the high pressure phase $Ba_9V_3S_{15}$ and at DFT study of its magnetic properties is presented.

**Chapter Ⅴ :** A new thiovanadate series $Ba_5(VS_\alpha O_{4-\alpha})_3X$ (X: Cl, F, I) (triple anion) inspired from $Ba_5(VO_2S_2)_2(S_2)_2$ (chapter1_part1) and Apatite is presented with its photoconduction properties.

# Chapter I

**Generalities about mixed anion compounds with focus on oxychalcogenides and heteroleptic transition metal**

# Chapter I

## I. Generalities about mixed anion compounds with focus on oxychalcogenides and heteroleptic transition metal building blocks

The main objective of this work is to synthesis innovative functional materials by anionic manipulation. While cationic substitution is very common to tune the properties, anionic substitution is less explored despite the fact that it offers further and greater possibilities to alter the chemical bonding, the electronic structure and thus the properties. In the current and challenging context where it is necessary to anticipate the future energetical transition and maintain the technological progress, the discovery of materials responding to those challenges and strategies to reach them is of primary importance. The large range of mixed anion compounds properties (photocatalytic activity[1], superconductivity[2], non-linear optic (NLO)[3], thermoelectric[4], magnetic[5], make them suitable for novel functional materials exploration. Then taking advantage of mixed anion to control and enhance properties appears as one of the most promising strategy.

A mixed anion compound contains more than one anion type. The coexistence of different anions with different characteristics. such as charge, ionic radii, electronegativity and polarizability can lead to unusual or enhanced properties like found in several oxypnictides, oxychalcogenides, oxyhydrides and oxyhalides…

In a review, Kageyama *et al*[6], discuss the potentialities of multiple anions (see **Figure 1**) to increase the local degree of freedom, to control the crystal field splitting (CFS), the band gap and the local coordination asymmetry which is useful for materials design. It may have also an impact on the structure dimensionality. For the band gap features, considering transition metal-based phases, the conduction band maximum (CBM) is often determined by the 3$d$ electron states.

Since the anions states are found in the valence band maximum (VBM). In a mixed anion system, the band gap is determined by the states higher in the VBM. For instance, incorporating sulfur in an oxide matrix will narrow the band gap due to the lower electronegativity of sulfur. Thus, mixing anions supply band gap engineering tools in order to reach suitable features for many applications like water splitting photocatalysis. Compounds with distinct anions having very different ionic radii and electronegativities will often lead to layered structures[7]. The later have aspect have great advantages such anisotropic electronic properties or the possibility to have different types of layers stacked having their proper function. In thermoelectrics for instance, layered oxychalcogenides are of great interest because one layer is providing electronic conduction while the second one provides phonon glass properties. It gave access to the design of new functional compounds based on 2D elementary building blocks.

In the following part we will present a selection of remarkable mixed anion compounds, with large variety of properties enhanced by anionic manipulation.
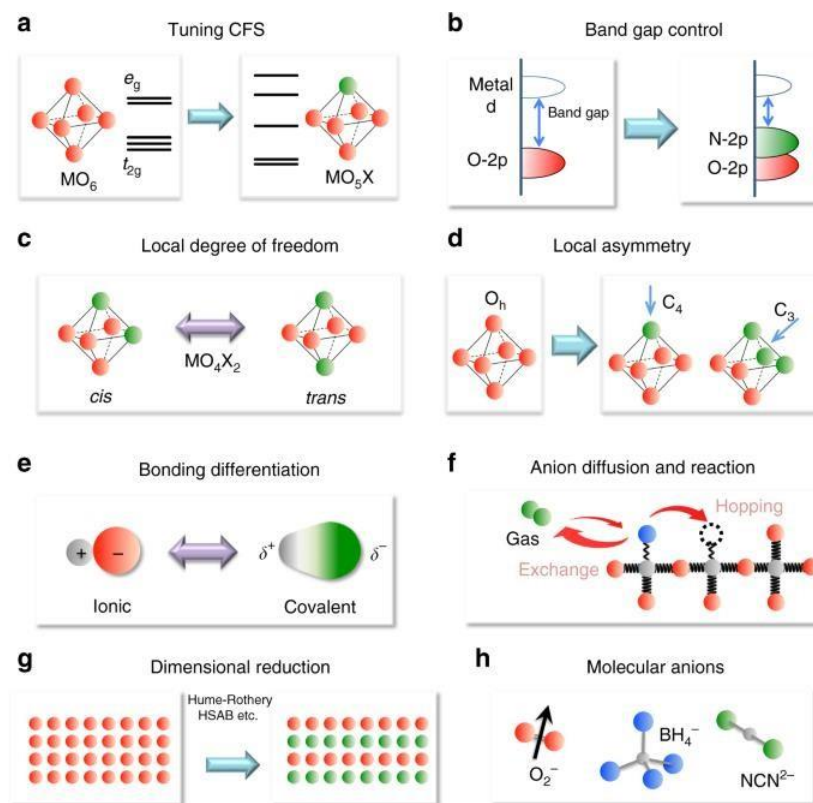
***Figure 1.*** *What mixed-anion compounds can do.[6]*

## a) The superconductor oxypnictide LaOFeAs

In this part we will discuss briefly the well-known layered oxypnictide superconductor LaOFeAs. It had conducted to a regain of interest for those systems and opened new perspectives in the field of superconductors which was dominated by oxide cuprates[8]. LaOFeAs was reported as a superconductor at low temperature Tc = 3.5 K[9] in 2006. It is built from alternating layers (**Figure 2**) lanthanum cation coordinated to oxygen anions and of $FeAs_4$ tetrahedra arranged in the second layer. In 2008, the critical temperature could be increased to Tc = 26 K[10] and even higher under pressure in the fluorine-doped compound $LaO_{1-x}F_xFeAs$. The critical temperature Tc reached 55 K[11] in the samarium phase $Sm[O_{1-x}F_x]FeAs$ doped with fluorine.
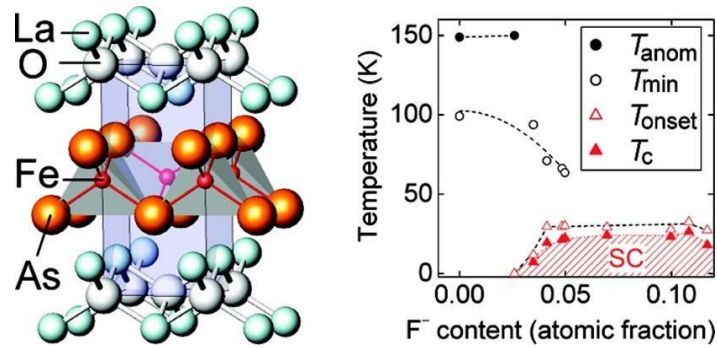
**Figure 2**. *crystal structure of LaOFeAs and $T_c$, $T_{onset}$, and $T_{min}$ in the $\rho$-T curves as a function of $F^-$ content (x) for La[$O_{1-x}F_x$]FeAs. $T_c$ is defined as the temperature where the $\rho$ value becomes half of that at $T_{onset}$. $T_{anom}$ values for the undoped and LaO$_{0.97}$F$_{0.03}$FeAs are also shown. Dotted curves are guides for eyes.* [10]

In mixed anion compounds, the coordination of different types of anions to the same transition metal cation gives heteroleptic entities, which proved in many cases, their ability to enhance certain properties. For example, the unique layered structure with good chemical stability BiO*X* (*X* = Cl, Br and I) have superior photocatalytic activity[13] compared to their similar metal oxide semiconductors.

## b) The enhanced NLO properties in the oxychalcogenide BaGeOSe$_2$

By following the same concept, a stronger SHG response mainly induced by the polarizable GeO$_2$Se$_2$ tetrahedra and BaOSe$_6$ polyhedra (**Figure 3**)[14] was found in BaGeOSe$_2$ compared to its pure oxide analogue based on GeO$_4$ tetrahedra[15].

SrGeOSe$_2$ was also reported. Its analogue oxide SrGeO$_3$ crystallizes in the centrosymmetric space group *P*-62*m* with zero-dimensional (0D) [Ge$_3$O$_9$] clusters that are made up of tetrahedral [GeO$_4$] building units and does not possess NLO activity. The partial substitution of oxygen in SrGeO$_3$ lead to symmetry breaking when forming SrGeOSe$_2$[16] which crystallizes in the orthorhombic system in space group P2$_1$2$_1$2$_1$ with NLO properties.
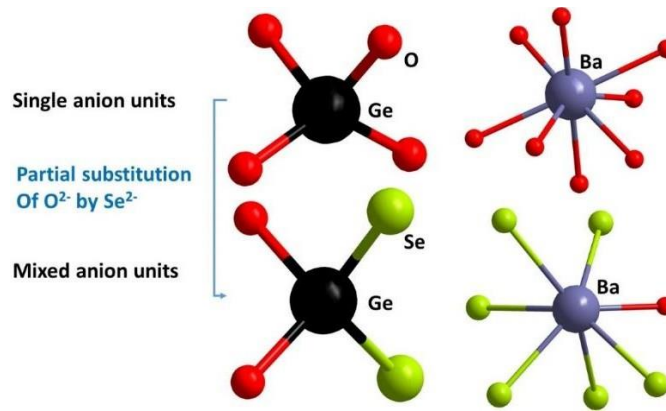
**Figure 3.** *BBUs of GeO$_4$ and BaO$_7$, GeO$_2$Se$_2$ and BaOSe$_6$ polyhedron in BaGeO$_3$ and BaGeSe$_2$O.* [14,15]

Only a small number of non-centrosymmetric (NCS) oxychalcogenides have been reported as promising NLO materials (cited in the following text). This fact encourages us to search out new oxychalcogenides with NLO properties.

c) The layered oxysulfides CaZnOS and CaOFeS with heteroleptic *M*OS$_3$ units

The layered polar semiconductor CaZnOS [17] with a wide band gap exhibits a SHG response and a piezoelectric behavior. Those properties can be attributed to the polar heteroleptic ZnS$_3$O tetrahedra. In addition, Mn doping on Zn sites leads to CaZnOS:Mn$^{2+}$ with elastico-mechanoluminescent (EML) properties with intense red emission[18]. We can also mention the doping with Eu$^{2+}$ (red emission)[19] and Ce$^{3+}$ (green emission)[20] confirming the interest of this compound as a host for optical applications (LED field).

Other interesting examples can be cited like Sr$_8$Al$_{12}$O$_{24}$S$_2$:Eu$^{2+}$ is a yellowish-orange phosphors[22].

On another hand, CaOFeS[23] (isostructural to CaOZnS) incorporates a magnetic metal Fe$^{2+}$. It shows magnetodielectric effects at 33 K induced by the polar distorted O-Fe-S$_3$[24]. This polar layered phase crystallized in the space group P6$_3$mc is a promising thermoelectric material[25]. In addition, the internal built-in electrical field induced by the spontaneous polarization should favors the separation of photogenerated electron-holes and photovoltaic effects are predicted[26]. Those features may provide other functionalities with potential applications[27]

24

### d) Remarkable layered oxychalcogenides semiconductors

In this context, we were interested to the particular mixed anion family formed by oxychalcogenides, containing oxygen and the more polarized chalcogenide anions (Ch: S, Se and Te), which are among the most promising materials. They exhibit wide band gap $p$-type semiconductor members and often adopt layered structures[7]. In most cases, the oxygen and the chalcogenide anions are segregated in different layers, like in LaCuOS[4] where alternate stacking of (LaO) and (CuCh) layers along the c-axis is observed. The conduction band minimum is mainly composed of Cu 4s, and the VBM are mainly composed of well-hybridized band of Cu 3d and chalcogenide $np$ states proving that the (CuCh) layers work as carrier transport layers[28]. The latter give LaCuOCh promising properties for an emitting layer in light-emitting devices as well as a transparent hole-injection layer[29]. The Se addition $LaCuOS_{1-x}Se_x$ [30] (x = 0–1) decrease the band gap and simultaneously increases the electrical conductivity. BiCuOSe is another example of layered oxyselenides which hold interesting thermoelectric properties[31]

In a recent review, Shi, Y.-F. *and al* summarized the oxychalcogenide compounds with IR-NLO proeprties[32]. They mentioned that none of those NCS oxychalcogenides crystallize in 3D anionic framework, which make our magnetic oxychalcogenide presented in chapter 4 a rare example of three-dimensional NCS oxysulfide.

Eleven phases were cited: $BaGeOS_2$, $SrGeOS_2$[33], $SrGeOSe_2$ $BaGeOSe_2$[34], $CaZnSO$[35], $SrZn_2OS_2$[36], $Sr_8Ga_8O_3S_{14}$[37], $Sr_6Cd_2Sb_6O_7S_{10}$[38], $Sr_4Pb_{1.5}Sb_5O_5Se_8$[39], $Sr_3Ge_2O_4Se_3$[40] and $\alpha$-$Na_3PO_3S$[41], they can combine the strong second-harmonic generation (SHG) responses of chalcogenides with the wide energy gaps of oxides (**Figure 4**).

**Table 1** Summary of the crystal system, space group, dimension, and key properties of the reported IR-NLO oxychalcogenides

| Number | Compounds | Crystal system | Space group | Dimension | Mixed-anion frequency-doubling building unit | Synthetic method | $E_g{}^a$ (eV) |
|---|---|---|---|---|---|---|---|
| 1 | CaZnOS | Hexagonal | $P6_3mc$ (no. 186) | 2D | $[ZnS_3O]$ | Solid state reaction | 3.71 |
| 2 | $SrZn_2OS_2$ | Orthorhombic | $Pmn2_1$ (no. 31) | 2D | $[ZnS_3O]$ | Solid state reaction | 3.86 |
| 3 | $Sr_5Ga_8O_3S_{14}$ | Orthorhombic | $P2_12_12$ (no. 18) | 2D | $[GaOS_3]$ | Solid state reaction | 3.9 |
| 4 | $Sr_6Cd_2Sb_6O_7S_{10}$ | Monoclinic | $Cm$ (no. 8) | 2D + 1D | $[SbOS_4]$ | Solid state reaction | 1.89 |
| 5 | $Sr_4Pb_{1.5}Sb_5O_5Se_8$ | Monoclinic | $Cm$ (no. 8) | 2D + 1D | — | Solid state reaction | 0.92 |
| 6 | $SrGeOS_2$ | Orthorhombic | $P2_12_12_1$ (no. 19) | 1D | $[GeO_2S_2]$ | Solid state reaction | 3.9 |
| 7 | $BaGeOS_2$ | Orthorhombic | $P2_12_12_1$ (no. 19) | 1D | $[GeO_2S_2]$ | Solid state reaction | 4.1 |
| 8 | $SrGeOSe_2$ | Orthorhombic | $P2_12_12_1$ (no. 19) | 1D | $[GeO_2Se_2]$ | Solid state reaction | 3.16 |
| 9 | $BaGeOSe_2$ | Orthorhombic | $P2_12_12_1$ (no. 19) | 1D | $[GeO_2Se_2]$ | Solid state reaction | 3.2 |
| 10 | $Sr_3Ge_2O_4Se_3$ | Trigonal | $R3m$ (no. 160) | 0D | $[GeOSe_3]$ | Solid state reaction | 2.96 |
| 11 | $\alpha$-$Na_3PO_3S$ | Trigonal | $R3c$ (no. 161) | 0D | $[PO_3S]$ | Solid state reaction or solution reaction | N/A$^d$ |

*Figure 4. Summary of the crystal system, space group, and key properties of the reported IR-NLO oxychalcogenides.[32]*

e) Band gap engineering in the systems A-V-S-O (A: K$^+$, Na$^+$) containing versatile thiovanadates

Among the Oxychalcogenides, those containing the heteroleptic $VO_xS_y$ thiovanadates took important place in our studies. These tetrahedral entities, by the different possible anionic composition and arrangement promote material design, and by consequence favor properties control. In the following part, we will describe the reported compounds containing the disconnected $VO_xS_y$ entities. In those tetrahedra, Vanadium exhibits the oxidation state $V^{5+}$.

The compounds $A_3(V(O, S)_4)$ (A = K$^+$, Na$^+$), although consisting of simple tetrahedra separated by A$^+$ cations (K$^+$ or Na$^+$), crystallize in different space groups, depending on the type of cation A$^+$ and sulfur / oxygen ratio. Thus, while the $Na_3VSO_3$[42] phase displays the non-centrosymmetric space group R3c, the analog phase $K_3VSO_3$ crystallizes in the $P2_1/m$ centrosymmetric space group. In the first one, the $R3c$ space group is due to the cooperative polar alignment of the $VSO_3$ units found in this compound. A description of the arrangement of the tetrahedra and their orientation in the different phases is given in the corresponding literature.

Such as in the compound $K_3(VOS_3)$[43], the 3$p$ states of sulfur lie just below the fermi level and thus dictate the width of the band gap. This behavior is well illustrated with the case of the compound

26

$A_3V(O_{4-x}S_x)_3$ (A = $Na^+$, $K^+$ and x = 0, 1, 2, 3 or 4) where the evolution of the band gap causes a color change of sample. More precisely, the increase in the amount of sulfur in the tetrahedra results in a change of the crystals from yellow ($Na_3(VO_4)$) to red ($Na_3(VS_4)$) (see **Figure 5**).
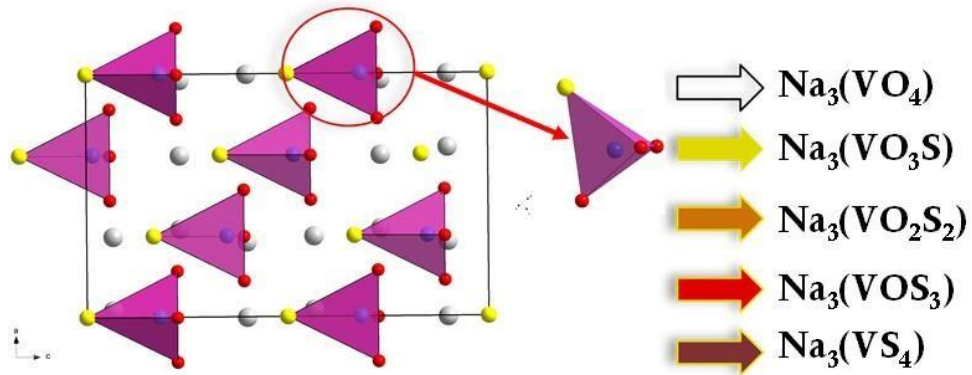


**Figure 5.** *Presentation of $Na_3(VSO_3)$ structure and colors range for $Na_3(VO_4)$, $Na_3(VO_3S)$, $Na_3(VO_2S_2)$, $Na_3(VOS_3)$ and $Na_3(VS_4)$.*

*Table 1. Summary of the crystal system, space group, and mixed-anion tetrahedra of the reported oxychalcogenides. CS and NCS mean respectively centrosymmetric and non-centrosymmetric.*

| Compounds | Crystal system | Space group | Mixed-anion tetrahedra | symmetry |
|---|---|---|---|---|
| α-$Na_3(VS_3O)$ | | *Pnma* | $VOS_3$ | CS |
| β-$Na_3(VS_3O)$ | Orthorhombic | *Cmc*$2_1$ | $VOS_3$ | NCS |
| $Na_3(VS_2O_2)$ | | *Pbca* | $VO_2S_2$ | CS |
| $Na_3(VSO_3)$ | Trigonal | *R*3*c* | $VO_3S$ | NCS |
| $K_3[VS_{3.4}O_{0.6}]$[44] | Orthorhombic | *Pnma* | $VO_{0.6}S_{3.4}$ | CS |
| $K_3(VS_{2.6}O_{1.4})$ [44] | | *P*$2_1$/*c* | $VO_{1.4}S_{2.6}$ | CS |
| $K_3(VS_2O_2)$ | Monoclinic | *P*$2_1$/*c* | $VO_2S_2$ | CS |
| $K_3(VSO_3)$ | | *P*$2_1$/*m* | $VO_3S$ | CS |
| $Ba_6V_4O_5S_{11}$ | Orthorhombic | *Pnma* | $VOS_3$, $VO_2S_2$ | CS |
| $CsBa_6V_4S_{12}ClO_4$ | Trigonal | *R*-3H | $VOS_3$ | CS |
| $Sr_6V_9O_2S_{22}$ | Rhombohedral | *R*-3 | $VOS_3$ | CS |
| $[Ba_{10}][S][(VO_3S)_6]$ | Hexagonal | *P*$6_3$ | $VO_3S$ | NCS |
| $Ba_3V_2O_3S_4$ | Hexagonal | *P*$6_3$ | $VO_3S$ | NCS |
| $Ba_{15}V_{12}S_{34}O_3$ | Monoclinic | *P*$2_1$/*c* | $VOS_3$ | CS |

**Table 1** compiles various $A_3V(O_{4-x}S_x)_3$ phases and their symmetry. Four phases among 14 phases were found in NCS space group: $\beta$-$Na_3(VOS_3)$, $Na_3(VO_3S)$, $Ba_{10}S(VO_3S)_6$ and $Ba_3V_2O_3S_4$. The later NCS phases all contain a polar tetrahedra $VS_3O$ or $VSO_3$. Only $Na_3(VSO_3)$ present a polar space group and the local asymmetry caused by mixed anion should enhance the polar character. e **Figure 6** shows the vanadium environment $VSO_3$ in $Na_3(VSO_3)$ and the more complex structure $Ba_{10}S(VO_3S)_6$. A regular V-O distance is shown for $Na_3(VSO_3)$ with relatively large distance V-S which induce the structure orientation. Those distances are much more distorted in $Ba_{10}S(VO_3S)_6$. The latter may be a result of geometric constraints imposed by the large cations $Ba^{2+}$ in this symmetry and the isolated inserted $S^{2-}$ anions.
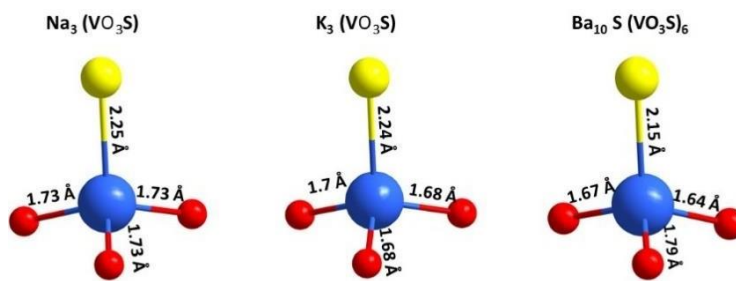


***Figure 6.*** *Distortion of $VO_3S$ in $Na_3 (VO_3S)$, $K_3 (VO_3S)$, $Ba_{10} S (VO_3S)_6$.*

This geometric effect of cations is clearly shown in the comparison of the isotype $Na_3(VS_3O)$ and $K_3(VS_3O)$. In case of the larger alkaline, the structure change space group and lose the non-centrosymmetry. Those examples show the complexity to reach non-centrosymmetry at the macromolecular scale. Another remarkable example, the BaOZnS[45] published in 2005 exhibits a $ZnO_2S_2$ tetrahedra and CS space group *Cmcm* but by substitution de $Ba^{2+}$ by the smaller $Ca^{2+}$ cation CaOZnS[17] become polar (**Figure 7**).
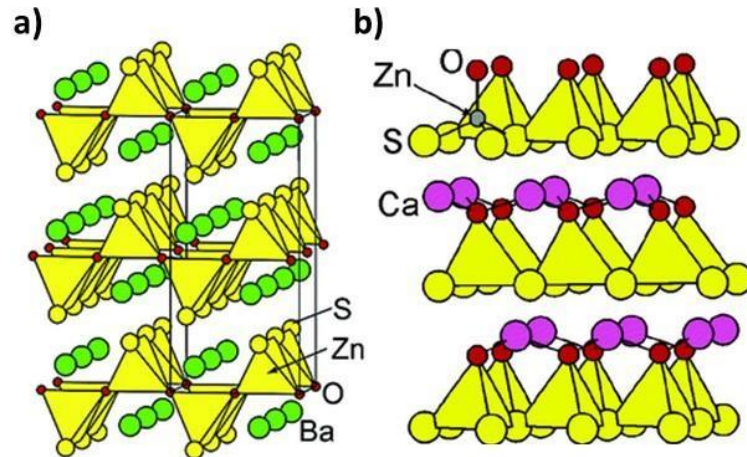
*Figure 7. Structural presentation of BaOZnS and CaOZnS [17]*

We notice that in the system Ba-V-S-O, the NCS is observed in case of $VSO_3$ building units.
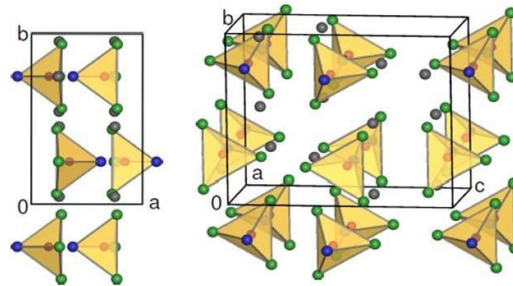


Abbildung 4.5: Kristallstruktur von $\alpha$-$Na_3VS_3O$; links: Projektion in [0 0 1]-Richtung, rechts: perspektivische Ansicht der Elementarzelle.
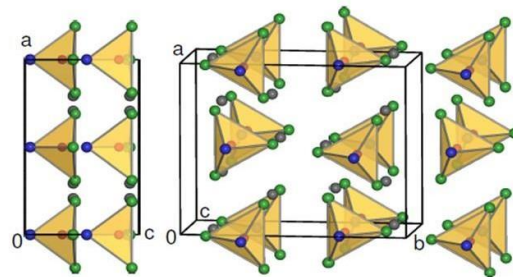


Abbildung 4.6: Kristallstruktur von $\beta$-$Na_3VS_3O$; links: Projektion entlang der [0 1 0]-Richtung, rechts: Elementarzelle in perspektivischer Ansicht.

*Figure 8. Structural presentation of α-Na₃(V S₃O) and β-Na₃(V S₃O)[46]*

In **Figure 8**, depending on the synthesis temperature $Na_3VS_3O$ adapts two different crystalline structure. Switching from *Pnma* to *Cmc*2₁.

In this system, the alkaline cation plays the role of spacer and its characteristics (radii, charge) may affect the whole structure due to chemical pressure effect.

| $^{11}$Na | | ❖ A$_3$ (V(O, S)$_4$) (A = K$^+$, Na$^+$) system |
| 22.99 | | |
| $^{19}$K | $^{20}$Ca | ❖ No existing phase in the Ca-V-S-O system |
| 39.098 | 40.078 | |
| | $^{38}$Sr | ❖ One complex phase in Sr-V-S-O |
| | 87.62 | |
| | $^{56}$Ba | ❖ More opportunities and complexity in Ba-V-S-O system |
| | 137.33 | |

## f) Complex example in the limited system Sr-V-S-O

To the best of our knowledge, $Sr_6V_9O_2S_{22}$ [47,48] is the only existing structure in the system Sr-V-S-O (**Figure 9**). It was published in 2000 and crystallizes in a rhombohedral cell within the centrosymmetric space group $R$-3. This complex layered compound with alternating $[V_7S_{14}]^{4-}$ and $[Sr_6(VOS_3)_2(S_2)]^{4+}$ layers contains the $VOS_3$ tetrahedra and $S_2^{2-}$ disulfide units separated by $Sr^{2+}$ ions. The local polarity of $VOS_3$ is cancelled because by their geometric arrangement. Vanadium shows oxidation states $V^{5+}$ in the tetrahedra and a mixed valence $V^{3.5+}$ in $[V_7S_{14}]^{4-}$ layer. The latter induces a small band gap semiconductor. The magnetic susceptibility shows essentially temperature-independent paramagnetism above 80 K and AFM interactions.
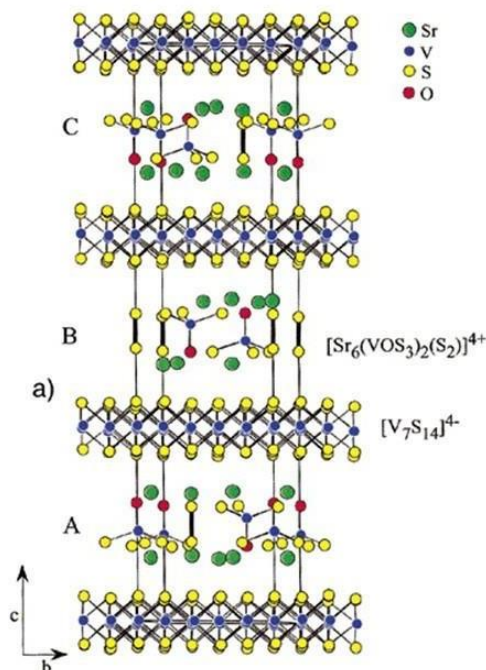
**Figure 9.** Layered structure of $Sr_6V_9O_2S_{22}$ [47]

### g) The promising system Ba-V-S-O: thiovanadates and beyond

$Ba_6V_4O_2S_{11}$ [49] structure was published in 1997 and it contains isolated $(VS_4)^{3-}$, $(VOS_3)^{3-}$, and $(VO_2S_2)^{3-}$ tetrahedra separated by large $Ba^{2+}$ cations. It crystallizes in an orthorhombic unit cell with the centrosymmetric space group *Pnma*.

The dark-red mixed anion $CsBa_6V_4S_{12}ClO_4$ [50] compound was reported in 2019 and crystallizes in the CS space group R3H and shows near-infrared fluorescence. It contains the units $VS_3O$ and large distorted Ba environment $BaS_7ClO_2$.

The orange $[Ba_{10}]^{20+}[S]^{2-}[(VO_3S)_6]^{18-}$ [51] phase was reported in the group within the NCS space group $P6_3$ and contains the thiovanadate units $(VO_3S)$ separated by $Ba^{2+}$ cations which delimit one-dimensional hexagonal-like cavities filled by disordered sulfur $S^{2-}$ anions.

$Ba_3V_2O_3S_4$ [52] crystallizes also in the NCS space group $P6_3$, it consists of face-sharing $VS_6$ octahedral chains separated by discrete $VO_3S$ tetrahedra and $Ba^{2+}$ cations.

$Ba_{15}V_{12}S_{34}O_3$ [53] crystallizes in the monoclinic $P2_1/c$ space group. The interconnected Quasi-one-dimensional face-sharing Vanadium zigzag chains form a fence-like lattice stacked along the *a-*

axis. The chains consist of face-sharing $VS_6$ distorted octahedra along the body of the chain and octahedral-like $VS_5O$. Polar tetrahedral $VS_3O$ reside in the fence cavities.

The complexity and diversity of the reported phases in the system Ba-V-S-O not fully explored, encouraged us to investigate it further.

(1) Nakada, A.; Kato, D.; Nelson, R.; Takahira, H.; Yabuuchi, M.; Higashi, M.; Suzuki, H.; Kirsanova, M.; Kakudou, N.; Tassel, C.; et al. Conduction Band Control of Oxyhalides with a Triple-Fluorite Layer for Visible Light Photocatalysis. *J. Am. Chem. Soc.* **2021**, *143* (6), 2491–2499.

(2) Al-Mamouri, M.; Edwards, P. P.; Greaves, C.; Slaski, M. Synthesis and Superconducting Properties of the Strontium Copper Oxy-Fluoride $Sr_2CuO_2F_{2+\delta}$. *Nature* **1994**, *369* (6479), 382–384.

(3) Li, Y.-Y.; Wang, W.-J.; Wang, H.; Lin, H.; Wu, L.-M. Mixed-Anion Inorganic Compounds: A Favorable Candidate for Infrared Nonlinear Optical Materials. *Cryst. Growth Des.* **2019**, *19* (7), 4172–4192.

(4) Palazzi, M.; Carcaly, C.; Laruelle, P.; Flahaut, J. Crystal Structure and Properties of (LaO) CuS and (LaO) AgS. In *The Rare Earths in Modern Science and Technology*; Springer US: Boston, MA, 1982; pp 347–350.

(5) Valldor, M.; Adler, P.; Prots, Y.; Burkhardt, U.; Tjeng, L. H. S = 2 Spin Ladders in the Sulfide Oxide BaFe 2 S 2 O. *Eur. J. Inorg. Chem.* **2014**, *2014* (36), 6150–6155.

(6) Kageyama, H.; Hayashi, K.; Maeda, K.; Attfield, J. P.; Hiroi, Z.; Rondinelli, J. M.; Poeppelmeier, K. R. Expanding Frontiers in Materials Chemistry and Physics with Multiple Anions. *Nat. Commun.* **2018**, *9* (1), 772.

(7) Sheath, B. C.; Cassidy, S. J.; Clarke, S. J. Cation Site Preferences in Layered Oxide Chalcogenides, Synthesis, Structures and Magnetic Ordering in $Sr_{3-x}Ca_xFe_2O_5Cu_2Ch_2$ (Ch = S, Se; x = 1, 2). *J. Solid State Chem.* **2021**, *293*, 121761.

(8) Xu, X.; Jones, M. A.; Cassidy, S. J.; Manuel, P.; Orlandi, F.; Batuk, M.; Hadermann, J.; Clarke, S. J. Magnetic Ordering in the Layered Cr(II) Oxide Arsenides $Sr_2CrO_2Cr_2As_2$ and $Ba_2CrO_2Cr_2As_2$. *Inorg. Chem.* **2020**, *59* (21), 15898–15912.

(9) Kamihara, Y.; Hiramatsu, H.; Hirano, M.; Kawamura, R.; Yanagi, H.; Kamiya, T.; Hosono, H. Iron-Based Layered Superconductor: LaOFeP. *J. Am. Chem. Soc.* **2006**, *128* (31), 10012–10013.

(10) Kamihara, Y.; Watanabe, T.; Hirano, M.; Hosono, H. Iron-Based Layered Superconductor $La[O_{1-x}F_x]FeAs$ ( x = 0.05–0.12) with T c = 26 K. *J. Am. Chem. Soc.* **2008**, *130* (11), 3296–3297.

(11) EndNote_EN - 快捷方式.

(12) Yin, Z. P.; Lebègue, S.; Han, M. J.; Neal, B. P.; Savrasov, S. Y.; Pickett, W. E. Electron-Hole Symmetry and Magnetic Coupling in Antiferromagnetic LaFeAsO. *Phys. Rev. Lett.* **2008**, *101* (4), 47001.

(13) Li, Y.; Jiang, H.; Wang, X.; Hong, X.; Liang, B. Recent Advances in Bismuth Oxyhalide

Photocatalysts for Degradation of Organic Pollutants in Wastewater. *RSC Adv.* **2021**, *11* (43), 26855–26875.

(14)  Liu, B.-W.; Jiang, X.-M.; Wang, G.-E.; Zeng, H.-Y.; Zhang, M.-J.; Li, S.-F.; Guo, W.-H.; Guo, G.-C. Oxychalcogenide BaGeOSe$_2$ : Highly Distorted Mixed-Anion Building Units Leading to a Large Second-Harmonic Generation Response. *Chem. Mater.* **2015**, *27* (24), 8189–8192.

(15)  Wan, S.; Zeng, Y.; Yao, Y.; Mutailipu, M.; Han, J.; Jiang, S.; Zhang, S.; Pan, S. BaGeO$_3$ : A Mid-IR Transparent Crystal with Superstrong Raman Response. *Inorg. Chem.* **2020**, *59* (6), 3542–3545.

(16)  Ran, M. Y.; Ma, Z.; Chen, H.; Li, B.; Wu, X. T.; Lin, H.; Zhu, Q. L. Partial Isovalent Anion Substitution to Access Remarkable Second-Harmonic Generation Response: A Generic and Effective Strategy for Design of Infrared Nonlinear Optical Materials. *Chem. Mater.* **2020**, *32* (13), 5890–5896.

(17)  Sambrook, T.; Smura, C. F.; Clarke, S. J.; Ok, K. M.; Halasyamani, P. S. Structure and Physical Properties of the Polar Oxysulfide CaZnOS. *Inorg. Chem.* **2007**, *46* (7), 2571–2574.

(18)  Zhang, J.-C.; Xu, C.-N.; Kamimura, S.; Terasawa, Y.; Yamada, H.; Wang, X. An Intense Elastico-Mechanoluminescence Material CaZnOS:Mn$^{2+}$ for Sensing and Imaging Multiple Mechanical Stresses. *Opt. Express* **2013**, *21* (11), 12976.

(19)  Qiu, Z.; Rong, C.; Zhou, W.; Zhang, J.; Li, C.; Yu, L.; Liu, S.; Lian, S. A Strategy for Synthesizing CaZnOS:Eu$^{2+}$ Phosphor and Comparison of Optical Properties with CaS:Eu$^{2+}$. *J. Alloys Compd.* **2014**, *583*, 335–339.

(20)  Zhang, Z.-J.; Feng, A.; Sun, X.-Y.; Guo, K.; Man, Z.-Y.; Zhao, J.-T. Preparation, Electronic Structure and Luminescence Properties of Ce$^{3+}$-Activated CaZnOS under UV and X-Ray Excitation. *J. Alloys Compd.* **2014**, *592*, 73–79.

(21)  Zhang, L.; Xu, C.-N.; Yamada, H. Strong Mechanoluminescence from Oxynitridosilicate Phosphors. *IOP Conf. Ser. Mater. Sci. Eng.* **2011**, *18* (21), 212001.

(22)  Kuo, T.-W.; Huang, C.-H.; Chen, T.-M. Novel Yellowish-Orange Sr$_8$Al$_{12}$O$_{24}$S$_2$:Eu$^{2+}$ Phosphor for Application in Blue Light-Emitting Diode Based White LED. *Opt. Express* **2010**, *18* (S2), A231.

(23)  Delacotte, C.; Pérez, O.; Pautrat, A.; Berthebaud, D.; Hébert, S.; Suard, E.; Pelloquin, D.; Maignan, A. Magnetodielectric Effect in Crystals of the Noncentrosymmetric CaOFeS at Low Temperature. *Inorg. Chem.* **2015**, *54* (13), 6560–6565.

(24)  Zhang, Y.; Lin, L.; Zhang, J.-J.; Huang, X.; An, M.; Dong, S. Exchange Striction Driven Magnetodielectric Effect and Potential Photovoltaic Effect in Polar CaOFeS. *Phys. Rev. Mater.* **2017**, *1* (3), 034406.

(25)  Reshak, A. H. CaCoSO Diluted Magnetic Antiferromagnet Semiconductor as Efficient Thermoelectric Materials. *Mater. Res. Bull.* **2017**, *94*, 22–30.

(26)  Butler, K. T.; Frost, J. M.; Walsh, A. Ferroelectric Materials for Solar Energy Conversion: Photoferroics Revisited. *Energy Environ. Sci.* **2015**, *8* (3), 838–848.

(27)  Peng, J.; Zhang, Y.; Lin, L.-F.; Lin, L.; Liu, M.; Liu, J.-M.; Dong, S. New Iron-Based Multiferroics with Improper Ferroelectricity. *J. Phys. D. Appl. Phys.* **2018**, *51* (24), 243002.

(28)  Williamson, B. A. D.; Limburn, G. J.; Watson, G. W.; Hyett, G.; Scanlon, D. O. Computationally

Driven Discovery of Layered Quinary Oxychalcogenides: Potential p-Type Transparent Conductors *Matter* **2020**, *3* (3), 759–781.

(29) Hiramatsu, H.; Kamihara, Y.; Yanagi, H.; Ueda, K.; Kamiya, T.; Hirano, M.; Hosono, H. Layered Mixed-Anion Compounds: Epitaxial Growth, Active Function Exploration, and Device Application. *J. Eur. Ceram. Soc.* **2009**, *29* (2), 245–253.

(30) Ueda, K.; Hosono, H. Crystal Structure of LaCuOS1–xSex Oxychalcogenides. *Thin Solid Films* **2002**, *411* (1), 115–118.

(31) Li, J.; Zhai, W.; Zhang, C.; Yan, Y.; Liu, P.-F.; Yang, G. Anharmonicity and Ultralow Thermal Conductivity in Layered Oxychalcogenides BiAgOCh (Ch = S, Se, and Te). *Mater. Adv.* **2021**, *2* (14), 4876–4882.

(32) Shi, Y.-F.; Wei, W.-B.; Wu, X.-T.; Lin, H.; Zhu, Q.-L. Recent Progress in Oxychalcogenides as IR Nonlinear Optical Materials. *Dalt. Trans.* **2021**, *50* (12), 4112–4118.

(33) Shi, Y.-F.; Wei, W.-B.; Wu, X.-T.; Lin, H.; Zhu, Q.-L. Recent Progress in Oxychalcogenides as IR Nonlinear Optical Materials. *Dalt. Trans.* **2021**, *50* (12), 4112–4118.

(34) Liu, B.-W.; Jiang, X.-M.; Wang, G.-E.; Zeng, H.-Y.; Zhang, M.-J.; Li, S.-F.; Guo, W.-H.; Guo, G.-C. Oxychalcogenide $BaGeOSe_2$ : Highly Distorted Mixed-Anion Building Units Leading to a Large Second-Harmonic Generation Response. *Chem. Mater.* **2015**, *27* (24), 8189–8192.

(35) Gulyaeva, R. I.; Selivanov, E. N.; Vershinin, A. D.; Chumarev, V. M. Thermal Expansion of CaZnSO. *Inorg. Mater.* **2006**, *42* (8), 897–900.

(36) Chen, C.; Zhuang, Y.; Tu, D.; Wang, X.; Pan, C.; Xie, R.-J. Creating Visible-to-near-Infrared Mechanoluminescence in Mixed-Anion Compounds $SrZn_2S_2O$ and SrZnSO. *Nano Energy* **2020**, *68*, 104329.

(37) Wang, R.; Guo, Y.; Zhang, X.; Xiao, Y.; Yao, J.; Huang, F. $Sr_5Ga_8O_3S_{14}$ : A Nonlinear Optical Oxysulfide with Melilite-Derived Structure and Wide Band Gap. *Inorg. Chem.* **2020**, *59* (14), 9944–9950.

(38) Wang, R.; Liang, F.; Wang, F.; Guo, Y.; Zhang, X.; Xiao, Y.; Bu, K.; Lin, Z.; Yao, J.; Zhai, T.; et al. $Sr_6 Cd_2Sb_6O_7S_{10}$ : Strong SHG Response Activated by Highly Polarizable Sb/O/S Groups. *Angew. Chemie Int. Ed.* **2019**, *58* (24), 8078–8081.

(39) Wang, Y.; Luo, M.; Zhao, P.; Che, X.; Cao, Y.; Huang, F. $Sr_4Pb_{1.5}Sb_5O_5Se_8$ : A New Mid-Infrared Nonlinear Optical Material with a Moderate SHG Response. *CrystEngComm* **2020**, *22* (20), 3526–3530.

(40) Xing, W.; Fang, P.; Wang, N.; Li, Z.; Lin, Z.; Yao, J.; Yin, W.; Kang, B. Two Mixed-Anion Units of $[GeOSe_3]$ and $[GeO_3S]$ Originating from Partial Isovalent Anion Substitution and Inducing Moderate Second Harmonic Generation Response and Large Birefringence. *Inorg. Chem.* **2020**, *59* (22), 16716–16724.

(41) Takas, N. J.; Aitken, J. A. Phase Transitions and Second-Harmonic Generation in Sodium Monothiophosphate. *Inorg. Chem.* **2006**, *45* (7), 2779–2781.

(42) Schnabel, S.; Röhr, C. Gemischte Thio/Oxo-Orthovanadate $Na_3 [VS_xO_{4-x}]$ (x = 2, 3): Darstellung – Strukturen – Eigenschaften / Mixed Thio/Oxo Orthovanadates $Na_3 [VS_xO_{4-x}]$ (x = 2, 3): Synthesis –

Crystal Structures – Properties. *Zeitschrift für Naturforsch. B* **2005**, *60* (5), 479–490.

(43)  Schnabel, S.; Röhr, C. Kalium-Thio/Oxo-Vanadate(V) $K_3[VS_xO_{4-x}]$ (x = 1–4) Und $Na_3[VSO_3]$: Synthese, Strukturchemie, Eigenschaften. *Zeitschrift für Naturforsch. B* **2008**, *63* (7), 819–833.

(44)  Vs, K. O. V. K.; Schnabel, S. Kalium-Thio/Oxo-Vanadate(V) $K_3VS$. **2008**, No. V.

(45)  Broadley, S.; Gál, Z. A.; Corà, F.; Smura, C. F.; Clarke, S. J. Vertex-Linked $ZnO_2S_2$ Tetrahedra in the Oxysulfide BaZnOS: A New Coordination Environment for Zinc in a Condensed Solid. *Inorg. Chem.* **2005**, *44* (24), 9092–9096.

(46)  Schnabel, S. Strukturchemie, Elektronische Strukturen Und Spektroskopische Eigenschaften Der Alkalimetallthiooxovanadate ( V ) $A_3VS_xO_{4-x}$. **2008**, No. V, 1–138.

(47)  Litteer, J. B.; Chen, B.-H.; Fettinger, J. C.; Eichhorn, B. W.; Ju, H. L.; Greene, R. L. Synthesis and Magnetic and Transport Properties of $Sr_6V_9S_{22}O_2$ : "$AM_2S_5$" Phases Revisited. *Inorg. Chem.* **2000**, *39* (3), 458–462.

(48)  Gourdon, O.; Evain, M.; Jobic, S.; Brec, R.; Koo, H.-J.; Whangbo, M.-H.; Corraze, B. On the Origin of the × Superstructure and the Anomalous Magnetic and Transport Properties of the Layered Compound $Sr_6V_9S_{22}O_2$. *Inorg. Chem.* **2001**, *40* (12), 2898–2904.

(49)  Litteer, J. B.; Fettinger, J. C.; Eichhorn, B. W. Ba 6 V 4 O 5 S 11. *Acta Crystallogr. Sect. C Cryst. Struct. Commun.* **1997**, *53* (2), 163–165.

(50)  Valldor, M.; Galle, L.; Eichler, F.; Wolf, A.; Morrow, R. Synthesis, Crystal Structure, and Optical Characterization of the Sulfide Chloride Oxide $CsBa_6V_4S_{12}ClO_4$ with a Near-Infrared Fluorescence. *Inorg. Chem.* **2019**, *58* (21), 14728–14733.

(51)  Nicoud, S.; Mentré, O.; Kabbour, H. The $Ba_{10}S(VO_3S)_6$ Oxysulfide: One-Dimensional Structure and Mixed Anion Chemical Bonding. *Inorg. Chem.* **2019**, *58* (2), 1349–1357.

(52)  Calvagna, F.; Zhang, J.; Li, S.; Zheng, C. Synthesis and Structural Analysis of $Ba_3V_2O_3S_4$. *Chem. Mater.* **2001**, *13* (2), 304–307.

(53)  Wong, C. J.; Hopkins, E. J.; Prots, Y.; Hu, Z.; Kuo, C.-Y.; Pi, T.-W.; Valldor, M. Anionic Ordering in $Ba_{15}V_{12}S_{34}O_3$ , Affording Three Oxidation States of Vanadium and a Quasi-One-Dimensional Magnetic Lattice. *Chem. Mater.* **2016**, *28* (6), 1621–1624.

# Chapter II

## New oxychalcogenides in Ba-V-S-O and Ba-V-Se-S-O systems

# II. Chapter II: New oxychalcogenides in Ba-V-S-O and Ba-V-Se-S-O systems

## Introduction

In the first chapter we have introduced in a general way the interest of mixing anions. It may allow to reach properties which are inaccessible in the case of a single anion phase. The examples cited exhibit a wide range of properties found in mixed anion compounds. Among them, we have discussed those which are reported built with heteroleptic entities $V^{5+}O_{4-x}S_x$, *i.e.* thiovanadates In those systems the tetrahedra are disconnected and separated by alkali or alkaline earth cations. Studies consisting in varying the anionic ratio highlight the power of anionic manipulation allowing band gap control and consequently the control of properties.

As part of the search of new mixed anion compounds with non-centrosymmetric structure, we formulated hypothetical phases based on such thiovanadate structural entities. This strategy has led to the discovery of five innovative and complex systems.

This chapter is composed of two linked parts, each one encompasses a new layered structure solved and refines from the X-ray diffraction analysis carried out on single crystals. High purity polycrystalline powders, diffuse reflectance spectra, DFT calculations and suitable property measurements were carried out.
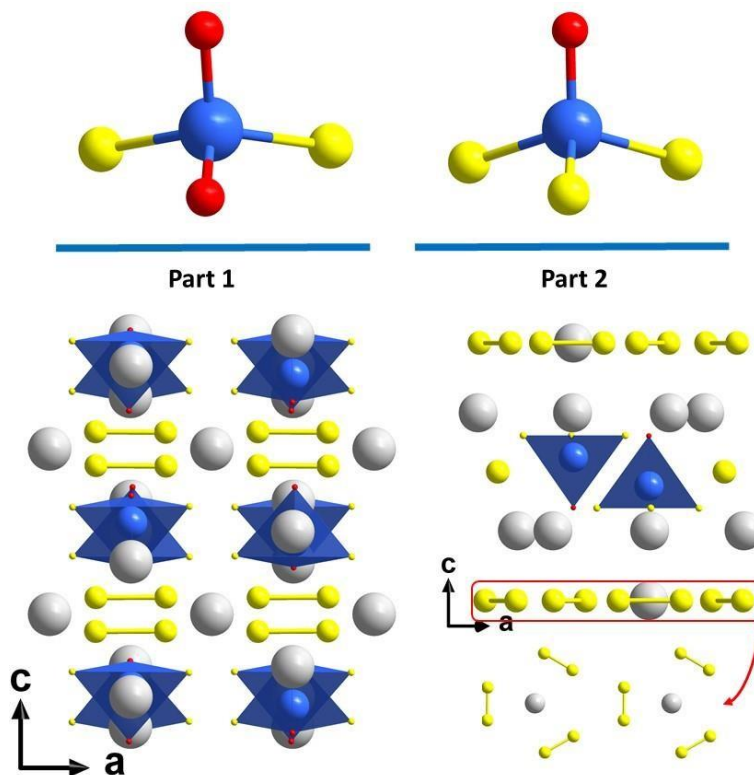
Each phase can be described by two alternating layers: In the first one, at least two anions are surrounding the vanadium cations which form disconnected tetrahedra separated by the large $Ba^{2+}$ cation. While the dichalcogenide pairs and the $Ba^{2+}$ inserted in the voids constitute the second one. These combined characteristics make the originality of those new compounds.

First, $Ba_5(VO_2S_2)_2(S_2)_2$ is presented, and it is found to have a third harmonic generation response. Then $Ba_7S(VOS_3)_2(S_2)_3$ shows an additional anionic species (isolated $S^{2-}$) comparing to $Ba_5(VO_2S_2)_2(S_2)_2$. It was discovered during attempts to modify the system $Ba_5(VO_2S_2)_2(S_2)_2$ under pressure. Then, it was possible to synthesize it at ambient pressure together with a series of compounds obtained by substitution of Sulfide by Selenide. We show that the later introduces a simultaneous disorder in dichalcogenide pairs and isolated chalcogenide. The Se/S ratio impact was studied by means of DFT calculations.

# Part 1: The Oxysulfide Ba$_5$(VO$_2$S$_2$)$_2$(S$_2$)$_2$ combining disulfide channels and mixed anion tetrahedra and its third harmonic generation properties

## A. Part 1: The Oxysulfide $Ba_5(VO_2S_2)_2(S_2)_2$ Combining Disulfide Channels and Mixed Anion Tetrahedra and its Third Harmonic Generation Properties

Batoul Almoussawi[1], Marielle Huvé[1], Valérie Dupray[2], Simon Clevers[2], Victor Duffort[1], Olivier Mentré[1], Pascal Roussel[1], Angel M. Arevalo-Lopez[1], Houria Kabbour[1]*

*1 Univ. Lille, CNRS, Centrale Lille, ENSCL, Univ. Artois, UMR 8181 – UCCS – Unité de Catalyse et Chimie du Solide, F-59000 Lille, France*

*2 Normandie Univ, UNIROUEN, SMS, 76000 Rouen, France*

### 1. Abstract

Mixed anion compounds are among the most promising systems to design functional materials with enhanced properties. In particular, heteroleptic environments around transition metals allow tuning of polarity or band gap engineering for instance. We present the original oxysulfide $Ba_5(VO_2S_2)_2(S_2)_2$, the fifth member in the quaternary system Ba-V-S-O. It exhibits the mixed anion building units $V^{5+}O_2S_2$ and isolated disulfide pairs $(S_2)^{2-}$. The structure is solved by combining single crystal and powder X-Rays Diffraction (XRD) and transmission electron microscopy (TEM). First-principles calculations were combined in order to highlight the anions roles. In particular, our DFT study shows that the $3p$ states of the disulfide pairs dictate the band gap. In this study, we point out *anionic* tools for band gap engineering, which can be useful to design phases for numerous applications. Finally, third Harmonic Generation (THG) was measured and compared to the large THG observed for $Cu_2O$, which reveals potentialities for non-linear optical properties that should be further investigated.

### 2. Introduction

Mixed anion compounds are among the most promising systems for the prospection of original phases and for the control/enhancement of functionalities. Despite this matter of fact, they remain less explored compared to single anion phases and in particular compared to oxides. A recent review[1] highlights the great interest of heteroleptic environments around transition metals ($O^{2-}$, $S^{2-}$, $N^{3-}$, $H^-$, $F^-$ *etc.*....) compared to oxides for numerous properties such as visible light

photocatalysis[2], batteries[3], thermoelectricity[4], magnetism[5, 6] *etc. ...* In that context, oxysulfides represent a remarkable family that opens several perspectives in various domains. For instance, layered oxychalcogenides are emerging as potential tunable thermoelectrics[7] thanks to the stack of versatile ionic oxide and more covalent chalcogenide layers. The contribution of the chalcogenide anion in the emergence of visible light photocatalytic activity is also promising such as in LaOInS$_2$ [8a] and its polymorph $\alpha$-LaOInS$_2$ for water splitting [8b]. It is important here to highlight the powerful "anionic" tool for band gap engineering. Indeed, solar water-splitting photocatalysis requires a band gap in the range 3.1 eV − 1.23 eV while the potential of the conduction band (CB) and of the valence band (VB) should encompass the reduction and oxidation potentials of water. The interplay between multiple anions is determinant for these crucial aspects, thus opening the route for the rational design of functional materials. On another hand, while the band gap can be tuned by the concomitant contribution of different anionic species[9], local geometric effects can benefit to nonlinear optical (NLO) materials[10]. For instance, the polar phase SrZn$_2$S$_2$O with ZnS$_3$O building blocks[11], forming unusual Wurtzite-like slabs, is the first phase matchable NLO oxysulfide and exhibits a large Second Harmonic Generation (SHG) response twice the KDP reference material one. Here, the heteroleptic building units have a more pronounced acentric character, then their polar arrangement lead to an enhanced dipolar momentum which directly impact the related properties. While second order nonlinear optical processes are observed in systems without inversion symmetry, the third order ones may be observed in any medium, centrosymmetric or not. In Third Harmonic Generation (THG), three photons interact together to give rise to new photon at the third of the fundamental wavelength ($\lambda$/3) (*i.e.* the frequency is triple)[12]. THG processes offer the possibility to extend the frequency conversion processes. In particular, materials allowing THG can be used to generate directly (and not via a series of second order NLO processes) coherent laser light in the UV region from commercially available laser sources[13]. Such UV sources are highly demanded in a variety of applications such as medical applications, short-range optical communication or chemical sensing. They have also potential interest in quantum optics with possible direct generation of photon triplets from the reverse process of THG[14]. THG has been investigated for instance on the centrosymmetric rutile oxide TiO$_2$ (*P*4$_2$/mnm) with efficient triple photon generation[15]. We find

such phenomenon in a new mixed anion phase, the centrosymmetric oxysulfide $Ba_5(VO_2S_2)_2(S_2)_2$, which we present here. Its original structure is made of heteroleptic ($VO_2S_2$) tetrahedra and of disulfide pairs forming a one-dimensional arrangement. Here we present the structure; the DFT computed electronic structure and the THG properties which are rarely investigated for this type of materials. It represents the fifth original phase reported in the quaternary system Ba-V-S-O. We analyze this phase's electronic structure in relation with the structural units building it. It opens interesting perspectives for the band gap engineering of inorganic compounds from mixed anionic matrices, including disulfide pairs.

3. Experimental section

**Synthesis:** Single crystals of $Ba_5(VO_2S_2)_2(S_2)_2$ (i.e. $Ba_5V_2O_4S_8$) were initially found during an exploratory synthesis that included the elements Ba-V-O-S. We attempted to synthesize a single phase material from a mixture of the precursors BaS/BaO/V/S in the molar ratio 1:4:2:7. Those precursors were mixed and thoroughly ground in an agate mortar before being pressed into pellets and heated in an evacuated sealed quartz tube. The heat treatment consisted in heating up to 400°C at a rate of 35°C/h for 10 hours, then to 800°C at a 50°C/h rate for 96 hours, before cooling down to 600°C at a 20°C/h rate, temperature at which the furnace was switched off.

**X-ray diffraction on single crystals diffraction** was performed on an X8 diffractometer equipped with a bi-dimensional CCD 4K detector and an Ag K$_\alpha$ source.

**Electron diffraction** study was performed on a FEI Technai G2-20 twin TEM microscope. The powder was crushed and dropped in the form of alcohol suspension on carbon supported copper grids followed by evaporation under ambient condition.

**The powder X-ray diffraction** pattern was collected on a Bruker D8 diffractometer equipped with a linear detector Lynxeye (Cu$_{K\alpha}$) in Bragg-Brentano geometry at room temperature.

**DFT calculations** were carried out by employing the projector augmented wave (PAW)[16, 17] method encoded in the Vienna ab initio simulation package (VASP)[18] and the generalized gradient approximation of Perdew, Burke and Ernzerhof[19] (PBE) for the exchange-correlation functionals. The full geometry optimizations were carried out using a plane wave energy cutoff of 550 eV and

12 $k$ points in the irreducible Brillouin zone. It converged with residual Hellman-Feynman forces on the atoms smaller than 0.03 eV/Å and led to a good match with the experimental structure, i.e. within a reasonable error expected for the GGA method. The relaxed structure was used for calculations of the electronic structure. For the later, the plane wave cutoff energies of 550 eV and the threshold of self-consistent-field energy convergence of $10^{-6}$ eV were used, with 90 $k$ points in the irreducible Brillouin Zone.

**Scanning electron microscopy (SEM)** experiments and EDX analysis were carried out on a Hitachi S400N.

**UV-Visible measurements:** The reflectance of the sample was measured from 250 to 800 nm on a Perkin Elmer Lambda 650 device.

**The thermogravimetric analysis (TGA)** where conducted on a TGA-92 thermobalance (Setaram) under synthetic air ($N_2/O_2$ 80%/20%) and pure argon. The evolved gases were monitored by an Omnistar quadrupole mass spectrometer (Pfeiffer) by continuously scanning in the range 0 – 100 amu. In order to control the atmosphere, the whole thermobalance was evacuated and filled with the carrier gas before heating up the samples up to 800 °C at a rate of 5 K/min.

**Non-linear optical measurements**

Insight X3 single laser with automated dispersion compensation (Spectra-Physics, Santa Clara, USA) and a TCS SP8 MP confocal microscope (Leica Microsystems, Wetzlar, Germany) have been used to perform confocal microscopy as well as two-photon microscopy analyses of the samples. The laser delivers over 2.54 W of average power at 900 nm and is tunable from 680 nm to 1300 nm. The repetition rate is 80 MHz and the temporal width at the output of the cavity is around 120 fs (<100fs between 850 nm and 1050 nm). The laser is controlled with the LASX Leicasoftware. Two Leica hybrid descanned detectors (HyD) were used to record images. For two- photon imaging experiments, fluorescence was collected after the microscope objective via a dichroic beamsplitter, transparent to wavelengths greater than 815 nm. Microscope objectives were long working distance dry Leica objectives (HC PL Fluotar 5X NA 0.15, HC PL Fluotar 10X NA

0.3 or HC PL APO 20X NA 0.4 CS2) or oil- immersion Leica objective (HC PL APO 40X NA 1.30 CS2). An electro-optical modulator was used to adjust the laser power at the entrance of the confocal system. The spectral acquisition was performed using an internal hybrid detector. Collected photons were dispersed by a prism and a specific motorized split mirror selecting the spectral detected band before the hybrid detector. Acquisitions were performed between 385 nm and 780 nm every 3 nm and with a spectral bandwidth of 5 nm.

Few milligrams of sample were deposited on a microscope slide. A cover slide was placed on the top of the sample and gently pressed on it.

**Emission spectral profile:** in order to check if the sample produces fluorescence, an emission spectral scan was performed. Typically, the sample is excited at a given wavelength (*e.g.* 1200 nm or 900 nm) while scanned through the emission wavelength (*e.g.* in the 385nm-780nm range). The SHG and THG should appear at the half and at the third of the excitation wavelength, respectively.

4. Results and Discussion

## a. Structure solution and description

The structure solution was carried out using XRD data obtained from a red single crystal with a platelet shape. The unit cell parameters a=9.8307(6) Å, b=18.3900(11) Å, c=10.0023(5) Å and the space group *Cmce* (64) (where *e* denotes both *a* and *b* glide planes, *Cmca* notation is also used in the literature) were determined. The data collection and refinement details are given in table 1. The refinement was carried out with the JANA2006[20] software based on a structure solution obtained using the charge flipping method[21]. The EDS analysis of the single crystals led to the average atomic ratio 50.3/17.5/32.2 for S/V/Ba, respectively, in good agreement with the composition found at end of the refinement, *i.e.* $Ba_5V_2O_4S_8$. As will be discussed later, the formulation can be written $Ba_5(S_2)_2(VO_2S_2)_2$ to consider the structural units involved, see **Figure 1**.

The original structure of $Ba_5(S_2)_2(VO_2S_2)_2$ is a rather opened framework that can be described by two alternating layers. The first layer is formed by disconnected $VO_2S_2$ tetrahedra separated from each other by the large $Ba^{2+}$ cations. In the mixed anion tetrahedra, we find V1-S1= 2.178 (2) Å (two set of distances), V1-O1=1.663 (5) Å and V1-O2= 1.680 (5) Å. This particular heteroleptic environment is found in $K_3(VO_2S_2)$[22] and $Na_3(VO_2S_2)$[23] in which similar V-O and V-S distances are found. In those phases the disconnected tetrahedra are separated by the alkaline cations. The second layer consists in disulfide pairs $(S_2)^{2-}$ surrounded by Ba atoms. The later delimit cavities in which the disulfide pairs are arranged in a 1D manner as depicted in **Figure 1**. Along the $b$ axis, the disulfide pairs are aligned following two parallel columns (1 and 2) shifted along $c$ and $a$ axis. The separation between the $(S_2)^{2-}$ pairs is of ~2.98 Å while a longer distance of 3.539 Å is found for $S^{2-}$–$S^{2-}$ at $[VO_2S_2]$ vertices. The disulfide pairs exhibit distances $d_{S2-S2}$= 2.117(2) Å which are typical distances for $(S_2)^{2-}$ pairs. The three independent barium atoms are 8-coordinated with mixed ($Ba1O_2S_6$ and $Ba2O_4S_4$) or mono-anionic ($Ba3S_8$) environments. The sulfur atoms from $(S_2)$ pairs are coordinated by four Ba atoms with distances in the range 3.103(1) – 3.341(1) Å slightly shorter in average than the Ba-$S^{2-}$ as expected from the lower charge per sulfur atom in a $(S_2)^{2-}$ pair. It can be also illustrated by the difference between the persulfide $BaS_2$ (Ba surrounded by disulfide pairs) with the lowest d(Ba-S)~3.15 Å (up to 3.22 Å) and the sulfide BaS with d(Ba-S) ~ 3.194 Å.

**Table 1.** *Data collection and refinement details*

| | |
|---|---|
| Formula | $Ba_5(S_2)_2(VO_2S_2)_2$ |
| Molecular weight (g. mol$^{-1}$) | 1109.1 |
| Symmetry | *Orthorhombic* |
| Space group | *Cmce* (64) |
| Unit cell dimensions (Å) | a = 9.8307(6) |
| | b = 18.3900(11) |
| | c = 10.0023(5) |
| Volume (Å$^3$) | 1808.28(18) |
| Z | 4 |
| Data Collection | |
| Equipment | Bruker D8 XRK900 |
| $\lambda$ [Ag K$_\alpha$; Å] | 0.56087 |
| Calculated density (g cm$^{-3}$) | 4.0738 |
| Crystal shape | Platelet |
| Crystal dimensions ($\mu$m) | 60×40×10 |
| Color | Red |
| Absorption correction | Analytical |
| Scan mode | $\omega$, $\varphi$ |
| $\theta$ (min–max) (°) | 2.21-35.51 |
| $\mu$ (mm$^{-1}$; for $\lambda$ K$\alpha$ = 0.56087Å) | 6.636 |
| F(000) | 1944 |
| Reciprocal space recording | $-16 \leq h \leq 16$ |
| | $-30 \leq k \leq 29$ |
| | $-16 \leq l \leq 16$ |
| No. of measured reflections | 38730 |
| No. of independent reflections | 2164 |
| I > 3$\sigma$(I) (total) | 1540 |

|  | Refinement |
|---|---|
| Number of refined parameters | 52 |
| Refinement method | Least-squares |
| Weighting scheme | Sigma |
| R1(F) [I > 3σ(I)]/R1(F$^2$) (all data, %) | 0.0288/0.0495 |
| wR2(F$^2$) [I > 3σ(I)]/wR2(F$^2$) (all data, %) | 0.0287/0.0392 |
| Goodness of Fit | 1.25 |
| Max/Min residual electronic density (e$^-$/Å$^3$) | 1.29/−1.28 |
| Tmin / Tmax | 0.6333 / 0.7456 |

**Table 2.** *Atomic positions and isotropic thermal displacement for Ba$_5$(S$_2$)$_2$(VO$_2$S$_2$)$_2$*

| Atom | Wyck. | x | y | z | U$_{eq.}$ |
|---|---|---|---|---|---|
| Ba1 | 8f | 1/2 | 0.10825(2) | 0.09128(4) | 0.01388(11) |
| Ba2 | 8e | 1/4 | 0.30635(2) | 1/4 | 0.01119(10) |
| Ba3 | 4a | 0 | 0 | 0 | 0.0230(2) |
| V1 | 8f | 1/2 | 0.28574(6) | -0.02699(10) | 0.0085(3) |
| S1 | 16g | 0.68001(14) | 0.34968(7) | -0.07497(13) | 0.0171(3) |
| S2 | 16g | 0.10767(14) | 0.46087(7) | 0.19892(13) | 0.0160(3) |
| O1 | 8f | 1/2 | 0.2069(2) | -0.1084(4) | 0.0122(13) |
| O2 | 8f | 1/2 | 0.2613(3) | 0.1348(4) | 0.0144(14) |

**Table 3.** *Anisotropic thermal parameters U$_{ij}$ (Å$^2$) for Ba$_5$(S$_2$)$_2$(VO$_2$S$_2$)$_2$*

| Atom | U$_{11}$ | U$_{22}$ | U$_{33}$ | U$_{12}$ | U$_{13}$ | U$_{23}$ |
|---|---|---|---|---|---|---|
| Ba1 | 0.0126(2) | 0.0112(2) | 0.0178(2) | 0.00000 | 0.00000 | 0.0034(1) |
| Ba2 | 0.0100(2) | 0.0124(2) | 0.0112(2) | 0.00000 | -0.0001(1) | 0.00000 |
| Ba3 | 0.0414(5) | 0.0125(3) | 0.0150(3) | 0.00000 | 0.00000 | -0.0005(2) |
| V1 | 0.0085(5) | 0.0085(5) | 0.0086(4) | 0.00000 | 0.00000 | -0.0008(3) |
| S1 | 0.0118(6) | 0.0158(6) | 0.0237(6) | -0.0034(5) | 0.0025(5) | -0.0006(5) |
| S2 | 0.0143(6) | 0.0137(6) | 0.0201(6) | 0.0020(5) | -0.0013(5) | 0.0011(4) |

| | | | | | |
|---|---|---|---|---|---|
| O1 | 0.014(3) | 0.010(2) | 0.012(2) | 0.00000 | 0.00000 | 0.001(2) |
| O2 | 0.015(3) | 0.017(2) | 0.010(2) | 0.00000 | 0.00000 | -0.003(2) |

**Table 4.** *Main distances (Å) for Ba$_5$(S$_2$)$_2$(VO$_2$S$_2$)$_2$*

| Atoms 1,2 | d 1,2 (Å) | Atoms 1,2 | d 1,2 (Å) |
|---|---|---|---|
| Ba1—S1 | 3.244(1)×2 | Ba3—S2 | 3.272(1)×4 |
| Ba1—S2 | 3.103(1)×2 | Ba3—S1 | 3.367(1)×4 |
| Ba1—S2 | 3.341(1)×2 | | |
| Ba1—O1 | 2.698(5) | V1—S1 | 2.178(2)×2 |
| Ba1—O2 | 2.848(5) | V1—O1 | 1.663(5) |
| Ba2—S2 | 3.208(1)×2 | V1—O2 | 1.680(5) |
| Ba2—S1 | 3.431(1) ×2 | | |
| Ba2—S1 | 3.417(1) ×2 | S2—S2 | 2.117(2) |
| Ba2—O1 | 2.847(2)×2 | | |
| Ba2—O2 | 2.838(2)×2 | | |
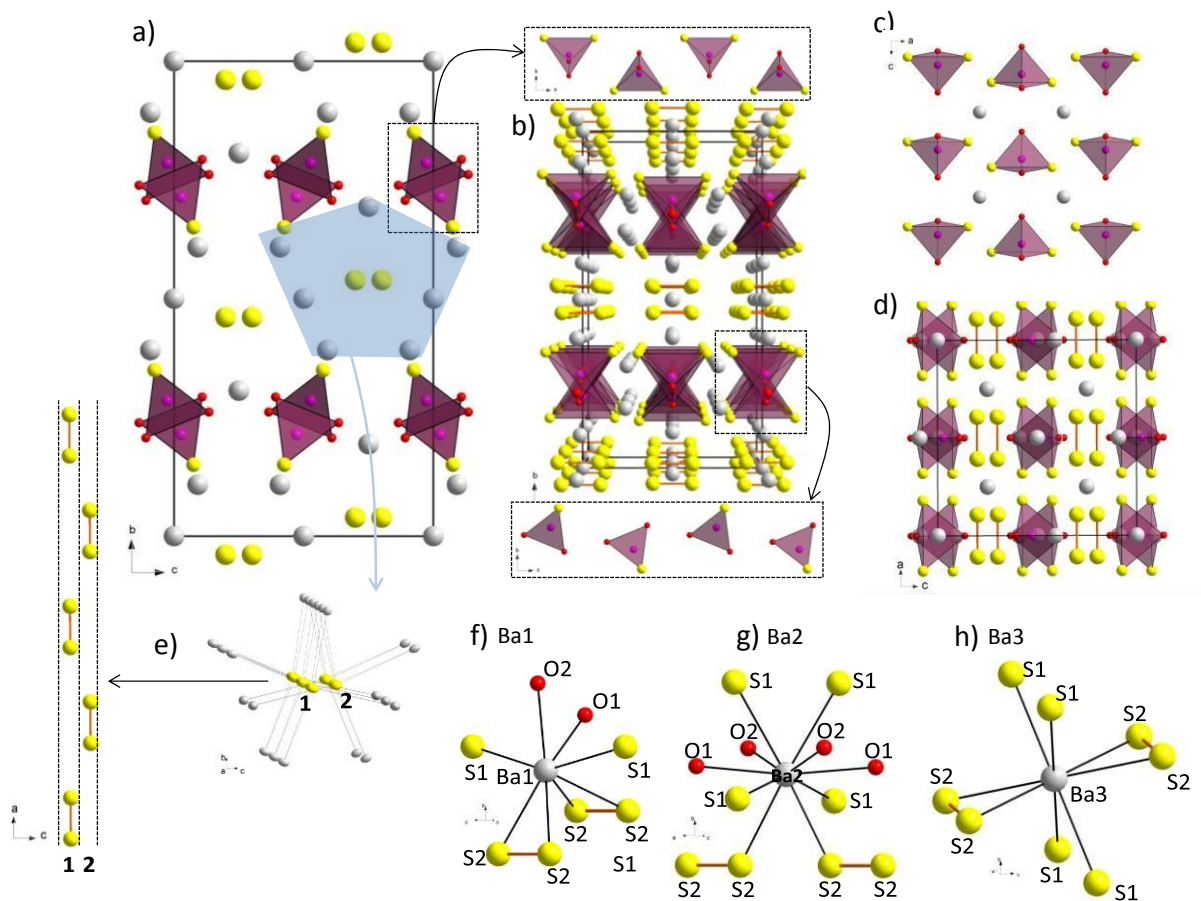
**Figure 1.** a) Structure of $Ba_5(S_2)_2(VO_2S_2)_2$ projected along a axis, b) projection along c axis, c) slice of the structure showing the tetrahedra $VO_2S_2$ arrangement into a layer, d) other view of the structure highlighting the disulfide pairs channel along a, e) view of the disulfide pairs and the surrounding Ba atoms forming a channel around them and projection showing the 1D arrangement between the disulfide pairs, f-g-h) Ba atoms environments with Ba-S distances indicated and S-S bonds represented when present in their vicinity: Ba1, Ba2 and Ba3.

## b. Polycrystalline phase analysis

The synthesis of the pure powder phase was attempted following the procedure described in the experimental section. As depicted in **Figure 2.a**, the title phase is formed while the minor impurity $Ba_6(VO_2S_2)_2(VS_3O)(VS_4)$, for which the structure is discussed later as part of the Ba-V-S-O system, is identified. A multiphase Rietveld refinement using Jana2006[20] based on the single crystal structural model was carried out and led to very good reliability factors ($R_{obs}$= 0.0474, $wR_{obs}$= 0.0478, $R_{all}$= 0.0488, $wR_{all}$= 0.0481 and GOF= 1.48). The Rietveld quantification indicates the ratio 0.918(3)/0.082(3) for the title phase/impurity.

50

### c. Relationship with other structure types in the Ba-V-S-O system

As mentioned above, the title phase represents the fifth member, to the best of our knowledge, in the quaternary system Ba-V-S-O which reveals complex and diversified structure types. The $Ba_{15}V_{12}S_{34}O_3$ phase[24] is formed of quasi-one-dimensional zigzag chains along the *c* axis connected by an oxygen atom. The chains are formed of face-sharing $VS_6$ octahedra and with $VS_5O$ at the bends. The zigzag chains and their interconnection give rise to a lattice (layer) resembling a fence. The fence layers are stacked along the *a* axis. The cavities of the fence exhibit the mixed anion $VS_3O$ tetrahedra. On another hand, $Ba_3V_2O_3S_4$ is a quasi-1D S=1 magnet and strongly correlated Mott insulator[25], with a cooperative polar arrangement of $VO_3S$ units leading to the non-centrosymmetric space group $P6_3$. These units together with $Ba^{2+}$, separate $(VS_3)_\infty$ chains built from face-sharing $V^{3+}S_6$ octahedra. Considering the two above mentioned structure, they are quite different from the title phase which is exclusively made of unconnected $V^{5+}O_2S_2$ tetrahedra. Another major difference is the mixed valence state of the vanadium associated to magnetism in those reported phases. Common features can be found however in the remarkable phase $Ba_6V_4O_5S_{11}$ which exhibits different unconnected mixed anion tetrahedra that coexist separated by the $Ba^{2+}$ cations, *i.e.* $Ba_6(VO_2S_2)_2(VS_3O)(VS_4)$, with $VOS_3$, $VO_2S_2$ (as found in our phase) and $VS_4$ units[26]. Finally, we have recently reported the orange oxysulfide $Ba_{10}V_6S_7O_{18}$, which can be written $Ba_{10}S(VO_3S)_6$ and crystallizes in the non-centrosymmetric $P6_3$ space group. It is formed of disconnected $VO_3S$ tetrahedra separated by $Ba^{2+}$ cations[27]. This phase represents a different structure type with a distinct symmetry but exhibits some similarities with the title phase, i.e. a framework with "channels" and unconnected oxysulfide tetrahedra. Then, the channels are occupied by isolated and disordered $S^{2-}$ anions while we observe aligned disulfide pairs. On another hand, $VO_3S$ tetrahedra are found versus $VO_2S_2$ in the title compound.

### d. Optical measurements

The UV–visible diffuse reflectance analysis of the polycrystalline $Ba_5V_2O_4S_8$ is represented in **Figure 2.b**. A Kubelka–Munk transformation[28] was applied to the measured diffuse reflectance (R) spectra using the function $F(R) = (1 − R)^2/2R$. Then a Tauc plot[29] was used to determine the optical band gap $E_g$, using the equation, $(F(R)·hv)^{1/n}= k(hv−E_g)$, where $hv$ is the photon energy, $k$ an energy-independent constant, $E_g$ the optical band gap and $n$, an exponent related to the type of transition. Assuming a direct allowed transition (exponent $n= ½$), the plot of $(F(R)·hv)^2$ versus $hv$ allowed, after drawing a tangent line at the inflection point, to determine $E_g= 2.2$ eV. This is consistent with the observed red color of the crystals and the red-brownish powder.

## e. DFT calculations

The total and projected densities of states are shown in **Figure 2.d**. and focus in the region around the Fermi level of the valence band (VB) and the conduction band (CB). Within the $VO_2S_2$ building units, the vanadium atoms $3d$ states are lying in the conduction band starting from ~1.3 eV up to ~5.8 eV with the main contribution up to 3.7 eV approximatively. In the VB, the vanadium $3d$ states contribution is found roughly in the range -5 to -1 eV. They are hybridized with the O $2p$ and S $3p$ states of the $VO_2S_2$ building units. As expected from their electronegativity difference, O $2p$ has the strongest contribution lower in the VB (with the main large peak centered around -4.5 eV) and the $S_{(VO2S2)}$ $3p$ states is found mainly around -2.5 eV, *i.e.* higher in the VB. In a previous report[27], we have studied the projected density of states (PDOS) on the different mixed anion tetrahedra $V(O,S)_4$ found in $Ba_6(VO_2S_2)_2(VS_3O)(VS_4)$. It illustrates the evolution of their contributions higher in the VB when increasing the sulfur content (from $VO_3S \rightarrow VS_4$).

Concerning the sulfur atoms involved in the disulfide pairs, their contributions is distinct within the VB. Those isolated species exhibit more localized states in comparison with the other anions of the structure, $S^{2-}$ and $O^{2-}$ around vanadium. Just below the Fermi level, $(S_2)^{2-}$ $3p$ states dominate while $S^{2-}$ involved in $VO_2S_2$ tetrahedra exhibit broader states lower in the VB as described above. Regarding the electronic structure description, the title phase may be decomposed as the combination of the structural entities $(Ba_5)^{10+}(S_2)_2^{4-}(VO_2S_2)_2)^{6-}$.

The electron localization function (ELF) has also been computed and allows the visualization of the nodal structure of the molecular orbital. The ELF maxima reflect localized electron pairs, in

particular it allows investigating covalent bonds and Lone Pair electrons[30]. On **Figure 2.c**, a slice of the ELF clearly shows the covalent bonding between two sulfur atoms involved in a disulfide pairs.
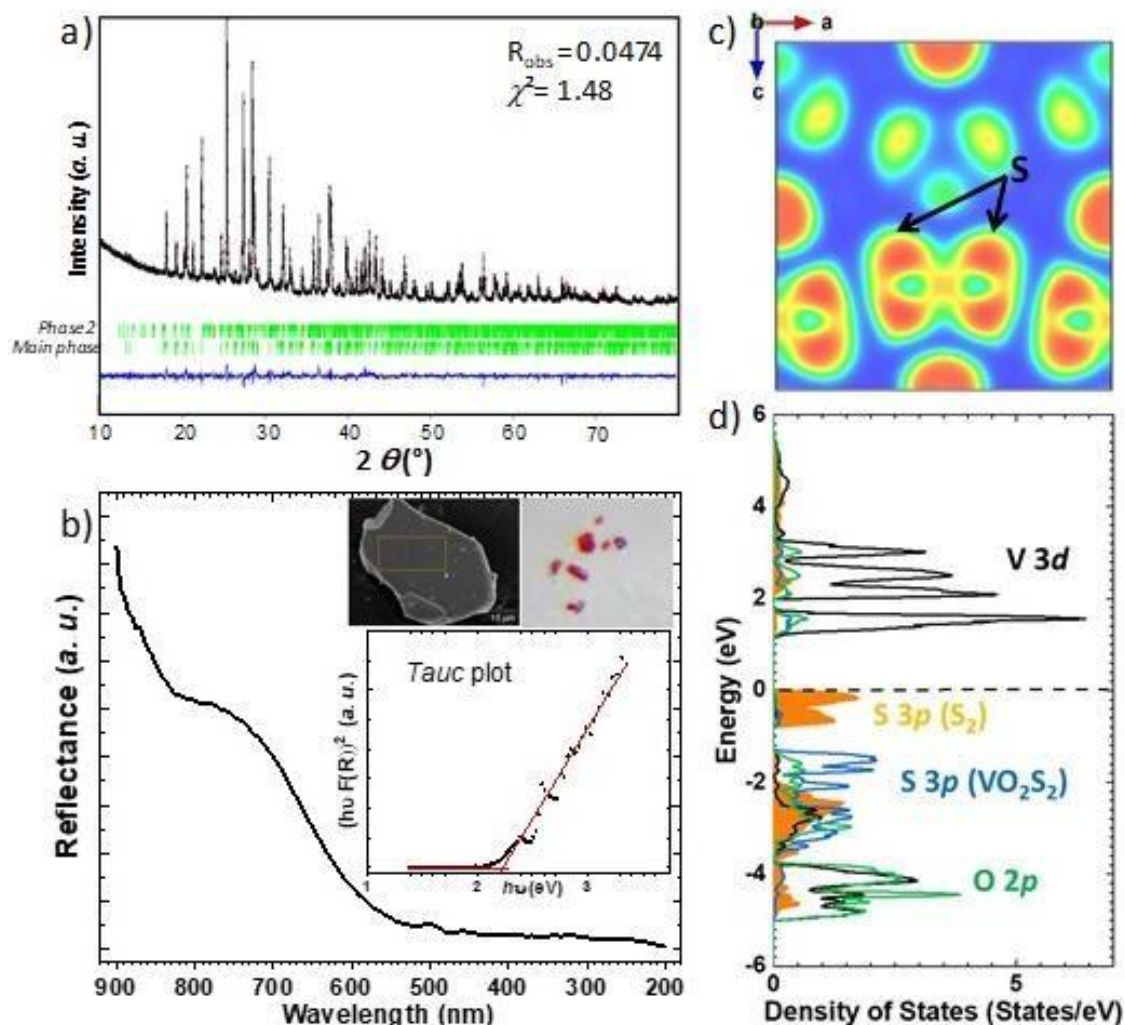


*Figure 2. a) Powder XRD Rietveld refinement: the experimental pattern (black) and calculated pattern (red) are superimposed; the difference curve and the Bragg positions are represented in blue and green, respectively. b) Diffuse reflectance spectra with a Tauc plot as an inset to determine the experimental band gap; a picture of the reddish crystals and of a crystal SEM image are also shown as insets. c) DFT computed Electron Localization Function (ELF) with an S-S bond highlighted and d) the density of states (DOS) calculated for the title phase. The projected DOS is shown for the V (3d), O (2p) and S (3p) states. For the later, sulfur from the $VO_2S_2$ tetrahedra and sulfur from the disulfide pairs are distinguished. The Fermi level is set to 0.*

## f. Band gap engineering

Band gap engineering possibilities from an heteroleptic coordination at the transition metal site is particularly well illustrated in the $A_3(VO_{4-x}S_x)$ ($A$= Na$^+$, K$^+$, $x$= 0 to 4) phases, constituted of alkaline cations $A^+$ and disconnected $V(O_{4-x}S_x)$ tetrahedra. The variable O/S ratios lead to colors ranging from white to deep red for $VO_4 \rightarrow VO_3S \rightarrow VO_2S_2 \rightarrow VOS_3 \rightarrow VS_4$. The cationic sub-lattice (Na$^+$ vs. K$^+$) and the symmetry differences impact the band gap. Besides, the S/O ratio of the $VO_{4-x}S_x$ tetrahedra seems to play a major role as shown from the DFT-GGA calculated band gaps of these series $A_3(VO_{4-x}S_x)$[23, 22]. From that assumption, we rationalized in a previous report the electronic structure of $Ba_{10}S(VO_3S)_6$[27] in relation with its crystallo-chemical characteristics. In particular, we put forward the role of isolated $S^{2-}$ that decrease the band gap compared to $A_3(VO_3S)$. Concerning the title phase, our DFT-GGA calculations with a similar level of approximation give a band gap of ~ 1.3 eV, underestimated as expected from the used functional. It compares better with the $A_3(VO_{4-x}S_x)$ (A= Na, K) phases exhibiting a higher ratio S/O ($x$>3) in $VO_{4-x}S_x$ tetrahedra than with the orange $A_3(VO_2S_2)$ phases due to the contribution of the disulfide pairs that lead to a narrower band gap.

They are a limited number of systems exhibiting such isolated sulfur species. They are found in the form of $S^{2-}$ anions or of disulfide pairs $(S_2)^{2-}$ in $Ba_{12}In_4S_{19}$[31] and BaFS[32] for instance, with a pivotal role in the band gap nature.

Considering other low dimensional systems, disulfide pairs are found in the layered phases $[A_2O_2](S_2)$ (A= La, Pr, Nd)[33] which are constituted by the alternative stack of fluorite-type $[A_2O_2]^{2+}$ layers and disulfide $(S_2)^{2-}$ layers arranged in a planar sheet. In particular, the $La_2O_2S_2$ phase (**Figure 3**) crystallizes in the *Cmce* space group[34] with a band gap ~2.55 eV and exhibits photoluminescent properties upon doping[35].
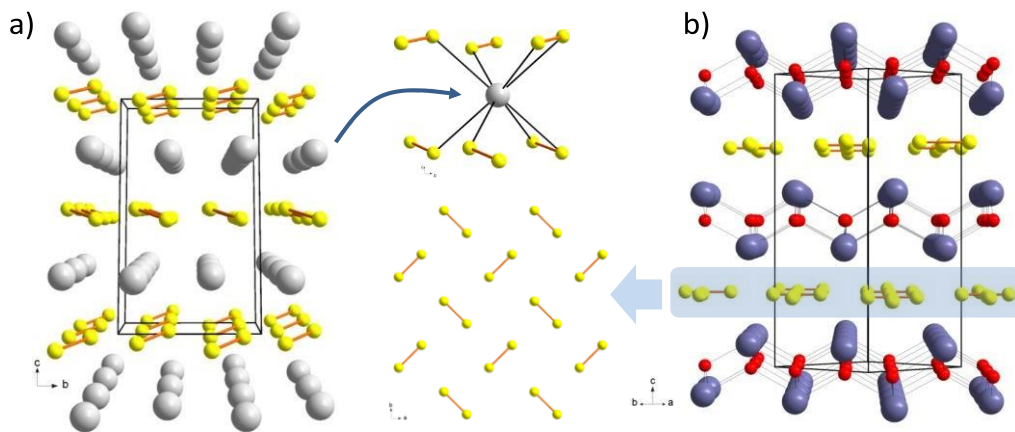
**Figure 3.** *a) Structure of BaS$_2$ with emphasize on Ba environment exhibiting $d_{Ba-S}$ ranging from ~3.15 to 3.22Å and b) structure of the phase La$_2$O$_2$S$_2$ with a projection of disulfide layers showing the disulfide pairs 2D arrangement, each (S$_2$) is 90° rotated with respect to its neighbors.*

## Thermal stability
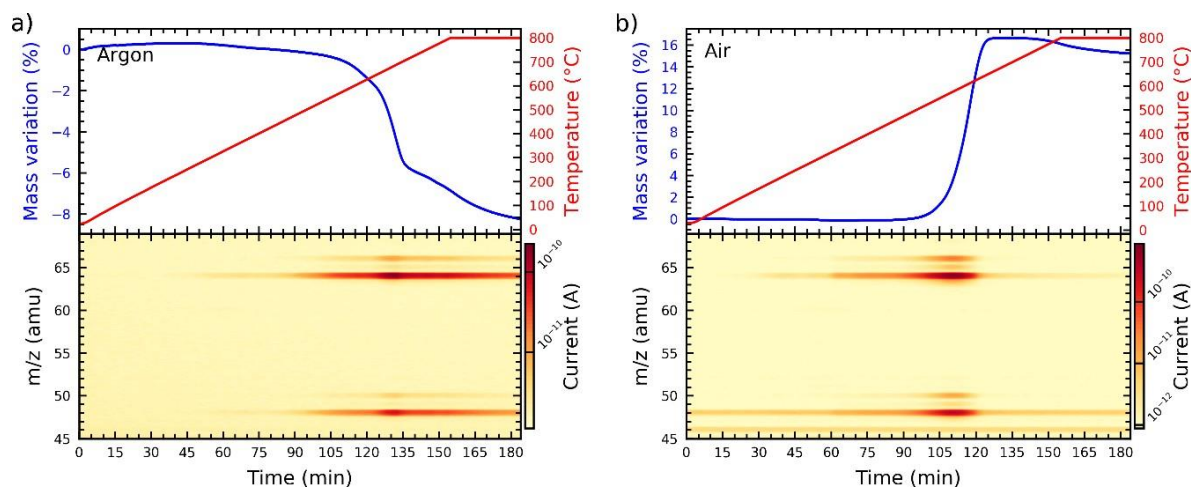


**Figure 4**: *Thermogravimetric analysis (upper panes) coupled with mass spectrometry (lower panes) of Ba$_5$(VO$_2$S$_2$)$_2$(S)$_2$ a) under argon and b) under synthetic air. The mass variation and the temperature are given as a function of time.*

The thermal stability of Ba$_5$(VO$_2$S$_2$)$_2$(S)$_2$ was investigated, under argon and air atmospheres, using thermogravimetric analysis coupled with mass spectrometry in the range 30 – 800 °C (**Figure 4**). In both cases a very slow release of SO$_{2(g)}$ is observed for temperature higher than ~300 °C. The nature of the evolved gas is clearly identified by the signals measured at m/z = 64 amu (SO$_2^+$) and

m/z = 48 amu ($SO^+$), interestingly we can rule out the evolution of hydrogen sulfide (m/z = 34 amu, not shown here). Under argon (**Figure 4.a**), this decomposition process suddenly accelerates around 600 °C resulting in a sharp mass loss of 5.6 %, close to the theoretical mass loss expected for the loss of two sulfur atoms per formulae unit (5.78 %). Typically, it may correspond to a disulfide pair as would be expected from their specific reactivity (compared to $S^{2-}$ within $VO_2S_2$ tetrahedra) as will be discussed later in the case of redox reactions. Then the observed mass loss would correspond to a $Ba_5V_2O_4S_6$ intermediary composition. In this case, if one disulfide pair is lost, the remaining one should break in a reductive process to form a compound with isolated $S^{2-}$ anions in order to keep the charge balance if we consider preserved $V^{5+}O_2S_2$, i.e. $Ba_5(VO_2S_2)_2(S)_2$. If the remaining ($S_2$) is preserved, another scenario would be a reduction of vanadium, but in that case it should be accompanied by drastic structural changes as observed for instance after the ammonolysis of $LaVO_4$ ($V^{5+}O_4$ disconnected tetrahedra) into the reduced Perovskite-type $LaVO_{2.78}N_{0.1}$ [36]. Further studies will be conducted to characterize this possible intermediate phase. Past 700 °C the decomposition of sulfur species continues at a slower rate. The XRD analysis of the residue show a decomposition into BaS, $Ba_3(VO_4)_3$ with a small amount of $Ba_6(VO_2S_2)_2(VS_3O)(VS_4)$ while some peaks remain unassigned and will be further investigated.

Under air (**Figure 4.b**), the sudden evolution of $SO_{2(g)}$ is observed at a lower temperature of about 550 °C, the mass loss associated with the release of sulfur is however covered by the oxidation of sulfides to sulfates. The mass increases up to 16.7 % and stay stable from 650 – 750 °C, further heating results in the slow decomposition of the product. The stability of the mass in the 650 – 750 °C also point at a stable composition which still need to be elucidated. The XRD analysis of the residue shows a full decomposition into $BaSO_4$ and $V_2O_5$.

It is interesting to mention the new and reversible topochemical route for copper insertion into $(Q_2)^{2-}$ (Q=S, Se) dimers to design layered transition metal chalcogenides using low-temperatures[37]. In particular copper was inserted in the $(S_2)^{2-}$-containing phases $La_2O_2S_2$ and $Ba_2F_2S_2$ to form the corresponding layered copper chalcogenides. Remarkably, the redox centers

upon Cu insertion are the chalcogen pairs. Our phase should be an interesting precursor for such topotactic modifications.

Considering other possible reactions, one can also imagine a reaction that may lead to an original phase exclusively formed of $VO_2S_2$ building blocks and $Ba^{2+}$ atoms that should have an increased band gap, i.e. $Ba_5(VO_2S_2)_2(S)_2 \rightarrow 2BaS_2 + Ba_3(VO_2S_2)_2$.

### g. Electron microscopy

We have also performed electron diffraction experiments to probe the structure at a different scale, see **Figure 5**. According to the work of Morniroli[38], the comparison of the difference of periodicity and shift between the zero (ZOLZ) and first order Laue zone (FOLZ) of the [010], [100], [001] zone axis electron diffraction pattern for the orthorhombic system leads to an extinction symbol. The determined extinction symbol gives the Bravais lattice and other information such as the existence of a glide plane. This information helps for the determination of the space group. In our case, the extinction symbol is *C - - e* (- means no glide plan). The analysis of this particular crystallite indicates no glide plane. A rotation along the basic axis (a, b, c) indicates a screw $2_1$ axis along c. This is consistent with the non-centrosymmetric (NCS) space group Cm2e and with the space group Cmme. Moreover, from the XRD single crystal analysis, those space groups are not relevant since no reflection violating the *c* glide plane (l= 2n+1) can be detected in the (h0l) plan presented on **Figure 5.d**. from our XRD data). Then, the reconstitution of the reciprocal space in diffraction, which allows confirming the cell parameters as well as highlighting the extinction conditions and supplementary structural phenomenon like superstructure, was not possible because the sample is very sensitive to the beam. It prevents any high resolution imaging to further analyze the structure and eventually reveal very local structural information like order, disorder *etc*…. From this study, one can deduce a possible reactivity of the sample or the potential occurrence of non-centrosymmetric crystallites or domains. This will be further investigated in next section.
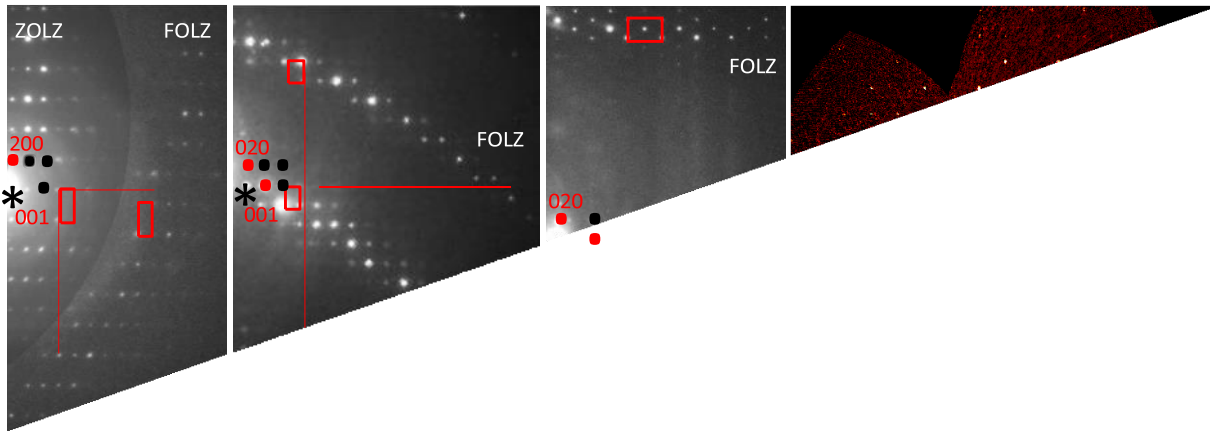
**Figure 5:** *Electron diffraction patterns: comparison between the zero and first order Laue Zone (ZOLZ and FOLZ) in the a) [010] b) [100] and c) [001] zone axis pattern. The deducted extinction is C - - a or C- - b. d) (h0l) plan from single crystal XRD data collection.*

*Non-linear optical properties*

SHG measurements were carried out, initially to investigate possible non-centrosymmetric contribution in the polycrystalline sample regarding electron microscopy results. Bright field and SHG images for excitation of $Ba_5(VO_2S_2)_2(S)_2$ at 900 nm are presented in **Figure 7**. The emission spectrum (integrated over the whole field of view) is plotted in **Figure 8**.

First, we note that the emission spectrum exhibits a typical SHG peak (half of the excitation wavelength, *i.e.* 450 nm) and a fluorescence emission mainly in the 500 nm -750 nm range. SHG and fluorescence, are however relatively low and seems to decrease with exposure time. More into details, the THG intensity only decreases by 10% in circa 3 sec and then remains constant under laser irradiation while SHG intensity is divided by 2.5 in circa 10 sec. This could be due to a chemical pollution partially degraded under laser beam. For an excitation wavelength of 1200 nm, behavior for SHG evolution is similar to the excitation at 900 nm.

Second, on **Figure 6.b** and **6.c**, it clearly appears that the SHG emission is not homogeneously distributed over the sample (sparsely distributed spots). To go deeper into this observation, the emission spectra from different regions of interest (ROI) marked by squares in **Figure 6**. were plotted in **Figure 8**. One can notice two main different spectra: (i) Spectra with strong SHG emission for ROI2 and ROI3 and (ii) Spectra with no SHG emission and only fluorescence in the

500 nm -750 nm range for ROI1 and ROI4. It means that the particles constituting the sample mainly correspond to a centrosymmetric crystalline phase whereas the SHG signal detected is mainly due to particular zones of non-centrosymmetry. The SHG signal could then be attributed to impurities (a possible explanation could be the presence of quartz slivers, observed with a binocular and stemming from the synthetic procedure). Nevertheless, regarding electron microscopy results, we cannot exclude that the SHG spots might arise from a non-centrosymmetric phase close but different from the predominant centrosymmetric $Ba_5(VO_2S_2)_2(S)_2$ crystalline phase either structurally (polymorph) or chemically (derivative).

*Figure 6:* $Ba_5(VO_2S_2)_2(S)_2$ *Bright Field (a), SHG (b) and overlay of both (c) images for excitation at 900 nm. ROI are represented by squares.*
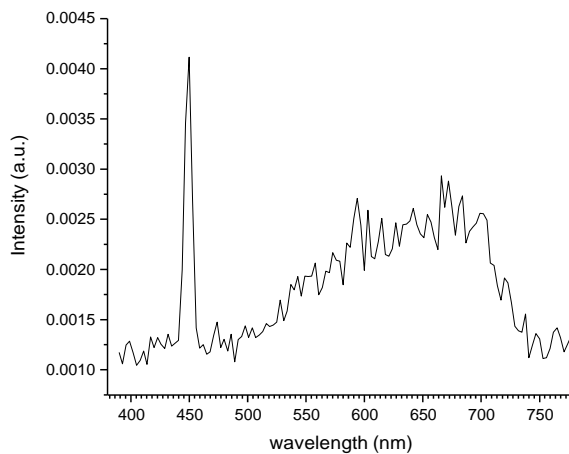


*Figure 7:* Emission spectrum of $Ba_5(VO_2S_2)_2(S)_2$ for excitation at 900 nm.
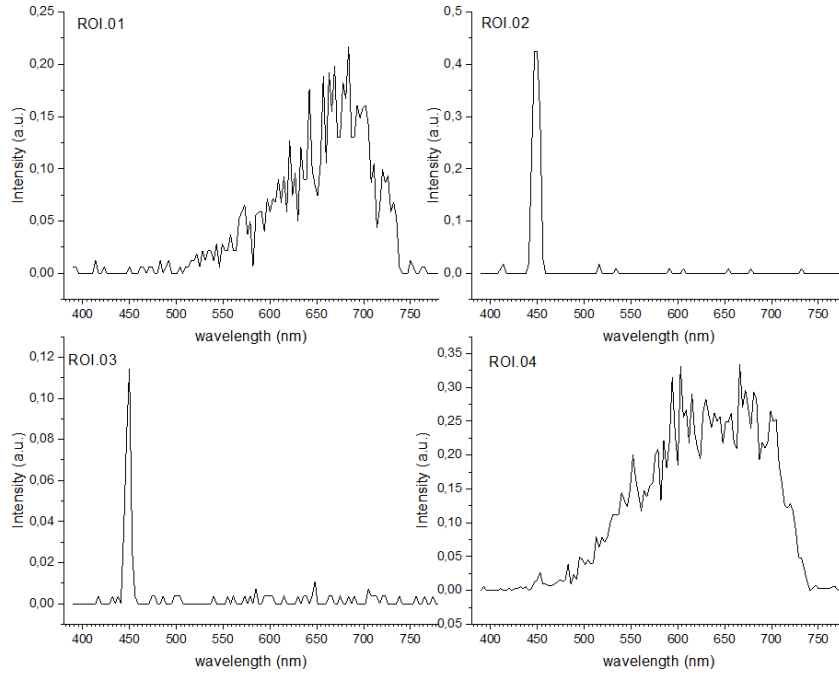
*Figure 8:* Emission spectra from ROIs in $Ba_5(VO_2S_2)_2(S)_2$ for excitation at 900 nm.

Third Harmonic Generation (THG) signal was also recorded and is evenly distributed across the sample as shown in **Figure 9**. One should recall that THG is not restricted to NCS structures and can occur either in centrosymmetric or NCS structures. **Figure 10** clearly shows a THG peak at 400 nm on the emission spectrum of the sample for excitation at 1200 nm.
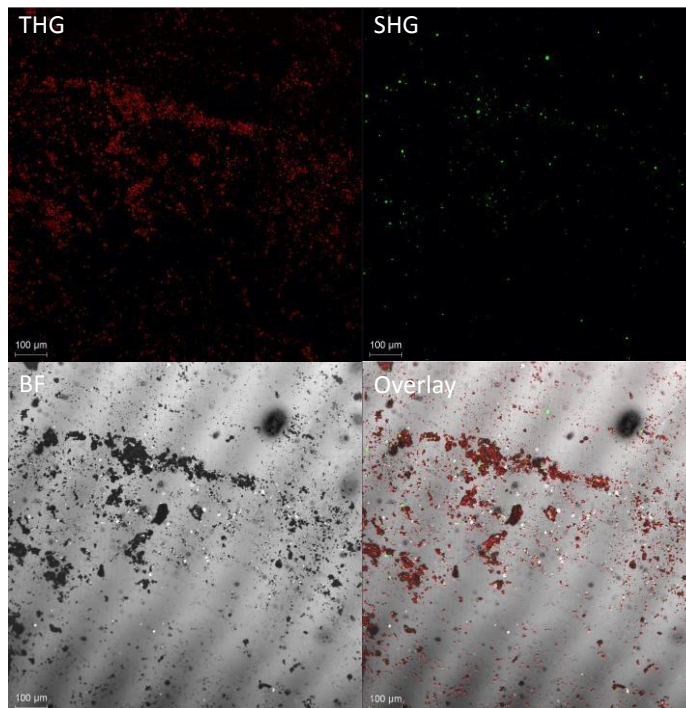
*Figure 9: THG, SHG, BF and overlay of both (right image) of Ba$_5$(VO$_2$S$_2$)$_2$(S)$_2$ for excitation at 1200 nm*

More into details, over the whole field of view, the ratio THG/SHG is 14. The conversion efficiency of THG is usually much lower than SHG[39]. The fact that THG is much higher than SHG also supports the assumption of a pollution of the sample. These observations are thus consistent with the centrosymmetric *Cmce* space group determined from XRD for Ba$_5$(VO$_2$S$_2$)$_2$(S)$_2$ which excludes the application of this phase for frequency doubling.

However, an interesting feature of this compound is its relatively high third-harmonic generation (THG) signal. Such non-linear optical properties have been for instance reported in centrosymmetric Cu$_2$O crystals which have shown large third-order susceptibility and third-harmonic generation[40]. To cite a few other inorganic crystalline solids, THG has also been investigated in other oxides such as LiKB$_4$O$_7$ [41] or the centrosymmetric rutile TiO$_2$ (*P*4$_2$/mnm) with efficient triple photon generation [15]. In non-oxides, the fluoride BaMgF$_4$ [42] has recently shown the highest direct UV-third harmonic generation conversion efficiency in a solid state system via pure $\chi^{(3)}$ nonlinear process. In the chalcogenide phases Ag$_x$Ga$_x$Ge$_{1-x}$Se$_2$, THG have been related to the anions coordination within (Ga, Ge)Se$_4$ tetrahedra and their resulting dipole moments that define the optical nonlinearities [43]. In our case, we report interesting THG properties in a

crystalline oxychalcogenide, which to the best of our knowledge is rather uncommon for this type of crystalline materials.

More into details, we have performed a comparison of THG intensity emitted by $Cu_2O$, known for its high THG signal as mentioned above, and $Ba_5(VO_2S_2)_2(S)_2$ powdered samples. Emission spectra of $Cu_2O$ and $Ba_5(VO_2S_2)_2(S)_2$ for excitation at 1200 nm are plotted in **Figure 10**. The peak at 400 nm is attributed to third harmonic generation of the samples. One can notice fluorescence of the samples in the 580 nm – 720 nm range. The average THG signal generated by the $Ba_5(VO_2S_2)_2(S_2)_2$ powder sample is approximately twice lower than the THG signal of a $Cu_2O$ also in the powder form. In the light of this information, $Ba_5(VO_2S_2)_2(S_2)_2$ single-crystal is prone to exhibit interesting $3^{rd}$ order nonlinear properties.
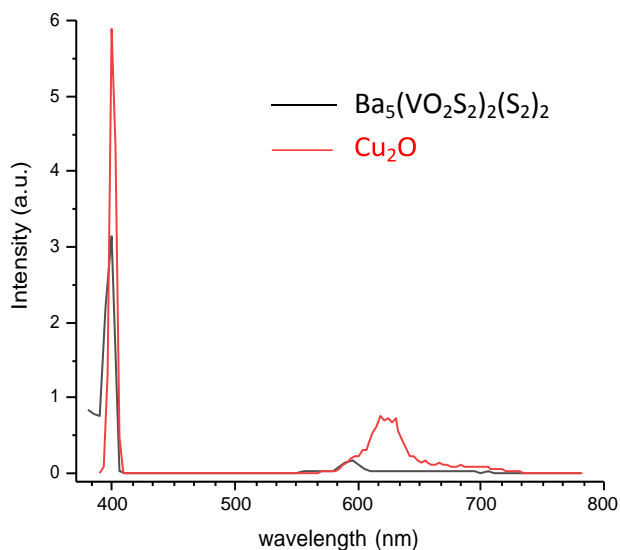


**Figure 10:** *Emission spectra of $Cu_2O$ and $Ba_5(VO_2S_2)_2(S)_2$ for excitation at 1200 nm*

## 5. Conclusion

The new oxysulfide $Ba_5(VO_2S_2)_2(S)_2$ was identified and its structure solved in the space group *Cmce*. It represents an original member, the fifth, in the quaternary system Ba-V-S-O. This phase exhibits the mixed anion building units $VO_2S_2$ and isolated disulfide pairs. The DFT study show that the $(S_2)^{2-}$ $3p$ states found just below the Fermi level dictate the band gap while the other anions involved in $VO_2S_2$ tetrahedra and in particular $S^{2-}$ anions exhibit broader states lower in

the VB. The rationalization of the structure with respect to the electronic structure show all the interest of designing new phases using such mixed anion building blocks and/or disulfide pairs. In particular, band gap engineering trough mastered approaches is important for a variety of properties. Despite the absence of second harmonic generation stemming from the existence of a center of inversion in the crystal structure, we show in this new phase third-harmonic generation properties. To the best of our knowledge, this is rather uncommon in oxychalcogenide or mixed anion crystalline solids. Thus, $Ba_5(VO_2S_2)_2(S)_2$ deserves further investigations in order to fully access the nonlinear optical $\chi^{(3)}$ coefficients. This will be crucial to evaluate its potential for nonlinear optical applications.

Crystal structure report

CCDC Deposition Number 1969802 contains the supplementary crystallographic data for this paper. The data can be obtained free of charge from The Cambridge Crystallographic Data Centre via https://www.ccdc.cam.ac.uk/structures

6. REFERENCES

[1] Kageyama, H.; Hayashi, K.; Maeda, K.; Attfield, J.-P.; Hiroi, Z.; Rondinelli, J. M.; Poeppelmeier, K. R. Expanding frontiers in materials chemistry and physics with multiple anions. *Nature Communications* **2018**, 9(1), 772.

[2] Ahmed, M.; Xinxin, G. A. Review of Metal Oxynitrides for Photocatalysis. *Inorg. Chem. Front.* **2016**, 3 (5), 578–590.

[3] Kim, S.-W.; Pereira, N.; Chernova, N. A.; Omenya, F.; Gao, P.; Whittingham, M. S.; Amatucci, G. G.; Su, D.; Wang, F. Structure Stabilization by Mixed Anions in Oxyfluoride Cathodes for High-Energy Lithium Batteries. *ACS Nano* **2015**, 9 (10), 10076–10084.

[4] Muhammady, S.; Kurniawan, Y.; Ishiwata, S.; Rousuli, A.; Nagasaki, T.; Nakamura, S.; Sato, H.; Higashiya, A.; Yamasaki, A.; Hara, Y.; et al. Electronic and Thermoelectric Properties of Layered Oxychalcogenides (BiO)CuCh (Ch = S, Se, Te). *Inorg. Chem.* **2018**, 57 (16), 10214–10223.

[5] Kabbour, H.; Janod, E.; Corraze, B.; Danot, M.; Lee, C.; Whangbo, M.-H. and Cario, L. Structure and Magnetic Properties of Oxychalcogenides $A_2F_2Fe_2OQ_2$ (A= Sr, Ba; Q= S, Se) with $Fe_2O$ Square Planar Layers Representing an Antiferromagnetic Checkerboard Spin Lattice. *J. Am. Chem. Soc.* **2008**, 130, 8261–8270.

[6] Blandy, J. N.; Liu, S.; Smura, C. F.; Cassidy, S. J.; Woodruff, D. N.; McGrady, J. E.; Clarke, S. J. Synthesis, Structure, and Properties of the Layered Oxide Chalcogenides $Sr_2CuO_2Cu_2S_2$ and $Sr_2CuO_2Cu_2Se_2$. *Inorg. Chem.* **2018**, 57 (24), 15379–15388. b) Lü, M.; Mentré, O.; Gordon, E. E.; Whangbo, M.-H.; Wattiaux, A.; Duttine, M.; Tiercelin, N.; Kabbour, H. A Comprehensive Study of Magnetic Exchanges in the Layered Oxychalcogenides $Sr_3Fe_2O_5Cu_2Q_2$ (Q=S, Se). *Journal of Magnetism and Magnetic Materials* **2017**, 444, 147–153.

[7] Luu, S. D. N.; Vaqueiro, P. Layered Oxychalcogenides: Structural Chemistry and Thermoelectric Properties. *Journal of Materiomics* **2016**, 2 (2), 131–140.

[8] a) Miura, A.; Oshima, T.; Maeda, K.; Mizuguchi, Y.; Moriyoshi, C.; Kuroiwa, Y.; Meng, Y.; Wen, X.-D.; Nagao, M.; Higuchi, M.; et al. Synthesis, Structure and Photocatalytic Activity of Layered $LaOInS_2$. *J. Mater. Chem. A* **2017**, 5 (27), 14270–14277. b) Kabbour, H. ; Sayede, A. ; Saitzek, S. ; Lefèvre, G. ; Cario, L. ; Trentesaux, M. and Roussel, P. Structure of the water-splitting photocatalyst oxysulfide α-$LaOInS_2$ and ab initio prediction of new polymorphs. *Chemical Communications* **2020,** 56, 1645.

[9] Kuriki, R.; Ichibha, T.; Hongo, K.; Lu, D.; Maezono, R.; Kageyama, H.; Ishitani, O.; Oka, K.; Maeda, K. A Stable, Narrow-Gap Oxyfluoride Photocatalyst for Visible-Light Hydrogen Evolution and Carbon Dioxide Reduction. *J. Am. Chem. Soc.* **2018**, 140 (21), 6648–6655.

[10] Liu, B. W.; Jiang, X.-M; Wang, G.-E; Zeng, H.-Y.; Zhang, M.-J.; Li, S.-F.; Guo, W.-H.; Guo, G.-C. Oxychalcogenide $BaGeOSe_2$: Highly Distorted Mixed-Anion Building Units Leading to a Large Second-Harmonic Generation Response. *Chem. Mater.* **2015**, 27, 24, 8189-8192.

[11] Tsujimoto, Y.; Juillerat, C. A.; Zhang, W.; Fujii, K.; Yashima, M.; Halasyamani, P. Shiv.; zur Loye, H.-C. Function of Tetrahedral $ZnS_3O$ Building Blocks in the Formation of $SrZn_2S_2O$: A Phase Matchable Polar Oxysulfide with a Large Second Harmonic Generation Response. *Chem. Mater.* **2018**, 30 (18), 6486–6493.

[12] Hongil, J.; Kim, H.-G.; Byun, H.-R.; Jang, J. I., Ok, K. M. Synthesis, structure, and third-harmonic generation measurements of a mixed alkali metal iodate, $KLi_2(IO_3)_3$. *Journal of Solid State Chemistry*, **2020**, 282, 121120.

**[13]** Boyd, R, W. Nonlinear Optics; 3rd Edition, Academic Press: San Diego USA, **2008**

[14] Hübel, H.; Hamel, D. R.; Fedrizzi, A.; Ramelow, S.; Resch, K. J.; Jennewein, T. Direct generation of photon triplets using cascaded photon-pair sources. *Nature* **2010**, 466, 601

[15] Gravier, F. and Boulanger, B. Cubic parametric frequency generation in rutile single crystal. *Optics Express* **2006**, 14, 11715

[16] Blöchl, P. E. Projector Augmented-Wave Method. *Phys. Rev. B* **1994**, 50 (24), 17953–17979.

[17] Kresse, G.; Joubert, D. From Ultrasoft Pseudopotentials to the Projector Augmented-Wave Method. *Phys. Rev. B* **1999**, 59 (3), 1758–1775.

[18] G. Kresse et al.: Vienna ab-initio simulation package (VASP), https://www.vasp.at

[19] Perdew, J. P.; Burke, K.; Ernzerhof, M. Generalized Gradient Approximation Made Simple. *Phys. Rev. Lett.* **1996**, 77 (18), 3865–3868.

[20] Petříček, V.; Dušek, M.; Palatinus, L. Crystallographic Computing System JANA2006: General Features. Zeitschrift für Kristallographie - *Crystalline Materials* **2014**, 229 (5), 345–352.

[21] Lee, A. van der. Charge Flipping for Routine Structure Solution. *J. Appl. Cryst.* **2013**, 46 (5), 1306–1315.

[22] Schnabel, S.; Röhr, C. Kalium-Thio/Oxo-Vanadate(V) $K_3[VS_xO_{4-x}]$ (x = 1–4) Und $Na_3[VSO_3]$: Synthese, Strukturchemie, Eigenschaften. *Zeitschrift für Naturforschung B* **2014**, 63 (7), 819–833.

[23] Schnabel, S.; Röhr, C. Gemischte Thio/Oxo-Orthovanadate $Na_3[VS_xO_{4-x}]$ (x = 2, 3): Darstellung – Strukturen – Eigenschaften / Mixed Thio/Oxo Orthovanadates $Na_3[VS_xO_{4-x}]$ (x = 2, 3): Synthesis – Crystal Structures – Properties. *Zeitschrift für Naturforschung B* **2014**, 60 (5), 479–490.

[24] Wong, C. J.; Hopkins, E. J.; Prots, Y.; Hu, Z.; Kuo, C.-Y.; Pi, T.-W.; Valldor, M. Anionic Ordering in $Ba_{15}V_{12}S_{34}O_3$, Affording Three Oxidation States of Vanadium and a Quasi-One-Dimensional Magnetic Lattice. *Chem. Mater.* **2016**, 28 (6), 1621–1624.

[25] Hopkins, E. J.; Prots, Y.; Burkhardt, U.; Watier, Y.; Hu, Z.; Kuo, C.-Y.; Chiang, J.-C.; Pi, T.-W.; Tanaka, A.; Tjeng, L. H.; Valldor, M. $Ba_3V_2S_4O_3$: A Mott Insulating Frustrated Quasi-One-Dimensional S=1 Magnet. *Chemistry A European Journal* **2015**, 28, 7938-7943.

*[26]* Litteer, J. B.; Fettinger, J. C.; Eichhorn, B. W. $Ba_6V_4O_5S_{11}$. *Acta Crystallographica Section C* **1997**, 53 (2), 163–165.

[27] Nicoud, S.; Mentré, O.; Kabbour, H. The $Ba_{10}S(VO_3S)_6$ Oxysulfide: One-Dimensional Structure and Mixed Anion Chemical Bonding. *Inorg. Chem.* **2019**, 58 (2),1349–1357.

[28] a) Tauc, J. *Optical Properties of Solids*, F. Abeles ed. 1972, North-Holland. b) Tauc, J.; Grigorovici, R. and Vancu, A. Optical Properties and Electronic Structure of Amorphous Germanium. *Phys. Status Solidi* 1966, 15, 627.

[29] a) Wendlandt, W.; Hecht, H. G. Reflectance Spectroscopy. New York; London Interscience, 1966. b) Kubelka, P.; Munk, F. Z. *Ein Beitrag Zur Optik Der Farbanstriche*. Tech. Phys. 1931, 11, 593–601.

[30] Silvi, B.; Savin, A. Classification of Chemical Bonds Based on Topological Analysis of Electron Localization Functions. *Nature* **1994**, 371 (6499), 683–686.

[31] Liu, J.-W.; Wang, P.; Chen, L. Contribution of Disulfide $S_2^{2-}$ Anions to the Crystal and Electronic Structures in Ternary Sulfides, $Ba_{12}In_4S_{19}$, $Ba_4M_2S_8$ (M = Ga, In). *Inorg. Chem.* **2011**, 50 (12), 5706–5713.

[32] Driss, D.; Cadars, S.; Deniard, P.; Mevellec, J.-Y.; Corraze, B.; Janod, E.; Cario, L. Crystal Structure and Chemical Bonding in the Mixed Anion Compound BaSF. *Dalton Trans.* **2017**, 46 (46), 16244–16250.

[33] Wichelhaus, W. The Rare-Earth Oxide Disulfides $La_2O_2S_2$, $Pr_2O_2S_2$, and $Nd_2O_2S_2$. *Naturwissenschaften* **1978**, 65, 593–594.

[34] Ostoréro, J.; Leblanc, M. Room-Temperature Structure of $La_2O_2S_2$. *Acta Cryst.* C **1990**, 46 (8), 1376–1378.

[35] Bera, D.; Maslov, S.; Qian, L.; Holloway, P. H. Low-Temperature Synthesis of Red-Emitting Nanostructured $La_2O_2S_2$:$Eu^{3+}$ Phosphor. *Solid State Communications* **2011**, 151 (2), 164–168.

[36] Yoon, S.; Maegli, A. E.; Karvonen, L.; Shkabko, A.; Populoh, S.; Gałązka, K.; Sagarna, L.; Aguirre, M. H.; Jakes, P.; Eichel, R. A.; et al. Synthesis, Crystal Structure, Electric and Magnetic Properties of LaVO2.78N0.10. *Zeitschrift für anorganische und allgemeine Chemie* **2014**, 640 (5), 797–804.

[37] Sasaki, S.; Driss, D.; Grange, E.; Mevellec, J.-Y.; Caldes, M. T.; Guillot-Deudon, C.; Cadars, S.; Corraze, B.; Janod, E.; Jobic, S.; et al. A Topochemical Approach to Synthesize Layered Materials Based on the Redox Reactivity of Anionic Chalcogen Dimers. *Angewandte Chemie International Edition* **2018**, 57 (41), 13618–13623.

[38] Morniroli, J. P.; Steeds, J. W. Microdiffraction as a Tool for Crystal Structure Identification and Determination. *Ultramicroscopy* 1992, 45 (2), 219–239. https://doi.org/10.1016/0304-3991(92)90511-H.

[39] Sauter, E. G. Nonlinear Optics; John Wiley & Sons, **1996**.

[40] Mani, S. E.; Jang, J. I.; Ketterson, J. B. Large Third-Order Susceptibility and Third-Harmonic Generation in Centrosymmetric $Cu_2O$ Crystal. *Opt. Lett.* **2009**, 34 (18), 2817–2819.

[41] B. Kulyk, V. Kapustianyk, Ya. Burak, V. Adamiv, B. Sahraoui. Third harmonic generation in $LiKB_4O_7$ single crystal. *Materials Chemistry and Physics* 120 (**2010**) 114–117

[42] Mateo, L.; Ramírez, M. O.; Carrasco, I.; Molina, P.; Galisteo-López, J. F.; Víllora, E. G.; De las Heras, C.; Shimamura, K.; Lopez, C. and Bausá, L. E. $BaMgF_4$: An Ultra-Transparent Two-Dimensional Nonlinear Photonic Crystal with Strong $\chi^{(3)}$ Response in the UV Spectral Region. *Adv. Funct. Mater.* **2014**, *24*, 1509–1518.

[43] Krymus, A.S.; Myronchuk, G.L.; Parasyuk, O.V.; Lakshminarayana, G.; Fedorchuk, A.O.; El-Naggar, A.; Albassam, A.; Kityk, I.V. Photoconductivity and nonlinear optical features of novel $Ag_xGa_xGe_{1-x}Se_2$ crystals. *Materials Research Bulletin* **2017**, 85, 74–79

**TOC**

**SYNOPSIS**

$Ba_5(VO_2S_2)_2(S_2)_2$ is an original oxysulfide which exhibits mixed anion unconnected tetrahedra $V^{5+}O_2S_2$ and isolated disulfide pairs $(S_2)^{2-}$ arranged in a 1D. The electronic structure below the Fermi level is dominated by the disulfide $3p$ states which dictate the band gap. We point out *anionic* tools for band gap engineering, which can be useful to design phases for numerous applications. In this study, we show promising third harmonic generation properties.

# Oxysulfide $Ba_5(VO_2S_2)_2(S_2)_2$ Combining Disulfide Channels and Mixed Anion Tetrahedra and its Third Harmonic Generation Properties

Batoul Almoussawi[1], Marielle Huvé[1], Valérie Dupray[2], Simon Clevers[2], Victor Duffort[1], Olivier Mentré[1], Pascal Roussel[1], Angel M. Arevalo-Lopez[1], Houria Kabbour[1]*

[1] *Univ. Lille, CNRS, Centrale Lille, ENSCL, Univ. Artois, UMR 8181 – UCCS – Unité de Catalyse et Chimie du Solide, F-59000 Lille, France*

[2] *Normandie Univ, UNIROUEN, SMS, 76000 Rouen, France*

*houria.kabbour@univ-lille.fr

7. SUPPLEMENTARY INFORMATION

**Table S1.** *Atomic positions of the DFT relaxed structure with the optimized unit cell parameters: a=9.9161 Å b=18.5839 Å c=10.2698 Å*

| Atom | Wyck. | x | y | z |
|------|-------|---|---|---|
| Ba1 | 8f | 1/2 | 0.10742 | 0.08093 |
| Ba2 | 8e | 1/4 | 0.30512 | 1/4 |
| Ba3 | 4a | 0 | 0 | 0 |
| V1 | 8f | 1/2 | 0.2857 | -0.0259 |
| S1 | 16g | 0.67958 | 0.3502 | -0.0679 |
| S2 | 16g | 0.10749 | 0.46154 | 0.19996 |
| O1 | 8f | 1/2 | 0.20825 | -0.11135 |
| O2 | 8f | 1/2 | 0.25853 | 0.13105 |

**Table S2.** *Optimized distances (Å) for $Ba_5V_2O_4S_8$ within the $VO_2S_2$ tetrahedra and the disulfide pairs*

| Atoms 1,2 | d 1,2 (Å) |
|-----------|-----------|
| V1—S1 | 2.1895 (×2) |
| V1—O1 | 1.6857 |
| V1—O2 | 1.6892 |
| S2—S2 | 2.1317 |

In addition, the distance between two disulfide pairs is 3.0074 Å close to the experimental value.

# Part 2:

**Versatile Interplay between chalcogenide and Perchalcogenide Anions in the Four Thiovandates Ba$_7$S(VOS$_3$)$_2$(S$_2$)$_3$ and its tripple-Anion Selenide-Derivatives: crystallochemical, optical and DFT meta-GGA study**

B. Part 2: Versatile Interplay between Chalcogenide and Perchalcogenide Anions in the Four Thiovanadates $Ba_7S(VOS_3)_2(S_2)_3$ and its Triple-Anion Selenide-Derivatives: crystallochemical, optical and DFT meta-GGA study

Batoul Almoussawi[1], Prof. Hiroshi Kageyama[2], Dr. Houria Kabbour[1, *]

[1] *Univ. Lille, CNRS, Centrale Lille, ENSCL, Univ. Artois, UMR 8181 – UCCS – Unité de Catalyse et Chimie du Solide, F-59000 Lille, France.*

[2] *Department of Energy and Hydrocarbon Chemistry, Graduate School of Engineering, Kyoto University, Nishikyo-ku, Kyoto, 615-8510, Japan.*

1. Abstract

Four original polychalcogenides compounds have been synthesized in the system Ba-V-Q-O (Q= S, Se). The new structure type found for $Ba_7V_2O_2S_{13}$, that can be decomposed as $Ba_7S(VOS_3)_2(S_2)_3$, was substituted to yield three selenide-derivatives $Ba_7V_2O_2S_{6.787}Se_{6.213}$, $Ba_7V_2O_2S_{6.904}Se_{6.096}$ and $Ba_7V_2O_2S_{9.263}Se_{3.737}$ that represent original triple anionic lattices. They exhibit heteroleptic tetrahedral units $V^{5+}OS_3$ and isolated $Q^{2-}$ anions in the same layer and isolated dichalcogenide pairs $(Q_2)^{2-}$ with $Q$= S or Se in the complementary layer. The selenide derivatives are the first members in the system Ba-V-Se-S-O. The elaboration of the selenides-derivatives was attempted by targeting selective substitution of the disulfide pairs by diselenide pairs but all our solid-state synthesis led to concomitant and partial substitution in both the isolated sulfide and disulfide pairs sites. It involves disorder with both $S_2$ and $Se_2$ pairs in the same sites visible from the Q-Q mean distance evolution upon substitution. DFT study using the meta-GGA SCAN functional and based on four hypothetical models with various selective substitutions show that selective substitution of sulfide in one of the two layers yield constraints that involve a certain flexibility. Experimentally, the systems stabilize with concomitant incorporation of selenide in both layers to avoid mismatch and constraints. In such systems, the interplay between the O/S anionic ratio around $V^{5+}$ together with the presence/nature of the dichalcogenides $(Q_2)^{2-}$ and *isolated $Q^{2-}$*

impact in unique manners the band gap and provide a rich background to tune the optical properties and the symmetry. A crystallochemical discussion combined with DFT calculations and optical measurements allow a comprehensive study of the anionic lattices and the band gap in this family and open new perspectives for band gap and symmetry engineering.

## 2. Introduction

Oxychalcogenides are, among mixed-anion compounds, growing the most in popularity because of their great versatility and tunable properties for a large scope of applications. They open new perspectives to overcome challenges and hindrances to the development of various applications such as thermoelectrics[1,2] or photocatalytic hydrogen production[3,4,5,6] and so on. The coexistence of oxide anions and more electronegative chalcogenide anions Q (Q= chalcogenide) leads to a highly distinctive structural chemistry[7].

In this context, many oxychalcogenides compounds exhibit 2D layered-type structures, such as the narrow band gap semiconductors $Sr_2CuO_2Cu_2Se_2$[8], $Bi_2YO_4Cu_2Se_2$ [9] or the superconductors $LaO_{1-x}F_xBiS_2$ [10]. Besides, few complex inorganic compounds show the presence of Q–Q bonds (such as dichalcogenides pairs) which drastically affects the electronic structure and therefore the physical properties[11]. Some "simple" binaries such as cobalt persulfide $CoS_2$[12] or perselenide $CoSe_2$[13] are well-known polychalcogenides compounds. They are widely studied for their catalytic properties. For instance, a synergetic effect has been highlighted in recent years within a nanostructured $CoS_2/CoSe_2$ hybrid that proved a superior hydrogen evolution reaction (HER) activity[14]. Polychalcogenides are also crucial in Lithium-Sulphur batteries which are among the most promising technology in this field[15]. Indeed, polychalcogenides are at the heart of the later with the use of elemental S or alternatively $SeS_2$. The main issue, *i.e.* the *shuttle effect* due to the migration of soluble lithium polysulfides, is overcome with the use of composites containing cobalt perselenide $CoSe_2$ nanoparticles at the cathode, with drastic improvement of the performances. Interestingly, polychalcogenides compounds are an important component of this technology as well as an issue but also the issues solution. Recently, new compounds could be designed by a redox metal insertion into dichalcogenide based phases[11,16]. Besides, complex polychalcogenides (ternary and especially beyond) remain less encountered. $La_2O_2S_2$ and its derivatives are well known materials for optics and is made of layers ($La_2O_2$) stacked with a layer of disulfide pairs[17]. In the ternary antimony–chalcogenides of trivalent lanthanides, compounds have been reported with both chalcogenide $Q^{2-}$ and dichalcogenide $(Q_2)^{2-}$ anions, where the anions of a pair are simultaneously capping antimony[18]. Recently, we have reported the phase $Ba_5(VO_2S_2)_2(S_2)_2$ [19] that contain dichalcogenide pairs occupying in a unique 1D manner channels

delimited by barium cations. This compound was the first in the Ba-V-S-O system with persulfide entities, while the *conventional* following oxysulfides were reported, $Ba_9V_9O_3S_{11}$[20], $Ba_3V_2S_4O_3$[21], $Ba_{15}V_{12}S_{34}O_3$[22] and $Ba_{10}S(VO_3S)_6$[23]. All those compounds exhibit tetrahedral thiovanadates as found in the simple series $A_3(VO_{4-x}S_x)$[24] (A= Na, K) with disconnected $VO_2S_2$ in the case of $Ba_5(VO_2S_2)_2(S_2)_2$.

In this work, we present four new complex polychalcogenides phases. The new phase $Ba_7S(VOS_3)_2(S_2)_3$ (phase 1) contains $VOS_3$ thiovanadates and isolated $S^{2-}$ anions into a layer and an original arrangement of persulfide $(S_2)^{2-}$ pairs into the second layer, thus leading to a complex anionic interplay. This is amplified in the three selenide-derivatives $Ba_7V_2O_2S_{6.787}Se_{6.213}$, $Ba_7V_2O_2S_{6.904}Se_{6.096}$ and $Ba_7V_2O_2S_{9.263}Se_{3.737}$ that represent original triple anionic lattices. For all phases, a comparative crystallochemical discussion based on single crystal XRD is complemented by electronic structure analysis calculated from density functional theory (DFT) together with optical properties of the pure powder samples. We show multiple possibilities and complex anionic interplay in this system and carry out a comprehensive study.

3. Experimental section

**Synthesis:** The powders were obtained from a mixture of 2BaO, 5BaS, 2V and 8S pressed into pellets and heated in an evacuated sealed quartz tube. The heat treatment consisted in heating up to 750°C for 24 hours, then cooling down to 650°C at a 5°C/h rate and finishing with a rapid cooling down to room temperature.

**X-ray diffraction on single crystals** was performed on a Rigaku XtaLab P200 diffractometer equipped with a Dectris Pilatus 200K detector and a Mo $K_\alpha$ source, for $Ba_7V_2O_2S_{13}$.

For the selenide-derivatives, an X8 diffractometer equipped with a two-dimensional (2D) CCD 4K detector and an Ag $K_\alpha$ source was used.

**The powder XRD** patterns were collected on a Bruker D8 diffractometer equipped with a Lynxeye linear detector (Cu Kα) in Bragg–Brentano geometry at room temperature.

**Scanning electron microscopy (SEM)** experiments and EDX analysis were carried out on a S-3400N (Oxford instruments) and on a Hitachi S400N microscope.

**DFT calculations** were carried out by employing the projector augmented wave (PAW)[25, 26] method encoded in the Vienna ab initio simulation package (VASP)[27] and the meta-GGA SCAN functional[28 29] for the exchange-correlation functionals. The full geometry optimizations were carried out using a plane wave energy cutoff of 550 eV and 30 $k$ points in the irreducible Brillouin zone for all models. It converged with residual Hellman-Feynman forces on the atoms smaller than 0.03 eV/Å and led to a good match with the experimental structure, i.e. within a reasonable error expected for the SCAN meta-GGA functional which lead in general to better match with experience than simple GGA functionals. The relaxed structure was used for calculations of the electronic structure. For the later, the plane wave cutoff energies of 550 eV and the threshold of self-consistent-field energy convergence of $10^{-6}$ eV were used, with 72 $k$ points in the irreducible Brillouin Zone for all models.

**UV−Visible Measurements.** The reflectance of the sample was measured from 250 to 800 nm on a PerkinElmer Lambda 650 device.

4. Results and Discussion

a) **Structures resolution and Description**

**$Ba_7S(VOS_3)_2(S_2)_3$.** A black single crystal with a platelet shape was selected for XRD data collection. The structure could be solved with the unit cell parameters a= 8.8172(4) Å and c = 17.3428(8) Å in the space group $P6_3/m$ (176). The data collection and refinement details are given in **Table 1**. The refinement was carried out with the JANA2006[30] software based on a structure solution obtained with the charge-flipping method implemented in JANA2006 within the SUPERFLIP module[31]. EDX analysis of the single crystals led to the average atomic ratio 59.53/8.70/31.77 for S/ V/Ba, respectively, in good agreement with the formula $Ba_7V_2O_2S_{13}$.

The original structure $Ba_7(S_2)_2(VO_2S_2)_2$ can be viewed as a rather open framework but can be described by two alternating layers (**Figure 2.d**). The first layer is formed by disconnected $VOS_3$ tetrahedra (**Figure 2.a**) separated from each other by Barium cations that also coordinate isolated sulfide $S^{2-}$ (S1) anions into $S1Ba_6$ octahedron with $d_{Ba1-S1}$= 3.282(2) Å, this distance is typical of a

$Ba^{2+}$-$S^{2-}$ distance and is for instance comparable to that found in $Ba_9V_3S_{11}(S_2)_2$[32] $d_{Ba-S}$=3.173(2) Å (see **Figure 2.c**). In the mixed-anion tetrahedra based on $V^{5+}$, we found V1−S4 = 2.121(1) Å (×3)) and V1−O1 = 1.688(3) Å. These distances are comparable to those found for instance in thiovanadates within $Ba_5V_2S_8O_4$, i.e. V1−S1= 2.178(2) Å and V1−O2 = 1.680(5) Å or in $Ba_{15}V_{12}S_{34}O_3$ with comparable distances. The polar $[VS_3O]^{3-}$ tetrahedral entities are arranged with their O vertices along the crystallographic unique axis $c$, but the space group inversion symmetry make them alternatively pointing in opposite direction along $c$, so that no polar arrangement raises from them (**Figure 2.e**) contrarily to $K_3(VO_3S)$[33] for instance. The second layer consists of disulfide pairs $(S_2)^{2-}$ surrounded by $Ba^{2+}$ cations (**Figure 2.g**). The latter are distributed such as forming cavities in which the disulfide pairs are arranged pointing in three different directions, every three distinct pair with a distinct orientation are coordinated to one Ba2. These two layers are linked via weak interactions Ba1-O1 (**Figure 2.b**). $Ba_7V_2S_{13}O_2$ can be written as $Ba_7$ $(S_2)_3(VOS_3)_2S$ to consider the structural units involved.

### b) Investigating selective substitution of sulfur by selenium

We have attempted a selective substitution of the disulfide pairs by diselenide pairs to form $Ba_7S(VOS_3)_2(Se_2)_3$. In the corresponding preparation, a single crystal was selected and its structure resolution revealed incorporation of selenide and disorder at both the isolated $S^{2-}$ site and the disulfide sites leading to mixed S/Se sites. Only the sulfur site of the thiovanadate is preserved. The disordered dichalcogenide pairs are arranged **Figure 3.a** in the same manner than the disulfide pairs in the oxysulfide member. Other attempts to selectively and fully substitute either the isolated site, the pairs sites or both, lead to the isolation of single crystals of phases showing disorder in all sites. Two other crystals with different ratio S/Se was then characterized. We thus have characterized in addition to $Ba_7S(VO_3S)_2(S_2)_3$, the three following selenide-derivatives $Ba_7S_{0.3682}Se_{0.6318}(VO_3S)_2((S_{0.4825}Se_{0.5175})_2)_3$, $Ba_7S_{0.1668}Se_{0.8332}(VO_3S)_2((S_{0.123}Se_{0.877})_2)_3$ and $Ba_7S_{0.0972}Se_{0.9028}(VO_3S)_2((S_{0.115}Se_{0.885})_2)_3$.

They may be named in the text respectively phase1, phase2, phase3 and phase4 (with increased selenide content from phase 1→4) for clarity. The main geometrical parameters and the refinement details are gathered in **Table 1** and **Table 4**. The parameters α and δ define the substitution ratio by selenide in the $Q_{isolated}$ site and in the $(Q_2)$ pair, respectively (**Table 4**). Clearly, both anionic entities are impacted in more or less similar proportions upon increased selenide incorporation. For phase 2, $Q_{isolated}$ is a bit more substituted. For phase 3, α and δ are very similar and for phase 4, $(Q_2)$ is slightly more substituted. Thus, for the lower selenide global content, $Q_{isolated}$ is favored then the $(Q_2)$ sites take over progressively upon increasing selenide content for phase 3 and 4. Having said that, both entities are filled in significant amount at all ratios investigated here. For $(Q_2)$, the distinct crystallographic sites for each anion involved in the pair show very close selenide ratio, thus in the final refinement they were constrained equal which did not alter the quality of the refinement and is consistent with the occurrence of either $S_2$ or $Se_2$ pairs. We note that for phase 4 with the greater selenide content, the two $(Q_2)$ sites occupancies show a moderate divergence when not constrained equal. This can be also related to the evolution of the refinements. For phase 1→3, the overall quality of the refinements is very high and the reliability factors are excellent. On another hand, while the average structure of phase 4 is refined without difficulties in this series, it stands apart from phase 1→3 with higher (although reasonable) reliability factors. The GOF is slightly above the 6.0 limit (6.8) and the residual electronic densities are also more significant. It points toward a possible structural evolution at this selenide ratio. A careful analysis of the precession images from the single crystals XRD data show the appearance of a few low intensity extra spots. compared to the other phases. Our preliminary analysis point toward a probable modulation of the structure but it turns out that the additional spots are not due to modulations but to additional crystals "stuck" on the main crystal.

In the three selenide-derivatives $Ba_7S_{0.3682}Se_{0.6318}(VO_3S)_2((S_{0.4825}Se_{0.5175})_2)_3$, $Ba_7S_{0.1668}Se_{0.8332}(VO_3S)_2((S_{0.123}Se_{0.877})_2)_3$, and $Ba_7S_{0.0972}Se_{0.9028}(VO_3S)_2((S_{0.115}Se_{0.885})_2)_3$, we found the distance Q2-Q3 between 2.325(2) Å and 2.383(1) Å lower than that found in $Ba_3Ta_2Se_9$ with $d_{Se-Se}$=2.50 Å[34] and in $Sr_4Sn_2Se_9$ and $Sr_4Sn_2Se_{10}$ with 2.459 Å and 2.462 Å respectively[35], also larger

than that for the oxysulfide parent compound $Ba_7S(VO_3S)_2(S_2)_3$ for which $d_{S-S}$= 2.122 Å. The distances in between of the selenide-derivatives are consistent with the mixing of the two types of pairs $(S_2)$ and $(Se_2)$ and depend on the selenide content. The large cation Ba1 with highly distorted environments is coordinated to 4 anions species $O^{2-}$, $(Se/S)_2^{2-}$, $(Se/S)^{2-}$ and $s^{2-}$ with characteristic Ba-O1 distance between 2.784(2)Å and 2.812(6)Å (**Figure 3.b**). The isolated chalcogenide anion $(Se1/S1)^{2-}$ is coordinated to six $Ba^{2+}$ cations to form octahedron $(Se1/S1)Ba_6$ with $d_{Ba1-(Se1/S1)}$ in the range 3.331(0) Å 3.341(1) Å in the range to that found in $Ba_7Sn_3Se_{13}$ [36] with $d_{Se-Ba}$ between 3.183 and 3.761 Å.

5.  Polycrystalline Phase Analysis.

The synthesis of the pure powder phases was attempted following the procedure described in the Experimental Section. As depicted in **Figure 1** the title phases are formed with a high purity. The minor impurity (sulfide) was found in phase 1. A multiphase Rietveld refinement using FullProf[37] based on the single-crystal structural model was carried out and led to very good reliability factors as shown in **Figure 1**. Rietveld quantification indicates the ratio 0.888/0.112 for the title phase $Ba_7S(VOS_3)_2(S_2)_3$ /impurity.
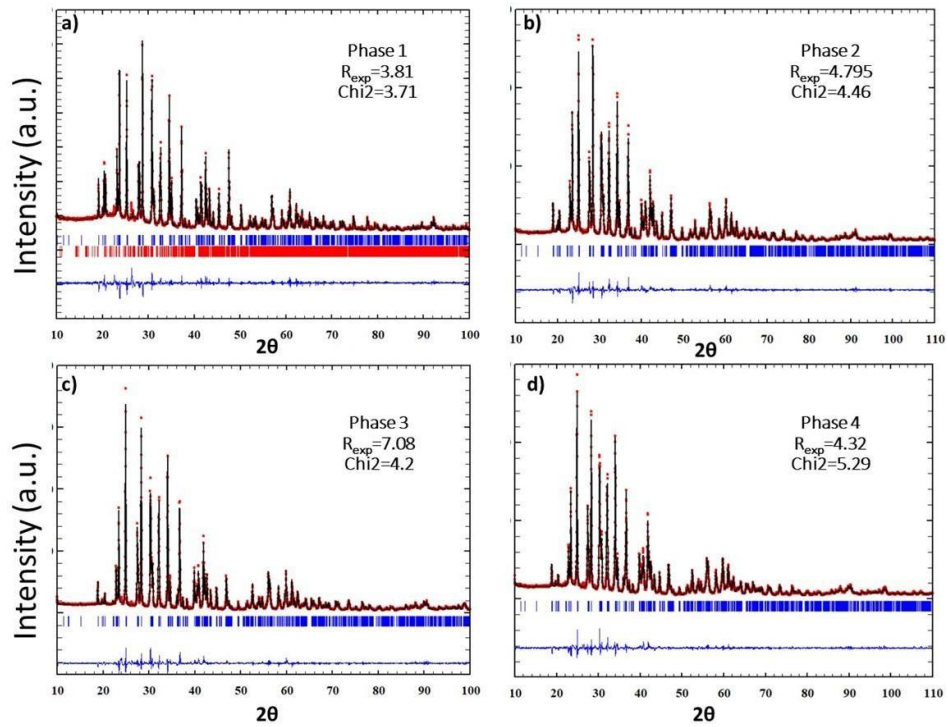
**Figure 1:** *a), b), c) and d) Powder XRD Rietveld refinement of Phase 1, 2, 3 and 4 respectively: the experimental (black) and calculated (red) patterns are superimposed; the difference curve and Bragg positions are represented in blue and green respectively.*

**Table 1.** *Main geometrical information for phase 1, 2, 3 and phase 4 from the single crystal refinement*

|  | Phase 1 | Phase 2 | Phase 3 | Phase 4 |
|---|---|---|---|---|
| Powder Unit cell | a=8.9088 Å<br>c=17.5491 Å | a= 8.9290(3) Å<br>c= 17.6052 Å | a= 8.9670 Å<br>c= 17.6747Å | a= 8.9706 Å<br>c= 17.6964 Å |
| Volume Å$^3$ | 1178.86(9) | 1215.56(7) | 1230.77(8) | 1233.27 (5) |
| $VO_3S$ (Td) distances (Å) | V-O= 1.683(7)<br>V-S= 2.129(3) | V-O = 1.687(4)<br>V-S =2.129(2) | V-O= 1.689(2)<br>V-S= 2.1355(8) | V-O= 1.6422(2)<br>V-S= 2.134(5) |
| Ch-Ch (Å) | 2.122(6) ($S_2$) | 2.325(1) | 2.3832(4) | 2.382(5) |
| Ba1-Ch$_{(isolé)}$ | 3.3002(5) | 3.3308(3) | 3.3323(2) | 3.3411(12) |
| Ba2-Ch$_{(paire)}$ | 3.289(2) | 3.3259(9)/ 3.3712(7) | 3.3940(3)/3.3557(4) | 3.397(2)/ 3.360(2) |
| Ba-Ch interlayer | 3.709(2) | 3.736(1) | 3.74258(7) | 3.758(4) |
| Bandgap(eV) | 1.45 | 1.4 | 1.3 | 1.27 |
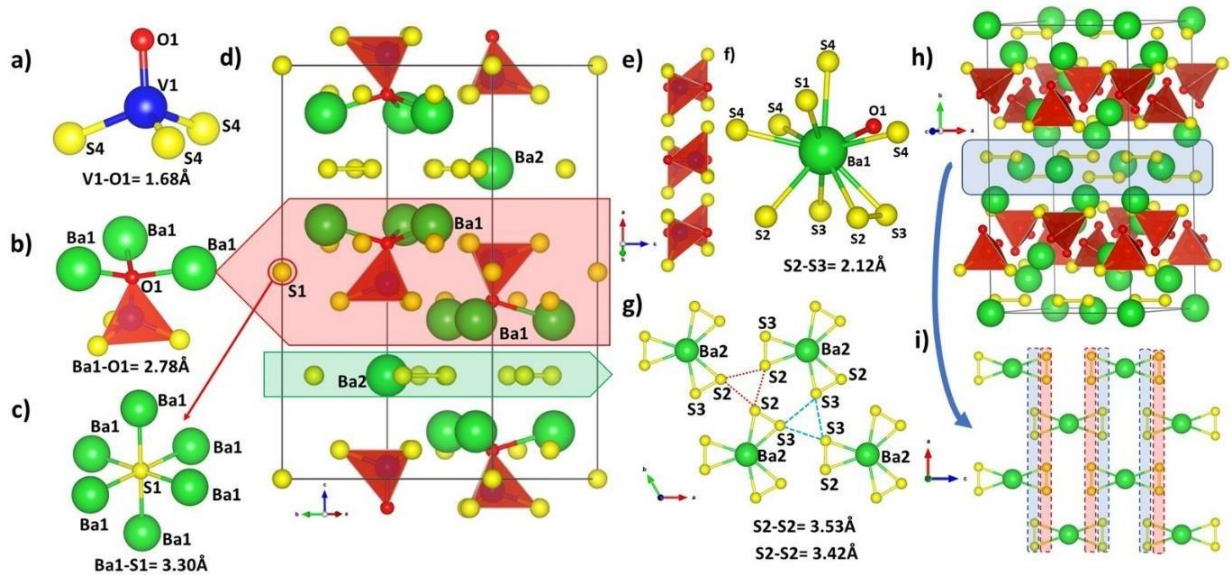


**Figure 2:** *(a) View of the heteroleptic entity $VS_3O$ with V1–O1 distance indicated (b) O1 atom environments with Ba–O1 distance (c) S1 atom environments with S1–Ba1 distance indicated (d) Structure of $Ba_7V_2S_{13}O_2$. (e) View of the tetrahedra arrangement projected along the deviated b axis (f) Ba1 environments with S2–S3 bonds and distances indicated (g) S2–S3 bonds arrangement represented around Ba2, the dotted lines represent the separations S2–S2 and S3–S3 (unconnected atoms). h) View of $Ba_5(VO_2S_2)_2(S_2)_2$ and its i) disulfide pairs rearrangement.*
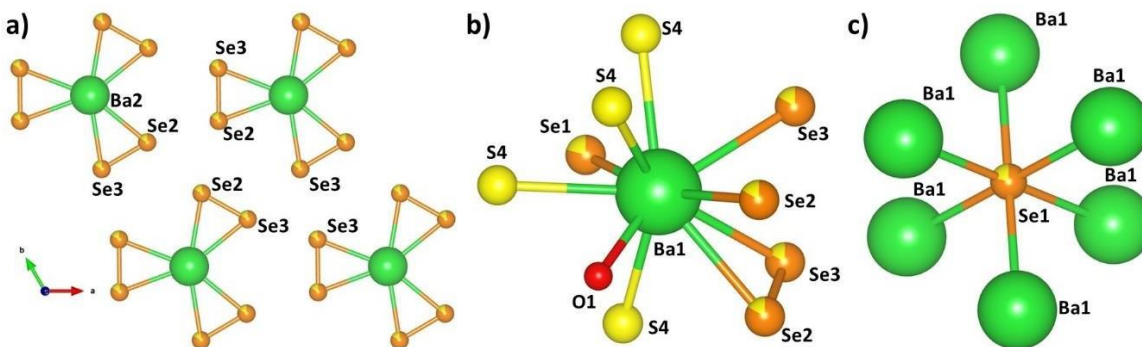
*Figure 3:* *a) Se2–Se3 bonds arrangement represented when present in their vicinity: Ba2 ant its connectivity with Se2–Se3 bonds. b) Ba1 environments. c) isolated Se1 atom environment. To simplify, the mixed sites Se1/S1 are designed by Se1 and so on for Se2 and Se3.*

6. Optical Measurements.

UV−visible diffuse-reflectance analysis of the polycrystalline phases (1→4) is represented in **Figure 4**. A Kubelka−Munk transformation[38] was applied to the measured diffuse-reflectance (R) spectra using the function $F(R) = (1 − R)^2/2R$. Then a Tauc plot[39,40] was used to determine the optical band gap $E_g$, using the equation $[F(R) hv]^{1/n} = k(hv − E_g)$, where hv is the photon energy, k an energy-independent constant, $E_g$ the optical band gap, and *n* an exponent related to the type of transition. Assuming an indirect transition (exponent n = 2), the plot of $[F(R) hv]^2$ versus *hv* allowed, after drawing a tangent line at the inflection point, to determine the band gap as shown in **Figure 4.** This is consistent with the observed dark color of the crystals and powders.
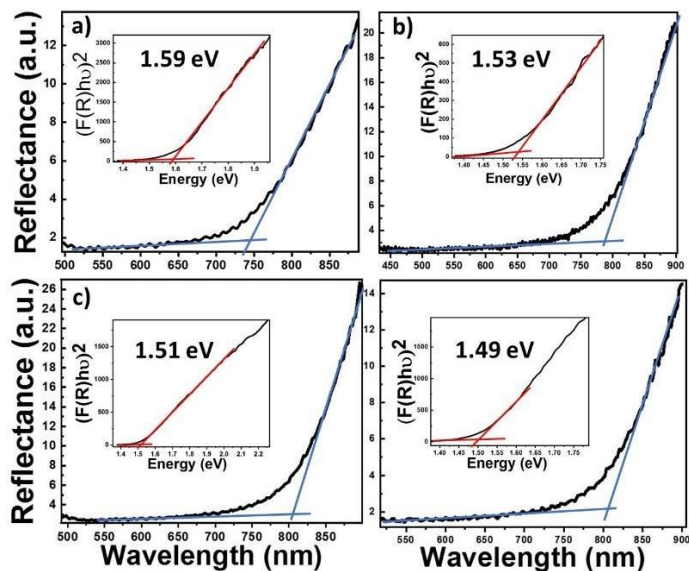
*Figure 4: Diffuse-reflectance spectra of phases 1, 2, 3 and phase 4 with a Tauc plot as an inset to determine the experimental band gap.*

7. DFT Calculations using the meta-GGA SCAN functional.

To better understand the local geometry of selective and ordered substitution, and by consequent the origin of the experimental disorder, DFT calculations were carried out on four hypothetical phases: $Ba_7S(VO_3S)_2(S_2)_3$, $Ba_7Se(VO_3S)_2(Se_2)_3$, $Ba_7S(VO_3S)_2(Se_2)_3$ and $Ba_7Se(VO_3S)_2(S_2)_3$. The unit cells with the band structures are shown in **Figure 5**. and focus in the region around the Fermi level at the top of the VB and the bottom of the conduction band (CB). The main crystallochemical information of the optimized geometries listed in

**Table 2.** show constant distances within $VOS_3$ tetrahedra and Q-Q bonds considering all hypothetical phases. It highlights the rigidity of the latter entities which are not disturbed by the substitutions. On the other hand, we show that the Barium environment constitutes the 'flexible part' and has to absorb the chemical pressure by adjusting the Ba-O and the Ba-Q distances when the complementary layer is substituted. This adaptation does not seem to be thermodynamically favorable in our experimental conditions. Instead, the systems stabilize with concomitant incorporation of selenide in both layers to avoid mismatch and constraints.

The band structures show an indirect band gap for $Ba_7S(VO_3S)_2(S_2)_3$, $Ba_7Se(VO_3S)_2(Se_2)_3$, $Ba_7S(VO_3S)_2(Se_2)_3$ then a transition to a direct band gap for $Ba_7Se(VO_3S)_2(S_2)_3$ is observed. The variation of the band gap width is coherent (decreases with the increase of Se/S ratio) except in the case of $Ba_7S(VO_3S)_2(Se_2)_3$ in comparison with $Ba_7Se(VO_3S)_2(Se_2)_3$ where the band gap slightly decreases by substitution of isolated Se by S. It can be explained by the positive chemical pressure induced by the smaller radius of sulfur leading to decreased Ba-$Q_{isolated}$ distances as well as closer layers. These structural changes impact the band gap toward a decrease contrarily to Sulfur incorporation, the overall effects add up and lead to the slight decrease observed.

The total density of states (DOS) of each hypothetical phase is shown in Figure 6. The contribution of each type of anionic species is also represented to compare their contribution. For $Ba_7S(VO_3S)_2(S_2)_3$, within the $VOS_3$ building units, the V states lie in the CB starting from ~1.0 eV up to ~2.5 eV for the major contribution to the CBM. In the VB, the V states contribution is found roughly in the range of −5 to −1 eV where they are hybridized with the O $2p$ and S $3p$ states involved in the $VOS_3$ building units. Owing to its more ionic bonding to vanadium and its higher electronegativity, O has a contribution of its $2p$ states more localized and lower in the VB (with the main large peak centered around −4.5 eV) compared to $S_{(VOS3)}$ states that are found higher in the VB mainly around −2.5 eV. In previous work, the projected DOS on distinct mixed-anion tetrahedra $V(O,S)_4$ as found in $Ba_6(VO_2S_2)_2(VS_3O)(VS_4)$ allowed to illustrate the evolution of their contributions higher in the VB when increasing the S content (from $VO_3S \rightarrow VS_4$) thus contributing to decrease the band gap.

The disulfide pairs and the isolated $S^{2-}$ behave in a similar way as they are both found just below the Fermi level, above the broader $S^{2-}$ states involved in the $VOS_3$ tetrahedra, with less localized states in the former due to the S-S covalent bonding. Regarding the electronic structure description and the crystallochemical situation of each anionic species, the title phase may be decomposed as a combination of the structural entities $(Ba_7)^{14+}(S^{2-})(S_2)_3{}^{6-}((VOS_3)_2)^{6-}$ . A similar analysis can be made for all hypothetical phases.

Considering all hypothetical phases, the dichalcogenide pairs and the isolated chalcogenide states are lying in very close energy range (without interacting). However the $(Q)_2$ pairs dominate except in the case of $Ba_7Se(VO_3S)_2(S_2)_3$ where the isolated Se is highly present at the top of the VBM.
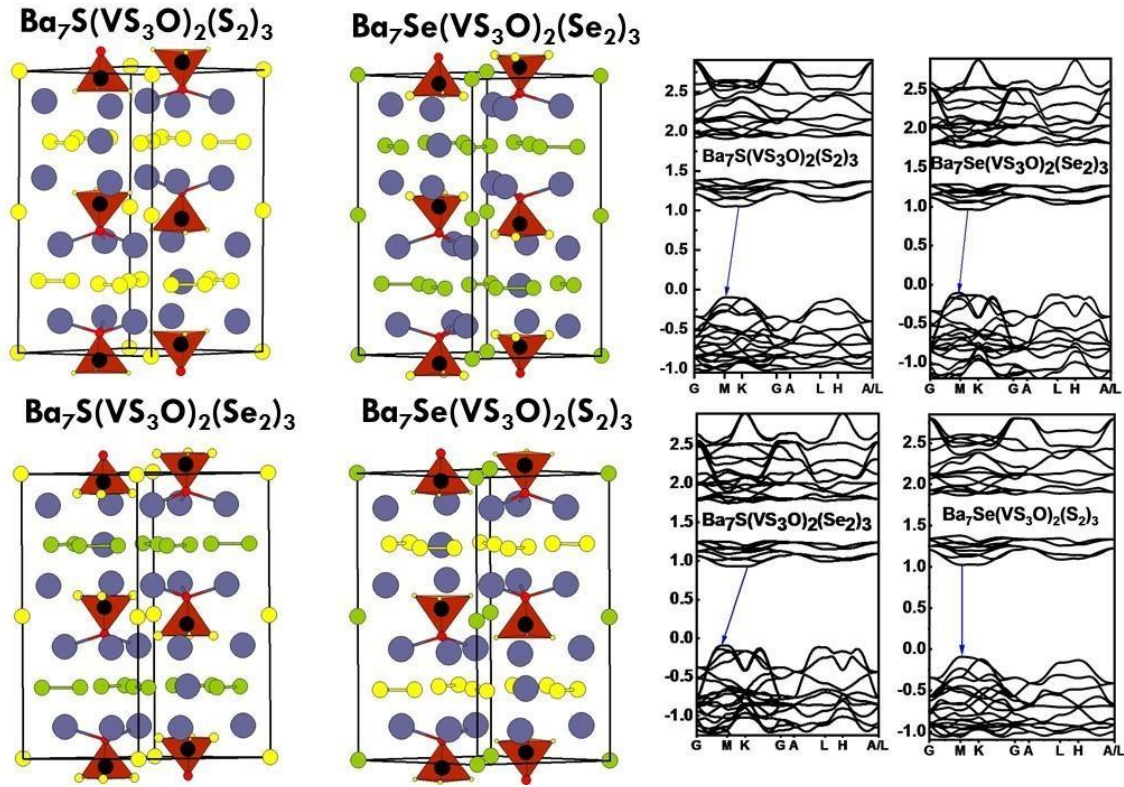


**Figure 5.** *Unit cell of the hypothetical phases and their band structure along high symmetry points of the Brillouin Zone.*
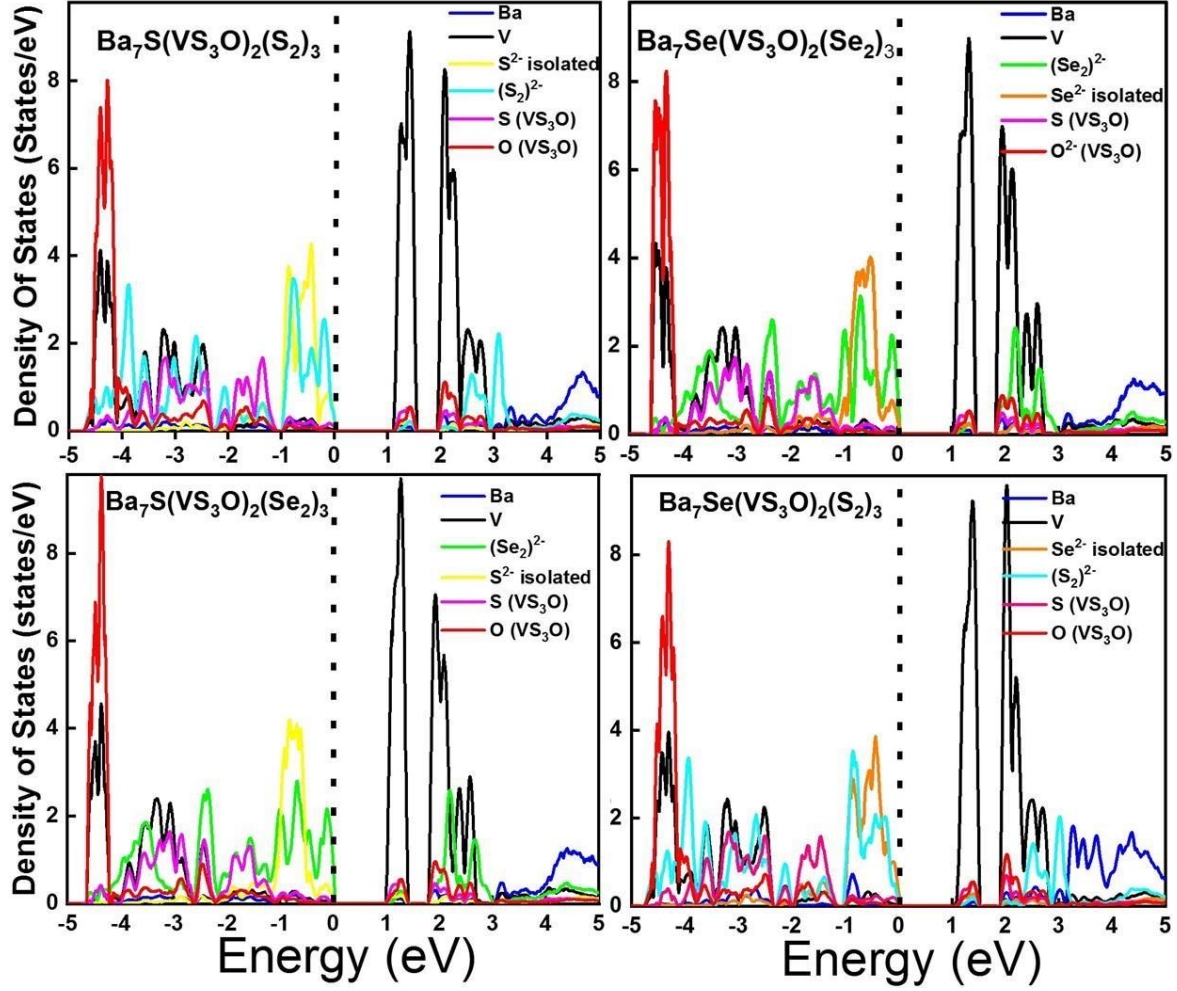
**Figure 6:** *Projected Density of States of the four hypothetical phases. The distinct contribution of each species is given: Ba; V, sulfur and oxygen involved in a tetrahedral (VO$_3$S); Q (Q= S, Se) in isolated sites and Q involved in a pair Q$_2$.*

**Table 2.** *Main geometrical information for hypothetical phases.*

|  | Ba$_7$S(VO$_3$S)$_2$(S$_2$)$_3$ | Ba$_7$Se(VO$_3$S)$_2$(Se$_2$)$_3$ | Ba$_7$S(VO$_3$S)$_2$(Se$_2$)$_3$ | Ba$_7$Se(VO$_3$S)$_2$(S$_2$)$_3$ |
|---|---|---|---|---|
| Unit cell | a=8.9088 Å<br><br>c=17.5491 Å | a=9.0677 Å<br>c=17.9483 Å | a=9.0391 Å<br>c=17.8805 Å | a=8.9359 Å<br>c=17.5970 |
| Volume | 1206.20 Å$^3$ | V=1278.05 Å$^3$ | V=1265.20 Å$^3$ | V=1216.88 Å$^3$ |
| VO$_3$S (Td) distances (Å) | V-O= 1.6848<br>V-S= 2.134 | V-O= 1.6903<br>V-S= 2.1387 | V-O= 1.6850<br>V-S= 2.1388 | V-O = 1.6906<br>V-S =2.1346 |
| Ch-Ch (Å) | 2.1141 (S$_2$) | 2.4334 (Se$_2$) | 2.4349 (Se$_2$) | 2.1138 (S$_2$) |

| | | | | |
|---|---|---|---|---|
| Ba-Ch$_{(isolé)}$ | 3.3163 | 3.3798 | 3.3211 | 3.3679 |
| Ba-Ch$_{(paire)}$ | 3.2630/3.3025 | 3.4088/3.4547 | 3.4048/3.4423 | 3.2716 / 3.3134 |
| Ba-Ch interlayer | 3.7346 | 3.7938 | 3.7819 | 3.746 |
| Bandgap(eV) | 1.15 (indirect) | 1.07 (indirect M→K) | 1.02 (indirect) | 1.12 (Direct M→M) |

## 8. Bader charge analysis

Bader charge analysis [41] was carried out from the DFT calculated electronic structure based on the meta-GGA SCAN functional [29] that allows in particular a 20 – 50 % band gap improvement[42] compared to the GGA functionals known to underestimate them and with no major additional computational cost compared to the costly hybrid functionals. We expect to get values closer to experience although here we focus on the comparison from one composition to another. **Table 1** gathers the band gap values and the net atomic Bader charges on the different types of atoms. For the later also, the comparative study is relevant while the absolute values are not to be taken literally. We found Bader net charges consistent with those reported for comparable entities in the literature. For instance (Se) values from a dichalcogenide pair are in the same range than reported in $Sn(Se_2)$ [43], $S^{2-}$ present comparable values than in $FePS_3$ [44]. On another hand, $LiMnVO_4$ exhibits for $V^{5+}$ a slightly higher value of +1.80 [45], which is consistent with the fact that $V^{5+}$ in our $VO_3S$ thiovanadate involves one more covalent V-S bond contribution compared to the vanadate $VO_4$.

- Overall, negligible variations of the atomic net Bader charge of ions involved in the $VO_3S$ entities is observed accordingly with the rigid geometry trough compositional change, except for O when the compositional change concern the layer it occupies and due to antagonist effect related to the Ba-$Q_{isolated}$ bond.
- Considering models with fixed thiovanadates layers and containing $S^{2-}_{(isolated)}$, a slight augmentation (0.019) of $S^{2-}_{(isolated)}$ net Bader charge is observed when the nature of the complementary layer goes from $(S_2)$ to $(Se_2)$ pairs. This is due to the negative chemical pressure induced by the complementary layer, $(S_2) \rightarrow (Se_2)$ which enhances the ionic character of the Ba-$S_{(isolated)}$ bonds. Oppositely, for $Se_{(isolated)}$ in fixed thiovanadates layers, a decrease (0.022) is observed due to the positive chemical pressure from $(Se_2) \rightarrow (S_2)$ in the complementary layer yielding more covalent Ba-$Se_{(isolated)}$ bonds. Similar analysis can be made for $Se_{(Se2)}$ which net Bader

charge decrease through exchange of $Se_{isolated}$ by S in the complementary layer that induce a positive chemical pressure that should enhance covalent bonding. However, the counterintuitive $S_{(S2)}$ net Bader charge decrease (more covalent bonding) through exchange of $S_{isolated}$ by $Se_{isolated}$ (negative chemical pressure) in the complementary layer stays apart and can be related to the band gap evolution described above for this case.

**Table 3.** *Net atomic Bader charges for the four hypothetical phases*

| Net atomic Bader charges | $Ba_7S(VO_3S)_2(S_2)_3$ | $Ba_7Se(VO_3S)_2(Se_2)_3$ | $Ba_7S(VO_3S)_2(Se_2)_3$ | $Ba_7Se(VO_3S)_2(S_2)_3$ |
|---|---|---|---|---|
| Ba1 | +1.49 | +1.472 | +1.476 | +1.485 |
| Ba2 | +1.46 | +1.442 | +1.441 | +1.464 |
| V | +1.584 | +1.588 | +1.585 | +1.583 |
| $S_{(VO3S)}$ | -0.994 | -1.007 | -1.008 | -0.994 |
| $Ch_{(isolated)}$ | -1.319 | -1.270 | -1.338 | -1.248 |
| $Ch1$-$Ch2_{(pair)}$ | -0.752/-0.662 | -0.701/-0.662 | -0.700/-0.655 | -0.695/-0.726 |
| O | -1.019 | -1.031 | -1.014 | -1.031 |

**Table 4.** *Data collection and Refinement Details of $Ba_7V_2O_2S_{13}$ and its selenide-derivatives (phase 1→4)*

| Phase | Phase 1-P.A. | Phase 2 | Phase 3 | Phase 4 |
|---|---|---|---|---|
| Formula | $Ba_7V_2O_2S_{13}$ | $Ba_7V_2O_2S_{9.304}Se_{3.696}$ | $Ba_7V_2O_2S_{7.15}Se_{5.85}$ | $Ba_7V_2O_2S_{6.568}Se_{6.432}$ |
| Detailed formula | $Ba_7S(VS_3O)_2(S_2)_3$ | $Ba_7S_{1-\alpha}Se_\alpha(VS_3O)_2(S_{1-\delta}Se_\delta)_6$ | $Ba_7S_{1-\alpha}Se_\alpha(VS_3O)_2(S_{1-\delta}Se_\delta)_6$ | $Ba_7S_{1-\alpha}Se_\alpha(VS_3O)_2(S_{1-\delta}Se_\delta)_6$ |
| $\alpha =$ | 0 | 0.496 | 0.790 | 0.921(14) |
| $\delta =$ | 0 | 0.533 | 0.843 | 0.9425 |
| Molecular weight (g. $mol^{-1}$) | 1512 | 1694.5 | 1786.4 | 1813.7 |
| Symmetry | *Hexagonal* | *hexagonal* | *hexagonal* | *hexagonal* |
| Space group | P 63/m (176) | P 63/m (176) | P 63/m (176) | P 63/m (176) |
| Unit cell dimensions (Å) | a= 8.8456(4) | a= 8.9290(3) | a= 8.9670(3) | a= 8.9706(2) |

| | | | | |
|---|---|---|---|---|
| | c= 17.3971(8) | c= 17.6052(5) | c= 17.6747(7) | c= 17.9706(2) |
| Volume (Å³) | 1178.86(9) | 1215.56(7) | 1230.77(8) | 1233.27 (5) |
| Z | 2 | 2 | 2 | 2 |

<div align="center">

**Data Collection**

</div>

| | | | | |
|---|---|---|---|---|
| Equipment | Bruker CCD (Mo Kα) | Bruker CCD (Mo Kα) | Bruker CCD (Mo Kα) | Bruker CCD (Ag Kα) |
| Λ [Å] | 0.71073 | 0.71073 | 0.71073 | 0.56087 |
| Calculated density (g cm⁻³) | 4.2597 | 4.6295 | 4.8204 | 4.8841 |
| Crystal shape | Platelet | Platelet | Platelet | Platelet |
| Crystal dimensions (μm) | 75×50×5 | 50×30×5 | 80×45×5 | 160×50×6 |
| Color | Black | Black | Black | Black |
| Absorption correction | analytical | analytical | analytical | analytical |
| Scan mode | ω, φ | ω, φ | ω, φ | ω, φ |
| θ (min–max) (°) | 2.34-27.88 | 2.31-28.7 | 2.3- 41.16 | 1.82-25.26 |
| μ (mm−1) | 13.391 | 18.477 | 20.981 | 11.482 |
| F(000) | 1324 | 1464 | 1535 | 1556 |
| Reciprocal space recording | −11 ≤ h ≤ 11 | −12 ≤ h ≤ 12 | −16 ≤ h ≤ 16 | −13 ≤ h ≤ 13 |
| | −11 ≤ k ≤ 11 | −11 ≤ k ≤ 12 | −16 ≤ k ≤ 16 | −13 ≤ k ≤ 13 |
| | −22 ≤ l ≤ 22 | −23 ≤ l ≤ 23 | −32 ≤ l ≤ 32 | −26 ≤ l ≤ 26 |
| No. of measured reflections | 18823 | 23554 | 87170 | 62907 |
| No. of independent reflections | 979 | 1084 | 2813 | 1554 |
| I > 3σ(I) (total) | 671 | 876 | 2044 | 1305 |

<div align="center">

**Refinement**

</div>

| | | | | |
|---|---|---|---|---|
| Number of refined parameters | 41 | 42 | 43 | 37 |
| Refinement method | Least-squares | Least-squares | Least-squares | Least-squares |
| Weighting scheme | sigma | sigma | sigma | sigma |

| | | | | |
|---|---|---|---|---|
| R1(F) [I > 3σ(I)]/R1(F²) (all data, %) | 0.0287/0.0551 | 0.0191/0.027 | 0.024/0.039 | 0.0636/0.0742 |
| wR2(F²) [I > 3σ(I)]/wR2(F²) (all data, %) | 0.0648/0.0720 | 0.0506/0.0517 | 0.0598/0.0627 | 0.1308/0.1308 |
| Goodness of Fit | 1.05 | 1.28 | 1.21 | 6.95 |
| Max/Min residual electronic density (e⁻/Å³) | 2.49/-1.56 | 2.47/-1.74 | 1.05/-1.78 | 6.69/-7.49 |
| Tmin/tmax | 0.6286/7456 | 0.5645/0.7458 | 0.5684/0.7481 | 0.6654/0.7452 |

**Table 2**. *Atomic Positions and Isotropic Thermal Displacement for $Ba_7O_2S_{13}V_2$ and the selenide-derivatives*

| | | $Ba_7S(VS_3O)_2(S_2)_3$ | | | |
|---|---|---|---|---|---|
| Atom | Wyck. | x | y | z | $U_{eq}$ |
| Ba1 | 12i | 0.08646(6) | 0.33068(6) | 0.11478(2) | 0.01591(19) |
| Ba2 | 2d | 0.666667 | 0.333333 | 0.25 | 0.0180(3) |
| V1 | 4f | 0.333333 | 0.666667 | -0.02776(11) | 0.0127(6) |
| S1 | 2b | 0 | 0 | 0 | 0.0225(14) |
| S2 | 6h | 0.2456 (4) | 0.1899(4) | 0.25 | 0.0165(11) |
| S3 | 6h | 0.3861(4) | 0.4669(3) | 0.25 | 0.0163(11) |
| S4 | 12i | 0.5628(3) | 0.6745(3) | -0.07033(11) | 0.0202(8) |
| O1 | 4f | 0.33333 | 0.66667 | 0.0690(2) | 0.014(2) |

|  |  |  |  |  |  |  |
|---|---|---|---|---|---|---|
| | | | **Ba₇V₂O₂S₉.₃₀₄Se₃.₆₉₆** | | | |
| Ba1 | 12i | | 0.66592(4) | 0.91171(3) | 0.612545(13) | 0.01688(11) |
| Ba2 | 2c | | 0.333333 | 0.666667 | 0.25 | 0.01914(17) |
| Se1 | 2d | 0.496 | 0 | 0 | 0 | 0.0161(4) |
| S1 | 2d | 0.504 | 0 | 0 | 0 | 0.0161(4) |
| Se2 | 6h | 0.533 | 0.17937(10) | 0.23646(10) | 0.25 | 0.0148(3) |
| S2 | 6h | 0.467 | 0.17937(10) | 0.23646(10) | 0.25 | 0.0148(3) |
| Se3 | 6h | 0.533 | 0.48006(11) | 0.38989(11) | 0.25 | 0.0187(3) |
| S3 | 6h | 0.467 | 0.48006(11) | 0.38989(11) | 0.25 | 0.0187(3) |
| V1 | 4f | | 0.33333 | 0.66667 | 0.47120(6) | 0.0147(3) |
| S4 | 12i | | 0.11451(15) | 0.67604(15) | 0.42932(6) | 0.0246(5) |
| O1 | 4f | | 0.33333 | 0.66667 | 0.5670(2) | 0.0116(12) |
| | | | **Ba₇V₂O₂S₇.₁₅Se₅.₈₅** | | | |
| Ba1 | 12i | | 0.665573(17) | 0.911645(16) | 0.611154(8) | 0.01484(5) |
| Ba2 | 2c | | 0.33333 | 0.66667 | 0.25 | 0.01917(8) |
| Se1 | 2b | 0.790 | 0 | 0 | 0 | 0.01425(15) |
| S1 | 2b | 0.21 | 0 | 0 | 0 | 0.01425(15) |
| Se2 | 6h | 0.843 | 0.05827(4) | 0.82327(4) | 0.25 | 0.01451(12) |
| S2 | 6h | 0.157 | 0.05827(4) | 0.82327(4) | 0.25 | 0.01451(12) |
| Se3 | 6h | 0.843 | 0.60907(4) | 0.09268(5) | 0.25 | 0.01585(12) |
| S3 | 6h | 0.157 | 0.60907(4) | 0.09268(5) | 0.25 | 0.01585(12) |
| V1 | 4f | | 0.33333 | 0.66667 | 0.4708(0) | 0.01344(13) |
| S4 | 12i | | 0.11448(8) | 0.67543(8) | 0.42889(4) | 0.0217(2) |
| O1 | 4f | | 0.33333 | 0.66667 | 0.56637(15) | 0.0129(6) |
| | | | **Ba₇V₂O₂S₆.₅₆₈Se₆.₄₃₂** | | | |
| Ba1 | 12i | | 0.24726(13) | 0.91247(12) | 0.61138(5) | 0.0115(4) |
| Ba2 | 2c | | 0.33333 | 0.66667 | 0.25 | 0.0167(7) |
| Se1 | 2b | 0.921 | 0 | 0 | 0 | 0.0161(11) |

| | | | | | | |
|---|---|---|---|---|---|---|
| S1 | 2b | 0.079 | 0 | 0 | 0 | 0.0161(11) |
| Se2 | 6h | 0.921 | 0.0580(3) | 0.2348(3) | 0.25 | 0.0113(9) |
| S2 | 6h | 0.079 | 0.0580(3) | 0.2348(3) | 0.25 | 0.0113(9) |
| Se3 | 6h | 0.921 | 0.4834(3) | 0.0930(3) | 0.25 | 0.0136(10) |
| S3 | 6h | 0.079 | 0.4834(3) | 0.0930(3) | 0.25 | 0.0136(10) |
| V1 | 4f | | 0.33333 | 0.66667 | 0.4702(3) | 0.0105(11) |
| S4 | 12i | | 0.3242(5) | 0.8859(5) | 0.4295(2) | 0.0139(8) |
| O1 | 4f | | 0.33333 | 0.66667 | 0.5630(11) | 0.019(6) |

**Table 3**. Anisotropic Thermal Parameters $U_{ij}$ (Å$^2$) for the sulfide and the selenide-derivatives

| Atom | $U_{11}$ | $U_{22}$ | $U_{33}$ | $U_{12}$ | $U_{13}$ | $U_{23}$ |
|---|---|---|---|---|---|---|
| | | | $Ba_7S(VS_3O)_2(S_2)_3$ | | | |
| Ba1 | 0.0136(4) | 0.0173(2) | 0.0164 (2) | 0.00738(19) | 0.00092(18) | 0.00330(18) |
| Ba2 | 0.0151(4) | 0.0151(4) | 0.0237(6) | 0.00756(18) | 0 | 0 |
| V1 | 0.0146(7) | 0.0146(7) | 0.0089(10) | 0.0073(3) | 0 | 0 |
| S1 | 0.0173(15) | 0.0173(15) | 0.033(3) | 0.0087(8) | 0 | 0 |
| S2 | 0.0177(13) | 0.0162(14) | 0.0168(13) | 0.0093(12) | 0 | 0 |
| S3 | 0.0169(14) | 0.0158(14) | 0.0152(12) | 0.0074(11) | 0 | 0 |
| S4 | 0.0179(10) | 0.0198(10) | 0.0231(10) | 0.0095(9) | 0.0049(8) | 0.0019(8) |
| O1 | 0.018(3) | 0.018(3) | 0.004(4) | 0.0092(14) | 0 | 0 |
| | | | $Ba_7V_2O_2S_{9.304}Se_{3.696}$ | | | |
| Ba1 | 0.01742(15) | 0.01470(14) | 0.01734(14) | 0.00713(11) | -0.00319(10) | -0.00095(9) |
| Ba2 | 0.01528(19) | 0.01528(19) | 0.0269(3) | 0.00764(10) | 0.00000 | 0.00000 |
| Se1 | 0.0150(5) | 0.0150(5) | 0.0182(8) | 0.0075(3) | 0.00000 | 0.00000 |
| S1 | 0.0150(5) | 0.0150(5) | 0.0182(8) | 0.0075(3) | 0.00000 | 0.00000 |
| Se2 | 0.0149(4) | 0.0174(4) | 0.0137(4) | 0.0092(4) | 0.00000 | 0.00000 |

| | | | | | | |
|---|---|---|---|---|---|---|
| S2 | 0.0149(4) | 0.0174(4) | 0.0137(4) | 0.0092(4) | 0.00000 | 0.00000 |
| Se3 | 0.0185(4) | 0.0181(5) | 0.0181(4) | 0.0081(4) | 0.00000 | 0.00000 |
| S3 | 0.0185(4) | 0.0181(5) | 0.0181(4) | 0.0081(4) | 0.00000 | 0.00000 |
| V1 | 0.0171(4) | 0.0171(4) | 0.0099(5) | 0.00854(19) | 0.00000 | 0.00000 |
| S4 | 0.0238(6) | 0.0250(6) | 0.0286(6) | 0.0152(6) | -0.0061(4) | 0.0004(5) |
| O1 | 0.0128(14) | 0.0128(14) | 0.009(2) | 0.0064(7) | 0.00000 | 0.00000 |

$Ba_7V_2O_2S_{7.15}Se_{5.85}$

| | | | | | | |
|---|---|---|---|---|---|---|
| Ba1 | 0.01490(6) | 0.01390(6) | 0.01476(6) | 0.00648(5) | -0.00127(4) | -0.00065(4) |
| Ba2 | 0.01470(9) | 0.01470(9) | 0.02810(17) | 0.00735(4) | 0 | 0 |
| Se1 | 0.01362(19 | 0.01362(19) | 0.0155(3) | 0.00681(9) | 0 | 0 |
| S1 | 0.01362(19) | 0.01362(19) | 0.0155(3) | 0.00681(9) | 0 | 0 |
| Se2 | 0.01415(14) | 0.01366(14) | 0.01443(15) | 0.00599(12) | 0 | 0 |
| S2 | 0.01415(14) | 0.01366(14) | 0.01443(15) | 0.00599(12) | 0 | 0 |
| Se3 | 0.01602(15) | 0.01745(16) | 0.01547(16) | 0.00941(12 | 0 | 0 |
| S3 | 0.01602(15) | 0.01745(16) | 0.01547(16) | 0.00941(12 | 0 | 0 |
| V1 | 0.01568(16) | 0.01568(16) | 0.0090(2) | 0.00784(8) | 0 | 0 |
| S4 | 0.0210(3) | 0.0223(3) | 0.0247(3) | 0.0130(2) | -0.0057(2) | 0.0006(2) |
| O1 | 0.0152(7) | 0.0152(7) | 0.0082(10) | 0.0076(3) | 0 | 0 |

$Ba_7V_2O_2S_{6.568}Se_{6.432}$

| | | | | | | |
|---|---|---|---|---|---|---|
| Ba1 | 0.0123(5) | 0.0094(5) | 0.0116(5) | 0.0045(4) | 0.0004(3) | -0.0003(3) |
| Ba2 | 0.0133(8) | 0.0133(8) | 0.0234(13) | 0.0067(4) | 0 | 0 |
| Se1 | 0.0141(13) | 0.0141(13) | 0.020(2) | 0.0070(6) | 0 | 0 |
| S1 | 0.0141(13) | 0.0141(13) | 0.020(2) | 0.0070(6) | 0 | 0 |
| Se2 | 0.0123(12) | 0.0138(13) | 0.0110(11) | 0.0088(9) | 0 | 0 |
| S2 | 0.0123(12) | 0.0138(13) | 0.0110(11) | 0.0088(9) | 0 | 0 |
| Se3 | 0.0129(12) | 0.0169(13) | 0.0129(11) | 0.0089(10) | 0 | 0 |
| S3 | 0.0129(12) | 0.0169(13) | 0.0129(11) | 0.0089(10) | 0 | 0 |
| V1 | 0.0083(13) | 0.0083(13) | 0.015(2) | 0.0041(7) | 0 | 0 |

| | | | |
|---|---|---|---|
| S4 | 0.0129(12) | 0.0169(13) | 0.0129(11) | 0.0089(10) | 0 | 0 |
| O1 | 0.027(7) | 0.027(7) | 0.003(8) | 0.013(4) | 0 | 0 |

**Table 7**. *Main Distances (Å) for Ba$_7$O$_2$S$_{13}$V$_2$ and the selenide-derivatives*

| Atoms 1,2 | d 1,2 [Å] | Atoms 1,2 | d 1,2 [Å] |
|---|---|---|---|
| | Ba$_7$S(VS$_3$O)$_2$(S$_2$)$_3$ | | |
| Ba1-V1 | 3.6420(13) | Ba1-O1 | 2.783(2) |
| Ba1-S1 | 3.3002(5) | Ba2-S2 | 3.280(3)*3 |
| Ba1-S2 | 3.289(2) | Ba2-S3 | 3.238(4)*3 |
| Ba1-S3 | 3.289(3) | V1-O1 | 1.684(2) |
| Ba1-S4 | 3.3309(19) | V1-S4 | 2.129(2)*3 |
| Ba1-S4 | 3.220(3) | S2-S3 | 2.122(4) |
| Ba1-S4 | 3.251(2) | | |

| Atoms 1,2 | d 1,2 [Å] | Atoms 1,2 | d 1,2 [Å] |
|---|---|---|---|
| | Ba$_7$V$_2$O$_2$S$_{9.304}$Se$_{3.696}$ | | |
| Ba1-V1 | 3.6471(8) | Ba1-O1 | 2.7842(11) |
| Ba1-Se1 | 3.3308(3) | Ba2-Se2 | 3.3709(9)*3 |
| Ba1-Se2 | 3.3678(8) | Ba2-Se3 | 3.3261(10)*3 |
| Ba1-Se2 | 3.4313(6) | V1-O1 | 1.687(4) |
| Ba1-Se3 | 3.3611(6) | V1-S4 | 2.129(2)*3 |
| Ba1-S4 | 3.2744(15) | Se2-Se3 | 2.3253(16) |
| Ba1-S4 | 3.257(2) | | |
| | Ba$_7$V$_2$O$_2$S$_{7.15}$Se$_{5.85}$ | | |
| Ba1-V1 | 3.6484(6) | Ba1-O1 | 2.7891(10) |

| | | | |
|---|---|---|---|
| Ba1-Se1 | 3.3310(8) | Ba2-Se2 | 3.3944(6))*3 |
| Ba1-Se2 | 3.4075(5) | Ba2-Se3 | 3.3552(5)*3 |
| Ba1-Se3 | 3.3981(4) | V1-O1 | 1.692(4) |
| Ba1-S4 | 3.3310(8) | V1-S4 | 2.1364(7) |
| Ba1-S4 | 3.2855(8) | Se2-Se3 | 2.3832(4) |
| Ba1-S4 | 3.2664(12) | | |

**$Ba_7V_2O_2S_{6.568}Se_{6.432}$**

| | | | |
|---|---|---|---|
| Ba1-V1 | 3.661(4) | Ba1-O1 | 1.642(18) |
| Ba1-Se1 | 3.3411(10) | Ba2-Se2 | 3.397(3)*3 |
| Ba1-Se2 | 3.4127(18) | Ba2-Se3 | 3.360(3)*3 |
| Ba1-Se3 | 3.399(2) | V1-O1 | 1.689(5) |
| Ba1-S4 | 3.324(4) | V1-S4 | 2.133(4)*3 |
| Ba1-S4 | 3.277(4) | Se2-Se3 | 2.3820(47) |
| Ba1-S4 | 3.283(4) | | |

### 9. Conclusion

A new series of thiovanadate polychalcogenide phases $Ba_7V_2S_{13}O_2$ and three selenide-derivatives $Ba_7V_2O_2S_{6.787}Se_{6.213}$, $Ba_7V_2O_2S_{6.904}Se_{6.096}$ and $Ba_7V_2O_2S_{9.263}Se_{3.737}$ were elaborated and their structures solved in the space group $P6_3/m$ (176). They represent an original and complex multi-anionic manipulation example. $Ba_7V_2S_{13}O_2$ is the sixth member in the quaternary system Ba−V−S−O (the first with disulfide pairs) while the three selenide-derivatives are the first ones in the system Ba−V−Se−S−O. These phases exhibit the mixed-anion building units $VOS_3$, isolated $Q^{2-}$ (Q= S, Se) sites (present in one layer) and isolated dichalcogenide pairs $Q_2$ (in the second layer). We show that all attempts of a selective substitution of sulfur by selenide in our synthetic conditions led to concomitant incorporation of Se in both the isolated Q and $Q_2$ pairs sites with mixed S/Se occupancy. It involves that the two types of pairs $S_2$ and $Se_2$ are present in the selenide-derivatives which can be monitored by the mean Q-Q distance refined and that evolve with respect of the substitution level. Our meta-GGA DFT calculations, including Bader charge analysis, on the sulfide and three ordered selenide-derivatives showed that the substitution in one layer only leads to local structural variation that are absorbed by the Ba sublattice while $VO_3S$ and $Q_2$ pairs remain rigid. This might explain the experimental disorder to avoid such constraints. Rationalization of the structure with respect to the electronic structure shows all the interest of designing new phases using such mixed-anion building blocks and/or dichalcogenide pairs. In particular, band-gap engineering through mastered approaches is important for a variety of properties.

## 10. REFERENCES

(1)    Nayak, S.; Nagaraja, K. K. *J. Alloys Compd.* **2020**, *814*, 152137.

(2)    Labégorre, J.-B.; Al Rahal Al Orabi, R.; Virfeu, A.; Gamon, J.; Barboux, P.; Pautrot-d'Alençon, L.; Le Mercier, T.; Berthebaud, D.; Maignan, A.; Guilmeau, E. *Chem. Mater.* **2018**, *30* (3), 1085–1094.

(3)    Wang, Q.; Nakabayashi, M.; Hisatomi, T.; Sun, S.; Akiyama, S.; Wang, Z.; Pan, Z.; Xiao, X.; Watanabe, T.; Yamada, T.; Shibata, N.; Takata, T.; Domen, K. *Nat. Mater.* **2019**, *18* (8), 827–832.

(4)    Kabbour, H.; Sayede, A.; Saitzek, S.; Lefèvre, G.; Cario, L.; Trentesaux, M.; Roussel, P. *Chem. Commun.* **2020**, *56* (11), 1645–1648.

(5)    Sasaki, S.; Caldes, M. T.; Guillot-Deudon, C.; Braems, I.; Steciuk, G.; Palatinus, L.; Gautron, E.; Frapper, G.; Janod, E.; Corraze, B.; Jobic, S.; Cario, L. *Nat. Commun.* **2021**, *12* (1), 1–8.

(6)    Kageyama, H.; Hayashi, K.; Maeda, K.; Attfield, J. P.; Hiroi, Z.; Rondinelli, J. M.; Poeppelmeier, K. R. *Nat. Commun.* **2018**, *9* (1), 772.

(7)    Luu, S. D. N.; Vaqueiro, P. *J Mater.* **2016**, *2* (2), 131–140.

(8)    Blandy, J. N.; Liu, S.; Smura, C. F.; Cassidy, S. J.; Woodruff, D. N.; McGrady, J. E.; Clarke, S. J. *Inorg. Chem.* **2018**, *57* (24), 15379–15388.

(9)    Evans, J. S. O.; Brogden, E. B.; Thompson, A. L.; Cordiner, R. L. *Chem. Commun.* **2002**, No. 8, 912–913.

(10)   Deguchi, K.; Mizuguchi, Y.; Demura, S.; Hara, H.; Watanabe, T.; Denholme, S. J.; Fujioka, M.; Okazaki, H.; Ozaki, T.; Takeya, H.; Yamaguchi, T.; Miura, O.; Takano, Y. *Epl* **2013**, *101* (1), 2–7.

(11)   Sasaki, S.; Lesault, M.; Grange, E.; Janod, E.; Corraze, B.; Cadars, S.; Caldes, M. T.; Guillot-Deudon, C.; Jobic, S.; Cario, L. *Chem. Commun.* **2019**, *55* (44), 6189–6192.

(12)   Nowack, E.; Schwarzenbach, D.; Hahn, T. *Acta Crystallogr. Sect. B* **1991**, *47* (5), 650–659.

(13)   Adachi, K.; Matsui, M.; Kimura, F.; Omata, Y. *J. Phys. Soc. Japan* **1980**, *49* (4), 1629–1630.

(14)   Guo, Y.; Shang, C.; Wang, E. *J. Mater. Chem. A* **2017**, *5* (6), 2504–2507.

(15)   Hao, J.; Xu, X.; You, H.; Min, H.; Liu, X.; Yang, H. *Chem. Eng. J.* **2021**, *418*, 129475.

(16)   Leriche, R. T.; Palacio-Morales, A.; Campetella, M.; Tresca, C.; Sasaki, S.; Brun, C.; Debontridder, F.; David, P.; Arfaoui, I.; Šofranko, O.; Samuely, T.; Kremer, G.; Monney, C.; Jaouen, T.; Cario, L.; Calandra, M.; Cren, T. *Adv. Funct. Mater.* **2021**, *31* (6), 1–10.

(17)   Kabbour, H.; Sayede, A.; Saitzek, S.; Lefèvre, G.; Cario, L.; Trentesaux, M.; Roussel, P. *Chem. Commun.* **2020**, *56* (11), 1645–1648.

(18)   Babo, J.-M.; Albrecht-Schmitt, T. E. *J. Solid State Chem.* **2012**, *187*, 264–268.

(19)   Almoussawi, B.; Huvé, M.; Dupray, V.; Clevers, S.; Duffort, V.; Mentré, O.; Roussel, P.; Arevalo-Lopez, A. M.; Kabbour, H. *Inorg. Chem.* **2020**.

(20)   Litteer, J. B.; Fettinger, J. C.; Eichhorn, B. W. *Acta Crystallogr. Sect. C* **1997**, *53* (2), 163–165.

(21)   Hopkins, E. J.; Prots, Y.; Burkhardt, U.; Watier, Y.; Hu, Z. **2015**, No. sample 2, 7938–7943.

(22) Hoggins, J. M. J. J. T.; Steinfink, L. E. R. S. C. H. **1978**, *17* (7), 1773–1775.

(23) Nicoud, S.; Mentre, O.; Kabbour, H. **2019**, *3*, 6–14.

(24) Thio, M.; Orthovanadates, O.; Vs, N.; Structures, S. C.; Schnabel, S.; Caroline, R. **2005**.

(25) Blöchl, P. E. *Phys. Rev. B* **1994**, *50* (24), 17953–17979.

(26) Kresse, G.; Joubert, D. *Phys. Rev. B* **1999**, *59* (3), 1758–1775.

(27) Kresse, G. . et al. .

(28) Tao, J.; Perdew, J. P.; Staroverov, V. N.; Scuseria, G. E. *Phys. Rev. Lett.* **2003**, *91* (14), 146401.

(29) Yang, Z.; Peng, H.; Sun, J.; Perdew, J. P. *Phys. Rev. B* **2016**, *93* (20), 205205.

(30) Petříček, V.; Dušek, M.; Palatinus, L. *Zeitschrift für Krist. - Cryst. Mater.* **2014**, *229* (5).

(31) van der Lee, A. *J. Appl. Crystallogr.* **2013**, *46* (5), 1306–1315.

(32) Almoussawi, B.; Tomohiri, H.; Kageyama, H.; Kabbour, H. *Eur. J. Inorg. Chem.* **2021**, ejic.202001166.

(33) Schnabel, S.; Röhr, C. *Zeitschrift fur Naturforsch. - Sect. B J. Chem. Sci.* **2008**, *63*, 819–833.

(34) Chung, M.-Y.; Lee, C.-S. *ChemInform* **2014**, *45* (10), no-no.

(35) Pocha, R.; Johrendt, D. *Inorg. Chem.* **2004**, *43* (21), 6830–6837.

(36) Assoud, A.; Kleinke, H. *ChemInform* **2005**, *36* (45), 4509–4513.

(37) Rodriguez-Carvajal, J. *IUCr Newsl.* **2001**, *26*.

(38) Tauc, J.; Grigorovici, R.; Vancu, A. *Phys. Status Solidi* **1966**, *15* (2), 627–637.

(39) Kubelka, P. and Munk, F. *Techn. Phys.* **1931**, *12*, 593–601.

(40) Wendlandt, W.; Hecht, H. G. *Reflectance Spectroscopy*; London Interscience: New York, 1966.

(41) Yu, M.; Trinkle, D. R. *J. Chem. Phys.* **2011**, *134* (6), 64111.

(42) Sun, J.; Remsing, R. C.; Zhang, Y.; Sun, Z.; Ruzsinszky, A.; Peng, H.; Yang, Z.; Paul, A.; Waghmare, U.; Wu, X.; Klein, M. L.; Perdew, J. P. *Nat. Chem.* **2016**, *8* (9), 831–836.

(43) Choe, J. S.; Lee, C.; Kim, M. J.; Lee, G.-G.; Shim, J.-H.; Lim, Y. S. *J. Appl. Phys.* **2020**, *127* (18), 185706.

(44) Sen, P.; Chouhan, R. K. *Electron. Struct.* **2020**, *2* (2), 25003.

(45) Clemens, O.; Haberkorn, R.; Kohlmann, H.; Springborg, M.; Beck, H. P. *Zeitschrift für Anorg. und Allg. Chemie* **2012**, *638* (7–8), 1134–1140.

11. Supporting Information:

**Table S1**. *Data collection and Refinement Details of $Ba_7V_2O_2S_{13}$ obtained at high pressure.*

| | |
|---|---|
| Formula | $Ba_7V_2O_2S_{13}$ (HP) |
| Detailed formula | $Ba_7S(VS_3O)_2(S_2)_3$ |
| $\alpha$ = | 0 |
| $\delta$= | 0 |
| Molecular weight (g. $mol^{-1}$) | 1512 |
| Symmetry | *Hexagonal* |
| Space group | P 63/m (176) |
| Unit cell dimensions (Å) | a= 8.8172(4) |
| | c= 17.3428(8) |
| Volume ($Å^3$) | 1167.65(9) |
| Z | 2 |
| | |
| Equipment | Rigaku XtaLab (Mo K$\alpha$) P200 |
| $\Lambda$ [Å] | 0.71073 |
| Calculated density (g $cm^{-3}$) | 4.3006 |
| Crystal shape | platelet |
| Crystal dimensions ($\mu$m) | 80x50x5 |
| Color | Dark |
| Absorption correction | analytical |
| Scan mode | $\omega$, $\varphi$ |
| $\theta$ (min–max) (°) | 2.35-30.56 |
| $\mu$ (mm$-1$) | 13.52 |
| F(000) | 1324 |
| Reciprocal space recording | $-8 \leq h \leq 12$ |
| | $-12 \leq k \leq 12$ |
| | $-22 \leq l \leq 24$ |

| | |
|---|---|
| No. of measured reflections | 7607 |
| No. of independent reflections | 1184 |
| I > 3σ(I) (total) | 900 |
| | |
| Number of refined parameters | 41 |
| Refinement method | Least-squares |
| Weighting scheme | sigma |
| R1(F) [I > 3σ(I)]/R1(F$^2$) (all data, %) | 0.0165/0.0322 |
| wR2(F$^2$) [I > 3σ(I)]/wR2(F$^2$) (all data, %) | 0.0361/0.0403 |
| Goodness of Fit | 1.05 |
| Max/Min residual electronic density (e$^-$/Å$^3$) | 0.93/-1.05 |
| Tmin/tmax | 0.96723/1.00000 |

**Table S2.** *Atomic Positions and Isotropic Thermal Displacement for Ba$_7$V$_2$O$_2$S$_{13}$ obtained at high pressure.*

| Ba$_7$S(VS$_3$O)$_2$(S$_2$)$_3$ (HP) | | | | | |
|---|---|---|---|---|---|
| Atom | Wyck. | x | y | z | U$_{eq}$ |
| Ba1 | 12i | 0.91345(2) | 0.67011(2) | 0.614532(10) | 0.01281(8) |
| Ba2 | 2d | 0.666667 | 0.333333 | 0.25 | 0.01563(12) |
| V1 | 4f | 0.333333 | 0.666667 | 0.47221(5) | 0.0117(2) |
| S1 | 2b | 0 | 0 | 0 | 0.0151(5) |
| S2 | 6h | 0.24559(15) | 0.18978(15) | 0.25 | 0.0136(4) |
| S3 | 6h | 0.38664(15) | 0.46756(15) | 0.25 | 0.0145(4) |
| S4 | 12i | 0.43709(11) | 0.32487(12) | 0.42953(5) | 0.0197(3) |
| O1 | 4f | 0.666667 | 0.333333 | 0.56961(19) | 0.0121(9) |

**Table S3.** *Anisotropic Thermal Parameters $U_{ij}$ (Å$^2$) for the sulfide obtained at high pressure.*

| Atom | $U_{11}$ | $U_{22}$ | $U_{33}$ | $U_{12}$ | $U_{13}$ | $U_{23}$ |
|---|---|---|---|---|---|---|
| | | | Ba$_7$S(VS$_3$O)$_2$(S$_2$)$_3$ (HP) | | | |
| Ba1 | 0.01144(10) | 0.01292(10) | 0.01332(10) | 0.00551(8) | -0.00055(7) | -0.00165(8) |
| Ba2 | 0.01255(14) | 0.01255(14) | 0.0218(2) | 0.00627(7) | 0 | 0 |
| V1 | 0.0138(3) | 0.0138(3) | 0.0076(4) | 0.00690(14) | 0 | 0 |
| S1 | 0.0141(6) | 0.0141(6) | 0.0169(9) | 0.0071(3) | 0 | 0 |
| S2 | 0.0148(5) | 0.0111(5) | 0.0144(5) | 0.0060(5 | 0 | 0 |
| S3 | 0.0156(5) | 0.0116(5) | 0.0151(5) | 0.0060(5) | 0 | 0 |
| S4 | 0.0160(4) | 0.0195(4) | 0.0232(4) | 0.0086(4) | -0.0059(3) | -0.0010(3) |
| O1 | 0.0136(11) | 0.0136(11) | 0.0090(16) | 0.0068(6) | 0 | 0 |

**Table S4.** *Main Distances (Å) for Ba$_7$V$_2$O$_2$S$_{13}$ obtained at high pressure.*

| Atoms 1,2 | d 1,2 [Å] | Atoms 1,2 | d 1,2 [Å] |
|---|---|---|---|
| | Ba$_7$S(VS$_3$O)$_2$(S$_2$)$_3$ (HP) | | |
| Ba1-V1 | 3.6307(7) | Ba1-O1 | 2.7745(10) |
| Ba1-S1 | 3.2815(3) | Ba2-S2 | 3.269(2)*3 |
| Ba1-S2 | 3.2779(12) | Ba2-S3 | 3.229(2)*3 |
| Ba1-S3 | 3.2834(11) | V1-O1 | 1.689(4) |
| Ba1-S4 | 3.3204(9) | V1-S4 | 2.1214(10)*3 |
| Ba1-S4 | 3.2055(10) | S2-S3 | 2.1213(11) |
| Ba1-S4 | 3.2351(9) | | |
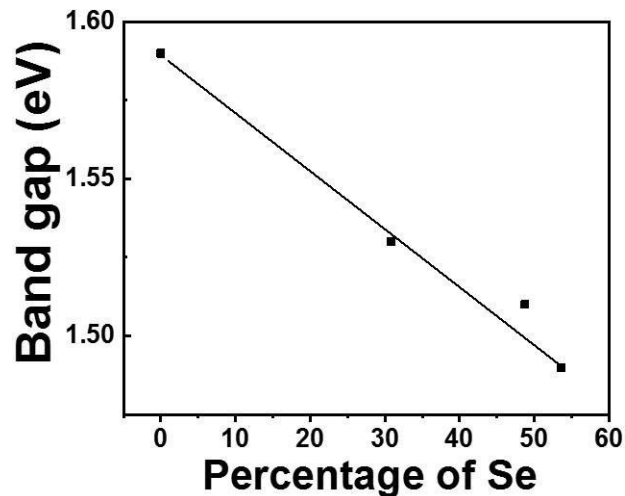
*Figure S1.* The band gap variation as function of atomic Se percentage.
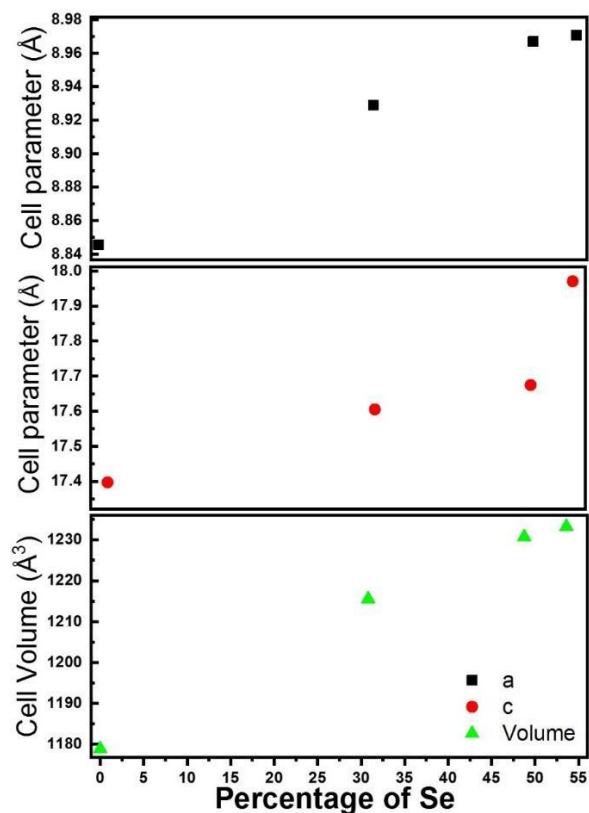


*Figure S2.* The cell parameters (a and c) and cell volume progress while Se percentage increase.

The volume variation shape looks like that for a parameter, whereas the c parameter variation changes deviate for %Se=53.6.

Chapter **III**

# New Polar oxychalcogenides

# III. Chapter III

# New Polar oxychalcogenides

### Introduction:

In the previous chapter, new phases in the systems Ba-V-S-O and Ba-V-Se-S-O, with thiovanadates heteroleptic building blocks and dichalcogenide pairs, and their optical properties were presented.
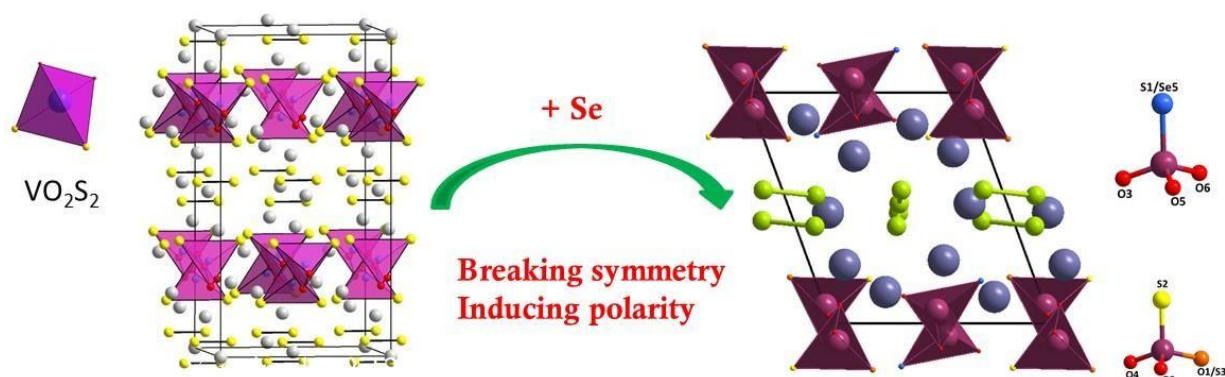


In this chapter, two new polar phases $Ba_5V_2O_{5.29}S_{2.55}Se_{4.16}$ and $Ba_2SnSi_2O_7S$ with non-linear optical properties are presented. This layered compound is the first oxysulfide in the mineral family Fresnoite, the well-known oxide member $Ba_2TiSi_2O_7(O)$ has been widely studied. The layered structure is built from $M^{4+}O_5$ (M= Ti, V ...) square pyramids connected to $A_2O_7$ tetrahedral dimers (A=Si, Ge, P ...) oriented in the direction of the polar c-axis. Large cations like $Ba^{2+}$ and $Sr^{2+}$ are inserted in the voids.

In the current work, the originality of $Ba_2SnSi_2O_7S$, solved and refines using single crystal XRD, is related to the square pyramid $Sn^{4+}O_4S$. Both the O/S environment and the square pyramid around $Sn4+$ are remarkable in this phase. Both tin in the M site and the oxysulfide character are reported for the first time in Fresnoite family. The more polarizable sulfide anions are oriented along the c axis. High purity yellow powder was obtained and characterized. While most Fresnoite reported absorbs in the UV or DUV, this new phase absorbs in the visible range. It shows a strong

second harmonic generation response with a peculiar mechanism regarding the contribution to the SHG response as found from DFT calculations.
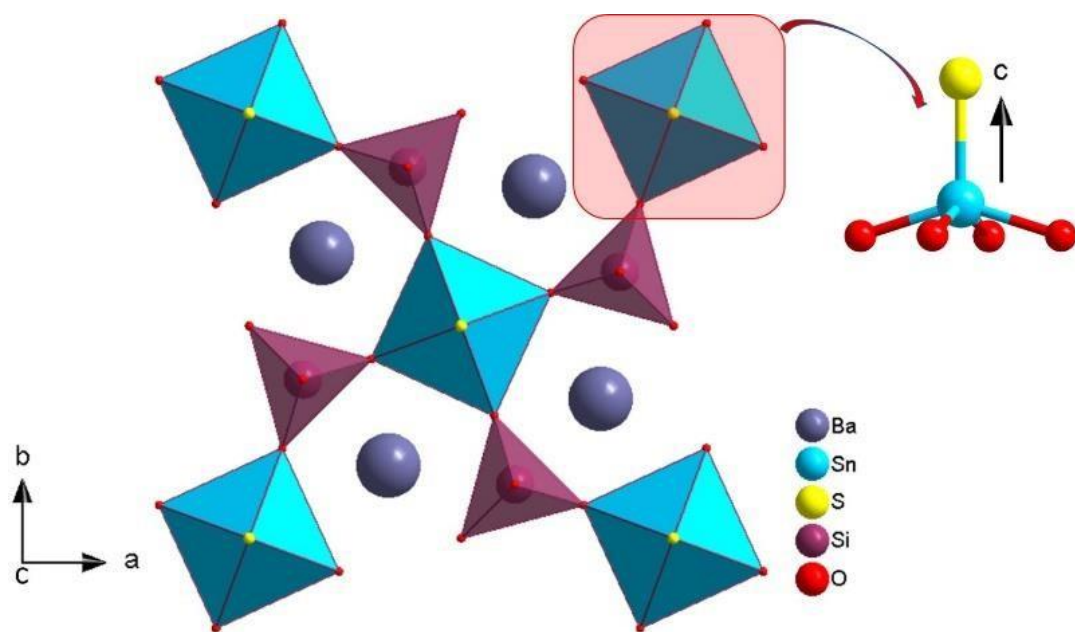
# Part 1:

# Second-Harmonic-Generation response in a new complex polar oxychalcogenide built from disordered thiovanadates and diselenide pairs

A. Part **I:** Second-Harmonic-Generation response in a new complex polar oxychalcogenide built from disordered thiovanadates and diselenide pairs

1. Abstract

The new oxychalcogenide phase $Ba_5V_2O_{5.29}S_{2.55}Se_{4.16}$ crystallizes in the polar space group $P2_1$. It was synthesized using solid-state reaction. It is the first oxychalcogenide combining triple anion thiovanadates with $O^{2-}$, $S^{2-}$ and $Se^{2-}$ around $V^{5+}$ and diselenide $(Se_2)^{2-}$ pairs, giving rising to a polar arrangement. It is associated to a second-harmonic generation (SHG) response. The structure was solved by single crystal XRD data and a high purity powder could be synthesized. This phase can be described by two alternating layers. The first one is characterized by disconnected distorted polar thiovanadates entities separated by the large cations $Ba^{2+}$. The second one is formed by isolated di-selenide pairs arranged into two different columns (different orientations) and $Ba^{2+}$ cations inserted in the voids. The Tauc plot lead to a band gap in the visible range around 1.56 eV. DFT calculations show a band gap dictated by the diselenide pairs states. The SHG measurements show a SHG response (under progress with the Fujian Institute) which makes this phase of great interest as a non-linear optical material.

2. Introduction

Non-linear optical materials (NLO) by their ability to convert the frequency [1] have attracted a lot of attention. Recently, mixed-anion inorganic compounds are pointed as promising IR-NLO materials which can optimize comprehensive performances[5]. Several types of crystals with mixed anions have been reported with excellent NLO properties[2], like second harmonic generation (SHG) property in $SrZn_2S_2O^{34}$. More particularly, the heteroleptic building units with SHG properties in oxychalcogenides show larger distortion of the coordination polyhedra, which enhance the polarity and the nonlinear optical intensity compared to their oxide analogue like in $BaGeOS_2$, $SrGeOS_2$[6], $SrGeOSe_2$ $BaGeOSe_2$[7]. On another hand, several oxysulfides structure types involving highly distorted units have also shown interesting SHG properties like $CaZnSO$[8], $SrZn_2OS_2$[3], $Sr_8Ga_8O_3S_{14}$[9], $Sr_6Cd_2Sb_6O_7S_{10}$[10], $Sr_4Pb_{1.5}Sb_5O_5Se_8$[11], $Sr_3Ge_2O_4Se_3$[12] and $\alpha$-$Na_3PO_3S$[13]. Their

mixed anion units contribute to the large anisotropy due to the different size and

electronegativity of anions, which is advantageous to achieve large birefringence and phase matchability[6].

Many structures with thiovanadates $VO_{4-x}S_x$ heteroleptic units were reported. In this paper we present an original polar oxychalcogenide with highly distorted units due to the presence of three anions types coordinated to vanadium ($V^{5+}$) cations ($VO_{2.65}S_{1.275}Se_{0.08}$). It also exhibits diselenide pairs as additional anionic species. This rich mixed-anion coordination environment is discussed with support of DFT calculations. Clear interesting non-linear optical properties have been identified but cannot be presented at this stage as full comprehension is still under progress.

3. Experimental section

**Synthesis:** Single crystals of $Ba_5V_2O_{5.29}S_{2.55}Se_{4.16}$ were initially found during attempts to substitute selected sulfur sites by selenide in the reported phase $Ba_5V_2S_4(S_2)_2O_4$. We attempted to synthesize a single-phase material from a stoichiometric mixture of the precursors $BaO/V_2O_5/V/Se/S$. Those precursors were mixed and thoroughly ground in an agate mortar before being pressed into pellets and heated in an evacuated sealed quartz tube. The heat treatment consisted in heating up to 750°C for 24 hours, then cooling down to 650°C at a 5°C/h rate, temperature at which the furnace was switched off.

**X-ray diffraction on single crystals diffraction** was performed on an X8 diffractometer equipped with a bi-dimensional CCD 4K detector and an Ag $K_\alpha$ source.

**The powder X-ray diffraction** pattern was collected on a Bruker D8 diffractometer equipped with a linear detector Lynxeye ($Cu_{K\alpha}$) in Bragg-Brentano geometry at room temperature.

**DFT calculations** were carried out by employing the projector- augmented-wave[14],[15] method encoded in the Vienna ab initio simulation package (VASP)[16] and the generalized gradient approximation (GGA) of Perdew, Burke and Ernzerhof[17] for the exchange-correlation functionals. Full geometry optimizations were carried out using a plane-wave energy cutoff of 550 eV and 120 k points in the irreducible Brillouin zone. It converged with residual Hellman−Feynman forces on atoms smaller than 0.03 eV $Å^{-1}$ and led to a good match with the experimental structure, i.e., within a reasonable error expected for the GGA method. The relaxed structure was used for

calculations of the electronic structure. For the latter, a plane-wave cutoff energy of 550 eV and a threshold of the self-consistent-field energy convergence of $10^{-6}$ eV were used, with 1215 k points in the irreducible Brillouin zone.

**Scanning electron microscopy (SEM)** experiments and EDX analysis were carried out on a Hitachi S400N.

**UV−Visible Measurements**

The reflectance of the sample was measured from 250 to 800 nm on a PerkinElmer Lambda 650 device.

4. Results and discussion

**a. Structure resolution**

The structure solution was carried out using XRD data obtained from a red and platelet-shape single crystal with the unit cell parameters a= 8.9665(3) Å, b= 10.4747(3) Å, and c= 10.0340(3) Å and the monoclinic polar space group $P2_1$ (4). The data collection and refinement details are given in **Table 1.** Refinement was carried out with the JANA2006[18] software based on a structure solution obtained using the charge-flipping method[19]. EDX analysis of the single crystals led to the average atomic ratio 36.46/12.9/30/20.7 for Ba/V/Se/S, respectively. Those values are close to ratios calculated from the refined formula: 36.47/14.59/30.34/18.6.

$Ba_5V_2O_{5.29}$ $S_{2.55}$ $Se_{4.16}$ formula can be deconvoluted as $Ba_5((VO_{2.5}(S_{1-x}Se_x)(S_{1-y}O_y))_2(Se_2)_2$ with x=0.16 and y=0.29. It is described by altering layers stacked along *c* axis as shown in **Figure 1.a**. Vanadium atoms occupy two Wyckoff positions 2*a* and are arranged in two columns (**Figure 1.b**). V1 is coordinated to one mixed site (S1/Se5) and three oxygen atoms, while V2 is coordinated to one mixed site (S/O), one sulfur and two oxygen atoms (see **Figure 1.d.** and **e**). The formed tetrahedra are oriented in alternating opposite direction. Two distinct diselenide $(Se_2)^{2-}$ pairs are observed with four crystallographic sites: Se1 and Se4 build pair 1 while Se2 and Se3 constitute the second pair. Those pairs are arranged in two different columns (see **Figure 1.c**) and exhibit close Se-Se distances of 2.399(26) and 2.389Å for $d_{Se1-Se4}$ and $d_{Se2-Se3}$, respectively. The latter

values are slightly smaller but comparable with the one found in $Sr_4Sn_2Se_9$ and $Sr_4Sn_2Se_{10}$ with 2.459 Å and 2.462 Å, respectively[20]. Within the thiovanadates, $d_{V2\text{-}S/O}$ was found in the range 1.919(18) Å slightly lower than the distance in the similarly disordered tetrahedral environment reported in $K_3VO_{1.38}S_{2.62}$[21] with $d_{V\text{-}S/O}$ =2.035(5) Å, but the mean distance will also depend on the S/O ratio in the mixed site, there is more sulfur in the later reference accordingly with the slightly greater distance. Similarly, $d_{V1\text{-}S/Se}$=2.255(15) Å is in the range distance found in $Cu_3 V^{5+}(S_2Se_2)$ with $d_{V\text{-}S/Se}$= 2.3255 Å which also contain a mixed S/Se site coordinating $V^{5+}$.

**Table 1.** *Data Collection and Refinement Details of $Ba_5V_2O_{5.29}S_{2.55}Se_{4.16}$.*

| Formula | $Ba_5V_2O_{5.29}S_{2.55}Se_{4.16}$ |
|---|---|
| Molecular weight (g. mol$^{-1}$) | 1283.4 |
| Symmetry | Monoclinic |
| Space group | P 1 2$_1$ 1 (4) |
| Unit cell dimensions (Å) | a= 8.9883(4) |
| | b= 10.4221(6) |
| | c= 10.0233(5) |
| | β= 110.1541(19) |
| | |
| Volume (Å$^3$) | 881.46(8) |
| Z | 2 |
| **Data Collection** | |
| Equipment | Bruker CCD |
| Λ [Ag K$_\alpha$; Å] | 0.56087 |
| Calculated density (g cm$^{-3}$) | 4.8356 |
| Crystal shape | Platelet |
| Crystal dimensions (μm) | 75-35-5 |
| Color | Red |

| | |
|---|---|
| Absorption correction | Analytical |
| Scan mode | ω, φ |
| θ (min–max) (°) | 1.71- 18.63 |
| μ (mm−1 ; for λ Kα = 0.56087Å) | 11.031 |
| F(000) | 1101 |
| Reciprocal space recording | $-10 \leq h \leq 10$ |
| | $-11 \leq k \leq 11$ |
| | $-11 \leq l \leq 11$ |
| | |
| No. of measured reflections | 28977 |
| No. of independent reflections | 2698 |
| I > 3σ(I) (total) | 2366 |
| Refinement | |
| Number of refined parameters | 142 |
| **Refinement method** | Least-squares |
| Weighting scheme | Sigma |
| R1(F) [I > 3σ(I)]/R1(F$^2$) (all data, %) | 0.0329/ 0.0411 |
| wR2(F$^2$) [I > 3σ(I)]/wR2(F$^2$) (all data, %) | 0.0337/ 0.0360 |
| Goodness of Fit | 1.29 |
| Max/Min residual electronic density (e$^-$/Å$^3$) | 0.94/ -1.03 |
| *T(min/max)* | 0.6398 /0.7443 |

### b.  Polycrystalline Phase Analysis

The synthesis of the pure ordered powder phase $Ba_5V_2S_4(Se_2)_2O_4$ was carried out following the procedure described in the Experimental Section. As depicted in **Figure 2.a**, the phase is formed together with a minor contribution of the centrosymmetric and white impurity $Ba_3V_2O_8$. A

Rietveld refinement using Jana2006 and the single crystal determined structural model was carried out and led to very good reliability factors Bragg with main phase/impurity ratio 0.94/0.06.

### c. Optical Measurements

UV–visible diffuse-reflectance analysis of the polycrystalline powder is represented in **Figure 2.b**. A Kubelka–Munk transformation[22] was applied to the measured diffuse-reflectance (R) spectra using the function $F(R) = (1 − R)^2/2R$. Then a Tauc plot[23] was used to determine the optical band gap $E_g$, using the equation $[F(R) h\nu]1/n = k(h\nu − E_g)$, where $h\nu$ is the photon energy, k an energy-independent constant, $E_g$ the optical band gap, and $n$ is an exponent related to the type of transition. Assuming a direct transition (exponent n = 1/2), the plot of $[F(R) h\nu]^{1/2}$ *versus* $h\nu$ leads to $E_g$=1.52 eV.
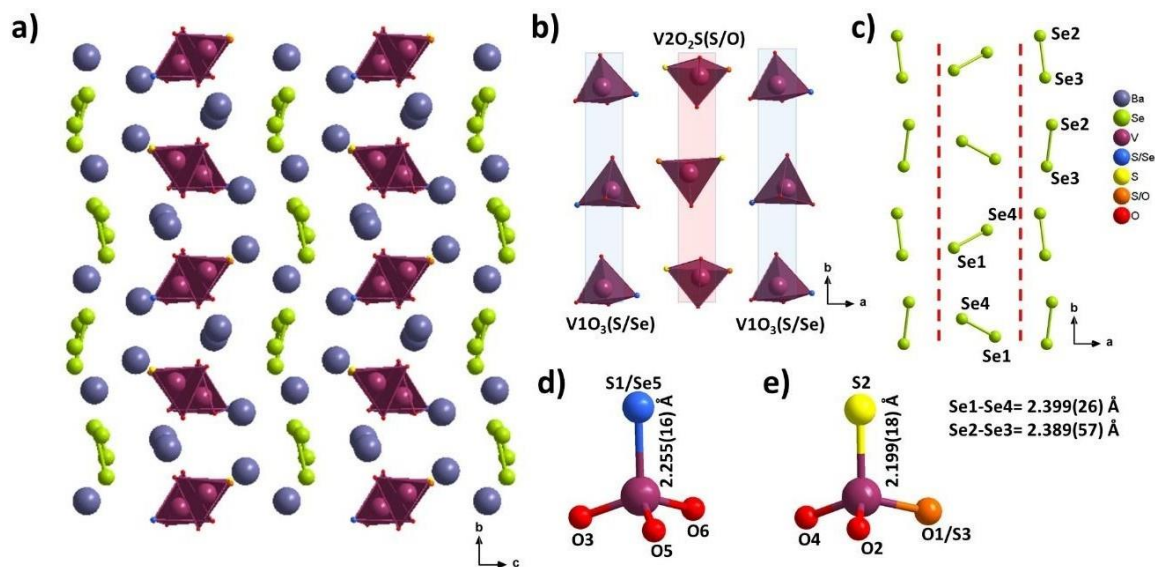


**Figure 1:** (a) $Ba_5V_2O_{5.29}S_{2.55}Se_{4.16}$ projected along a-axis (b) Projection of the tetrahedral units along the c-axis. (c) Slice of the structure showing the $(Se_2)^{2-}$ pairs along the c-axis. (d) (e) Slice of the structure showing the tetrahedral $V1O_3(S/Se)$ and $V2O_2S(S/O)$ units.
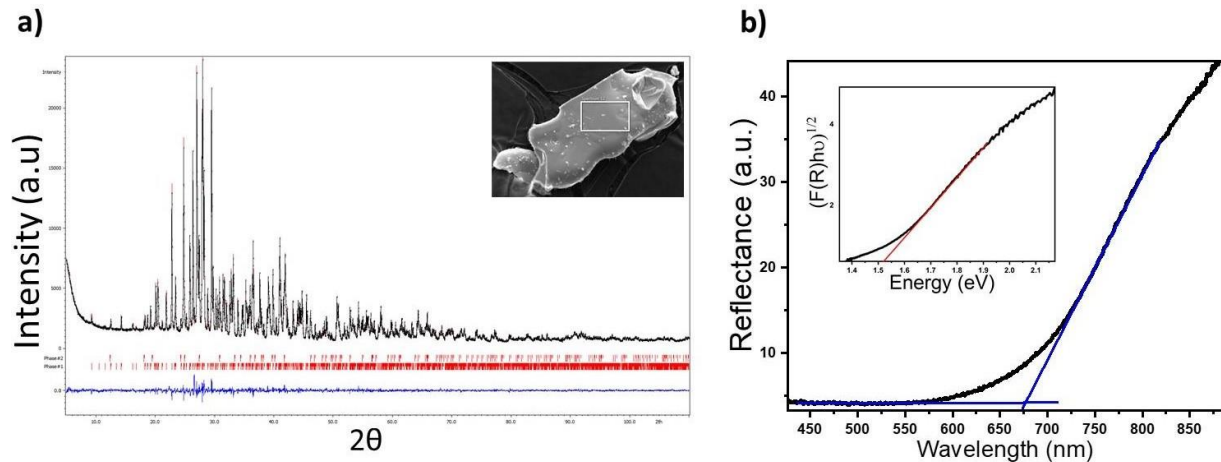
**Figure 2:** *(a) Powder XRD Rietveld refinement: the experimental (black) and calculated (red) patterns are superimposed; the difference curve and Bragg positions are represented in blue and red respectively for the main phase (1) and the impurity (2). A SEM image of a single crystal is shown as inset. (b) Diffuse-reflectance spectra and the corresponding Tauc plot as an inset.*

**Table 2**. *Atomic Positions and Isotropic Thermal Displacements for* $Ba_5V_2O_{5.29}S_{2.55}Se_{4.16}$

| Atom | Wyck. | S.O.F. | x | y | z | U$_{eq}$ |
|------|-------|--------|------|------|------|------|
| Ba1 | 2a | | 0.78641(12) | 0.670(4) | 0.11619(11) | 0.0137(4) |
| Ba2 | 2a | | 0.17038(12) | 0.931(4) | 0.48052(11) | 0.0154(4) |
| Ba3 | 2a | | 0.15892(12) | 0.332(4) | 0.25460(11) | 0.0162(4) |
| Ba4 | 2a | | 0.29945(12) | 0.711(4) | 0.13695(11) | 0.0165(4) |
| Ba5 | 2a | | 0.38278(17) | 0.566(4) | 0.72595(13) | 0.0455(6) |
| Se1 | 2a | | 0.0870(2) | 0.627(4) | 0.42133(19) | 0.0176(6) |
| Se2 | 2a | | 0.4911(2) | 0.762(4) | 0.48019(19) | 0.0203(7) |
| Se3 | 2a | | 0.4595(2) | 0.539(4) | 0.42201(19) | 0.0240(7) |
| Se4 | 2a | | 0.8573(2) | 0.727(4) | 0.44578(19) | 0.0248(7) |
| V1 | 2a | | 0.4999(3) | 0.399(4) | 0.0561(3) | 0.0114(10) |

| | | | | | | |
|---|---|---|---|---|---|---|
| V2 | 2a | | -0.0026(4) | 0.464(4) | 0.9227(3) | 0.0220(12) |
| S1 | 2a | 0.84 | 0.7521(4) | 0.347(4) | 0.1851(4) | 0.0204(13) |
| Se5 | 2a | 0.16 | 0.7521(4) | 0.347(4) | 0.1851(4) | 0.0204(13) |
| S2 | 2a | | -0.2476(6) | 0.525(4) | 0.8074(5) | 0.0238(17) |
| O1 | 2a | 0.29 | 0.1113(8) | 0.511(4) | 0.7995(8) | 0.065(4) |
| S3 | 2a | 0.71 | 0.1113(8) | 0.511(4) | 0.7995(8) | 0.065(4) |
| O2 | 2a | | 0.0008(13) | 0.306(4) | 0.9620(11) | 0.013(4) |
| O3 | 2a | | 0.4836(14) | 0.562(4) | 0.0387(12) | 0.022(5) |
| O4 | 2a | | 0.0715(14) | 0.538(4) | 1.0809(13) | 0.025(3) |
| O5 | 2a | | 0.4567(12) | 0.341(4) | -0.1104(11) | 0.014(2) |
| O6 | 2a | | 0.3750(14) | 0.325(4) | 0.1190(12) | 0.024(5) |

**Table 3.** *Anisotropic Thermal Parameters Uij ($\mathring{A}^2$) for $Ba_5V_2O_{5.29}S_{2.55}Se_{4.16}$*

| Atom | $U_{11}$ | $U_{22}$ | $U_{33}$ | $U_{12}$ | $U_{13}$ | $U_{23}$ |
|---|---|---|---|---|---|---|
| Ba1 | 0.0131(5) | 0.0150(6) | 0.0099(6) | -0.0004(4) | 0.0001(4) | 0.0023(4) |
| Ba2 | 0.0201(6) | 0.0126(5) | 0.0135(6) | -0.0002(4) | 0.0058(4) | -0.0009(5) |
| Ba3 | 0.0176(6) | 0.0195(6) | 0.0108(6) | 0.0008(5) | 0.0039(4) | 0.0032(5) |
| Ba4 | 0.0127(5) | 0.0168(6) | 0.0194(6) | 0.0002(5) | 0.0049(5) | 0.0056(5) |
| Ba5 | 0.0568(9) | 0.0546(10) | 0.0122(7) | 0.0384(8) | -0.0046(6) | 0.0040(6) |
| Se1 | 0.0187(9) | 0.0180(9) | 0.0125(9) | -0.0004(7) | 0.0010(7) | 0.0003(7) |

| | | | | | |
|------|------------|------------|------------|-------------|-------------|-------------|
| Se2 | 0.0171(9) | 0.0199(10) | 0.0193(11) | 0.0032(8) | 0.0004(8) | -0.0050(8) |
| Se3 | 0.0244(10) | 0.0179(10) | 0.0228(11) | 0.0029(8) | -0.0005(8) | 0.0002(8) |
| Se4 | 0.0324(11) | 0.0230(10) | 0.0187(10) | -0.0007(9) | 0.0084(8) | -0.0013(8) |
| V1 | 0.0103(14) | 0.0118(16) | 0.0089(16) | 0.0004(12) | -0.0006(12) | -0.0002(12) |
| V2 | 0.0276(18) | 0.0110(17) | 0.0161(18) | -0.0023(13) | -0.0069(14) | 0.0022(13) |
| S1 | 0.0182(19) | 0.025(2) | 0.0154(19) | -0.0010(17) | 0.0018(15) | 0.0014(17) |
| Se5 | 0.0182(19) | 0.025(2) | 0.0154(19) | -0.0010(17) | 0.0018(15) | 0.0014(17) |
| S2 | 0.030(3) | 0.019(2) | 0.013(2) | 0.006(2) | -0.005(2) | -0.004(2) |
| O1 | 0.033(4) | 0.118(8) | 0.044(5) | -0.010(5) | 0.012(4) | 0.005(5) |
| S3 | 0.033(4) | 0.118(8) | 0.044(5) | -0.010(5) | 0.012(4) | 0.005(5) |
| O2 | 0.013(6) | 0.008(7) | 0.016(7) | -0.001(5) | 0.001(5) | 0.001(5) |
| O3 | 0.034(8) | 0.020(7) | 0.016(7) | 0.001(6) | 0.012(6) | 0.000(6) |
| O6 | 0.026(7) | 0.032(8) | 0.018(7) | -0.008(6) | 0.013(6) | -0.010(6) |

**Table 4**. *Main Distances (Å) for* $Ba_5V_2O_{5.29}S_{2.55}Se_{4.16}$

| Atom1 | Atom2 | d 1,2 [Å] | Atom1 | Atom2 | d 1,2 [Å] |
|-------|--------|-----------|-------|--------|-----------|
| Ba1 | **O2** | 2.70(3) | **Ba4** | **O5** | 2.67(3) |
| Ba1 | **O3** | 2.79(3) | **Ba5** | **Se1** | 3.347(11) |
| Ba1 | **O5** | 2.81(4) | **Ba5** | **Se3** | 3.359(6) |
| Ba1 | **O6** | 2.81(3) | **Ba5** | **S1/Se5** | 3.40(5) |
| Ba2 | **Se1** | 3.26(6) | **Ba5** | **S2** | 3.165(10) |

| | | | | | |
|------|--------|-----------|------|--------|-----------|
| Ba2 | Se2 | 3.38(3) | Ba5 | O1 | 2.841(15) |
| Ba2 | Se3 | 3.32(2) | Ba5 | S3 | 2.841(15) |
| Ba2 | Se4 | 3.20(6) | Ba5 | O5 | 2.81(5) |
| Ba2 | S1/Se5 | 3.298(16) | V1 | S1/Se5 | 2.255(15) |
| Ba2 | S3/O1 | 3.176(17) | V1 | O3 | 1.71(6) |
| Ba3 | Se2 | 3.425(13) | V1 | O5 | 1.69(2) |
| Ba3 | Se3 | 3.41(4) | V1 | O6 | 1.66(3) |
| Ba3 | Se4 | 3.25(2) | V2 | S2 | 2.199(18) |
| Ba3 | O2 | 2.797(11) | V2 | S3/O1 | 1.919(18) |
| Ba3 | O4 | 2.70(5) | V2 | O2 | 1.69(6) |
| Ba3 | O6 | 2.728(11) | V2 | O4 | 1.68(3) |
| Ba4 | Se2 | 3.317(10) | Se1 | Se4 | 2.399(26) |
| Ba4 | Se3 | 3.26(3) | Se2 | Se3 | 2.389(57) |
| Ba4 | S1/Se5 | 3.41(2) | | | |
| Ba4 | O2 | 2.72(2) | | | |
| Ba4 | O3 | 2.69(4) | | | |
| Ba4 | O4 | 2.64(4) | | | |

## d.  DFT Calculations

were carried out using the ideally ordered structure which was fully relaxed; The band structure and the total and projected density of states are represented in **Figure 3** with focus on the valence band (VB) and conduction band (CB) area based on the content of a unit cell and the total contribution of each type of atom. The DFT calculated band gap is found ~0.7 eV which is shifted from the experimental determination even considering the expected underestimation from the GGA-PBE functional. The bottom of the CB and top of the VB are occupied by selenide states,

thus the later anions are dictating the band gap. Then from 1 to 3.5 eV the CB is dominated by V 3$d$ states. Above 3.5 eV the CB is dominated by Ba 5$d$ states which occupied states are deep in the VB (not shown) as expected from its strong ionic character. The top of the VB on another hand shows a greater contribution from selenide atoms states which are globally contributing higher in the VB just below the Fermi level. Others ions contributions are shown below -2 eV. Moreover, the band gap is found direct as shown on the band structure.
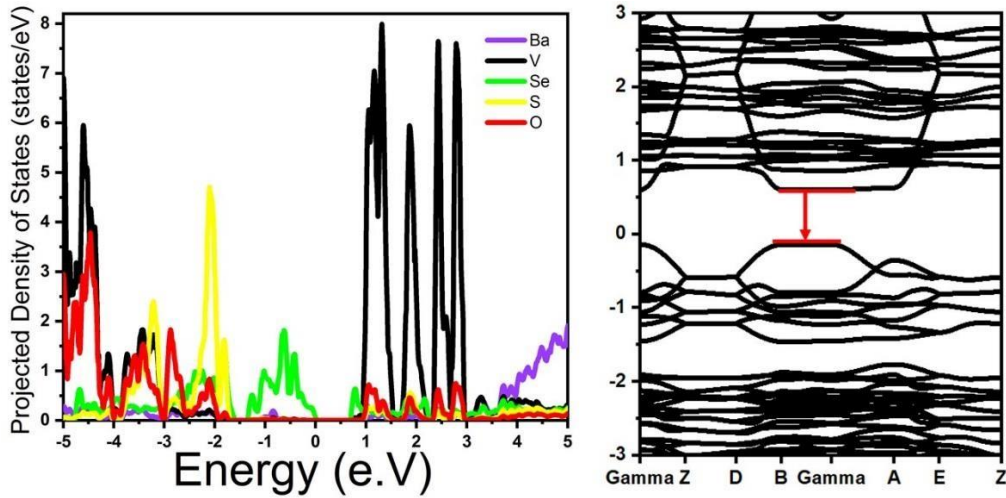


*Figure 3:* Total DOS and PDOS (left). Band structure (right) for Ba$_5$V$_2$Se$_4$S$_2$O$_6$

## 5. Conclusion

The new polar phase Ba$_5$V$_2$O$_{5.29}$S$_{2.55}$Se$_{4.16}$ was elaborated and its structure solved and refined using single crystal XRD data. This original mixed anion compound is the first polar one in the system Ba-V-O-S-Se. This phase exhibits highly distorted mixed-anion building units VO$_3$(S/Se), VO$_2$S(S/O), and isolated disulfide pairs Se$_2$ (in the second layer). The diffuse reflectance spectrum shows an absorption edge in the visible light range with a band gap of 1.52 eV. The DFT electronic structure calculations evidence the primary role of the diselenide pairs which are dictating the band gap by their dominant contribution both at the top of the VB and the bottom of the CB. Non-linear optical measurements show a strong SHG response and the full comprehension of the results is still under progress in collaboration with Fujian institute. This phase opens new perspectives in the design of non-linear optical materials with greater performances.

6. References:

(1) Ran, M. Y.; Ma, Z.; Chen, H.; Li, B.; Wu, X. T.; Lin, H.; Zhu, Q. L. Partial Isovalent Anion Substitution to Access Remarkable Second-Harmonic Generation Response: A Generic and Effective Strategy for Design of Infrared Nonlinear Optical Materials. *Chem. Mater.* **2020**, *32* (13), 5890–5896. https://doi.org/10.1021/acs.chemmater.0c02011.

(2) Pan, Y.; Guo, S. P.; Liu, B. W.; Xue, H. G.; Guo, G. C. Second-Order Nonlinear Optical Crystals with Mixed Anions. *Coord. Chem. Rev.* **2018**, *374*, 464–496. https://doi.org/10.1016/j.ccr.2018.07.013.

(3) Chen, C.; Zhuang, Y.; Tu, D.; Wang, X.; Pan, C.; Xie, R.-J. Creating Visible-to-near-Infrared Mechanoluminescence in Mixed-Anion Compounds $SrZn_2S_2O$ and SrZnSO. *Nano Energy* **2020**, *68*, 104329. https://doi.org/10.1016/j.nanoen.2019.104329.

(4) Almoussawi, B.; Huvé, M.; Dupray, V.; Clevers, S.; Duffort, V.; Mentré, O.; Roussel, P.; Arevalo-Lopez, A. M.; Kabbour, H. Oxysulfide $Ba_5(VO_2S_2)_2(S_2)_2$ Combining Disulfide Channels and Mixed-Anion Tetrahedra and Its Third-Harmonic-Generation Properties. *Inorg. Chem.* **2020**, *59* (9), 5907–5917. https://doi.org/10.1021/acs.inorgchem.9b03674.

(5) Li, Y. Y.; Wang, W. J.; Wang, H.; Lin, H.; Wu, L. M. Mixed-Anion Inorganic Compounds: A Favorable Candidate for Infrared Nonlinear Optical Materials. *Cryst. Growth Des.* **2019**, *19* (7), 4172–4192. https://doi.org/10.1021/acs.cgd.9b00358.

(6) Shi, Y.-F.; Wei, W.-B.; Wu, X.-T.; Lin, H.; Zhu, Q.-L. Recent Progress in Oxychalcogenides as IR Nonlinear Optical Materials. *Dalt. Trans.* **2021**, *50* (12), 4112–4118. https://doi.org/10.1039/D1DT00222H.

(7) Liu, B.-W.; Jiang, X.-M.; Wang, G.-E.; Zeng, H.-Y.; Zhang, M.-J.; Li, S.-F.; Guo, W.-H.; Guo, G.-C. Oxychalcogenide $BaGeOSe_2$ : Highly Distorted Mixed-Anion Building Units Leading to a Large Second-Harmonic Generation Response. *Chem. Mater.* **2015**, *27* (24), 8189–8192. https://doi.org/10.1021/acs.chemmater.5b03649.

(8) Gulyaeva, R. I.; Selivanov, E. N.; Vershinin, A. D.; Chumarev, V. M. Thermal Expansion of CaZnSO. *Inorg. Mater.* **2006**, *42* (8), 897–900. https://doi.org/10.1134/S0020168506080188.

(9) Wang, R.; Guo, Y.; Zhang, X.; Xiao, Y.; Yao, J.; Huang, F. $Sr_5Ga_8O_3S_{14}$ : A Nonlinear Optical Oxysulfide with Melilite-Derived Structure and Wide Band Gap. *Inorg. Chem.* **2020**, *59* (14), 9944–9950. https://doi.org/10.1021/acs.inorgchem.0c01111.

(10) Wang, R.; Liang, F.; Wang, F.; Guo, Y.; Zhang, X.; Xiao, Y.; Bu, K.; Lin, Z.; Yao, J.; Zhai, T.; Huang, F.

$Sr_6Cd_2Sb_6O_7S_{10}$ : Strong SHG Response Activated by Highly Polarizable Sb/O/S Groups. *Angew. Chemie Int. Ed.* **2019**, *58* (24), 8078–8081. https://doi.org/10.1002/anie.201902806.

(11)    Wang, Y.; Luo, M.; Zhao, P.; Che, X.; Cao, Y.; Huang, F. $Sr_4Pb_{1.5}Sb_5O_5Se_8$ : A New Mid-Infrared Nonlinear Optical Material with a Moderate SHG Response. *CrystEngComm* **2020**, *22* (20), 3526–3530. https://doi.org/10.1039/D0CE00084A.

(12)    Xing, W.; Fang, P.; Wang, N.; Li, Z.; Lin, Z.; Yao, J.; Yin, W.; Kang, B. Two Mixed-Anion Units of $[GeOSe_3]$ and $[GeO_3S]$ Originating from Partial Isovalent Anion Substitution and Inducing Moderate Second Harmonic Generation Response and Large Birefringence. *Inorg. Chem.* **2020**, *59* (22), 16716–16724. https://doi.org/10.1021/acs.inorgchem.0c02709.

(13)    Takas, N. J.; Aitken, J. A. Phase Transitions and Second-Harmonic Generation in Sodium Monothiophosphate. *Inorg. Chem.* **2006**, *45* (7), 2779–2781. https://doi.org/10.1021/ic0520216.

(14)    Blöchl, P. E. Projector Augmented-Wave Method. *Phys. Rev. B* **1994**, *50* (24), 17953–17979. https://doi.org/10.1103/PhysRevB.50.17953.

(15)    Kresse, G.; Joubert, D. From Ultrasoft Pseudopotentials to the Projector Augmented-Wave Method. *Phys. Rev. B* **1999**, *59* (3), 1758–1775. https://doi.org/10.1103/PhysRevB.59.1758.

(16)    Kresse, G. ; Vogtenhuber, D.; Marsman, M.; Kaltak, M.; Karsai, F. ; Schlipf, M. Vienna ab-initio simulation package (VASP) https://www.vasp.at.

(17)    Perdew, J. P.; Burke, K.; Ernzerhof, M. Generalized Gradient Approximation Made Simple. *Phys. Rev. Lett.* **1996**, *77* (18), 3865–3868. https://doi.org/10.1103/PhysRevLett.77.3865.

(18)    Petříček, V.; Dušek, M.; Palatinus, L. Crystallographic Computing System JANA2006: General Features. *Zeitschrift für Krist. - Cryst. Mater.* **2014**, *229* (5), 345–352. https://doi.org/10.1515/zkri-2014-1737.

(19)    van der Lee, A. Charge Flipping for Routine Structure Solution. *J. Appl. Crystallogr.* **2013**, *46* (5), 1306–1315. https://doi.org/10.1107/S0021889813020049.

(20)    Pocha, R.; Johrendt, D. Crystal Structures of $Sr_4Sn_2Se_9$ and $Sr_4Sn_2Se_{10}$ and the Oxidation State of Tin in an Unusual Geometry. *Inorg. Chem.* **2004**, *43* (21), 6830–6837. https://doi.org/10.1021/ic049663y.

(21)    Schnabel, S.; Röhr, C. Potassium Thio/Oxo-Vanadates(V) $K_3[VS_xO_{4-x}]$ (x = 1-4) and $Na_3[VSO_3]$: Synthesis, Structural Chemistry, Properties. *Zeitschrift fur Naturforsch. - Sect. B J. Chem. Sci.* **2008**, *63*, 819–833.

(22)    Tauc, J.; Grigorovici, R.; Vancu, A. Optical Properties and Electronic Structure of Amorphous Germanium. *Phys. status solidi* **1966**, *15* (2), 627–637. https://doi.org/10.1002/pssb.19660150224.

(23)    Hecht, H. G. The Interpretation of Diffuse Reflectance Spectra. *J. Res. Natl. Bur. Stand. Sect. A Phys. Chem.* **1976**, *80A* (4), 567. https://doi.org/10.6028/jres.080A.056.

# Part 2:

# First Fresnoite-type oxysulfide $Ba_2SnSSi_2O_7$ with $SnO_4S$ square pyramids: Preparation and characterization of its nonlinear optical properties

Part 2: First Fresnoite-type oxysulfide $Ba_2SnSSi_2O_7$ with $SnO_4S$ square pyramids: Preparation and characterization of its nonlinear optical properties

1. Introduction

Fresnoite $Ba_2TiOSi_2O_7$[1-2] is a non-centrosymmetric layered compound that has received much attention. In the $TiOSi_2O_7$ layers of Fresnoite, $TiO_5$ square pyramids are corner-shared with $Si_2O_7$ groups such that the apical Ti-O bonds of the $TiO_5$ pyramids are oriented along the c-axis, and so are the apical Si-O bonds of the $SiO_4$ tetrahedra forming the $Si_2O_7$ units. Since the $TiOSi_2O_7$ layers are stacked along the c-direction with $Ba^{2+}$ ions lying in between the layers, Fresnoite has no inversion symmetry and exhibits nonlinear optical (NLO) properties. All known Fresnoite-type compounds are oxides except for a few oxychlorides, namely, $Ba_2MnClSi_2O_7$[3], $KBaCuClV_2O_7$[4] and $Ba_2NaClP_2O_7$[5], in which the $MO_4Cl$ (M = Mn, Cu, Na) square pyramids have the M-Cl apical bonds pointed along the c-axis while the $V_2O_7$ and $P_2O_7$ units play the role of the $Si_2O_7$ units. NLO compounds exhibit strong second harmonic generation (SHG) responses when they possess groups composed of mixed anions; $BaGeSe_2O$[6] with $GeO_2Se_2$ tetrahedra shows a strong SHG response. A large SHG response is found in oriented single crystals of oxysulfide $CaCoSO$[7] consisting of $CoOS_3$ tetrahedra. In addition, the presence of groups with polarizable elements enhances SHG responses, e.g., $Sr_6Cd_2Sb_6O_7S_{10}$[8] contains $SbOS_4$ and $SbS_5$ square pyramids composed of polarizable $S^{2-}$ and $Sb^{3+}$ ions. These observations suggest that a Fresnoite-type phase with enhanced SHG response can be produced by replacing the $TiO_5$ pyramids with another pyramidal groups composed of mixed polarizable ions. In our search for such a phase, we prepared a Fresnoite-type oxysulfide, $Ba_2SnSSi_2O_7$ (hereafter, BSSSO), which has $SnO_4S$ square pyramids with Sn-S apical bonds pointed along the c-axis. Our analysis of its NLO properties show that it has strong SHG responses as expected.

The remarkable Fresnoite-oxychlorides mentioned above were reported based on a strategy involving synthesis in molten chlorides flux. It allowed mixed anion environment around the Jahn-

Teller distorted $d^4$ Mn$^{3+}$ and $d^9$ Cu$^{2+}$. In Ba$_2$MnClSi$_2$O$_7$[3], KBaCuClV$_2$O$_7$[4] and Ba$_2$NaClP$_2$O$_7$[5], the equatorial Mn$^{3+}$-O, Cu$^{2+}$-O and Na-O measure 1.8945, 1.93 and 2.3 Å, respectively, while Ti-O ~1.9994 Å. From the ionic radii sum, Mn-O, Cu-O and Na-O equatorial distances are expected of 2.025, 1.95 and 2.4 Å, respectively. Mn-O and Na-O are significantly lower than expected while Cu-O is very close. Therefore, a certain degree of adaptability is required for some ions to fit the structure.

More specifically, it is interesting to further compare the primary Fresnoite Ba$_2$TiSi$_2$O$_8$ and other Fresnoites where only the $M$ site and its environment vary while Si$_2$O$_7$ groups and Ba atoms are fixed. In Ba$_2$TiSi$_2$O$_8$, equatorial Ti-O is longer than the expected 1.89 Å distance and approaches 2 Å. In Ba$_2$MnClSi$_2$O$_7$, Mn-O is expected around 2.025 Å and it is found 0.13 Å shorter due to compensation of the JT tetragonal elongation along apical Mn-Cl. The comparison here is not straightforward because of the particular synthesis route in molten salt flux. Then, if we consider the square pyramid in the Ti-Fresnoite and target a simple substitution to tune the properties, Sn$^{4+}$ with coordination (V) would be expected to yield an Sn-O bond of 2.0 Å, close to the one experimentally obtained for Ti-O suggesting that this site would be favourable for Sn$^{4+}$ without much deviation. On another hand, Ba$_2$TiOSi$_2$O$_7$[9] and Ba$_2$MnClSi$_2$O$_7$ have an absorption band edge in the UV while it is in the deep-UV (DUV) for Ba$_2$NaClP$_2$O$_7$. Then, the effect of inserting a chalcogenide, for instance S$^{2-}$, would give mixed anion environment and in the meantime impact oppositely by raising the valence band toward a band gap in the Visible. This would allow to expand the variety of the Fresnoite compositions and properties. The association of Sn and S$^{2-}$ should allow some flexibility for the apical site as with the $M$-Cl bonds which are either much shorter or much longer than expected and providing octahedral environment in some cases. Surprisingly, we could obtain a regular square pyramid with Sn-O distance of 2.03 Å very close to what we have predicted. It is a rare element of the main group forming a square pyramid.

2. Results and discussion

BSSO was synthesize using a standard solid-state procedure at 800° C in quartz tube sealed under vacuum. The structure of BSSSO was solved by x-ray diffraction (XRD) using a yellow and platelet-shape single crystal. BSSSO crystallizes into the polar space group $P4bm$ (no. 100)

with unit cell parameters a = 9.8307(6) Å, b = 8.5880(7) Å, and c = 5.4675(5) Å. The data collection and refinement details are given in **Table S1**. The XRD refinement was carried out using the JANA2006[10] software based on a structure solution obtained with the charge-flipping method[11]. Our EDX analysis of the single crystals led to the average atomic ratio of 36.1:16.7:15.8:31.4 for Ba, Sn, S and Si, respectively, in good agreement with the composition found at the end of the refinement, i.e., $Ba_2SnSSi_2O_7$. As depicted in **Figure 4. a**, **b**, $Ba_2SnSSi_2O_7$ shows a typical Fresnoite structure. The heteroleptic square pyramids $SnO_4S$ (**Figure 4.c**) is an unusual coordination environment for Sn. The Sn-S distance of 2.3126(2) Å is comparable to those in $Ba_2F_2SnS_3$[12] (2.242 – 2.553 Å) and $Ba_{12}Sn_4S_{23}$[13] (2.331 – 2.398 Å). The basal Sn-O distance of 2.0286(1)Å is close to that in $BaSnO_3$[14](2.0532(1) Å) and $Ba_2SnO_4$[15] (2.0655(1) Å).
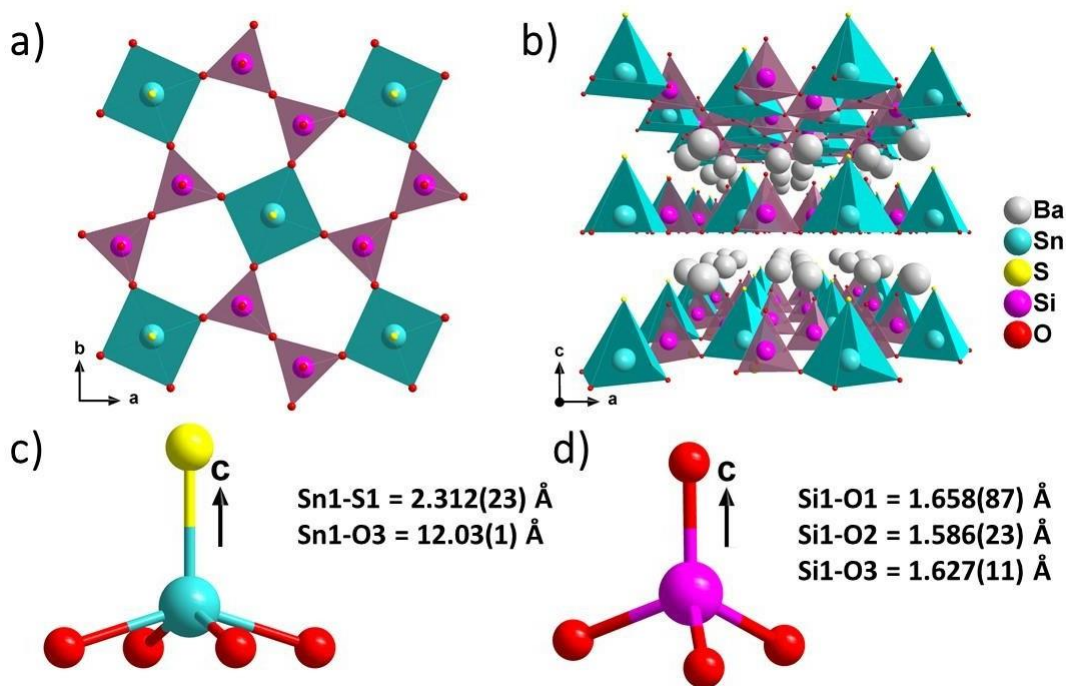


***Figure 4:*** *(a) Prospection view of a SnSSi₂O₇ layer along the c-axis. (b) A perspective view of Ba₂SnSSi₂O₇ along the a-axis. (c) The structures of a SnO₄S square pyramid and a SiO₄ tetrahedron.*

The synthesis of the pure powder phase of BSSSO was carried out following the procedure described in the Experimental Section. As depicted in **Figure 5.a** BSSSO is formed as a major phase with minor impurity of $Ba_4Si_4O_{16}$. A multiphase Rietveld refinement using FullProf led to very

good reliability factors with the ratio 0.9363(0.01)/0.0637(0.001) for the BSSSO/impurity. From the polycrystalline $Ba_2SnSi_2O_7S$, the Tauc plot[16] (**Figure 5b** and **SI**) yield an optical bandgap $E_g$ = 2.4 eV, which is consistent with the indirect bandgap of ~2.2 eV obtained from DFT calculations (**Figure 6**). With respect to other Fresnoite-type oxides and oxychlorides with a closed-shell metal site, the sulfur contribution narrows the bandgap.
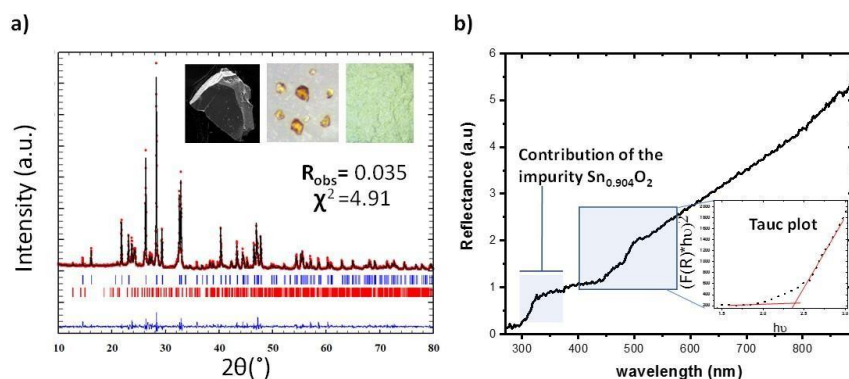


*Figure 5: (a) Powder XRD Rietveld refinement: the experimental (black) and calculated (red) patterns are superimposed; the difference curve and Bragg positions are represented in blue and red, respectively. A SEM image of a single crystal, a photo of several yellowish crystals and of the powder are also shown as insets. (b) Diffuse-reflectance spectra and the corresponding Tauc plot.*
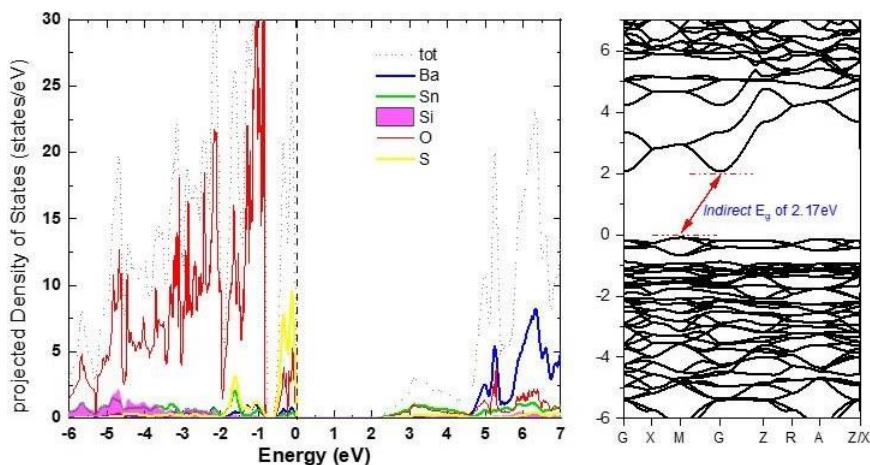


*Figure 6: Total DOS and PDOS (left). Band structure (right) for $Ba_2SnSi_2O_7S$*

**Figure 7a** compares the dependence of the SHG response on particle size measured for BSSSO and AgGaS$_2$. The phase-matching material AgGaS$_2$ shows a steady increase in the SHG response with increasing the particle size. In contrast, the SHG response of BSSSO fluctuates as the particle size increases, which is characteristic of a non-phase-matching material[17]. The measured SHG response attains the highest value when the particle sizes fall into the range of 25-45 $\mu$m. The result measured with SiO$_2$ as standard is shown in **Figure 7b**. Our measurements indicate that the SHG intensity of BSSSO is about twice that of SiO$_2$, and the effective SHG coefficient *(d*$_{eff}$*)* of BSSSO is calculated as 1.54 pm/V based on Eq. ($d_{eff}^{SiO2}$ = 0.139 pm/V ).
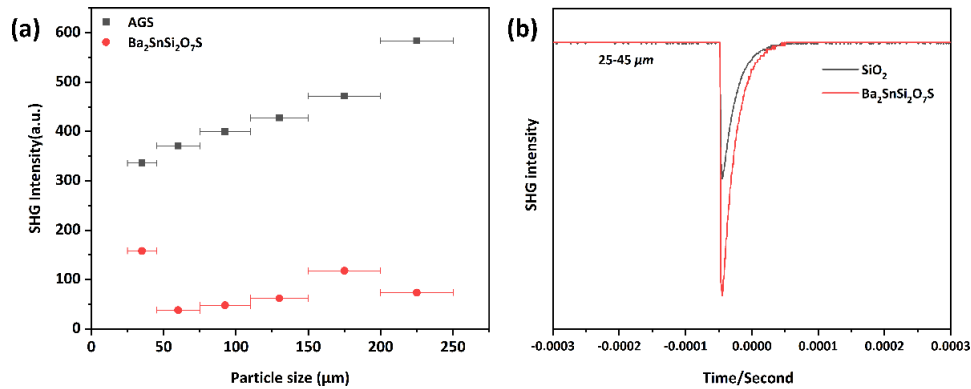


**Figure 7:** *(a) Size-dependent SHG responses of Ba$_2$SnSi$_2$O$_7$S and AGS measured with a 2.1 μm incident laser; (b) SHG intensities of Ba$_2$SnSi$_2$O$_7$S and SiO$_2$ measured by oscilloscope traces of the SHG signals.*

We now examine the origin of the NLO response of BSSSO based on the density functional theory (DFT). For the point group of *4mm,* the SHG tensor have five nonzero SHG components, *i.e.*, $d_{15}$ (=$d_{24}$), $d_{31}$ (=$d_{32}$), $d_{33}$. The calculated components of the static SHG tensor are $d_{15}$ = 1.70 pm/V, $d_{31}$ = 0.88 pm/V and $d_{33}$ = -4.21 pm/V. With these values, the effective SHG coefficient is calculated as 2.26 pm/V by using **Eq. S1** in the Supporting Information. The theoretical value agrees reasonably with the experimental one (1.54 pm/V).

The atom response theory analysis for BSSSO was performed to explore the atomic origin of its SHG response by considering the largest component $d_{33}$ (absolute value) as an example. As shown in **Figure 8**, $\zeta$(E$_B$) changes drastically in the range of -2.5 eV – 0 eV where the nonbonding

O 2p and S 3p states dominate. In the region of the conduction band from ~2.4 eV up to 15.0 eV, the $\zeta(E_B)$ curve shows a rapid downward trend, which corresponds to the antibonding interaction between the Ba 5d states and the O 2p states, indicating that these states contribute dominantly to the SHG response. By means of the ART analysis[18,19] [11,12],
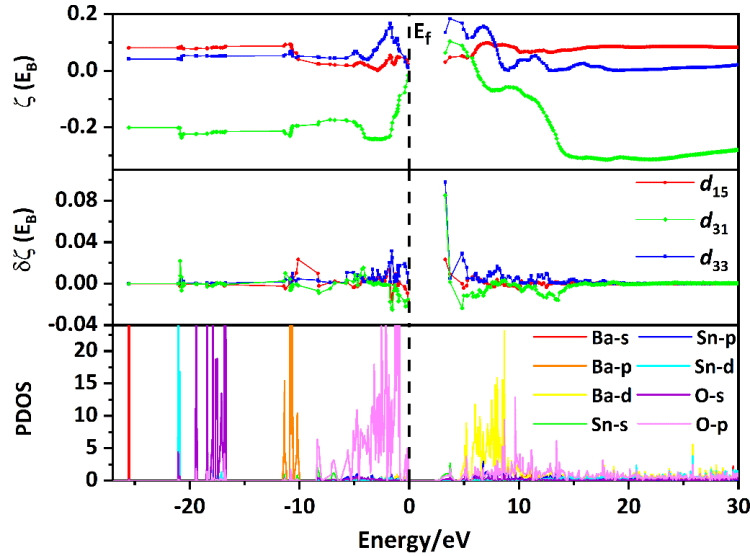


**Figure 8:** *$\zeta(E_B)$-vs-$E_B$ plot, $\delta\zeta(E_B)$-vs-$E_B$ plot and selected PDOS plots of Ba$_2$SnSi$_2$O$_7$S.*

one can obtain the individual atom contributions of the BSSSO. As can be seen from **Table 5**, in terms of the individual atom contribution, the order is Ba > S > O > Si, where the contribution of O atom is an average of three symmetrically different O atoms in the structure. The absolute contribution of Sn atom is substantially negative. As can be seen from the $\zeta(E)$-vs-E and DOS-vs-E curves (**Figure 8**, **S5**), the energy dependence of the partial response functional $\zeta(E)$ of Sn 4d at around -20.0 eV and that of the main contributors O 2p and S 3p in the range of -2.5 - 0.0 eV show the opposite energy dependence, a similar behavior has also been found for the Sn 5s at around 2.5 eV and that of the Ba 5d in the range from ~2.4 to 15.0 eV. This means that, to the oscillating electric field of light, the atomic states of each Sn$^{4+}$ cation respond out-of-phase while those of the surrounding O$^{2-}$ and S$^{2-}$ anions do in-phase. The exact cause for the out-of-phase response is unknown at present, but one might speculate if it arises from the covalent bonding of a Sn$^{4+}$ cation with the surrounding O$^{2-}$ and S$^{2-}$ anions in each SnO$_4$S square pyramid.

126

With individual atom contributions at hand (**Table 5**), one can estimate the contributions of the atom groups centered around $Ba^{2+}$, $Sn^{4+}$ and $Si^{4+}$ cations using the partition principle based on topological considerations[20] [13]. The bonds connected to each $Ba^{2+}$ ion are more ionic than are those connected to each $Sn^{4+}$ or $Si^{4+}$ ion. Considering the connectivity of each anion to various cations in BSSSO, the $Ba^{2+}$-, $Sn^{4+}$- and $Si^{2+}$-centered group are described by $[BaO1_{1/4}O2_{3/4}O3_{4/4}S_{2/5}]$, $[SnO3_{4/4}S_{1/5}]$ and $[SiO1_{1/4}O2_{1/4}O3_{2/4}]$, respectively, if the Ba-S ionic bonds are included, but by $BaO1_{1/4}O2_{3/4}O3_{4/4}]$, $[SnO3_{4/4}]$ and $[SiO1_{1/4}O2_{1/4}O3_{2/4}]$, respectively, if the Ba-S ionic bonds are excluded, where the subindex $n/m$ of an atom indicates that each of this type of atoms ($n$) is shared by $m$ groups defined in the text. In addition, we note that BSSSO has four $Ba^{2+}$-, two $Sn^{4+}$- and four $Si^{2+}$-centered groups per unit cell. The total contributions of the $Ba^{2+}$-, $Sn^{4+}$- and $Si^{4+}$-centered groups to $d_{33}$ component are calculated to be 89.9%, -8.45% and 18.51%, respectively, by including the Ba-S ionic bonds, and 78.03%, 3.44% and 18.51%, respectively, by excluding the Ba-S ionic bonds. These results indicate clearly that the atom group with more ionic bonding character has a larger SHG response than do the groups with more covalent bonding character. The ART analyses for the other components of the SHG tensor are given in **Table S6**. As shown in **Table S5**, the calculated birefringence $\Delta n$ = 0.082 which falls into the range of 0.03-0.1, a criterion usually used to judge a phase-matching property of a NLO material. Our study indicates that it is not always true in every cases.

**Table 5**. *The calculated atomic contributions (in %) to the SHG coefficients $d_{33}$. $W_A$ denotes the number of the same type of atoms in a unit cell; $^{VB}A_\tau$, $^{CB}A_\tau$, $A_\tau$, $C_A$ refer to contributions (in%) from the valence bands, conduction bands, a single atom and the total of the same type of atoms, respectively.*

| Atom | $W_A$ | $^{VB}A_\tau$ | $^{CB}A_\tau$ | $A_\tau$ | $C_A$ |
|---|---|---|---|---|---|
| Ba | 4 | 3.59 | 8.34 | 11.93 | 47.73 |
| Sn | 2 | -4.17 | -4.07 | -8.24 | -16.48 |
| Si | 4 | -0.18 | 1.51 | 1.33 | 5.32 |

| | | | | | |
|---|---|---|---|---|---|
| S | 2 | 8.28 | -0.84 | 7.43 | 14.87 |
| O | 14 | 2.87 | 0.60 | 3.47 | 48.56 |

In summary, we prepared the first Fresnoite-type oxysulfide, $Ba_2SnSSi_2O_7$, which amounts to replacing the $TiO_5$ square pyramids of $Ba_2TiOSi_2O_7$ with $SnO_4S$ square pyramids. Our work opens the possibility of other Frenoite-type oxychalcogenides. The bandgap of $Ba_2SnSSi_2O_7$ lies the visible range while those of most Fresnoite-type compounds fall into the UV or deep UV range. $Ba_2SnSSi_2O_7$ exhibits good SHG properties with an incident laser of 2.1 µm.

**Crystal structure report**

CCDC Deposition Number xxx contains the supplementary crystallographic data for this paper. The data can be obtained free of charge from The Cambridge Crystallographic Data Centre via https://www.ccdc.cam.ac.uk/structures

**Acknowledgments**

3. REFERENCES

(1)    Weber, S.; Lebedinskaya, A.; Rudsky, D.; Kabirov, Y.; Rudskaya, A.; Kupriyanov, M. Structural

Features of the A2TiSi2O8 ( A -Ba and Pb) Compounds. *J. Adv. Dielectr.* **2020**, *10* (05), 2050022.

(2)     Kristallstruktur, D.; Triplit, M. The Crystal Structure. **1969**, *14*, 1–3.

(3)     Mo, X.; Hwu, S. J. Salt-Inclusion Synthesis of $Ba_2MnSi_2O_7Cl$. A Fresnoite-Type Polar Framework Containing the Acentric $[Si_2O_7]^{6-}$ Polyanion in the Anti-$ReO_3$ Type $[(Ba_2Mn)Cl]^{6+}$ Cage. *Inorg. Chem.* **2003**, *42* (13), 3978–3980.

(4)     Martin, F.-D.; Müller-Buschbaum, H. Synthese Und Kristallstruktur Eines Alkali-Erdalkali-Kupfer-Halogeno-Oxovanadats: $KBaCuV_2O_7Cl$ / Synthesis and Crystal Structure of an Alkaline Alkaline-Earth Halide Oxide of Copper and Vanadium: $KBaCuV_2O_7Cl$. *Zeitschrift für Naturforsch. B* **1994**, *49* (3), 355–359.

(5)     Chen, J.; Xiong, L.; Chen, L.; Wu, L. M. $Ba_2NaClP_2O_7$: Unprecedented Phase Matchability Induced by Symmetry Breaking and Its Unique Fresnoite-Type Structure. *J. Am. Chem. Soc.* **2018**, No. 1, 6–10.

(6)     Liu, B.; Jiang, X.; Wang, G.; Zeng, H.; Zhang, M.; Li, S.; Guo, W.-H.; Guo, G. Oxychalcogenide $BaGeOSe_2$ : Highly Distorted Mixed-Anion Building Units Leading to a Large Second-Harmonic Generation Response. *Chem. Mater.* **2015**, *27* (24), 8189–8192.

(7)     Salter, E. J. T.; Blandy, J. N.; Clarke, S. J. Crystal and Magnetic Structures of the Oxide Sulfides CaCoSO and BaCoSO. *Inorg. Chem.* **2016**, *55* (4), 1697–1701.

(8)     Wang, R.; Liang, F.; Wang, F.; Guo, Y.; Zhang, X.; Xiao, Y.; Bu, K.; Lin, Z.; Yao, J.; Zhai, T.; et al. $Sr_6Cd_2Sb_6O_7S_{10}$ : Strong SHG Response Activated by Highly Polarizable Sb/O/S Groups. *Angew. Chemie Int. Ed.* **2019**, *58* (24), 8078–8081.

(9)     Alfors, J. T.; Stinson, M. C.; Matthews, R. A.; Pabst, A. Seven New Barium Minerals from Eastern Fresno County, California. *Am. Mineral.* **1965**, *50* (3–4), 314–340.

(10)    Petříček, V.; Dušek, M.; Palatinus, L. Crystallographic Computing System JANA2006: General Features. *Zeitschrift für Krist. - Cryst. Mater.* **2014**, *229* (5), 345–352.

(11)    van der Lee, A. Charge Flipping for Routine Structure Solution. *J. Appl. Crystallogr.* **2013**, *46* (5), 1306–1315.

(12)    Kabbour, H.; Cario, L.; Danot, M.; Meerschaut, A. Design of a New Family of Inorganic Compounds $Ae_2F_2SnX_3$ (Ae = Sr, Ba; X = S, Se) Using Rock Salt and Fluorite 2D Building Blocks. *Inorg. Chem.* **2006**, *45* (2), 917–922.

(13)    Duan, R. H.; Liu, P. F.; Lin, H.; Huangfu, S. X.; Wu, L. M. Syntheses and Characterization of Three New Sulfides with Large Band Gaps: Acentric $Ba_4Ga_4SnS_{12}$, Centric $Ba_{12}Sn_4S_{23}$ and $Ba_7Sn_3S_{13}$. *Dalt. Trans.* **2017**, *46* (43), 14771–14778.

(14)    Phelan, D.; Han, F.; Lopez-Bezanilla, A.; Krogstad, M. J.; Gim, Y.; Rong, Y.; Zhang, J.; Parshall, D.; Zheng, H.; Cooper, S. L.; et al. Structural Properties of Barium Stannate. *J. Solid State Chem.* **2018**, *262* (January), 142–148.

(15)    Green, M. A.; Prassides, K.; Day, P.; Stalick, J. K. Structural Properties of $A_2SnO_4$ (A = Ba,Sr). *J. Chem. Soc. Faraday Trans.* **1996**, *92* (12), 2155–2159.

(16)    Hecht, H. G. The Interpretation of Diffuse Reflectance Spectra. *J. Res. Natl. Bur. Stand. Sect. A*

*Phys. Chem.* **1976**, *80A* (4), 567.

(17)    Kurtz, S. K.; Perry, T. T. A Powder Technique for the Evaluation of Nonlinear Optical Materials. *J. Appl. Phys.* **1968**, *39* (8), 3798–3813.

(18)    Cheng, X.; Whangbo, M.-H.; Hong, M.; Deng, S. Dependence of the Second-Harmonic Generation Response on the Cell Volume to Band-Gap Ratio. *Inorg. Chem.* **2019**, *58* (15), 9572–9575.

(19)    Cheng, X.; Li, Z.; Wu, X.-T.; Hong, M.; Whangbo, M.-H.; Deng, S. Key Factors Controlling the Large Second Harmonic Generation in Nonlinear Optical Materials. *ACS Appl. Mater. Interfaces* **2020**, *12* (8), 9434–9439.

(20)    Cai, Z.; Cheng, X.; Whangbo, M.-H.; Hong, M.; Deng, S. The Partition Principles for Atomic-Scale Structures and Their Physical Properties: Application to the Nonlinear Optical Crystal Material $KBe_2BO_3F_2$. *Phys. Chem. Chem. Phys.* **2020**, *22* (34), 19299–19306.

# The first oxysulfide in the polar Fresnoite-type $Ba_2Si_2SnO_7S$ with heteroleptic tin and non-linear optical properties

## 4. SUPPLEMENTARY INFORMATION

### 4.1. S1. Experimental section and Methods

**Synthesis:** We attempted to synthesize a single-phase material from a stoichiometric mixture of the precursors $BaO/SnO_2/SiO_2/Si/S$ with ratio 2/1/1.5/0.5/1 respectively. Those precursors were mixed and thoroughly ground in an agate mortar before being pressed into pellets and heated in an evacuated sealed quartz tube. The heat treatment consisted in heating up to 500°C at a rate of 32°C/ for 5 hours, then heating up to 750°C at a rate of 21°C/ for 24 hours, temperature at which the furnace was switched off.

**X-ray diffraction on single crystals diffraction** was performed on an X8 diffractometer equipped with a bi-dimensional CCD 4K detector and an Ag $K\alpha$ source.

**The powder X-ray diffraction** pattern was collected on a Bruker D8 diffractometer equipped with a linear detector Lynxeye ($Cu_{K\alpha}$) in Bragg-Brentano geometry at room temperature.

**DFT calculations** were carried out by employing the projector- augmented-wave[1,2] method encoded in the Vienna ab initio simulation package (VASP)[3] and the generalized gradient approximation (GGA) of Perdew, Burke and Ernzerhof[4] for the exchange-correlation functionals. Full geometry optimizations were carried out using a plane-wave energy cutoff of 550 eV and 120 k points in the irreducible Brillouin zone. It converged with residual Hellman–Feynman forces on atoms smaller than 0.03 eV $\text{Å}^{-1}$ and led to a good match with the experimental structure, i.e., within a reasonable error expected for the GGA method. The relaxed structure was used for calculations of the electronic structure. For the latter, a plane-wave cutoff energy of 550 eV and a threshold of the self-consistent-field energy convergence of $10^{-6}$ eV were used, with 1215 k points in the irreducible Brillouin zone.

**DFT calculations for NLO properties**

The SHG tensor was calculated based on the "sum over states (SOS)" method implemented in our own code[5] based on the calculated electronic structures from VASP[6,7] calculations. The used SOS formalism for second order susceptibility was first derived by Aversa and Sipe[8] and later modified by Rashkeev et al.[9,10] and Sharma et. al[11,12]. The underestimation of the calculated

bandgap due to the deficiency of the LDA like methods was corrected by using the scissor operation[13]. All atom response theory related calculations were performed using our own code[14].

([‡] The software that allows one to carry out the ART analysis can be obtained upon request until it is publicly released.)

**Scanning electron microscopy (SEM)** experiments and EDX analysis were carried out on a Hitachi S400N.

## UV−Visible Measurements

The reflectance of the sample was measured from 250 to 800 nm on a PerkinElmer Lambda 650 device.

## Second Harmonic Generation (SHG) Measurements

Powder SHG measurement of $Ba_2SnSi_2O_7S$ (BSSOS) sample was performed by using a modified Kurtz-NLO system with 2.1 $\mu m$ Q-switch laser radiation[15]. Polycrystalline powder sample of BSSOS was grounded and sieved into samples with different sizes (25–45, 45–75, 75–110, 110-150, 150–200 and 200-250 $\mu m$). Standard AGS powder crystals with similar distribution of sizes were measured under the same conditions to calibrate the measurements of the samples. As the samples shows non-phase-matching behavior, the standard non-phase-matching $SiO_2$ powder crystal sample with particle sizes in the range of 25-45 $\mu m$ was measured under the similar conditions. The SHG signals were detected by a photomultiplier tube.

The experimental SHG coefficient was estimated using the equation below, where $I^{2\omega}$ is the SHG signal intensity of a sample and $lc$ is the coherence length derived from $\lambda/4(n_{2\omega}-n_{\omega})$; the refractive indexes, calculated values for both $n_{2\omega}$ and $n_{\omega}$ were used in this work[15] .

$$\frac{I^{2\omega}(A)}{I^{2\omega}(SiO_2)} = \frac{<(d(A)_{ijk}^{2\omega})^2>(lc_A^2)}{<(d(SiO_2)^{2\omega})^2>(lc_{SiO_2}^2)} \qquad \textit{Équation 1}$$

**Table S1.** *Data Collection and Refinement Details of Ba$_2$SnSi$_2$O$_7$S*

| Formula | Ba$_2$SnSSi$_2$O$_7$ |
|---|---|
| Molecular weight (g. mol$^{-1}$) | 593.6 |
| Symmetry | *tetragonal* |
| Space group | P 4 b m (100) |
| Unit cell dimensions (Å) | a=b=8.5888(3) |
| | c=5.4674(5) |
| Volume (Å$^3$) | 403.32(4) |
| Z | 2 |
| Data Collection | |
| Equipment | Bruker CCD |
| Λ [Ag K$_\alpha$; Å] | 0.56087 |
| Calculated density (g cm$^{-3}$) | 4.8881 |
| Crystal shape | Patlet |
| Crystal dimensions (μm) | 125×100×15 |
| Color | Yellow |
| Absorption correction | analytical |
| Scan mode | ω, φ |
| θ (min–max) (°) | 2.65-43.16 |
| μ (mm−1 ; for λ Kα = 0.56087Å) | 7.02 |
| F(000) | 524 |
| Reciprocal space recording | −20 ≤ h ≤ 20 |
| | −20 ≤ k ≤ 19 |
| | −13 ≤ l ≤ 13 |
| No. of measured reflections | 51987 |
| No. of independent reflections | 3228 |
| I > 3σ(I) (total) | 3086 |

|  | Refinement |
|---|---|
| Number of refined parameters | 38 |
| Refinement method | Least-squares |
| Weighting scheme | sigma |
| R1(F) [I > 3σ(I)]/R1(F$^2$) (all data, %) | 0.0211/0.0223 |
| wR2(F$^2$) [I > 3σ(I)]/wR2(F$^2$) (all data, %) | 0.0796/ 0.0799 |
| Goodness of Fit | 2.44 |
| Max/Min residual electronic density (e$^-$/Å$^3$) | 18.09/ -15.28 |
| Tmin/Tmax | 0.6036/0.7486 |

**Table S2**. *Atomic Positions and Isotropic Thermal Displacement for Ba$_2$SnSi$_2$O$_7$S*

| Atom | Wyck. | S.O.F. | x | y | z | $U_{eq}$ |
|---|---|---|---|---|---|---|
| Ba1 | 4c | 1 | 0.328433(1) | 0.828433(10) | 0.01(4) | 0.00828(2) |
| Sn1 | 2a | 1 | 0 | 0 | 0.55(4) | 0.00666(3) |
| Si1 | 4c | 1 | 0.12661(6) | 0.62661(6) | 0.52(4) | 0.00564(9) |
| S1 | 2a | 1 | 0 | 0 | 0.13(4) | 0.01022(14) |
| O1 | 2b | 1 | 0 | 0.5 | 0.64(4) | 0.0166(6) |
| O2 | 4c | 1 | 0.12575(20) | 0.62575(20) | 0.23(4) | 0.0102(3) |
| O3 | 8d | 1 | 0.2867(2) | 0.5781(3) | 0.66(4) | 0.0184(4) |

**Table S3**. *Anisotropic Thermal Parameters Uij (Å2)*

| Atom | U$_{11}$ | U$_{22}$ | U$_{33}$ | U$_{12}$ | U$_{13}$ | U$_{23}$ |
|------|------|------|------|------|------|------|
| Ba1 | 0.00809(3) | 0.00809(3) | 0.00868(4) | -0.00127(3) | 0.00024(3) | 0.00024(3) |
| Sn1 | 0.00601(4) | 0.00601(4) | 0.00797(6) | 0.000000 | 0.000000 | 0.000000 |
| Si1 | 0.00589(12) | 0.00589(12) | 0.0051(2) | 0.00048(15) | -0.00003(12) | -0.00003(12) |
| S1 | 0.0115(2) | 0.0115(2) | 0.0077(3) | 0.000000 | 0.000000 | 0.000000 |
| O1 | 0.0210(10) | 0.0210(10) | 0.0079(9) | -0.0146(12) | 0.000000 | 0.000000 |
| O2 | 0.0116(4) | 0.0116(4) | 0.0074(6) | -0.0004(5) | 0.0006(4) | 0.0006(4) |
| O3 | 0.0090(5) | 0.0338(10) | 0.0123(6) | 0.0103(6) | -0.0018(4) | -0.0042(6) |

**Table S4.** *Main Distances (Å) for Ba2SnSSi2O7*

| Atom1 | Atom2 | d1-2 (Å) | Atom1 | Atom2 | d1-2 (Å) |
|-------|-------|----------|-------|-------|----------|
| Ba1 | Ba1 | 4.1682(5) | Sn1 | S1 | 2.31(3) |
| Ba1 | Ba1 | 4.5007(7)4 | Sn1 | O3 | 2.039(10)*4 |
| Ba1 | S1 | 3.251(6)*2 | Si1 | O1 | 1.67(12) |
| Ba1 | O2 | 2.74(14) | Si1 | O2 | 1.5856(4) |
| Ba1 | O3 | 2.85(2)*2 | Si1 | O3 | 1.611(15)*2 |

## 4.2. S2. Optical Measurements

UV–visible diffuse-reflectance analysis of the polycrystalline $Ba_2SnSi_2O_7S$ is represented in **Figure 5.b.** A Kubelka–Munk transformation[16] was applied to the measured diffuse-reflectance (R) spectra using the function $F(R) = (1 − R)2/2R$. Then a Tauc plot[17] was used to determine the optical band gap $E_g$, using the equation $[F(R) h\nu]1/n = k(h\nu − E_g)$, where $h\nu$ is the photon energy, k an energy-independent constant, $E_g$ the optical band gap, and *n* is an exponent related to the type of transition. Assuming an indirect transition (exponent n = 2) as found from the DFT band structure below, the plot of $[F(R) h\nu]^2$ *versus* $h\nu$ leads to $E_g$=2.4 eV.

## 4.3. S3. Band structure

The band structure and the total and projected density of states are represented in **Figure 6** with focus on the valence band (VB) and conduction band (CB) area based on the content of a unit cell and the total contribution of each type of atom. The DFT calculated band gap is found ~2.2 eV in good agreement with the experimental determination considering the expected underestimation from the GGA-PBE functional. The bottom of the CB is occupied by tin states ($5s$, $5p$) mixed with O states. Above 4.5 eV the CB is dominated by Ba $d$ states which occupied states are deep in the VB (not shown) as expected from its strong ionic character. The top of the VB on another hand show a greater contribution from sulfur atoms $3p$ states which are globally contributing higher in the VB and rather just below the Fermi level compared to O $2p$ states as expected from their lower electronegativity. Both are hybridized to tin states. On another hand, Si-states in the VB are found in the same region than the O $2p$ states mainly below -2 eV. Compared to other Fresnoite type structures of oxide and oxychloride nature with a closed-shell metal site, the sulfur contribution is responsible of the narrower band gap that falls into the visible range. Moreover, the band gap is found indirect as shown on the band structure with the VBM at Gamma point and the CBM in the vicinity of M point (0.5 0.5 0) and precisely at (0.5 0.5 0.079).

## 4.4. S4. Electronic structure calculations for NLO properties

The structural and electronic properties of BSSOS was calculated within the framework of density functional theory (DFT)[5-15] by using the Vienna ab-initio simulation package (VASP) [6,7] with the projector augmented wave (PAW) method[8] . The generalized gradient approximation (GGA) within the Perdew-Burke-Ernzerhof (PBE)-type exchange-correlation potentials[9] was used throughout this work. The employed PAW-PBE pseudopotentials[10] of Ba, Sn, Si, O and S treat 5s, 5p, 6s; 4d, 5s, 5p; 3s, 3p; 2s, 2p and 3s, 3p as the valence states, respectively. The plane wave cutoff energy for the expansion of wave functions was set at 550 eV and the tetrahedron method with Blöchl corrections was used for integrations. The numerical integrations in the Brillouin zones were performed by utilizing 8 × 8 × 12 Monkhorst-Pack $k$-point mesh, which showed an excellent convergence of the energy differences (0.01 meV) and stress (0.002 eV/ Å). The quasi-Newton algorithm as implemented in the VASP code was used in all structural relaxations. In this work, both the cell volume and the atomic positions were all allowed to relax to minimize the internal forces.

## 4.5. S5. Effective SHG response $d_{eff}$

To compare with the experimentally measured SHG response of powder crystal samples, the effective $d_{eff}^{2\omega}$ is calculated using the formula derived by Kurtz-Perry[11] and Cyvin[12] et al. with the calculated SHG tensors $d_{abc}^{2\omega}$, i.e., $\frac{1}{2}\chi_{abc}^{2\omega}$,

$$\langle (d_{eff}^{2\omega})^2 \rangle = \frac{19}{105}\sum_a (d_{aaa}^{2\omega})^2 + \frac{13}{105}\sum_{a\neq b} d_{aaa}^{2\omega} d_{abb}^{2\omega} + \frac{44}{105}\sum_{a\neq b}(d_{aab}^{2\omega})^2 +$$

$$\frac{13}{105}\times\sum_{abc,cyclic} d_{aab}^{2\omega}d_{bcc}^{2\omega} + \frac{5}{7}(d_{abc}^{2\omega})^2 \qquad\qquad \text{Équation 2}$$

For the point group 4mm of BSSOS, $\langle (d_{eff}^{2\omega})^2 \rangle = \frac{19}{105}\sum_a (d_{aaa}^{2\omega})^2 +$

$$\frac{13}{105}\sum_{a\neq b} d_{aaa}^{2\omega} d_{abb}^{2\omega} + \frac{44}{105}\sum_{a\neq b}(d_{aab}^{2\omega})^2 + \frac{13}{105}\times\sum_{abc,cyclic} d_{aab}^{2\omega}d_{bcc}^{2\omega} +$$

$$\frac{5}{7}(d_{abc}^{2\omega})^2 \qquad\qquad \text{Équation 2 can be simplified as,}$$

$$\langle (d_{eff}^{2\omega})^2 \rangle = \frac{19}{105}(d_{333}^{2\omega})^2 + \frac{13}{105}(d_{333}^{2\omega}d_{311}^{2\omega} + d_{333}^{2\omega}d_{322}^{2\omega})$$

$$+ \frac{44}{105}((d_{113}^{2\omega})^2 + (d_{223}^{2\omega})^2) + \frac{13}{105}\times(d_{113}^{2\omega}d_{322}^{2\omega} + d_{223}^{2\omega}d_{311}^{2\omega})$$

**Table S5.** Calculated static dielectric constants and refractive indices n at 0 eV along the three main directions [100], [010] and [001], as well as the calculated birefringence Δn for Ba₂SnSi₂O₇S.

| Compound | $\varepsilon(xx)=\varepsilon(yy)$ | $\varepsilon(zz)$ | $n(xx)=n(yy)$ | $n(zz)$ | $\Delta n$ |
|---|---|---|---|---|---|
| Ba₂SnSi₂O₇S | 3.677 | 3.997 | 1.917 | 1.999 | 0.082 |

**Table S6.** Calculated SHG tensor $d_{ij}$ and the $d_{eff}$ at 0 eV and 0.59 eV (2.1 μm) for Ba₂SnSi₂O₇S.

| Compound | $d_{ij}$(pm/V) (ω=0) | $d_{eff}$(pm/V) (ω=0) | $d_{ij}$(pm/V) (ω=0.59 eV) | $d_{eff}$(pm/V) (ω=0.59 eV) |
|---|---|---|---|---|
|  |  |  |  |  |

| Ba$_2$SnSi$_2$O$_7$S | d$_{15}$=d$_{24}$=1.70 | 2.26 | d$_{15}$=d$_{24}$=1.75 | 2.69 |
|---|---|---|---|---|
| | d$_{31}$=d$_{32}$=0.88 | | d$_{31}$=d$_{32}$=0.91 | |
| | d$_{33}$=-4.21 | | d$_{33}$=-5.53 | |

**Table S7.** *The calculated atomic contributions (in %) to the SHG coefficients $d_{15}$ and $d_{31}$ using the partial response functional and the atom response theory analysis. $W_A$ denotes the number of the same type of atoms in a unit cell; $^{VB}A_\tau$, $^{CB}A_\tau$, $A_\tau$, $C_A$ refer to contributions (in%) from the valence bands, conduction bands, a single atom and the total of the same type of atoms, respectively.*

| $d_{15}$ | Atom | $W_A$ | $^{VB}A_\tau$ | $^{CB}A_\tau$ | $A_\tau$ | $C_A$ |
|---|---|---|---|---|---|---|
| | Ba | 4 | 8.70 | 2.25 | 10.95 | 47.81 |
| | Sn | 2 | 2.71 | 5.07 | 7.78 | 15.55 |
| | Si | 4 | 0.56 | -0.02 | 0.54 | 2.17 |
| | S | 2 | -2.86 | 1.65 | -1.21 | -2.42 |
| | O | 14 | 2.34 | 0.58 | 2.92 | 40.90 |

| $d_{31}$ | Atom | $W_A$ | $^{VB}A_\tau$ | $^{CB}A_\tau$ | $A_\tau$ | $C_A$ |
|---|---|---|---|---|---|---|
| | Ba | 4 | 2.62 | 30.77 | 33.40 | 133.59 |
| | Sn | 2 | -8.60 | -18.68 | -27.28 | -54.57 |
| | Si | 4 | -0.56 | 0.77 | 0.21 | 0.83 |
| | S | 2 | 20.72 | -5.99 | 14.73 | 29.46 |
| | O | 14 | -0.34 | -0.33 | -0.67 | -9.32 |

REFERENCES

(1)     Blöchl, P. E. Projector Augmented-Wave Method. *Phys. Rev. B* **1994**, *50* (24), 17953–17979.

(2)     Kresse, G.; Joubert, D. From Ultrasoft Pseudopotentials to the Projector Augmented-Wave Method. *Phys. Rev. B* **1999**, *59* (3), 1758–1775.

(3)     Kresse, G. ; Vogtenhuber, D.; Marsman, M.; Kaltak, M.; Karsai, F. ; Schlipf, M. Vienna ab-initio simulation package (VASP) https://www.vasp.at.

*(4)*     Perdew, J. P.; Burke, K.; Ernzerhof, M. Generalized Gradient Approximation Made Simple. *Phys.*

*Rev. Lett.* **1996**, *77* (18), 3865–3868.

(5)     Cheng, X.; Whangbo, M.-H.; Guo, G.-C.; Hong, M.; Deng, S. The Large Second-Harmonic Generation of LiCs 2 PO 4 Is Caused by the Metal-Cation-Centered Groups. *Angew. Chemie* **2018**, *130* (15), 3997–4001.

(6)     Kresse, G.; Furthmüller, J. Efficiency of Ab-Initio Total Energy Calculations for Metals and Semiconductors Using a Plane-Wave Basis Set. *Comput. Mater. Sci.* **1996**, *6* (1), 15–50.

(7)     Kresse, G.; Furthmüller, J. Efficient Iterative Schemes for Ab Initio Total-Energy Calculations Using a Plane-Wave Basis Set. *Phys. Rev. B* **1996**, *54* (16), 11169–11186.

(8)     Aversa, C.; Sipe, J. E. Nonlinear Optical Susceptibilities of Semiconductors: Results with a Length-Gauge Analysis. *Phys. Rev. B* **1995**, *52* (20), 14636–14645.

(9)     Rashkeev, S. N.; Lambrecht, W. R. L.; Segall, B. Efficient Ab Initio Method for the Calculation of Frequency-Dependent Second-Order Optical Response in Semiconductors. *Phys. Rev. B* **1998**, *57* (7), 3905–3919.

(10)    Rashkeev, S. N.; Lambrecht, W. R. L. Second-Harmonic Generation of I-III-${\mathrm{VI}}_{2}$ Chalcopyrite Semiconductors: Effects of Chemical Substitutions. *Phys. Rev. B* **2001**, *63* (16), 165212.

(11)    Sharma, S.; Dewhurst, J. K.; Ambrosch-Draxl, C. Linear and Second-Order Optical Response of III-V Monolayer Superlattices. *Phys. Rev. B* **2003**, *67* (16), 165332.

(12)    Sharma, S.; Ambrosch-Draxl, C. Second-Harmonic Optical Response from First Principles. *Phys. Scr.* **2004**, *T109*, 128.

(13)    Gonze, X.; Lee, C. Dynamical Matrices, Born Effective Charges, Dielectric Permittivity Tensors, and Interatomic Force Constants from Density-Functional Perturbation Theory. *Phys. Rev. B* **1997**, *55* (16), 10355–10368.

(14)    The Software That Allows One to Carry out the ART Analysis Can Be Obtained upon Request until It Is Publicly Released.

(15)    Kurtz, S. K.; Perry, T. T. A Powder Technique for the Evaluation of Nonlinear Optical Materials. *J. Appl. Phys.* **1968**, *39* (8), 3798–3813.

(16)    Tauc, J.; Grigorovici, R.; Vancu, A. Optical Properties and Electronic Structure of Amorphous Germanium. *Phys. status solidi* **1966**, *15* (2), 627–637.

(17)    Hecht, H. G. The Interpretation of Diffuse Reflectance Spectra. *J. Res. Natl. Bur. Stand. Sect. A Phys. Chem.* **1976**, *80A* (4), 567.

# Chapter IV

# New oxy(chalcogenides) with magnetic properties

# IV. Chapter IV: New oxy(chalcogenides) with magnetic properties

## Introduction

In the third chapter, two new polar compounds were presented, their heteroleptic entities and nonlinear optical properties were detailed. The followed strategy to get $Ba_2SnSi_2O_7S$ was to introduce a second anion species to a known polar oxide with the aim to accentuate the polarity and enhance the associated properties.

Besides NLO materials, this strategy can also be used to get control on electric and magnetic properties like multiferroic properties. Based on this idea and the recent evidence of heteroleptic magnetic units such as ($FeOS_3$), we targeted new phases polar mixed anion phases. More precisely, we aimed at inserted magnetic metal cations and mixed anion in relevant polar matrices such as the NLO wide band gap family of $Sr_5ZnGa_6S_{15}$. In the target hypothetical phases, we aimed to substitute a some tetrahedral cationic site by a $Fe^{3+}S_3O$ tetrahedra. Synthesis attempts with many combinations of cations led to the new polar and magnetic $Ba_5Fe_2ZnIn_4S_{15}$ compound in which $FeS_4$ tetrahedra are connected to form a one dimensional zigzag chain with strong antiferromagnetic intra-chain coupling and weak interchain interactions as shown from DFT calculations.

If in this case a sulfide was obtained, the polar magnetic phase is of great interest and opens several perspectives to tune the magnetic properties and probe the electric polarization. Then, a new three-dimensional and non-centrosymmetric oxysulfide $Ba_{10}Fe_{7.75}Zn_{5.25}S_{18}Si_3O_{12}$ was finally synthesized with $(Fe/Zn)O_3S$ building blocks. The phase crystallizes in a cubic cell and shows strong antiferromagnetic interactions and a spin glass behavior at low temperature. While most of oxychalcogenides are found with layered structures, this phase represents an original 3D spatial network in which the elementary building blocks can be defined as large magnetic clusters. They are interconnected trough silicate groups to form the whole framework.

The magnetic phases described in this chapter open new perspectives in magnetic materials exploration. Another new magnetic phase was also obtained during the exploration of high-pressure techniques for our thiovanadate/dichalcogenide based phases to further control the symmetry. $Ba_9V_3S_{11}(S_2)_2$ consists of spin chains made of face-sharing $VS_6$ octahedra running along the c-axis. Those chains are separated by large cations $Ba^{2+}$ and disulfide pairs $(S)_2$. Theoretical calculations show the existence of magnetic clusters within the spin chains.

# Part 1

# A high Dimensional Oxysulfide Build from Large Iron-based Clusters with partial charge-Ordering

# A. Part 1. A High Dimensional Oxysulfide Built from Large Iron-based Clusters with Partial Charge-Ordering

Batoul Almoussawi, Angel M. Arevalo-Lopez, Pardis Simon and Houria Kabbour

## 1. Abstract

We report in here the original $Ba_{10}Fe_{7.75}Zn_{5.25}S_{18}Si_3O_{12}$ oxychalcogenide. Contrarly to the usual layered compounds, it presents a 3D and non-centrosymmetric structure built from large magnetic clusters consisting of twelve $(Fe^{2+/3+}/Zn)S_3O$ tetrahedra decorating a central $Fe^{2+}S_6$ octahedra and exhibiting a spin glass state.

## 2. Introduction

Mixed anion compounds frequently contain transition metals in unusual chemical environments and states due to heteroleptic coordination. These may lead to fascinating properties[1] with new perspectives opened in several fields such as superconductors[2,3]. Among the latter, Fe-based pnictide or chalcogenide layers have attracted much attention. Synthetic strategies based on mixed anions chemistry have given access to original phases[4] and such desired physical properties[5]. It has also enhanced performances in various field of applications as photocatalysis or ionic conductivity[6]. In this context, oxychalcogenides are increasingly investigated for diverse applications such as non-linear optics[7] or thermoelectrics[8] and are also emerging as visible light water-splitting photocatalysts[9-10-11]. It is well established that oxychalcogenides tend to form layered structures which is detailed in several reviews [8, 12,13]. This is favored by the very different ionic radii and electronegativities of $O^{2-}$ ($\chi = 3.44$) and $S^{2-}$ ($\chi = 2.58$) which arrange in distinct layers. Specific cation-anion affinities such as a soft cation (more polarisable) and a hard cation (non-polarisable) would prefer to bond to the larger chalcogenide and the smaller oxide anions respectively, influence the structuration. Such distinct layers can be defined as 2D building blocks. This has allowed the prediction of new functional compounds by stacking complementary layers of distinct chemical natures[14-15]. The polar layered oxysulfide CaOFeS, a member of a larger family including non-linear optical materials[9,10] is characterized by uncommon heteroleptic $FeS_3O$ tetrahedra and magnetodielectric effects[16]. Other peculiar

145

electronic and magnetic behavior[18]-[19]-[20] are found among oxychalcogenides. For instance, spin-glass behavior promoted by the mixed anion interactions has been observed in the layered oxysulfides $Sr_4Mn_{2.91}O_{7.40}Cu_2S_2$[21] and $Ba_2Mn_2O_4Cu_{0.9}S$[22]. Magnetic frustration is a required ingredient on the observation of exotic quantum states[23]-[24]-[25]. These are often studied in 3D oxides with corner sharing tetrahedral lattices such as spinels[26] or pyrochlores[27]. Apart from oxides, the fluoride $CsFe_2F_6$[28] pyrochlore and the In-diluted thiospinel $CdCr_{2x}In_{2(1-x)}S_4$[29]-[30] are spin-glass materials. In $Bi_{1.8}Fe_{1.2}SbO_7$ [31] pyrochlore, anion mixing trough fluorination led to variation of the spin glass dynamics.

We present an original oxysulfide with a non-centrosymmetric 3D-network involving corner-sharing tetrahedra. The structure is built with 0D Fe-based large magnetic clusters $Fe_{13}O_{12}S_{18}$ diluted with Zn and inter-connected through silicate groups. The sulfur atoms provide intra-cluster bonding while oxygen atoms are located on the outer shell of the clusters. The material orders into a spin-glass state at low temperature. Such 3D networks are scarce[32] for oxysulfides, which are dominated by low-dimensional structures. Furthermore, the elementary building blocks are large *clusters* instead of the common *layered* building blocks found in this class of materials. While the layered character brings interesting anisotropic electronic properties, a pressure-induced 2D–3D structural transition allowed drastic enhancement of electrical conductivity and photoelectric response in $Bi_9O_{7.5}S_6$ oxysulfide.[33] Here, the original Fe-based oxysulfide building block opens new perspectives for the design of functional phases combining oxide and chalcogenide anions in high dimensional structures.

3. Results and discussion

The new oxysulfide phase $Ba_{10}Fe_{7.75}Zn_{5.25}S_{18}Si_3O_{12}$ was synthesized trough a solid-state reaction in evacuated sealed quartz tube (see **S1**). Its structure was solved and refined using single crystal X-Ray diffraction (XRD) data (**Table S1**, **S2** and **S3**). The treatment of the data was performed with Jana2006[34] and charge flipping[35] for structural solution and least squares method for refinement. This phase crystallizes in the unit cell parameters $a$ = 13.3380(1) Å and the non-centrosymmetric space group *I*-43*m*. Centrosymmetric trials led to unreasonable solutions. In addition, if inversion twinning is allowed to refine, it leads to a Flack Parameter of 0.04 (8), indicating that the measured crystal was single domain. Energy dispersive X-Rays analysis on single crystals led to

the average atomic ratio 23.7/16.33/13.2/7.03/39.76 for Ba/Fe/Zn/Si/S, respectively. This is in good agreement with the composition found at the end of the refinement, *i.e.* 22.7/17.6/11.9/6.8/40.9. In particular the Zn/Fe distribution was determined to 0.56/0.44 at the Fe2 site, see **Table S2**. The structure can be described as a 3D framework formed by repetitive 0D units. The later are interconnected along the three crystallographic directions trough $Si^{4+}$ bridges. The $Si^{4+}$ form silicate groups having their oxygen atoms shared with the clusters.
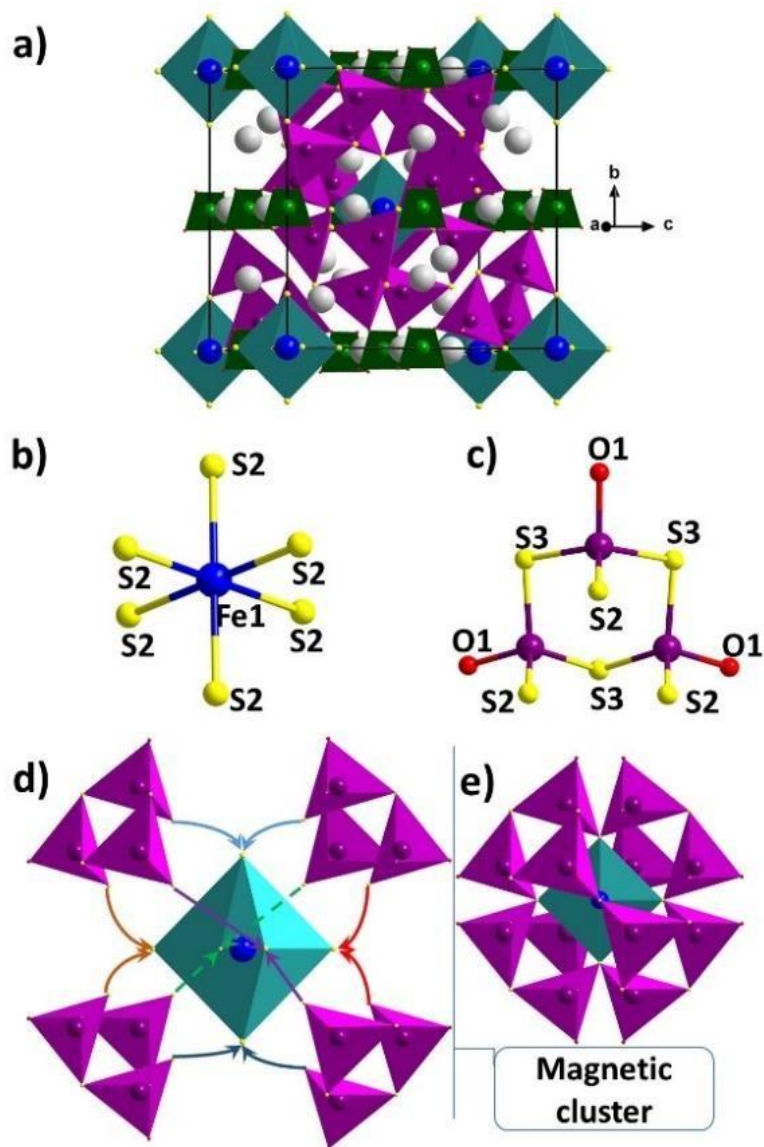


*Figure 1:* a) View of the unit cell of $Ba_{10}Fe_{7.75}Zn_{5.25}S_{18}Si_3O_{12}$. b) The octahedra $FeS_6$. c) Three heteroleptic tetrahedra $FeS_3O$ connected by sharing S3, d) connection of a) and b). e) the magnetic cluster $Fe_{13}O_{12}S_{18}$ with $(Fe,Zn)S_3O$ tetrahedra, $FeS_6$ octahedra and $SiO_4$ groups in purple, blue and green respectively; Ba, O and S atoms are represented in grey, red and yellow respectively.

These elementary cluster units (**Figure .1** and **2**) are composed of one octahedron $Fe1S_6$ (**Figure 1.b**) decorated by twelve heteroleptic tetrahedra $(Fe2/Zn1)S_3O$ (**Figure 1.c**) arranged into four trimers. Thus, defining a complex arrangement of $(Fe_{13}O_{12}S_{18})$ magnetic clusters, see **Figure 2.d** and **e**. In the tetrahedra $(Fe/Zn)S_3O$, $Fe2(Zn1)$ is coordinated to two different types of anions with $d_{Fe2-S2}= 2.311(2)$ Å, $d_{Fe2-S3}= 2.332(2)$ Å and $d_{Fe2-O1}= 1.972(6)$ Å. The anionic segregation is such that the sulfur atoms provide intra-cluster bonding while oxygen atoms are located at the outer shell of the clusters and linking them through $Si^{4+}$ bridges. The observed environments follow well the Pearson's HSAB theory. Then one can explain why a 3D structure is obtained in this particular case. Considering the coordination polyhedra stable in this structure $Fe^{2+}S_6$, $(Fe/Zn)S_3O$ and $SiO_4$, the cluster arrangement allows fulfilling the coordination preferences: $FeS_6$ at the core shares its sulphur with the surrounding $Fe/ZnS_3O$ which point their unique apical oxygen outside the cluster to bond with the $Si^{4+}$, the later having the strongest affinity for oxygen.

Similar heteroleptic $FeOS_3$ are present in the layered oxysulfide $CaFeSO$[9] where they share corners to build layers separated by calcium sheets; similarly, $CaOZnS$[36-37] contains tetrahedral $ZnOS_3$. This Fe(Zn) environment remains uncommon. It is also found in the distinct structural type of $SrFe_2S_2O$[38] and $BaFe_2S_2O$[39] with more complex layers involving also tetrahedral edge sharing. The $Fe1S_6$ octahedra are connected to the tetrahedral $FeOS_3$ and characterized by a longer bonding distance ($d_{Fe1-S2}= 2.559(3)$ Å) than in $FeOS_3$ ($d_{Fe2-S2}= 2.311(2)$ Å, $d_{Fe2-S3}= 2.332(2)$)) Å consistently with the calculated $Fe^{2+}$ oxidation state. Regarding the mean oxidation state $Fe^{+2.26}$ in the phase, it is consistent with the charge distribution deduced from the XPS and magnetic analysis shown later. The clusters are separated by $SiO_4$ (**Figure 2**) by sharing all oxygen corners of $(Fe/Zn)S_3O$ with $d_{Si1-O1}= 1.628(5)$ Å. Each silicate group is connected to two different clusters. $Ba^{2+}$ are located in the voids and their arrangement is shown and discussed in **Figure S1**.

The almost pure powders could be obtained from the refined composition after many synthetic efforts. The Rietveld refinement based on the single crystal structure model converged with the unit cell parameter $a = 13.3350$ (1) Å and the reliability factors $R_{obs}= 0.0323$, $wR_{obs} = 0.0384$, $R_{all} = 0.0328$, $wR_{all} = 0.0388$ and $GOF = 3.29$. The results are discussed in the **SI** with **Figure S2**, **Table**

**S6** and **Table S7**. A few low intensity peaks are found with the majority phase and could not be indexed with certainty with any existing phase. They do not indicate any straightforward symmetry change compared to the single crystal refinement either. Nevertheless, regarding the minor contribution of those peaks, we used our highest purity powder for the physical measurements keeping on mind the presence of a minor impurity for the interpretation.
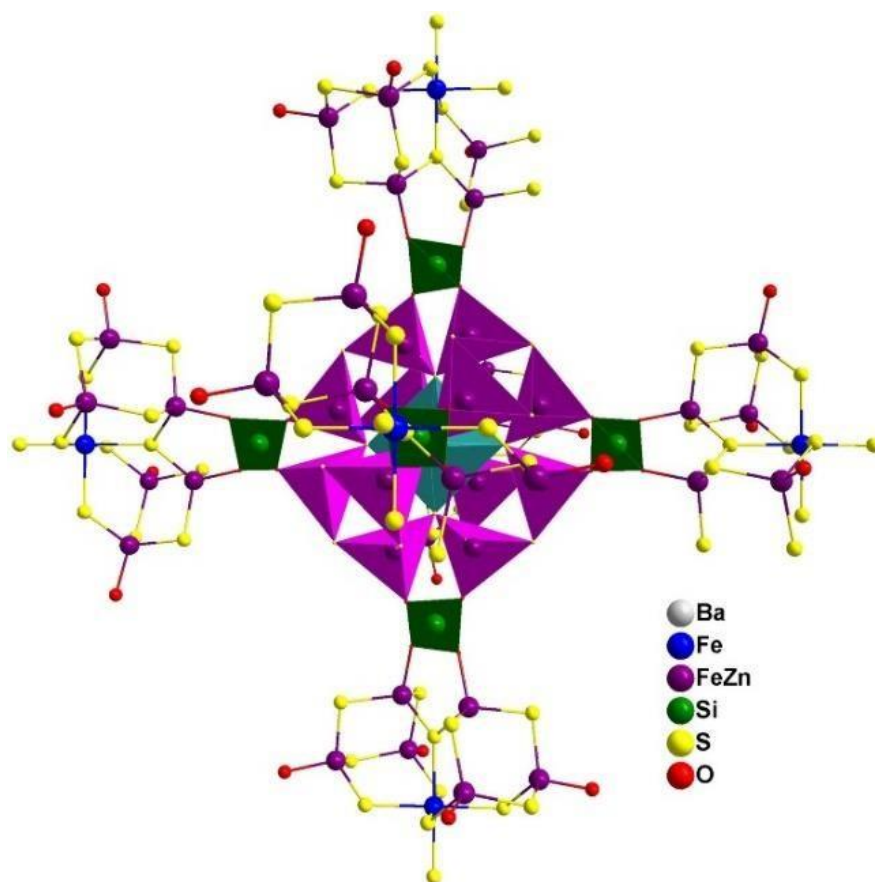


*Figure 2: Representation of how clusters connect each other through the (SiO$_4$) groups. (Fe/Zn)OS$_3$, SiO$_4$ and FeS$_6$ polyhedra are represented respectively in purple, green and blue. Only the central cluster is fully represented to highlight the inter-clusters connection, Ba atoms are also omitted for clarity*

In order to confirm the presence of both charges in (Fe$^{2+/3+}$)S$_3$O tetrahedra and the general Fe charge distribution, Fe-2p core level spectrum was examined. Reference data was taken on both vacuum fractured pyrrhotite (Fe$_7$S$_8$) and air-oxidized pyrrhotite (Fe$_2$O$_3$) as reported by Pratt *et al.*[40]. In this study, Fe$_7$S$_8$ multiplet structure was generated based on theoretical *p* core levels multiplet structures for free transitional metal ions calculated by Gupta and Sen[41] and compared

to the work of McIntyre and Zetaruk[42] on Fe(II) and Fe(III) ions in iron oxides. The calculated, integrated envelope (red line) is a reasonable fit to our experimental data, thus confirming the presence of mixed cation charge $Fe^{3+}/Fe^{2+}$. The major Fe(II) peak has a binding energy of 708.6 eV, which is similar to fitted Fe(II)-S bonded peak binding energy of $Fe_7S_8$ from Pratt *et al.*, but slightly shifted to higher binding energy. Whereas the binding energy of the main Fe(III) peak is 710.4 eV, which is similar to the fitted Fe(III)-O binding energy of $\alpha$-$Fe_2O_3$ from McIntyre and Zetaruk which was 711.0 eV, although the Fe(III) peaks are slightly shifted to lower binding energies. The fact that Fe(III) peak have been shifted to lower binding energies as compared to those observed for pure Fe (III) oxides, and that Fe(II) peak have been shifted to higher binding energies as compared to those observed for pure Fe(II) sulfides reflects the mixed Fe-S/Fe-O coordination in our system for both Fe(II) and Fe(III) species. Indeed, the percentage of the total signal derived from Fe(III) components in the spectrum is 36 %, whereas the expected distribution of iron in $Ba_{10}Fe_{7.75}Zn_{5.25}Si_3S_{18}O_{12}$ corresponds to 25 % of total iron with $Fe^{3+}$ oxidation state ($2*Fe^{3+}$ and $5.75*Fe^{2+}$ ; $1*Fe^{2+}$ in the octahedral site). This suggests that some Fe(II) (S or O bonded) in the near-surface has been oxidized to Fe(III) and bonded to oxygen.
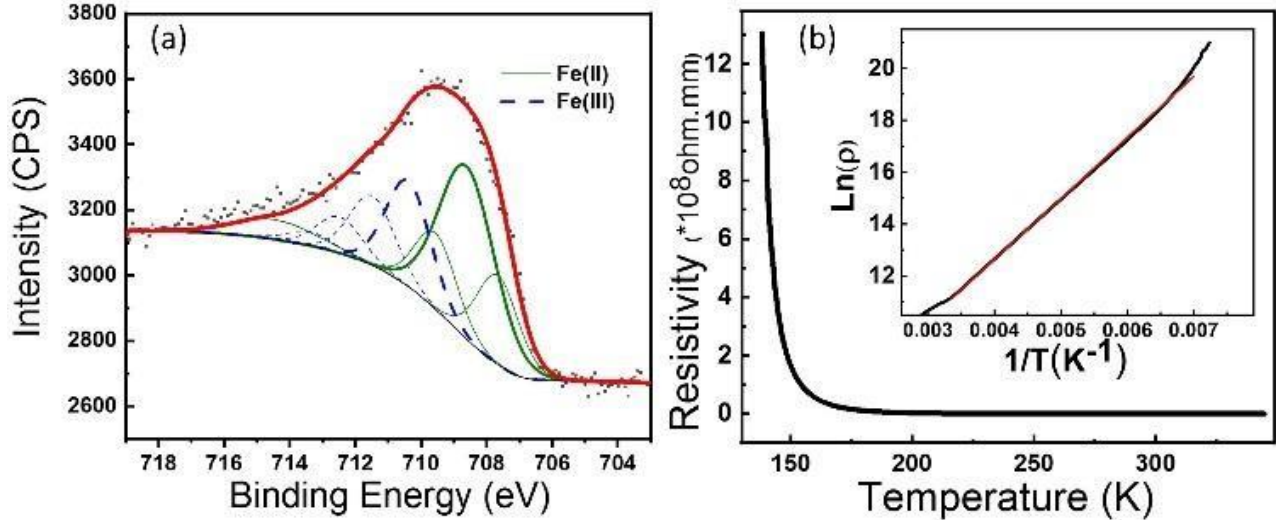
**Figure 3:** a) Fe $2p_{3/2}$ XPS spectrum of the $Ba_{10}Fe_{7.75}Zn_{5.25}S_{18}Si_3O_{12}$ sample (squares symbols). The green solid lines correspond to Fe(II) (multiplets and satellite), the blue dotted lines correspond to Fe(III) (multiplet structure). The solid red line represents the calculated integrated fit. b) Temperature-dependent resistivity of $Ba_{10}Fe_{7.75}Zn_{5.25}S_{18}Si_3O_{12}$, ln(ρ) versus $T^{-1}$ is fitted and shown as inset.

**Figure 3.b** shows the temperature dependence of the resistivity for $Ba_{10}Fe_{7.75}Zn_{5.25}Si_3S_{18}O_{12}$ which is typical of a semiconductor. The resistivity curve can be well fitted with the relation ρ a $\exp\left(\frac{\Delta g}{2k_BT}\right)$, where $\Delta g$ is the semiconductor band gap and kB is the Boltzmann's constant, leading to $\Delta g = 0.4$ eV. The zero field-cooled/field cooled (ZFC/FC) magnetic measurements under a 1000 Oe field are shown in **Figure 4.a** and **Figure 4.b**. The ZFC exhibits a maximum ~2.6 K and diverges from the FC data below this temperature. The inverse ZFC data were fit between 150 and 300K with the Curie–Weiss law, $1/\chi = T/C - \theta_{cw}/C$, resulting in a large negative value $\vartheta_{cw} = -343.9$ K indicating strong antiferromagnetic (AFM) interactions between Fe ions, and $C = 25.075$ emu.K.mol$^{-1}$. The effective moment $\mu_{eff} = 5.09$ $\mu_B$/Fe shows good agreement with the expected theoretical value for the refined distribution of high spin ($S = 2$) Fe$^{3+}$ and ($S = 5/2$) Fe$^{2+}$. Indeed, the calculation of the effective moment of 7.75 iron atoms per formula unit (2*Fe$^{3+}$ and 5.75*Fe$^{2+}$) leads to 5.16 $\mu_B$/Fe, close to the experimental value of 5.09. The value $|(T_{cw})/T_N| \approx$ 137.2 indicates a strong frustration[43] close for instance to the frustration parameter ≈135 of $SrGa_{12-x}Cr_xO_{19}$[44]. The evolution of $T_f$ as a function of the applied magnetic field is well-fitted with the Almeida-Thouless relation[45] (**Figure 4.d**) which is a good indicator for a spin-glass transition.

AC magnetic susceptibility confirmed the spin-glass transition, as shown in **Figure 4.e**. The temperature dependence of the real part of the AC susceptibility at different frequencies with zero external DC magnetic field and an oscillating field of 16 Oe, shows a typical temperature shift of a spin-glass. The AC susceptibility is frequency-dependent and has a nonzero imaginary component. It could be modeled by the Vogel–Fulcher law[46]-[47] $\omega = \omega_0 \exp[-E_a/kB(T_f - T_0)]$, where $\omega_0$ is the characteristic frequency fixed to typical values for spin-glass following reported procedures[48], $E_a$ is the activation energy, kB the Boltzmann constant, $T_f$ the freezing temperature and $T_0$ the Vogel-Fulcher temperature that gives a measure of the interaction effect. $T_f$ should be in proportion to $1/\ln(\omega/\omega 0)$ for a spin glass. A linear variation is indeed obtained for each frequency. The fits to the data give $T_0$ from 1.36K to 2.21K (**Figure 4.f**, **Table S8**) in good agreement with the freezing temperature found by DC. For these values, $t^* = (T_f-T_0)/T_f$ is found in the range 0.15-0.48; $t^*$ above 0.15 is common for cluster spin-glass materials[48,49].
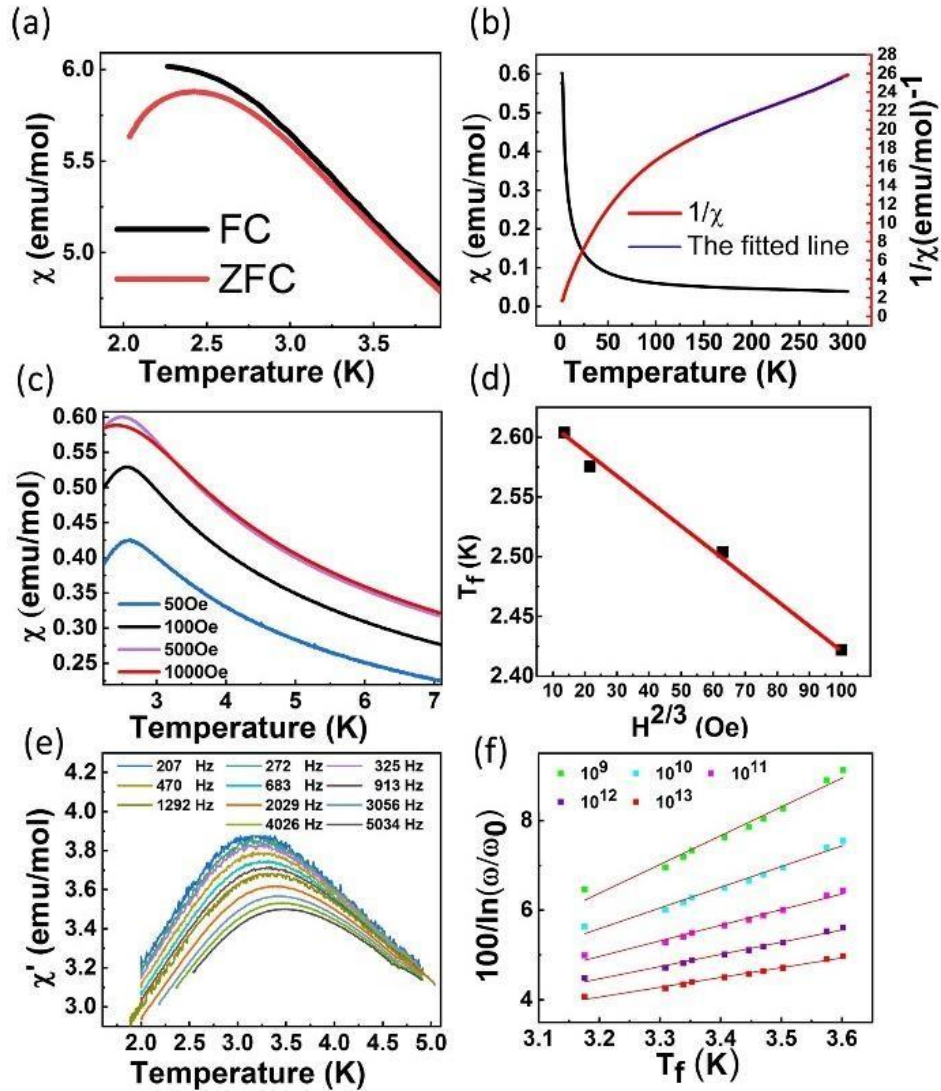
***Figure 4:*** *a) Inset: zoom of ZFC/FC at low temperature. b) ZFC/FC dc magnetic susceptibility with $1/\chi$ fitted between150-300K. c) Isothermal M(H) at 2 and 300K. d) Evolution of $T_f$ as a function of the applied magnetic field and the Almeida-Thouless fit as inset e) Temperature dependence of $\chi(T)$. e) $\chi'(T)$ measured at several fixed frequencies. f) Vogel-Fulcher fit with different fixed $\omega_0/2\pi$ in the typical range 109–1013Hz for spin-glass.*

Comparatively, the layered CaOFeS and spin ladders $Ba(Sr)Fe_2S_2O$ phases described above show a partial long range AFM ordering[10] and (canted)-AFM ordering respectively. The behavior of CaOFeS is related to its frustrated triangular sheets and shows complex magnetodielectric effects[9, 16,17,50]. The later phases are remarkable examples of 2D magnetic units based on $FeS_3O$ entities. The $Ba_5Fe_{6+x}S_{4+x}O_8$ [51] phases represent another type of oxysulfide with spin-glass members and a complex structure with distorted $FeS_4O_2$ and $FeS_2O_4$ octahedral perovskite sub-

units forming tunnels partially occupied by Fe and S. In the title phase, we observe a new and remarkable arrangement of the $FeS_3O$ tetrahedra combined to decorate one $Fe^{2+}S_6$ octahedra to form large magnetic clusters. Note that distinctly, magnetic clustering is known for ions without forming distinct entities such as in the Zn-diluted frustrated lattice $Zn_3V_3O_8$[52] or in $Ba_3V_8S_{15}$[53]. Despite strong AFM interactions in our phase, frustration raises from competing intra-cluster interactions and Zn disturbing magnetic exchanges.

The properties discussed above are coherent with the complex magnetic exchange paths (**Figure S4**, **Table S5**) involving mixed valence. The magnetic paths J1-J6 are discussed in the **SI**. Intra-cluster magnetic interactions are mediated trough sulfide anions while weaker inter-cluster super-super exchanges involve oxide anions.


The original cubic non-centrosymmetric oxysulfide $Ba_{10}Fe_{7.75}Zn_{5.25}S_{18}Si_3O_{12}$ shows a 3D-structure made of large magnetic clusters, therefore standing apart from more commonly encountered layered oxychalcogenide. This partially charge-ordered phase presents strong AFM interactions with a spin-glass state arising from cluster geometry and disorder. It provides an exceptional new structure type and a rich playground for exotic physics.


### 4. Notes and references

‡ **Supporting Information**. Experimental procedures and synthesis; Table S1 with structure solution and refinement details; Table S2-S3 with atomic positions and anisotropic thermal parameters; Table S4 with main distances, Table S5 with magnetic exchange paths details (fig. S4) and discussion; Vogel-Fulcher parameters (Table S6); $Ba^{2+}$ environments (fig. S1); Rietveld refinement (fig. S2) and its discussion; ZFC/FC magnetic measurements (fig. S3).

(1)    Kageyama, H.; Hayashi, K.; Maeda, K.; Attfield, J. P.; Hiroi, Z.; Rondinelli, J. M.; Poeppelmeier, K. R. Expanding Frontiers in Materials Chemistry and Physics with Multiple Anions. *Nat. Commun.* **2018**, *9* (1), 772. https://doi.org/10.1038/s41467-018-02838-4.

(2)    Kamihara, Y.; Watanabe, T.; Hirano, M.; Hosono, H. Iron-Based Layered Superconductor La[$O_{1-x}F_x$]FeAs (X= 0.05-0.12) with Tc = 26 K. *J. Am. Chem. Soc.* **2008**, *130* (11), 3296–3297. https://doi.org/10.1021/ja800073m.

(3)     Lynn, J. W.; Dai, P. Neutron Studies of the Iron-Based Family of High TC Magnetic

        Superconductors. *Phys. C Supercond.* **2009**, *469* (9–12), 469–476.

        https://doi.org/10.1016/j.physc.2009.03.046.

(4)     Almoussawi, B.; Huvé, M.; Dupray, V.; Clevers, S.; Duffort, V.; Mentré, O.; Roussel, P.;

        Arevalo-Lopez, A. M.; Kabbour, H. Oxysulfide $Ba_5(VO_2S_2)_2(S_2)_2$ Combining Disulfide

        Channels and Mixed-Anion Tetrahedra and Its Third-Harmonic-Generation Properties.

        *Inorg. Chem.* **2020**. https://doi.org/10.1021/acs.inorgchem.9b03674.

(5)     Motohashi, T.; Ito, M.; Masubuchi, Y.; Wakeshima, M.; Kikkawa, S. Crystal Structure and

        Superconducting Properties of Hexagonal Lithium–Niobium Oxynitride. *Inorg. Chem.*

        **2012**, *51* (20), 11184–11189. https://doi.org/10.1021/ic301870n.

(6)     Limburn, G. J.; Stephens, M. J. P.; Williamson, B. A. D.; Iborra-Torres, A.; Scanlon, D. O.;

        Hyett, G. Photocatalytic, Structural and Optical Properties of Mixed Anion Solid Solutions

        $Ba_3Sc_{2-x}In_xO_5Cu_2S_2$ and $Ba_3In_2O_5Cu_2S_{2-y}Se_y$. *J. Mater. Chem. A* **2020**, *8* (38), 19887–

        19897. https://doi.org/10.1039/D0TA06629J.

(7)     Shi, Y. F.; Wei, W. B.; Wu, X. T.; Lin, H.; Zhu, Q. L. Recent Progress in Oxychalcogenides as

        IR Nonlinear Optical Materials. *Dalt. Trans.* **2021**, *50* (12), 4112–4118.

        https://doi.org/10.1039/d1dt00222h.

(8)     Luu, S. D. N.; Vaqueiro, P. Layered Oxychalcogenides : Structural Chemistry and

        Thermoelectric Properties. *J Mater.* **2016**, *2* (2), 131–140.

        https://doi.org/10.1016/j.jmat.2016.04.002.

(9)     Cui, J.; Li, C.; Zhang, F. Development of Mixed-Anion Photocatalysts with Wide Visible-

        Light Absorption Bands for Solar Water Splitting. *ChemSusChem* **2019**, *12* (9), 1872–1888.

        https://doi.org/10.1002/cssc.201801829.

(10)    Wang, Q.; Nakabayashi, M.; Hisatomi, T.; Sun, S.; Akiyama, S.; Wang, Z.; Pan, Z.; Xiao, X.;

        Watanabe, T.; Yamada, T.; Shibata, N.; Takata, T.; Domen, K. Oxysulfide Photocatalyst for

        Visible-Light-Driven Overall Water Splitting. *Nat. Mater.* **2019**, *18* (8), 827–832.

        https://doi.org/10.1038/s41563-019-0399-z.

(11)    Kabbour, H.; Sayede, A.; Saitzek, S.; Lefèvre, G.; Cario, L.; Trentesaux, M.; Roussel, P.

Structure of the Water-Splitting Photocatalyst Oxysulfide α-LaOInS$_2$ and Ab Initio Prediction of New Polymorphs. *Chem. Commun.* **2020**, *56* (11), 1645–1648. https://doi.org/10.1039/C9CC09797J.

(12)   Ueda, K.; Hiramatsu, H.; Hirano, M.; Kamiya, T.; Hosono, H. Wide-Gap Layered Oxychalcogenide Semiconductors: Materials, Electronic Structures and Optoelectronic Properties. *Thin Solid Films* **2006**, *496* (1), 8–15. https://doi.org/10.1016/j.tsf.2005.08.268.

(13)   Clarke, S. J.; Adamson, P.; Herkelrath, S. J. C.; Rutt, O. J.; Parker, D. R.; Pitcher, M. J.; Smura, C. F. Structures, Physical Properties, and Chemistry of Layered Oxychalcogenides and Oxypnictides. *Inorg. Chem.* **2008**, *47* (19), 8473–8486. https://doi.org/10.1021/ic8009964.

(14)   Cario, L.; Kabbour, H.; Meerschaut, A. Designing New Inorganic Compounds from 2D Building Blocks. *Chem. Mater.* **2005**, *17* (2), 234–236. https://doi.org/10.1021/cm048180p.

(15)   Kabbour, H.; Cario, L.; Jobic, S.; Corraze, B. P-Type Transparent Conductors Sr$_{1-x}$Na$_x$FCuS and SrF$_{1-x}$O$_x$CuS: Design, Synthesis and Physical Properties. *J. Mater. Chem.* **2006**, *16* (42), 4165–4169. https://doi.org/10.1039/b610457f.

(16)   Delacotte, C.; Pérez, O.; Pautrat, A.; Berthebaud, D.; Hébert, S.; Suard, E.; Pelloquin, D.; Maignan, A. Magnetodielectric Effect in Crystals of the Noncentrosymmetric CaOFeS at Low Temperature. *Inorg. Chem.* **2015**, *54* (13), 6560–6565. https://doi.org/10.1021/acs.inorgchem.5b00879.

(17)   Jin, S. F.; Huang, Q.; Lin, Z. P.; Li, Z. L.; Wu, X. Z.; Ying, T. P.; Wang, G.; Chen, X. L. Two-Dimensional Magnetic Correlations and Partial Long-Range Order in Geometrically Frustrated CaOFeS with Triangle Lattice of Fe Ions. *Phys. Rev. B* **2015**, *91* (9), 094420. https://doi.org/10.1103/PhysRevB.91.094420.

(18)   Kabbour, H.; Janod, E.; Corraze, B.; Danot, M.; Lee, C.; Whangbo, M. H.; Cario, L. Structure and Magnetic Properties of Oxychalcogenides A$_2$F$_2$Fe$_2$OQ$_2$ (A = Sr, Ba; Q = S, Se) with Fe 2O Square Planar Layers Representing an Antiferromagnetic Checkerboard Spin

Lattice. *J. Am. Chem. Soc.* **2008**, *130* (26), 8261–8270.
https://doi.org/10.1021/ja711139g.

(19)  He, J. B.; Wang, D. M.; Shi, H. L.; Yang, H. X.; Li, J. Q.; Chen, G. F. Synthesis, Structure, and
Magnetic Properties of the Layered Iron Oxychalcogenide $Na_2Fe_2Se_2O$. *Phys. Rev. B -
Condens. Matter Mater. Phys.* **2011**, *84* (20).
https://doi.org/10.1103/PhysRevB.84.205212.

(20)  Tippireddy, S.; D S, P. K.; Das, S.; Mallik, R. C. Oxychalcogenides as Thermoelectric
Materials: An Overview. *ACS Appl. Energy Mater.* **2021**, *4* (3), 2022–2040.
https://doi.org/10.1021/acsaem.0c02770.

(21)  Hyett, G.; Barrier, N.; Clarke, S. J.; Hadermann, J. Topotactic Oxidative and Reductive
Control of the Structures and Properties of Layered Manganese Oxychalcogenides. *J. Am.
Chem. Soc.* **2007**, *129* (36), 11192–11201. https://doi.org/10.1021/ja073048m.

(22)  Hyett, G.; Gál, Z. A.; Smura, C. F.; Clarke, S. J. $Ba_2Mn_2O_4Cu_{0.9}S$: A Layered Oxysulfide with
a New Perovskite-Related Manganese Oxide Fragment. *Chem. Mater.* **2008**, *20* (2), 559–
566. https://doi.org/10.1021/cm7021054.

(23)  Kundu, S.; Dey, T.; Mahajan, A. V.; Büttgen, N. $LiZn_2V_3O_8$: A New Geometrically Frustrated
Cluster Spin-Glass. *J. Phys. Condens. Matter* **2020**, *32* (11). https://doi.org/10.1088/1361-
648X/ab58dc.

(24)  Sheckelton, J. P.; Neilson, J. R.; Soltan, D. G.; McQueen, T. M. Possible Valence-Bond
Condensation in the Frustrated Cluster Magnet $LiZn_2Mo_3O_8$. *Nat. Mater.* **2012**, *11* (6),
493–496. https://doi.org/10.1038/nmat3329.

(25)  Bridges, C. A.; Hansen, T.; Wills, A. S.; Luke, G. M.; Greedan, J. E. Frustrated Magnetism
and the Effects of Titanium Substitution in the Mixed-Valence Oxide $BaV_{10-x}Ti_xO_{15}$. *Phys.
Rev. B - Condens. Matter Mater. Phys.* **2006**, *74* (2), 1–9.
https://doi.org/10.1103/PhysRevB.74.024426.

(26)  Kemei, M. C.; Barton, P. T.; Moffitt, S. L.; Gaultois, M. W.; Kurzman, J. A.; Seshadri, R.;
Suchomel, M. R.; Kim, Y. Il. Crystal Structures of Spin-Jahn-Teller-Ordered $MgCr_2O_4$ and
$ZnCr_2O_4$. *J. Phys. Condens. Matter* **2013**, *25* (32). https://doi.org/10.1088/0953-

8984/25/32/326001.

(27) Fuentes, A. F.; Boulahya, K.; Maczka, M.; Hanuza, J.; Amador, U. Synthesis of Disordered Pyrochlores, $A_2Ti_2O_7$ (A=Y, Gd and Dy), by Mechanical Milling of Constituent Oxides. *Solid State Sci.* **2005**, *7* (4), 343–353. https://doi.org/https://doi.org/10.1016/j.solidstatesciences.2005.01.002.

(28) Liu, S.; Xu, Y.; Cui, Y.; Wang, J.; Sun, K.; Yu, S.; Hao, X. Charge Ordering and Magnetic Frustration in $CsFe_2F_6$. *J. Phys. Condens. Matter* **2017**, *29* (31), 315501. https://doi.org/10.1088/1361-648X/aa76be.

(29) Vincent, E.; Dupuis, V. Spin Glasses: Experimental Signatures and Salient Outcomes. In *arXiv*; 2018; pp 31–56. https://doi.org/10.1007/978-3-319-96914-5_2.

(30) Vincent, E.; Hammann, J.; Ocio, M. 2 . A Few Experimental Facts at the Light of Mean-Field Spin-Glass Results. **2008**, 1–20.

(31) Egorysheva, A. V.; Ellert, O. G.; Gaitko, O. M.; Brekhovskikh, M. N.; Zhidkova, I. A.; Maksimov, Y. V. Fluorination of $Bi_{1.8}Fe_{1.2}SbO_7$ Pyrochlore Solid Solutions. *Inorg. Mater.* **2017**, *53* (9), 962–968. https://doi.org/10.1134/S0020168517090072.

(32) Meerschaut, A.; Lafond, A.; Palvadeau, P.; Deudon, C.; Cario, L. Synthesis and Crystal Structure of Two New Oxychalcogenides: Eu5V3S6O7 and La10Se14O. *Mater. Res. Bull.* **2002**, *37* (12), 1895–1905. https://doi.org/https://doi.org/10.1016/S0025-5408(02)00883-8.

(33) Zhang, G.; Zhang, Q.; Hu, Q.; Wang, B.; Yang, W. Giant Enhancements in Electronic Transport and Photoelectric Properties of Bismuth Oxysulfide by Pressure-Driven 2D–3D Structural Reconstruction. *J. Mater. Chem. A* **2019**, *7* (8), 4019–4025. https://doi.org/10.1039/C8TA11168E.

(34) Petříček, V.; Dušek, M.; Palatinus, L. Crystallographic Computing System JANA2006: General Features. *Zeitschrift für Krist. - Cryst. Mater.* **2014**, *229* (5), 345–352. https://doi.org/10.1515/zkri-2014-1737.

(35) van der Lee, A. Charge Flipping for Routine Structure Solution. *J. Appl. Crystallogr.* **2013**, *46* (5), 1306–1315. https://doi.org/10.1107/S0021889813020049.

(36)     Sambrook, T.; Smura, C. F.; Clarke, S. J.; Ok, K. M.; Halasyamani, P. S. Structure and Physical Properties of the Polar Oxysulfide CaZnOS. *Inorg. Chem.* **2007**, *46* (7), 2571–2574. https://doi.org/10.1021/ic062120z.

(37)     Petrova, S. A.; Mar'evich, V. P.; Zakharov, R. G.; Selivanov, E. N.; Chumarev, V. M.; Udoeva, L. Y. Crystal Structure of Zinc Calcium Oxysulfide. *Dokl. Chem.* **2003**, *393* (1–3), 255–258. https://doi.org/10.1023/B:DOCH.0000003458.35866.40.

(38)     Guo, H.; Fernández-Díaz, M.-T.; Komarek, A. C.; Huh, S.; Adler, P.; Valldor, M. Long-Range Antiferromagnetic Order on Spin Ladders $SrFe_2S_2O$ and $SrFe_2Se_2O$ As Probed by Neutron Diffraction and Mössbauer Spectroscopy. *Eur. J. Inorg. Chem.* **2017**, *2017* (32), 3829–3833. https://doi.org/10.1002/ejic.201700684.

(39)     Valldor, M.; Adler, P.; Prots, Y.; Burkhardt, U.; Tjeng, L. H. S = 2 Spin Ladders in the Sulfide Oxide $BaFe_2S_2O$. *Eur. J. Inorg. Chem.* **2014**, *2014* (36), 6150–6155. https://doi.org/10.1002/ejic.201402805.

(40)     Pratt, A. R.; Muir, I. J.; Nesbitt, H. W. X-Ray Photoelectron and Auger Electron Spectroscopic Studies of Pyrrhotite and Mechanism of Air Oxidation. *Geochim. Cosmochim. Acta* **1994**, *58* (2), 827–841. https://doi.org/https://doi.org/10.1016/0016-7037(94)90508-8.

(41)     Gupta, R. P.; Sen, S. K. Calculation of Multiplet Structure of Core p -Vacancy Levels. II. *Phys. Rev. B* **1975**, *12* (1), 15–19. https://doi.org/10.1103/PhysRevB.12.15.

(42)     McIntyre, N. S.; Zetaruk, D. G. X-Ray Photoelectron Spectroscopic Studies of Iron Oxides. *Anal. Chem.* **1977**, *49* (11), 1521–1529. https://doi.org/10.1021/ac50019a016.

(43)     Marik, S.; Singh, D.; Gonano, B.; Veillon, F.; Pelloquin, D.; Bréard, Y. Enhanced Magnetic Frustration in a New High Entropy Diamond Lattice Spinel Oxide. *Scr. Mater.* **2020**, *186*, 366–369. https://doi.org/10.1016/j.scriptamat.2020.04.027.

(44)     Martínez, B.; Sandiumenge, F.; Rouco, A.; Labarta, A.; Rodríguez-Carvajal, J.; Tovar, M.; Causa, M. T.; Galí, S.; Obradors, X. Magnetic Dilution in the Strongly Frustrated Kagome Antiferromagnet $SrGa_{12-x}Cr_xO_{19}$. *Phys. Rev. B* **1992**, *46* (17), 10786–10792. https://doi.org/10.1103/PhysRevB.46.10786.

(45) Sherrington, D. Stability of the Sherrington-Kirkpatrick Solution of a Spin Glass Model: A Reply. *J. Phys. A. Math. Gen.* **1978**, *11* (8). https://doi.org/10.1088/0305-4470/11/8/004.

(46) Shtrikman, S.; Wohlfarth, E. P. The Theory of the Vogel-Fulcher Law of Spin Glasses. *Phys. Lett. A* **1981**, *85* (8–9), 467–470. https://doi.org/10.1016/0375-9601(81)90441-2.

(47) Ikeda, M.; Aniya, M. Understanding the Vogel-Fulcher-Tammann Law in Terms of the Bond Strength-Coordination Number Fluctuation Model. *J. Non. Cryst. Solids* **2013**, *371–372*, 53–57. https://doi.org/10.1016/j.jnoncrysol.2013.04.034.

(48) Kumar, A.; Tandon, R. P.; Awana, V. P. S. Spin Dynamics, Short-Range Order and Superparamagnetism in Superconducting Ferromagnet $RuSr_2Gd_{1.4}Ce_{0.6}Cu_2O_{10-\delta}$. *J. Magn. Magn. Mater.* **2014**, *349*, 224–231. https://doi.org/10.1016/j.jmmm.2013.08.037.

(49) Mydosh, J. A. *Spin Glasses*; CRC Press, 2014. https://doi.org/10.1201/9781482295191.

(50) Zhang, Y.; Lin, L.; Zhang, J.-J.; Huang, X.; An, M.; Dong, S. Exchange Striction Driven Magnetodielectric Effect and Potential Photovoltaic Effect in Polar CaOFeS. *Phys. Rev. Mater.* **2017**, *1* (3), 034406. https://doi.org/10.1103/PhysRevMaterials.1.034406.

(51) Wright, T.; Prots, Y.; Valldor, M. Fused Perovskite Tunnel Structures in $Ba_5Fe_{6+x}S_{4+x}O_8$ ( $0.44 x 0.55$ ) with x -Dependent Two-Stage Magnetizations. **2016**, *8* (123), 11303–11309. https://doi.org/10.1002/chem.201600997.

(52) Chakrabarty, T.; Mahajan, A. V.; Kundu, S. Cluster Spin Glass Behavior in Geometrically Frustrated $Zn_3V_3O_8$. *J. Phys. Condens. Matter* **2014**, *26* (40). https://doi.org/10.1088/0953-8984/26/40/405601.

(53) Almoussawi, B.; Tomohiri, H.; Kageyama, H.; Kabbour, H. High Pressure Synthesis of the Spin Chain Sulfide $Ba_9V_3S_{11}(S_2)_2$. *Eur. J. Inorg. Chem.* **2021**, *2021* (13), 1271–1277. https://doi.org/10.1002/ejic.202001166.

# A high dimensional oxysulfide built from large Iron-based clusters with partial charge-ordering

## 5. SUPPLEMENTARY INFORMATION

### 5.1. S1. Experimental Methods

**Synthesis:** Single crystals of $Ba_{10}Fe_{7.75}Zn_{5.25}S_{18}Si_3O_{12}$ were initially found throughout a synthesis strategy aiming at forming original compounds with heteroleptic Fe-based oxysulfide units. We attempted to synthesize a single-phase material from a stoichiometric mixture of the precursors BaO/Fe/ZnO/Zn/Si/S. Those precursors were mixed and thoroughly ground in an agate mortar before being pressed into pellets and heated in an evacuated sealed quartz tube. The heat treatment consisted in heating up to 500°C at a rate of about 30°C/h for 5 hours, then cooling down to room temperature at a 50°C/h rate. Then a second treatment was applied to the obtained powder: it was thoroughly ground in an agate mortar before being pressed into pellets, heated up to 500°C at a rate of about 30°C/h for 5 hours, then to 750°C in 8 hours for 24 hours then cooling down to 650°C at a 10°C/h rate, temperature at which the furnace was switched off.

**Single crystal X-ray diffraction** was performed on an X8 diffractometer equipped with a bi-dimensional CCD 4K detector and an Ag $K_\alpha$ source.

**Powder X-ray diffraction** pattern was collected on a Bruker D8 diffractometer equipped with a linear detector Lynxeye ($Cu_{K\alpha}$) in Bragg-Brentano geometry at room temperature.

**Scanning electron microscopy (SEM)** SEM and energy dispersive X-ray spectrum (EDS) analysis were performed on monocrystals placed on a carbon tape and graphited to avoid surfaces charging. Samples were introduced in a field-emission gun SEM HITACHI S4700 device equipped with and EDS detector, operating at 20 kV electron beam energy.

**Resistivity measurements:** The resistivity vs temperature curve was measured under applied DC magnetic field of 1000 Oe and at temperatures in the range of 150–350 K using a four-probe method on a Physical Property Measurement System (PPMS) Dynacool 9T from Quantum Design.

**Magnetic measurements (DC and AC):** The magnetic properties were measured on the same PPMS. Magnetic measurements were perform using a grinded polycrystalline sample. Typical measurements were performed using zero field cooling (ZFC) and field cooling (FC) procedures under 1000 Oe. Magnetization *against field loops* were measured between −9 and 9 T at various temperatures. AC magnetic susceptibility measurements were carried out on 29 mg of sample loaded into a polycarbonate capsule, attached to the sample rod, and lowered into the cryostat of the PPMS. The in-phase and the out-of-phase components of the AC susceptibility were recorded over the temperature range from 2 K to 7 K upon heating at different frequencies between 500 Hz and 30 kHz. For all measurements the amplitude of the applied alternating magnetic field was 16 Oe.

**X-ray photoelectron spectroscopy (XPS)** experiments were performed using an AXIS Ultra DLD Kratos spectrometer equipped with a monochromatized aluminum source (Al $K_\alpha$= 1486.6 eV). The Kratos charge neutralizer system was used during all analysis. All Binding Energies (BE) were referenced to the carbon peak corresponding to C-C bonding in the C 1s core level at 284.8 eV. Simulation of the experimental photopeaks was carried out using a mixed Gaussian(70%)/Lorentzian(30%) peak fit procedure according to the software supplied by CasaXPS. Semiquantitative analysis accounted for a nonlinear Shirley type background subtraction.

**Table S1.** *Data Collection and Refinement Details from the single crystal XRD refinement*

| | |
|---|---|
| Formula | $Ba_{10}Fe_{7.75}Zn_{5.25}S_{18}Si_3O_{12}$ |
| Molecular weight (g. mol$^{-1}$) | 3002.7 |
| Symmetry | *cubic* |
| Space group | I -4 3 m (217) |
| Unit cell dimensions (Å) | a=13.33800(10) |
| Volume (Å$^3$) | 2372.86(3) |
| Z | 2 |
| *Data Collection* | |
| Equipment | Bruker CCD |
| Λ [Ag K$_\alpha$; Å] | 0.56087 |
| Temperature (K) | 293 |
| Calculated density (g cm$^{-3}$) | 2.1013 |
| Crystal shape and dimension ($\mu$m) | 70×50×10 |
| Color | Black |
| Absorption correction | analytical |
| Scan mode | $\omega, \phi$ |
| θ (min−max) (°) | 1.7-21.87 |
| μ (mm−1 ; for λ Kα = 0.56087Å) | 3.652 |
| F(000) | 2690 |
| Reciprocal space recording | $-16 \leq h \leq 17$ |
| | $-17 \leq k \leq 17$ |
| | $-17 \leq l \leq 17$ |
| No. of measured reflections | 33587 |
| No. of independent reflections | 586 |
| I > 3σ(I) (total) | 517 |
| *Refinement* | |
| Number of refined parameters | 29 |
| Refinement method | Least-squares |
| Weighting scheme | sigma |
| R1(F) [I > 3σ(I)]/R1(F$^2$) (all data, %) | 0.0223/0.0291 |
| wR2(F$^2$) [I > 3σ(I)]/wR2(F$^2$) (all data, %) | 0.0246/ 0.0275 |

| | |
|---|---|
| Goodness of Fit | 1.31 |
| Max/Min residual electronic density (e$^-$/Å$^3$) | 1.50/ -0.88 |
| Tmin/Tmax | 0.8727/1.000 |

**Table S2.** *Atomic Positions and Isotropic Thermal Displacement for Ba$_{10}$Fe$_{7.75}$Zn$_{5.25}$S$_{18}$Si$_3$O$_{12}$ from the single crystal XRD refinement*

| Atom | Wyck. | S.O.F. | x | y | z | U$_{eq}$ |
|------|-------|--------|---|---|---|----------|
| Ba1 | 12d | | 0.5 | 0.25 | 0 | 0.0122(2) |
| Ba2 | 8c | | 0.1759(1) | 0.1759(1) | 0.1759(1) | 0.03039(17) |
| Fe1 | 2a | | 0 | 0 | 0 | 0.0081(4) |
| Fe2 | 24g | 0.56 | 0.7101(1) | 0.1010(1) | 0.1010(1) | 0.0132(3) |
| Zn1 | 24g | 0.44 | 0.7101(1) | 0.1010(1) | 0.1010(1) | 0.0132(3) |
| Si1 | 6b | | 0.5 | 0 | 0 | 0.0085(8) |
| S2 | 12e | | 0.1919(2) | 0 | 0 | 0.0181(6) |
| S3 | 24g | | 0.7285(1) | 0.2715(1) | 0.0667(2) | 0.0257(7) |
| O1 | 24g | | 0.4316(5) | -0.0715(3) | 0.0715(3) | 0.0124(12) |

**Table S3.** *Anisotropic Thermal Parameters Uij (Å$^2$) for Ba$_{10}$Fe$_{7.75}$Zn$_{5.25}$S$_{18}$Si$_3$O$_{12}$ from the single crystal XRD refinement*

| Atom | U$_{11}$ | U$_{22}$ | U$_{33}$ | U$_{12}$ | U$_{13}$ | U$_{23}$ |
|------|----------|----------|----------|----------|----------|----------|
| Ba1 | 0.0136(2) | 0.0094(3) | 0.0136(2) | 0 | 0 | 0 |
| Ba2 | 0.0304(3) | 0.0304(3) | 0.0304(3) | -0.0005(3) | -0.0005(3) | -0.0005(3) |
| Fe1 | 0.0081(7) | 0.0081(7) | 0.0081(7) | 0 | 0 | 0 |
| Fe2 | 0.0120(7) | 0.0138(5) | 0.0138(5) | -0.0009(3) | -0.0009(3) | 0.0017(5) |
| Zn1 | 0.0120(7) | 0.0138(5) | 0.0138(5) | -0.0009(3) | -0.0009(3) | 0.0017(5) |
| Si1 | 0.0102(19) | 0.0076(11) | 0.0076(1) | 0 | 0 | 0 |
| S2 | 0.0159(14) | 0.0193(9) | 0.0193(9) | 0 | 0 | 0.0049(16) |
| S3 | 0.0154(8) | 0.0154(8) | 0.0463(2) | -0.0019(9) | -0.0086(8) | 0.0086(8) |

**Table S4.** *Main Distances (Å) for Ba$_{10}$Fe$_{7.75}$Zn$_{5.25}$S$_{18}$Si$_3$O$_{12}$ from the single crystal XRD refinement*

| Atom1 | Atom2 | d 1,2 [Å] |
|-------|-------|-----------|
| Ba1 | Fe2 | 3.6905(10)*4 |
| Ba1 | Si1 | 3.33450(5) *2 |

| | | |
|---|---|---|
| Ba1 | S3 | 3.189(2)*4 |
| Ba1 | O1 | 2.722(4)*4 |
| Ba2 | Fe1 | 4.0637(7) |
| Ba2 | Fe2 | 4.1172 (11)*6 |
| Ba2 | S2 | 3.3248(7)*3 |
| Ba2 | S3 | 3.705(3)*3 |
| Ba2 | S3 | 3.574(3)*3 |
| Fe1 | S2 | 2.559(3)*6 |
| Fe2 | S2 | 2.3110(19) |
| Fe2 | S3 | 2.332(2)*2 |
| Fe2 | O1 | 1.972(6) |
| Si1 | O1 | 1.627(5)*4 |
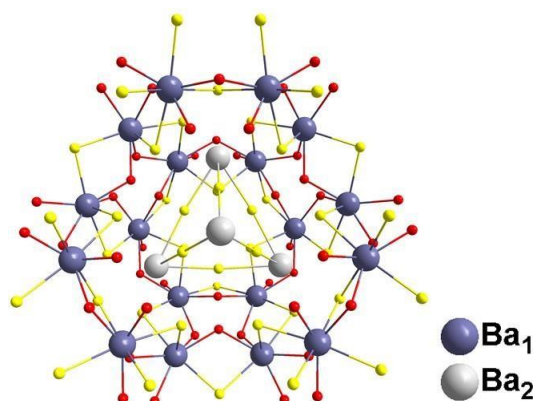


**Figure S1**. *Ba1 and Ba2 sub-lattice, for clarity only Ba atoms and their environment (O, S) are represented. Ba atoms are placed in the voids of the structure that we describe and it the voids occupied by Ba2 are larger than the one occupied by Ba1, this might be at the origin of the larger thermal displacement observed for Ba2. More into details, Ba1 has a set of rather symmetric distances with four equal Ba-O distances of 2.722(4) Å and four equal Ba-S distances of 3.189(2) Å. On another hand Ba2 is involved in twosets of three Ba-S distances, i.e. 3.325(1) Å and 3.574(3) Å, (forming a trigonal prism) and in another set of three longer distances also delimiting this cavity and equal to 3.705(3) Å. The Ba2-S distances are in the highest part of the range expected for Ba-S bonds compared to those found for Ba1.*
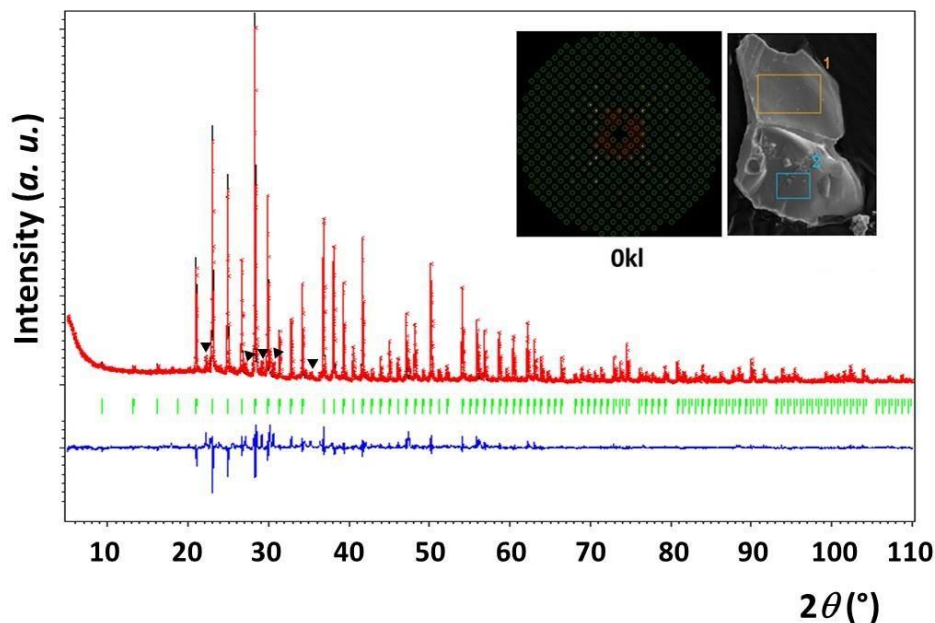
***Figure S2:*** *XRD Rietveld refinement of a powder of Ba$_{10}$Fe$_{7.75}$Zn$_{5.25}$S$_{18}$Si$_3$O$_{12}$. The experimental (red) and calculated (black) patterns are superimposed. The difference curve is represented in blue and the Bragg peaks positions in green. The most significant unindexed low intensity impurity peaks are pointed with black triangles. A SEM image of a single crystal and a precession image showing plane 0kl (single crystal XRD) are also shown as insets.*

The XRD data was collected at room temperature using the Cu K$_{\alpha1}$ and Cu K$_{\alpha2}$ radiation ($\lambda \approx$ 1.54187 Å) in the 2θ range 5 – 110° with a step size of 0.02° and an acquisition time of 1 second for each step. The profile and the cell parameters were refined with the Le Bail method. The background was fitted using a linear interpolation between a selection of points. A pseudo-Voigt function was used for the peak-shape model. Then the structure was refined using the Rietveld method[1] with the Program Jana2006[2]. The final Rietveld refinement converged with the cubic unit cell parameter a= 13.3350 (1) Å and the reliability factors R$_{obs}$= 0.0323, wR$_{obs}$= 0.0384, R$_{all}$= 0.0328, wR$_{all}$= 0.0388 and a goodness of fit (GOF) of 3.29. We could refine the thermal parameters of the heaviest atoms as anisotropic (Ba1, Ba2 and Fe2), see Table S7. The mixed site Fe2/Zn2 and Si1, S1, S2 and O1 were refined as isotropic. The atomic parameters and isotropic thermal displacements are given in **Table S6**. The complementary occupation of the Fe2/Zn1 mixed site was also refined and it converged to 0.47/0.53 for Fe/Zn. This is close to half/half occupancy as found from the single crystal refinement with 0.56/0.44. The minor discrepancy might be due to

the powder data versus single crystal refinements regarding this particular mixed site. In particular, from the powder only the heaviest atoms Ba1, Ba2 as well as Fe1 could be properly refined with anisotropic thermal displacement and not the mixed Fe/Zn site. Although very weak, the impurity peaks might also impact this ratio with a slight off-stoichiometry. Overall, this ratio is consistent with the initial refinement as well as with the XPS and magnetic fit results that depend on the Fe content.

Finally, the structure refined by the Rietveld method from powder XRD is consistent with the single crystal XRD refinement. The cubic unit cell parameter $a$ (13.3350(1) Å) is very close to the value found from the single crystal (a= 13.3380(1) Å).
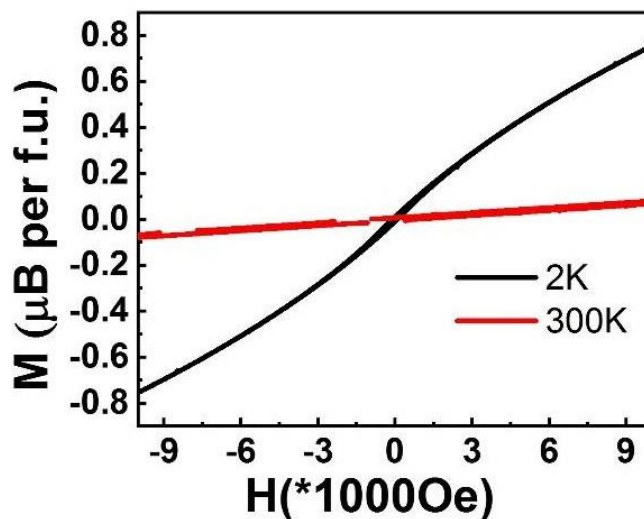


***Figure S3:*** *Field dependence of the magnetization for at constant temperatures of 2 and 300 K.*
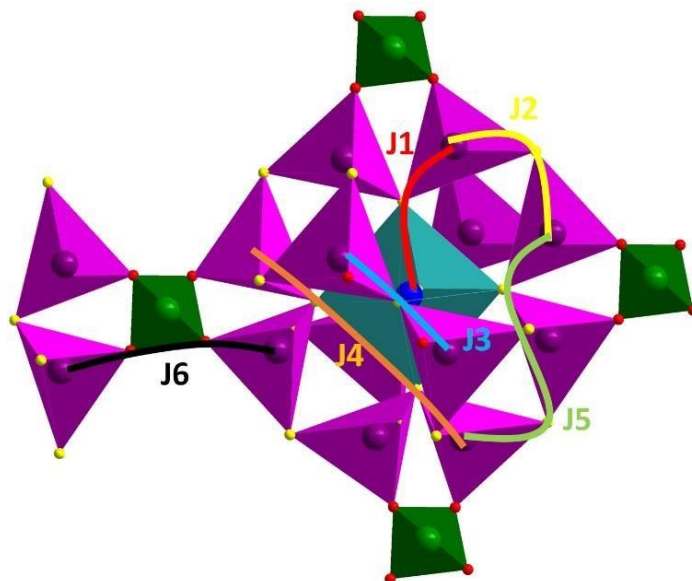
***Figure S4****: Magnetic paths in $Ba_{10}Fe_{7.75}Zn_{5.25}S_{18}Si_3O_{12}$.*

5.2. Magnetic exchanges in $Ba_{10}Fe_{7.75}Zn_{5.25}S_{18}Si_3O_{12}$.

The properties discussed above are coherent with the complex magnetic exchanges observed between iron ions. Six different magnetic paths (disturbed by Zn in the real structure) involving the complex magnetic cluster extended in the three directions are presented below. The $Fe1^{2+}$ localized in the octahedral site is coupled to $Fe2^{3+}$ with one Fe1-S2-Fe2 super-exchange (SE) path (J1). Then intra-cluster Fe2 ions (tetrahedra) coupling occur with two SE (J2 and J3) and two super-super-exchanges (SSE) paths (J4 and J5) while inter-clusters happen trough SSE only (J6). The geometrical parameters associated with these exchange paths are summarized in Table S5

and represented in **Figure S4**. Intra-clusters magnetic interaction are mediated trough sulfide anions while inter-cluster SSE involve oxide anions.

From a local point of view and for all different J paths, multiple Fe-Fe interactions are possible because the tetrahedral mixed valence $Fe^{2+/3+}$ site is always involved: i) For J1, $Fe^{2+}_{(Oh)}$-$Fe^{3+}_{(Td)}$ or $Fe^{2+}$-$Fe^{2+}_{(Oh)}$ ii) For J2-J6, $Fe^{2+}_{(Td)}$-$Fe^{3+}$ or $Fe^{2+}$-$Fe^{2+}_{(Td)}$ or $Fe^{3+}_{(Td)}$-$Fe^{3+}_{(Td)}$

**Table S5.** *Magnetic coupling with distances and angles in $Ba_{10}Fe_{7.75}Zn_{5.25}Si_3S_{18}O_{12}$*

| | atom1 | atom2 | d[1,2] | Fe-S…S-Fe | Fe-O…OFe | Fe-O-O-Fe or Fe-S-S-Fe | Fe-O-Fe (°) Fe-S-Fe (°) |
|---|---|---|---|---|---|---|---|
| **J1** | Fe1 | Fe2 | 4.310(1) | Fe1-S2=2.56(1) S2-Fe2=2.311(2) | - | - | Fe1-S2-Fe2=124.44(3) |
| **J2** | Fe2 | Fe2 | 3.562(1) | Fe2-S3=2.332(2) S3-Fe2=2.332(2) | | | Fe1-S2-Fe2=99.586(82) |
| **J3** | Fe2 | Fe2 | 3.811(1) | Fe2-S2=2.310(2) | - | - | Fe2-S2-Fe2 = 111.1(0) |
| **J4** | Fe2 | Fe2 | 7.374(1) | | Fe2-S2=2.311(2) | S2-S2=3.62(1) | Fe2-S2-S2=144.32(2) |
| **J5** | Fe2 | Fe2 | 6.387(1) | | Fe2-S2=2.311(2) S3-Fe2=2.332(2) | S2-S3=3.877(3) | Fe-S3-S2=82.9(1) Fe-S2-S3=121.58(3) |
| **J6** | Fe2 | Fe2 | 6.22(1) | - | Fe2-O1= 1.971(7) O1-Fe2= 1.971(7) | O1-O1 = 2.64(1) | Fe-O1-O1=143.85(21) |

168

**Table S6.** *Powder XRD Rietveld refinement: Atomic Positions and Isotropic Thermal Displacement for* $Ba_{10}Fe_{7.75}Zn_{5.25}S_{18}Si_3O_{12}$

| Atom | Wyck. | Site | S.O.F. | x/a | y/b | z/c | U [Å²] |
|------|-------|------|--------|-----|-----|-----|--------|
| Ba1 | 12d | -4.. | | 1/2 | 1/4 | 0 | 0.0092(9) |
| Ba2 | 8c | .3m | | 0.1755(2) | 0.1755(2) | 0.1755(2) | 0.0278(7) |
| Fe1 | 2a | -43m | | 0 | 0 | 0 | 0.018(2) |
| Fe2 | 24g | ..m | 0.47 | 0.7111(3) | 0.1006(3) | 0.1006(3) | 0.009(2) |
| Zn1 | 24g | ..m | 0.53 | 0.7111(3) | 0.1006(3) | 0.1006(3) | 0.009(2) |
| Si1 | 6b | -42.m | | 1/2 | 0 | 0 | 0.002(3) |
| S2 | 12$^e$ | 2.mm | | 0.1918(8) | 0 | 0 | 0.007(3) |
| S3 | 24g | ..m | | 0.7274(5) | 0.2726(5) | 0.0633(6) | 0.021(3) |
| O1 | 24g | ..m | | 0.433(1) | -0.0705(10) | 0.0705(10) | 0.011(6) |

**Table S7.** *Powder XRD Rietveld refinement: Anisotropic Thermal Displacement for* $Ba_{10}Fe_{7.75}Zn_{5.25}S_{18}Si_3O_{12}$

| Atom | $U_{11}$ | $U_{22}$ | $U_{33}$ | $U_{12}$ | $U_{13}$ | $U_{23}$ |
|------|----------|----------|----------|----------|----------|----------|
| Ba1 | 0.012(1) | 0.004(2) | 0.012(1) | 0 | 0 | 0 |
| Ba2 | 0.028(1) | 0.028(1) | 0.028(1) | -0.004(1) | -0.004(1) | -0.004(1) |
| Fe1 | 0.018(4) | 0.018(4) | 0.018(4) | 0 | 0 | 0 |

**Table S8.** *Vogel Fulcher parameters*

| $\omega_0/2\pi$ | $E_a$ (eV) | $T_0$ (K) |
|-----------------|------------|-----------|
| $10^9$ | $1.34 \times 10^{-3}$ | 2.21 |
| $10^{10}$ | $1.86 \times 10^{-3}$ | 2.00 |
| $10^{11}$ | $2.47 \times 10^{-3}$ | 1.78 |
| $10^{12}$ | $3.16 \times 10^{-3}$ | 1.57 |
| $10^{13}$ | $3.94 \times 10^{-3}$ | 1.36 |

(1)     Sleight, A. W. The Rietveld Method. *Mater. Res. Bull.* **1994**, *29* (6), 695. https://doi.org/10.1016/0025-5408(94)90128-7.

(2)     Petříček, V.; Dušek, M.; Palatinus, L. Crystallographic Computing System JANA2006: General Features. *Zeitschrift für Krist. - Cryst. Mater.* **2014**, *229* (5), 345–352. https://doi.org/10.1515/zkri-2014-1737.

# Part 2

# Synthesis, Structure, and electronic structure of Ba$_5$Fe$_2$ZnIn$_4$S$_{15}$

## B. Part 2: Synthesis, Structure and electronic structure of $Ba_5Fe_2ZnIn_4S_{15}$

### 1. Abstract

The new polar magnetic chalcogenide phase $Ba_5Fe_2ZnIn_4S_{15}$ was synthesized and its structure solved from single crystal XRD. Its structure is isostructural with a family of wide band gap materials showing SHG properties and represent the first magnetic member with the insertion of a 3$d$ metal, here high-spin $Fe^{3+}$. The three-dimensional (3D) framework is built from two type of chains connected via $[InS_4]$ tetrahedra. $[FeS_2]^-_\infty$ zigzag chain extended along the $c$ axis is built by $[FeS_4]^-$ tetrahedra are weakly connected by super-super-exchange mediated by $[InS_4]$, thus providing a low dimensional character of the magnetism with magnetic chains. $[In_3Zn_1S_9]^{7-}\infty$ (chain 2, chains of T2-supertetrahedra) is also extended along $c$ and connected by $[InS_4]$ tetrahedra. The $Ba^{2+}$ cations occupy the voids. Preliminary magnetic measurements and density functional theory calculations suggest dominating antiferromagnetic interactions with strong in-chain super-exchange coupling.

### 2. Introduction

The interest attributed to the search and study of transition metal chalcogenide compounds is due to the structural diversities and compositional complexities[1]. These characteristics lead to interesting magnetic properties[2,3]. Iron-based chalcogenides in particular attract considerable attention due to the appearance of superconductivity in some layered phases. For instance, in Cr-doped $FeTe_{0.8}S_{0.2}$, it is found that the ferromagnetism and superconductivity coexist[4]. On another hand, multiferroicity is found in several Fe-based systems (ref). In that sense, a strategy to target new multiferroic phases could be to insert magnetic ions in known strongly polar systems.

Following such direction, polar chalcogenides with SHG properties are perfect candidates. We focused on the polar structure type including $Sr_5ZnGa_6S_{15}$ [5] and $Pb_5Ga_6ZnS_{15}$[6] phases in order to insert $Fe^{3+}$ which in a high spin state (d$^5$) provides a maximal magnetic moment and strong magnetic coupling. The later phases crystallize in the polar space group Ama2. They are wide

171

band gap semiconductors and exhibit a strong SHG response. They are characterized by interconnected $Ga_4S_{10}$ T2-supertetrahedra, dimeric $Ga_2S_7$ tetrahedra and $ZnS_4$ tetrahedra to form a complex 3D NCS anionic framework with large cation residing in the irregular voids ($Sr^{2+}$ or $Pb^{2+}$ in the later examples). Here we could synthesize the first magnetic member $Ba_5Fe_2ZnIn_4S_{15}$. We present its structural characterization and a preliminary magnetic study combined with DFT calculations.

3. Experimental section

**Synthesis:** Single crystals of $Ba_5Fe_2ZnIn_4S_{15}$ were initially found during an exploratory synthesis that included the elements Ba-In-Zn-Fe-S. We attempted to synthesize a single-phase material from a mixture of the precursors $BaS/In_2S_3/Zn/Fe/S$. Those precursors were mixed and thoroughly ground in an agate mortar before being pressed into pellets and heated in an evacuated sealed quartz tube. The heat treatment consisted in heating up to 1000°C at a rate of 250°C/h for 7 hours, then cooling down to 700°C at a 30°C/h rate, temperature at which the furnace was switched off.

**X-ray diffraction on single crystals diffraction** was performed on an X8 diffractometer equipped with a bi-dimensional CCD 4K detector and an Ag $K\alpha$ source.

**The powder X-ray diffraction** pattern was collected on a Bruker D8 diffractometer equipped with a linear detector Lynxeye ($Cu_{K\alpha}$) in Bragg-Brentano geometry at room temperature.

**DFT calculations** were carried out by employing the projector augmented wave (PAW)[7-8] method encoded in the Vienna ab initio simulation package (VASP)[9] and the generalized gradient approximation of Perdew, Burke and Ernzerhof[10] (PBE) for the exchange-correlation functionals. The full geometry optimizations were carried out using a plane wave energy cutoff of 550 eV and 12 *k* points in the irreducible Brillouin zone. It converged with residual Hellman-Feynman forces on the atoms smaller than 0.03 eV/Å and led to a good match with the experimental structure, i.e. within a reasonable expected for the GGA method. The relaxed structure was used for calculations of the electronic structure. For the later, the plane wave cutoff energies of 550 eV

and the threshold of self-consistent-field energy convergence of $10^{-6}$ eV were used, with 24 $k$ points in the irreducible Brillouin Zone.

**Scanning electron microscopy (SEM)** experiments and EDX analysis were carried out on a Hitachi S400N.

### 4. Results and Discussion
### 4.1. Structure solution and description

The structure was solved using XRD single crystal data obtained from a black platelet crystal which crystalize in orthorhombic cell with parameters a = 23.4580(19) Å b= 18.551(6) Å, c= 6.464(5) Å and the polar space group A m a 2 (40). The data collection and refinement details are given in **Table 1**. The refinement was carried out with the JANA2006[11] software based on a structure solution obtained using the charge flipping method[12]. The EDS analysis of the single crystals led to the average atomic ratio 52.9.3/7.35/12.44/14.29/13.02 for S/Fe/Zn/In/Ba, respectively.

The new structure $Ba_5Fe_2ZnIn_4S_{15}$ is a 3D framework **Figure 6.a** combining between three different types of tetrahedron $InS_4$, $FeS_4$ and $ZnS_4$ (see **Figure 6.e. f**. and **g**.). We will describe it in two ways. The first one is the standard description which is reported for several chalcogenides of this type and in particular for the isostructural wide band gap SHG active compounds $Sr_5ZnGa_6S_{15}$ and $Pb_5Ga_6ZnS_5$[5,6]. The $[FeS_2]^-\infty$ zigzag chain (1) extended along $c$ axis is built from corner-sharing $[Fe1S_4]$ tetrahedra. This chain 1 is connected via $[In1S_4]^{5-}$ tetrahedra to the T2 supertetrahedra based chain (2) $[In_3Zn_1S_9]^{7-}\infty$ which is extended also along $c$ axis. In the later chain 2, the corner sharing $[In_3ZnS_{10}]^{8-}$ T2-supertetrahedra are constituted with one $[In2S_4]^{5-}$, two $[In3S_4]^{5-}$ and one $[Zn1S_4]^{6-}$ tetrahedra by sharing vertices. This composition $[In_3ZnS_{10}]^{8-}$ of T2-supertetrahedra is observed in the current work for the first time. Chains 2 are interconnected as shown in **Figure 6.d**. In the $FeS_4$ tetrahedra, the distances $d_{Fe-S}$ are found between 2.238 Å and

2.266 Å. This range is comparable to the one reported for instance in $Ba_5Fe_4S_{11}$ which also exhibits $Fe^{3+}$ in $FeS_4$ tetrahedra, with d($Fe^{3+}$-$S^{2-}$)=2.214-2.306 Å[13]. The In-S bond lengths ranging from

2.377Å to 2.484Å are comparable to the range of bond lengths in Ba2In2S5[14] (from 2.386Å to 2.503Å). $Ba^{2+}$ cations are localized in the voids.

**Table 1**. *Refinement parameters of $Ba_5Fe_2In_4ZnS_{15}$*

| Formula | $Ba_5Fe_2In_4ZnS_{15}$ |
|---|---|
| Molecular weight (g. mol$^{-1}$) | 1804 |
| Symmetry | *orthorhombic* |
| Space group | A m a 2 (40) |
| Unit cell dimensions (Å) | a = 23.4580(19) |
| | b= 18.551(6) |
| | c= 6.464(5) |
| Volume (Å$^3$) | 2813(2) |
| Z | 4 |
| Data Collection | |
| Equipment | Bruker CCD |
| Λ [Ag Kα; Å] | 0.56087 |
| Calculated density (g cm$^{-3}$) | 4.2599 |
| Crystal shape | Patelet |
| Crystal dimensions (μm) | 65×50×5 |
| Color | Black |
| Absorption correction | analytical |
| Scan mode | ω, φ |
| θ (min–max) (°) | 1.73-19.72 |
| μ (mm−1 ; for λ Kα = 0.56087Å) | 6.841 |
| F(000) | 3192 |
| Reciprocal space recording | −28 ≤ h ≤ 28 |
| | −22 ≤ k ≤ 22 |
| | −7 ≤ l ≤ 7 |

| | |
|---|---|
| No. of measured reflections | 37736 |
| No. of independent reflections | 2633 |
| I > 3σ(I) (total) | 2325 |
| Refinement | |
| Number of refined parameters | 245 |
| Refinement method | Least-squares |
| Weighting scheme | sigma |
| R1(F) [I > 3σ(I)]/R1(F$^2$) (all data, %) | 0.0315/0.0382 |
| wR2(F$^2$) [I > 3σ(I)]/wR2(F$^2$) (all data, %) | 0.0374/ 0.0386 |
| Goodness of Fit | 1.42 |
| Max/Min residual electronic density (e$^-$/Å$^3$) | 1.39/ -1.86 |
| Tmin / Tmax | 0.6607/0.7387 |
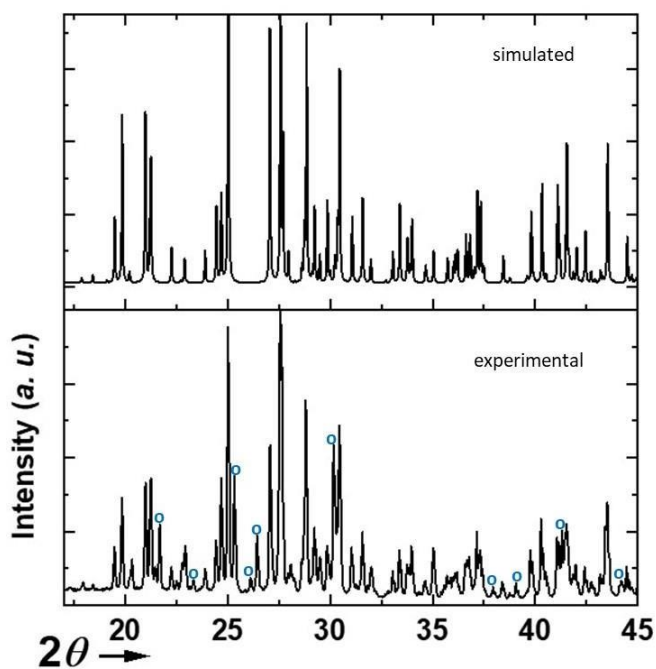


**Figure 1:** *X-ray diffraction pattern of $Ba_5Fe_2In_4ZnS_{15}$ calculated from single crystal refinement, and compared to x-ray experimental pattern of obtained powder, pics impurity are indexed by blue cercles.*
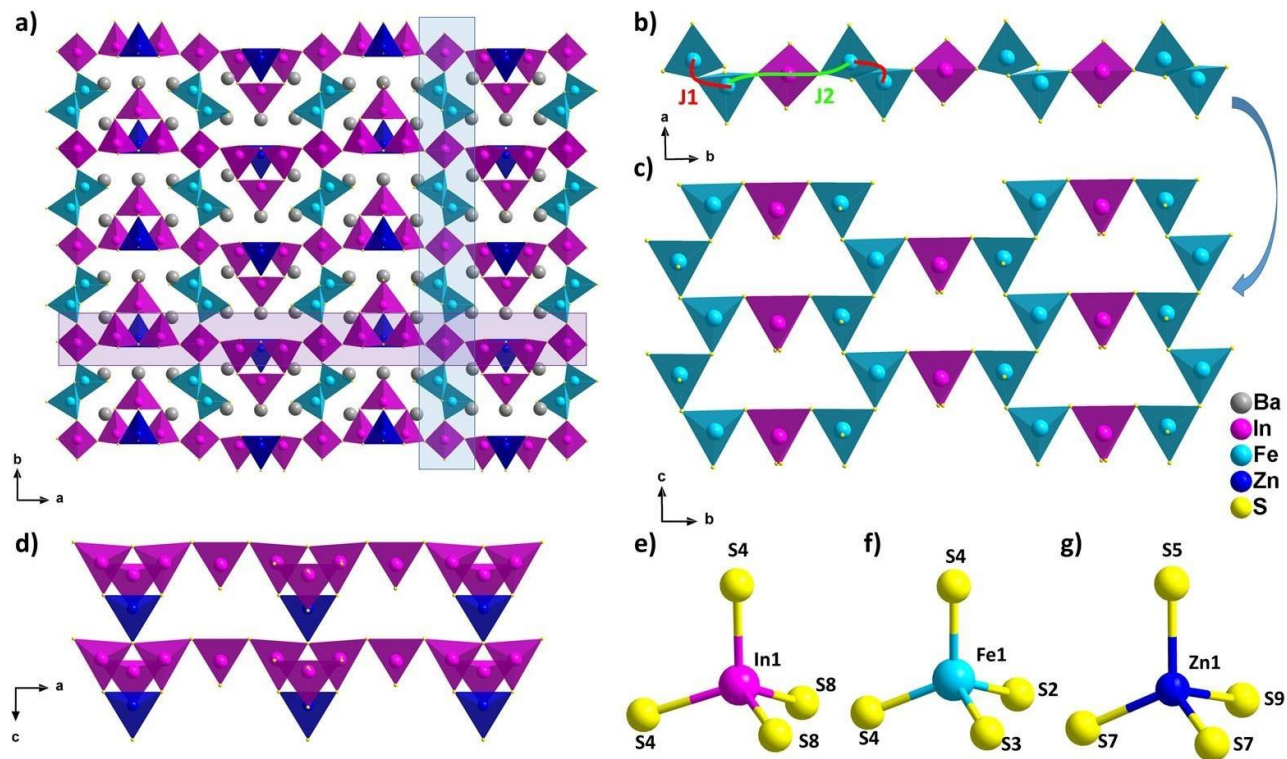
**Figure 2:** a) View of $Ba_5Fe_2In_4Zn_1S_{15}$ along c axis b) Magnetic exchange Coupling J1 and J2 in the chains extended along b axis c) interconnection between magnetic chains d) view of lined chains type 2 e) f) g) In1, Fe1 and Zn1 coordination respectively.

**Table 2**. Atomic positions and isotropic thermal displacement for $Ba_5Fe_2In_4Zn_1S_{15}$

| Atom | Wyck. | S.O.F. | x | Y | z | $U_{eq}$ |
|------|-------|--------|---|---|---|----------|
| Ba1 | 4b | | 3/4 | 0.34541(7) | 0.147(2) | 0.0128(4) |
| Ba2 | 8c | | 0.61457(3) | 0.13332(2) | 0.068(2) | 0.0110(2) |
| Ba3 | 8c | | 0.10987(3) | 0.16031(4) | 0.102(2) | 0.0126(2) |
| In1 | 4a | | 1/2 | 1/2 | 0.078(2) | 0.0118(4) |
| In2 | 4b | | 3/4 | 0.69547 | 0.183(2) | 0.0125(4) |
| In3 | 8c | | 0.66016(4) | 0.5262(2) | 0.055(2) | 0.0203(3) |
| Fe1 | 8c | | 0.47101(7) | 0.6962(1) | 0.130(2) | 0.0071(5) |
| Zn1 | 4b | | 3/4 | 0.52836(12) | 0.531(2) | 0.0079(6) |
| S1 | 4b | | 3/4 | 0.8245(3) | 0.142(2) | 0.0123(14) |
| S2 | 8c | | 0.37633(11) | 0.69643(16) | 0.088(2) | 0.0100(9) |
| S3 | 8c | | 0.51069(14) | 0.70254(19) | -0.186(2) | 0.0125(10) |

| | | | | | |
|---|---|---|---|---|---|
| S4 | 8c | 0.49966(15) | 0.60120(19) | 0.323(2) | 0.0125(10) |
| S5 | 4b | 3/4 | 0.6575(2) | 0.551(2) | 0.0112(13) |
| S6 | 8c | 0.65417(12) | 0.65980(17) | 0.066(2) | 0.0121(9) |
| S7 | 8c | 0.66700(13) | 0.47875(19) | 0.391(2) | 0.0133(10) |
| S8 | 8c | 0.58174(14) | 0.4932(2) | -0.158(2) | 0.0137(11) |
| S9 | 4b | 3/4 | 0.4937(3) | -0.113(2) | 0.0143(15) |

### 4.2. Powder sample and magnetic measurement

For further characterization, we have attempted to synthesize a pure powder phase. Numerous efforts allowed the phase to appear and to increase the purity up to the sample for which the powder XRD is presented in **Figure 1**. In our best sample, an impurity that could not be indexed with known phases persists. Although the title phase is the major phase as shown from the simulated and superimposed XRD pattern, the impurity is significant which makes difficult a magnetic characterization and its interpretation. Nevertheless, we have carried out a preliminary study.

**Figure 3.a** shows the temperature dependence of the magnetic susceptibilities in zero-field and field-cooled at H= 1000 Oe. At low temperature around 2-3 K, a slight divergence of the ZFC/FC is observed, however it is difficult to attribute it to a specific phenomenon such as spin glass state, because of the significant amount of the unidentified impurity. It could also originate from the presence of low dimensional short-range magnetic correlations and/or a complex long-range magnetic order.

Despite this matter of fact, we have tried to apply a Curie-Weiss fit allowed only on a small portion of the high temperature data range 200-350K, which led to $\theta_{cw}$= -358.08 K and an effective moment of $\mu_{eff}$= 6.689 $\mu B$ per formula unit ($Ba_5Fe_2ZnIn_4S_{15}$). It indicates dominating and

177

strong antiferromagnetic interaction which is agreement with the DFT calculated J1 and J2 described below. However, regarding the presence of $Fe^{3+}$ in a high spin state, the expected theoretical effective moment is of 5.92 µB. Our fitted value is far below considering two $Fe^{3+}$ per formula unit. As an alternative and accordingly with the suspicion of a temperature independent paramagnetic (TIP) contribution more visible at high temperature, we applied a Curie-Weiss fit including a TIP contribution. We used the following equation:

$$ x = \frac{c}{(T - \theta)} + \alpha $$

where C is the Curie constant, $\theta$ is the Curie-Weiss temperature and $\alpha$ is the TIP contribution. It leads to the following parameters with C= 1.540(2) emu.Oe$^{-1}$.g$^{-1}$, $\theta$= -7.03(5) K and $\alpha$= 0.00502(1) emu.Oe$^{-1}$.g$^{-1}$. The later TIP contribution is rather high. The extracted effective moment is found about 3.5 µB per formula unit, which is even lower than in the standard CW fit. In conclusion, although these preliminary magnetic measurements confirm the dominant antiferromagnetic interactions and point toward a phenomenon around 3 K, it is difficult to extract more information with the current amount of impurity.



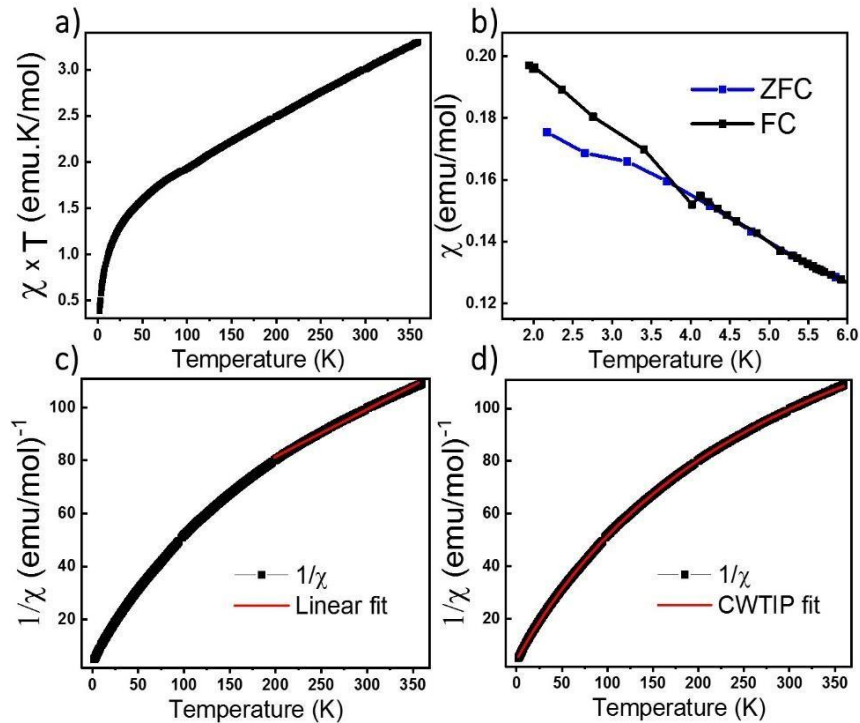**Figure 3:** a) Temperature dependance of magnetic susceptibility χ x T. b) Zoom of ZFC/FC at low temperature. c) Linear fit of the reciprocal magnetic susceptibility 1/χ between 200-350K. d) CW TIP fit of the reciprocal magnetic susceptibility 1/χ.

## 5. DFT calculations

The magnetic interactions within the title phase were investigated using DFT+U calculations at the GGA level. We have investigated several magnetic configurations using a $U_{eff} = 4$ eV which is in the typical range for similar systems. The structure was not relaxed to avoid slight geometrical changes in the spin chain that may affect the results.

Using the procedure detailed below and the magnetic configurations represented in **Figure 4** and **Table 3**. We extracted from our DFT+U calculations the magnetic interactions constants $J1$, J2 and $J3$. We consider decoupled 2D layers containing the spin chains weakly interacting. We estimate the super-exchange intra-chain coupling (J1) and the super-super exchange inter-chains couplings (J2) as well as the next-nearest neighbor interaction within the chain (J3). Another inter-chains path exists trough the T2 supertetrahedra but is not considered due to its exceedingly long inter-chain distance (path of four successive $InS_4$ tetrahedra between Fe atoms) providing a complete structural disconnection.

**Table 3.** *Distances, angles and number of magnetic exchanges coupling between iron atoms.*

|  | Atom1 | Atom2 | d[1,2] Å | Fe-S-Fe Å | Fe-S...S-Fe Å | Fe-S-Fe(°) | Number of coupling |
|---|---|---|---|---|---|---|---|
| **J1** | Fe1 | Fe1 | 4.0349(149) | Fe-S3=2.2478(167) |  | 126.8*(4)* | 2+8/2= 6 |
| **J2** | Fe1 | Fe1 | 6.464(57) |  | Fe1-S7=2.265(5) S7-S7= 3.7094(67) |  | 16/2 |
| **J3** | Fe1 | Fe1 | 7.4054(35) |  | Fe1-S4..S4-Fe1 Fe-S4= 2.2614(106) S4-S4=3.7548(5) |  | 1+ 9/2= 5.5 |
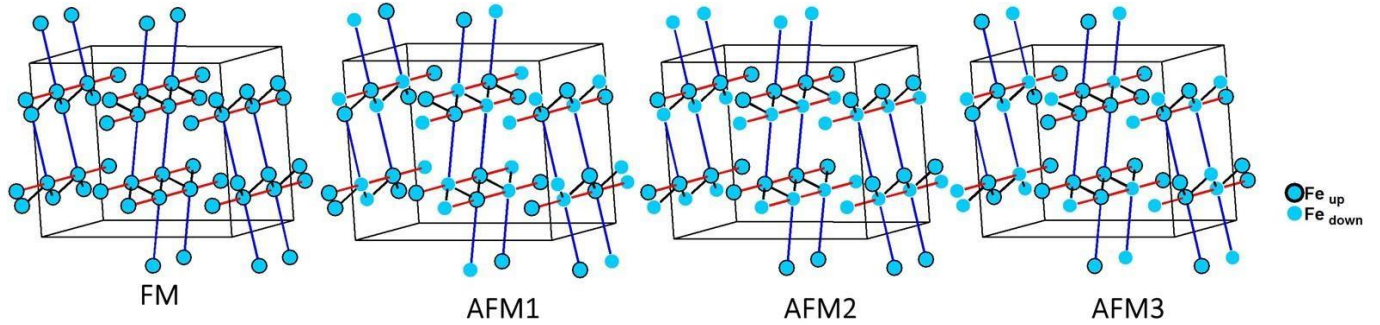
**Figure 8:** *Different magnetic configurations of $Ba_5Fe_2In_4Zn_1S_{15}$ used in the DFT+U calculations, J1, J2 and J3 are represented in black, red in blue colors respectively.*
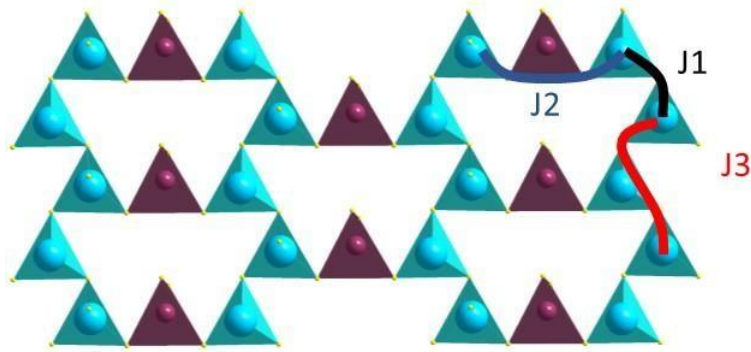


*Figure 5: Magnetic exchange couplings scheme of J1, J2 and J3 between iron atoms.*

E0: sum of the nonmagnetic part

Jij: the exchange interactions between spin $S_i$ and $S_j$ at sites i and j, respectively.

The positive (negative) $J_{ij}$ represents FM (AFM) coupling. Here, we only give the intra-chain exchange couplings J1 between the nearest neighboring Fe1–Fe1 (super-exchange (SE) path) and J2 for the next nearest neighbors (super-super-exchange (SSE) path) (The inter-chain exchange interactions are negligible because of the exceedingly long inter-chain distance. For one formula unit, the total energies associated with different magnetic orders can be written as:

(1) $E_{(FM)} = E0 - 16J1S^2 - 8J2S^2 - 16J3S^2$

(2) $E_{(AFM1)} = E0 + 8 J2S^2 + 16 J3S^2$

(3) $E_{(AFM2)} = E0 + 16J1S^2 + 8J2S^2 - 16J3S^2$

(4) $E_{(AFM3)} = E0 - 8J2S^2 + 8J3S^2$

Here, we use S =5/2, accordingly with the charge of Fe assumed in this work ($d^5$) corresponding to high spin $Fe^{3+}$). The later allows the J calculations using defined spin state on each site. Using the equations above and the energies of the magnetic configurations represented in **Figure 4**, we extracted from our DFT+U calculations the magnetic interactions constants J1=-206 K, J2=-9.08K and J3=-6.62 K, considering $U_{eff}$= 4 eV. All J couplings are found antiferromagnetic but J1 is largely dominating which avoid any competition between J1 and J2 (both in-chain and cannot be AFM at the same time) with |J1| >>> |J3|. J2, inter-chain, being as weak as J3. Therefore, this systemcan be described as S=5/2 AFM spin chain.
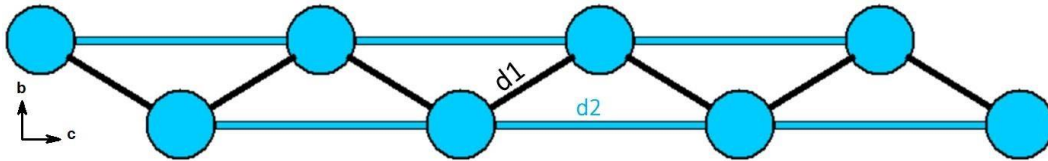


**Figure 6:** *Quasi one-dimensional zigzag magnetic chain built from iron atoms in blue with distances of J1 and J2 presented in black and blue successively.*

6. Conclusion

We describe here the synthesis and the structural and physical characterization of the new sulfide material $Ba_5Fe_2ZnIn_4S_{15}$. It adopts a polar structure type isostructural with a family of wide band gap SHG materials containing chains of T2-supertetrahedra and $[MS_2]_\infty$ chains made of corner-sharing tetrahedra. In the title phase we inserted the magnetic high-spin $Fe^{3+}$ ($d^5$) transition metal in this framework which incorporated the $(MS_2)_\infty$ chains. A powder sample could be obtained but a significant unidentified impurity hampers a deep physical characterization. Preliminary magnetic measurements show a divergence of the ZFC/FC at very low temperature around 3 K and dominant antiferromagnetic interactions. DFT calculations suggest a stable antiferromagnetic state with strong AFM intrachain Fe-S-Fe super exchanges and very weak interchain Fe-S-S-Fe coupling (via $InS_4$). It thus represents an AFM S=5/2 spin chain system. A pure powder or magnetic measurements based on single crystals are required to further investigate this sample. It represents a promising playground to measure electric polarization and tune the magnetic interactions toward multiferroic systems.

**Table 4.** *Anisotropic thermal parameters Uij (Å²) for Ba₅Fe₂In₄Zn₁S₁₅*

| Atom | $U_{11}$ | $U_{22}$ | $U_{33}$ | $U_{12}$ | $U_{13}$ | $U_{23}$ |
|---|---|---|---|---|---|---|
| Ba1 | 0.0048(5) | 0.0219(7) | 0.0116(7) | 0.0000(0) | 0.0000(0) | 0.0002(5) |
| Ba2 | 0.0075(3) | 0.0119(4) | 0.0136(5) | 0.0006(3) | 0.0016(4) | -0.0010(4) |
| Ba3 | 0.0081(3) | 0.0193(4) | 0.0105(5) | -0.0001(3) | 0.0006(4) | -0.0027(4) |
| In1 | 0.0187(5) | 0.0096(6) | 0.0084(4) | 0.0029(5) | 0.0000(4) | -0.0007(4) |
| Ba5 | 0.0199(5) | 0.0111(6) | 0.0072(4) | 0.0025(5) | 0.0002(4) | 0.0006(5) |
| In1 | 0.0110(6) | 0.0133(7) | 0.0112(7) | -0.0004(5) | 0.00000 | 0.00000 |
| In2 | 0.0084(6) | 0.0123(8) | 0.0169(8) | 0.000000 | 0.00000 | 0.0014(6) |
| In3 | 0.0194(5) | 0.0229(6) | 0.0187(6) | 0.0010(4) | -0.0019(5) | 0.0003(6) |
| Fe1 | 0.0044(8) | 0.0100(10) | 0.0069(10) | -0.0004(7) | 0.0007(8) | -0.0002(8) |
| Zn1 | 0.0046(9) | 0.0120(11) | 0.0072(13) | 0.000000 | 0.000000 | -0.0008(9) |
| S1 | 0.008(2) | 0.015(3) | 0.014(3) | 0.000000 | 0.000000 | 0.003(2) |
| S2 | 0.0031(13) | 0.0142(16) | 0.0127(18) | -0.0009(11) | -0.0011(15) | -0.0018(18) |
| S3 | 0.0128(17) | 0.0128(19) | 0.0118(19) | -0.0004(14) | 0.0050(14) | 0.0038(16) |
| S4 | 0.0110(15) | 0.0120(19) | 0.0144(19) | 0.0031(12) | -0.0032(14) | 0.0014(15) |
| S5 | 0.0065(19) | 0.013(2) | 0.014(3) | 0.000000 | 0.000000 | 0.000(2) |
| S6 | 0.0100(14) | 0.0135(16) | 0.0129(18) | -0.0004(12) | -0.0043(15) | -0.0005(19) |
| S7 | 0.0111(16) | 0.0161(19) | 0.0127(19) | -0.0021(14) | 0.0004(15) | 0.0016(16) |
| S8 | 0.0112(16) | 0.015(2) | 0.0147(19) | -0.0014(14) | 0.0062(15) | -0.0016(16) |
| S9 | 0.008(2) | 0.022(3) | 0.012(3) | 0.000000 | 0.000000 | 0.003(2) |

**Table 5**. *Main distances (Å) for Ba₅Fe₂In₄Zn₁S₁₅*

| Atoms 1,2 | d 1,2 [Å] | Atoms 1,2 | d 1,2 [Å] |
|---|---|---|---|
| Ba1-S1 | 3.29(2) | In1-S4 | 2.454(13)*2 |
| Ba1-S1 | 3.22(2) | In1-S8 | 2.456(12)*2 |
| Ba1-S2 | 3.087(4)*2 | In2-S1 | 2.407(6) |
| Ba1-S9 | 3.224(11) | In2-S5 | 2.484(19) |
| Ba2-S2 | 3.168(4) | In2-S6 | 2.461(6) *2 |
| Ba2-S3 | 3.179(10) | In3-S6 | 2.417(4) |
| Ba2-S4 | 3.184(10) | In3-S7 | 2.380(18) |
| Ba2-S5 | 3.2104(12) | In3-S8 | 2.395(11) |
| Ba2-S7 | 3.323(8) | In3-S9 | 2.463(9) |

| | | | |
|---|---|---|---|
| Ba2-S8 | 3.236(11) | Fe-S2 | 2.237(4) |
| Ba3-S1 | 3.3093(18) | Fe1-S3 | 2.246(18) |
| Ba3-S2 | 3.232(19) | Fe1-S3 | 2.265(11) |
| Ba3-S3 | 3.239(9) | Fe1-S4 | 2.263(11) |
| Ba3-S4 | 3.324(11) | Zn1-S5 | 2.399(5) |
| Ba3-S7 | 3.209(9) | Zn1-S7 | 2.335(8)*2 |
| Ba3-S8 | 3.310(10) | Zn1-S9 | 2.387(19) |

(1) Abudurusuli, A.; Wu, K.; Li, J.; Yalikun, A.; Yang, Z.; Pan, S. LiBa 2 M. **2019**, *4*. https://doi.org/10.1021/acs.inorgchem.9b01810.

(2) Nakayama, N. Studies on the Compounds in the Ba-Fe-S Antiferromagnetism of Ba , FeS , and Related System . I . Linear Chain Compounds Ba & OS ,. **1980**, *356*, 351–356.

(3) Lemley, J. T. Ba ,, Fe , S ,, and Ba , FeS , : Crystal Structures , Miissbauer , Magnetic , and Electrical Behavior. **1976**, *128*, 117–128.

(4) Li, T.; Feng, Z.; Hou, Q.; Wu, H.; Wang, K.; Ge, J.; Cao, S. Solid State Communications. **2020**, *309* (January). https://doi.org/10.1016/j.ssc.2020.113846.

(5) Lin, H.; Li, B. X.; Chen, H.; Liu, P. F.; Wu, L. M.; Wu, X. T.; Zhu, Q. L. $Sr_5ZnGa_6S_{15}$: A New Quaternary Non-Centrosymmetric Semiconductor with a 3D Framework Structure Displaying Excellent Nonlinear Optical Performance. *Inorg. Chem. Front.* **2018**, *5* (6), 1458–1462. https://doi.org/10.1039/c8qi00322j.

(6) Duan, R. H.; Yu, J. S.; Lin, H.; Zheng, Y. J.; Zhao, H. J.; Huang-Fu, S. X.; Khan, M. A.; Chen, L.; Wu, L. M. $Pb_5Ga_6ZnS_{15}$: A Noncentrosymmetric Framework with Chains of T2-Supertetrahedra. *Dalt. Trans.* **2016**, *45* (31), 12288–12291. https://doi.org/10.1039/c6dt02404a.

(7) Blöchl, P. E. Projector Augmented-Wave Method. *Phys. Rev. B* **1994**, *50* (24), 17953–17979. https://doi.org/10.1103/PhysRevB.50.17953.

(8) Kresse, G.; Joubert, D. From Ultrasoft Pseudopotentials to the Projector Augmented-Wave Method. *Phys. Rev. B* **1999**, *59* (3), 1758–1775. https://doi.org/10.1103/PhysRevB.59.1758.

(9) Kresse, G. . et al. Vienna Ab-Initio Simulation Package (VASP).

(10) Perdew, J. P.; Burke, K.; Ernzerhof, M. Generalized Gradient Approximation Made Simple. *Phys. Rev. Lett.* **1996**, *77* (18), 3865–3868. https://doi.org/10.1103/PhysRevLett.77.3865.

(11) Petříček, V.; Dušek, M.; Palatinus, L. Crystallographic Computing System JANA2006: General Features. *Zeitschrift für Krist. - Cryst. Mater.* **2014**, *229* (5), 345–352. https://doi.org/10.1515/zkri-2014-1737.

(12)    van der Lee, A. Charge Flipping for Routine Structure Solution. *J. Appl. Crystallogr.* **2013**, *46* (5), 1306–1315. https://doi.org/10.1107/S0021889813020049.

(13)    Cohen, S.; Kimizuka, N.; Steinfink, H. The Crystal Structure and Stability of $Ba_5Fe_4S_{11}$. *J. Solid State Chem.* **1980**, *35* (2), 181–186. https://doi.org/10.1016/0022-4596(80)90491-0.

(14)    Gao, W.; Wu, K.; Lai, K.; Yang, Z.; Pan, S. $Ba_2In_2Q_5$ ( Q = S , Se ): Synthesis , Crystal Structures , Electronic Structures ,. **2015**, No. 7, 1329–1333. https://doi.org/10.1002/zaac.201500113.

# Part 3

# High pressure synthesis of the spin chain sulfide Ba$_9$V$_3$S$_{11}$(S$_2$)$_2$

C. Part 3: High pressure synthesis of the spin chain sulfide $Ba_9V_3S_{11}(S_2)_2$

Batoul Almoussawi[1], Hayashi Tomohiri[2], Prof. Hiroshi Kageyama[2], Dr. Houria Kabbour[1, *]

[1] *Univ. Lille, CNRS, Centrale Lille, ENSCL, Univ. Artois, UMR 8181 – UCCS – Unité de Catalyse et Chimie du Solide, F-59000 Lille, France.*

[2] *Department of Energy and Hydrocarbon Chemistry, Graduate School of Engineering, Kyoto University, Nishikyo-ku, Kyoto, 615-8510, Japan.*

1. Abstract

The new compound $Ba_9V_3S_{11}(S_2)_2$ was synthesized using high pressure and high temperature. The single crystal XRD based structure solution and refinement show that it crystallizes in the hexagonal system with the space group $P\bar{6}c2$ (188) and the lattice parameters $a$= 9.1979(4) Å and $c$ = 18.0462(10) Å. Its one-dimensional structure is related to the high-pressure phase $Ba_9V_3Se_{15}$ ($Ba_9V_3Se_{11}(Se_2)_2$) and consists of chains made of face-sharing $VS_6$ octahedra running along the $c$-axis. The chains contain two distinct sites of Vanadium with a mixed valence state of $V^{3+}$ and $V^{2+}$. The space between the chains, two type of columns, is occupied by disulfides ($S^{2-}$) pairs and *isolated* sulfide anions $S^{2-}$ surrounded by $Ba^{2+}$ cations. The distributions within the columns are slightly different than in $Ba_9V_3Se_{11}(Se_2)_2$ making the two compounds not isostructural but polymorphs although they show the same symmetry and unit cell. We discuss this phase on the basis of crystallochemical analysis and DFT calculated electronic structure. Assuming a magnetic insulator as found from DFT+$U$ calculations, we discuss the existence of magnetic clusters within the spin chains.

2. Introduction

Despite the numerous studies carried out for decades, chalcogenides continue to attract considerable attention due to their wide range of physico-chemical properties [1-2], such as

magnetic, [3-4] electronic[5], NLO[6,7], photocatalytic or photovoltaic properties for instance. Especially, they may exhibit low-dimensional structuration and strongly correlated electronic systems leading to complex and exotic quantum ground states, superconductivity, charge and spin density waves, orbital ordering[8] *etc.*… In the system Ba-V-S, the $Ba_xV_6S_8$ (x = 0.41-0.48) phases consist of face-sharing distorted $VS_6$ octahedra forming a 3D framework and present a superconducting transition around 2.5 K [9]. In this chemical system, high pressure synthesis provides a way to favor other structural types which are metastable with non-conventional properties. It is the case of the *quasi*-one-dimensional hexagonal phase $BaVS_3$, based on face-sharing $VS_6$ octahedra forming spin-1/2 chains. It shows a weak anti-ferromagnetic behavior that switches to soft ferromagnetism with decreasing sulfur content[4]. $BaVS_3$ shows a complex behavior including several structural transitions, a metal-insulator transition and an incommensurate antiferromagnetic magnetic order. On another hand, the selenide analogue $BaVSe_3$ is quite different as it is a metallic ferromagnet below ~43 K. Their complex behavior can in addition be easily modified by chemical doping or by applying pressure. More recently, the selenide compound $Ba_9V_3Se_{15}$ with lattice parameters a = 9.5745(7) Å and c = 18.7814(4) Å in space group *P*-6*c*2 (188) was reported[10]. It was synthesized at high pressure and high temperature conditions (5.5 GPa and 1400°C) and exhibits similar face-shared $VSe_6$ chains. However, the separation between adjacent spin chains is larger than in $BaVSe_3$ with an interchain V-V distance of minimum 9.5745(7) Å due to a more complex interchain occupation. It is a semiconductor that shows a ferrimagnetic and a spin cluster glass transitions at 2.5 K and 3.3 K, respectively, under low magnetic field (10 Oe). The later disappear when the magnetic field exceeds 50 Oe. In the later system, a mixed valence of vanadium $V^{3+}/V^{2+}$ is observed contrarily to $BaVS_3$ or $BaVSe_3$ containing $V^{4+}$, with strong influence on physical properties. Similarly, the iron based analogue sulfide $Ba_9Fe_3S_{11}(S_2)_2$[11] is reported and involves $2Fe^{3+}$ and $1Fe^{2+}$.

In the current study, we show the existence of the sulfide vanadium-based phase $Ba_9V_3S_{11}(S_2)_2$. The synthetic route appears more challenging than the selenide analogue as pointed by previous authors but we could isolate single crystals of this phase. Initially the single crystals were found in a preparation within the Ba-V-S-O system. Then, attempts to obtain a powder from the correct stoichiometry appeared challenging. Here, we describe its synthesis, structure solution and

refinement based on single crystal XRD, crystalline structure, DFT electronic structure and make a comparison with other vanadium-based spin chains compounds.

3. Experimental section

**Synthesis:** Single crystals of $Ba_9V_3S_{15}$ were initially found in a preparation based on the precursors BaO/BaS/V/S. A mixture of the later precursors was grounded in an agate mortar in an Argon dry-glove box. The synthesis was carried out in a cubic-anvil high-pressure apparatus. The powder of the mixture was encapsulated into closed containers made up of boron nitride (BN) sleeve, and then embedded into solid pyrophyllite which transmit pressures typically up to several GPa to the sample. Pressure was slowly raised to 5 GPa, and the temperature to 800°C, then the conditions were kept for 60 minutes. The final product was a mixture of various phases including single crystals of $Ba_9V_3S_{15}$. Our attempts to synthesize a pure product from a stoichiometric mixture of the precursors BaS, V and S in similar high-pressure and high temperature (up to 1400°C) conditions did not allow to form the phase.

**X-ray diffraction on single crystals diffraction** was performed on a Rigaku XtaLab P200 diffractometer equipped with a Dectris Pilatus 200K detector and a Mo K$\alpha$ source.

**Scanning electron microscopy (SEM)** experiments and EDX analysis were carried out on a S-3400N (Oxford instruments)

**DFT calculations** were carried out by employing the projector-augmented-wave [12,13] method encoded in the Vienna ab initio simulation package (VASP)[14] and the generalized gradient approximation (GGA) of Perdew, Burke and Ernzerhof[15] for the exchange correlation functionals. We employed GGA plus on-site repulsion U (GGA+U) method[16] to account for strong electronic correlation associated with the 3$d$ states of V using the effective on-site repulsion of $U_{eff} = U - J$ = 3 to 8 eV. A plane-wave cutoff energy of 600 eV and a threshold of the self-consistent-field energy convergence of $10^{-6}$ eV were used, with 232 k points in the irreducible Brillouin zone.

### 4. Results and discussion
### 4.1. Structure resolution

A black single crystal with a needle shape was selected for XRD data collection. The procedure is reported in table 1 with the data collection and refinement details. The unit cell parameters $a$ = 9.1979(4) Å and $c$ = 18.0462(10) Å and the space group P Ƃc2 (188) were found. The refinement was carried out using JANA2006 program based on a structure solution obtained with the charge flipping method[17]. The EDX analysis carried out on the black needle shaped single crystals (SEM image and EDX spectrum of a typical single crystal are given in **Figure S1**) led to the average atomic ratio 35.2/10.0/54.8 for Ba/V/S, respectively, in very good agreement with the refined composition $Ba_9V_3S_{15}$, (33/11/56).

The structure of $Ba_9V_3S_{11}(S_2)_2$ is shown in **Figure 11** and **12**. Atomic positions, anisotropic thermal parameters and interatomic distances are given in **Table 2**, **3** and **4**. The structure consists of chains of face sharing octahedra $VS_6$ running along the $c$-axis giving the one-dimensional character of the structure (**Figure 11.a**). The chains contain two distinct vanadium sites that show slightly different set of V-S distances (see **Table 4**) which can be related to different valencestates as will be discussed further from the DFT calculated magnetic moments. We assume a similar charge ordering tendency than the selenide analogue because we observe the same situation with a slightly higher average distance between V1 and its ligands. We however note that the difference between V1 and V2 environments is less pronounced in our case. $V1^{2+}$ is coordinated to six sulfur atoms S1 with dV1-S1 = 2.5236(34) Å and $V2^{3+}$ is coordinated to three atoms S2 and three atoms S1 with dV2-S2=2.5056(27) Å and dV2-S1=2.5292(63) Å. These V-S distances are longer than those found in $BaVS_3$, *i.e.* dV-S=2.3847(64)[18] but comparable to those found in the deficient phase $Ba_{0.5}V_8S_5$[19] (2.532 Å). $V^{4+}$ in $BaVS_3$ lead to shorter distances than in the reduced form $Ba_{0.5}V_8S_5$ and the $V^{3+}/V^{2+}$ based title phase. The arrangement of V1 and V2 within the chain is such that one octahedron $V1S_6$ alternates with two $V2S_6$, see **Figure 11.c**. Thissequence results in variable V-V separations as sketched in **Figure 11.d** which also characterize the two different magnetic exchange paths.
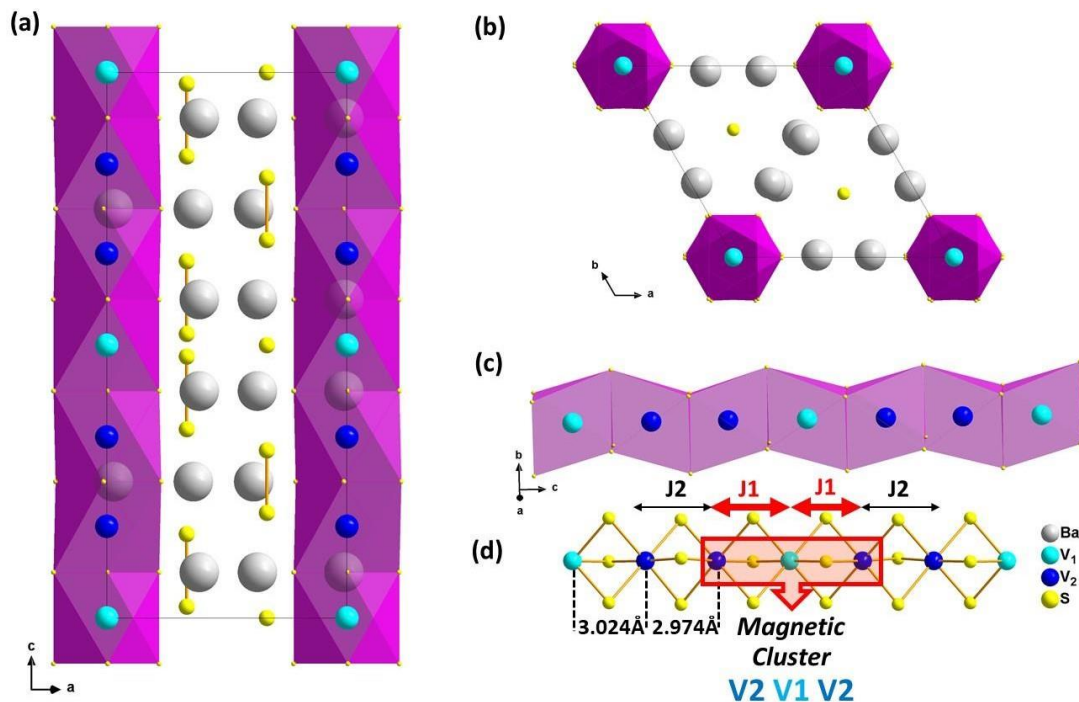
**Figure 1:** a) $Ba_9V_3S_{15}$ view along b-axis, b) $Ba_9V_3S_{15}$ view along c-axis c) $VS_6$ based one-dimensional chain d) arrangement of V1 and V2 in the spin chain showing strong J1 (magnetic coupling for V1-V2) and far weaker J2 (for V2-V2) magnetic exchange couplings. This interplay between J1 and J2 defines magnetic clusters with the sequence (V2-V1-V2).

The $VS_6$ based chains are arranged in a triangular lattice manner in the *ab* plane as shown in **Figure 1.c** and as found in $Ba_9V_3Se_{15}$. The space between the chains is occupied by barium cations surrounding sulfur-based columns running along the same direction than the chains. Two types of columns can be distinguished, see **Figure 2.a**. In the first column, S4 is half occupied (from this position S4-S4 distances of 0.7047(8) Å are generated). An ordered vision of those S4 sites to avoid short distances lead to either the formation of a disulfide pair with the adjacent S3 site, $d_{S3-S4}$ = 2.4038(65) Å, S3 distant of 3.4685(51) Å from next sulfur atom, an ordered scenario is given in **Figure 2.d**. In the second one, isolated $S^{2-}$ anions S6 alternate with $(S_2)^{2-}$ disulfide pairs S5-S5 with a distance of 2.0663(33) Å. S6 is located in a $Ba1_6$ octahedron **Figure 2.b** The distances found within the disulfide pairs are comparable with those found in the iron based isotype $Ba_9Fe_3S_{15}$[20] with 2.037 and 2.547 Å for the shortest and the longest respectively.
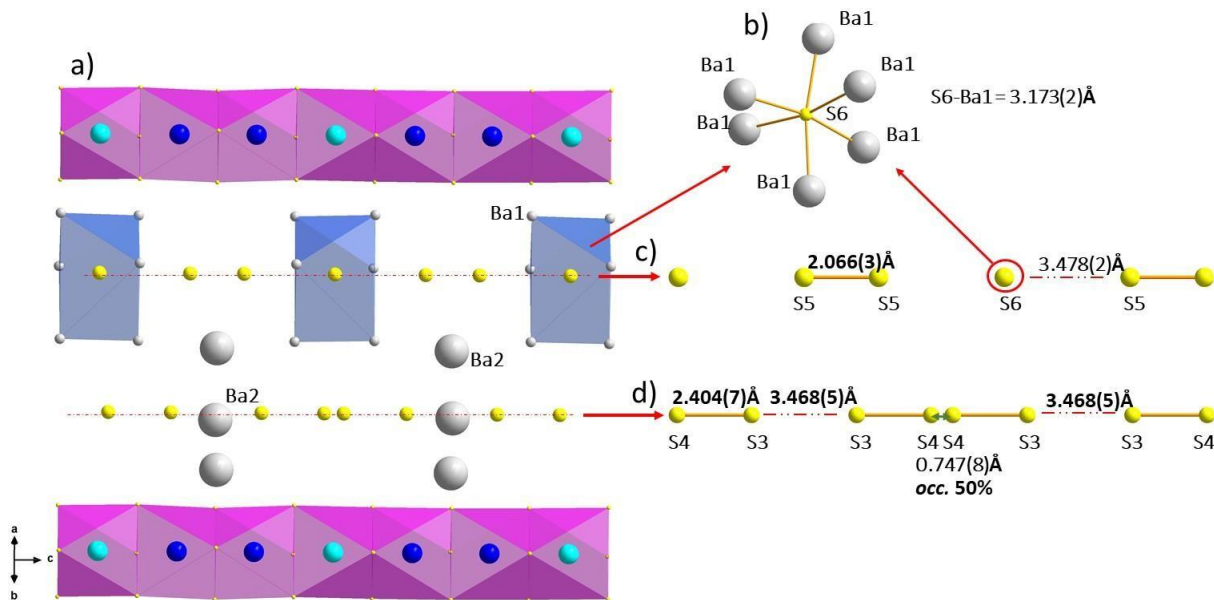
**Figure 2:** *a) View of Ba₉V₃S₁₅, b) octahedron SBa₆ geometry, c-d) distribution of disulfide pairs and isolated sulfur anions within the columns*

## 4.2. Sulfur distribution within the columns

The columns arrangement described above is slightly different from the one found in the selenide phase Ba₉V₃Se₁₅ as depicted in **Figure 3**. In the selenide phase, column 1 is ordered with diselenide pairs made of selenium atoms from a common 4*h* position and an isolated selenide in a 2*c* position. The disorder is found in column 2 with a split Se site inducing a Se-Se distance of ~1.90 Å imposing half occupancy, this site alternates with a fully occupied distinct 4*i* site, an ordered scenario imposes alternating diselenide pairs and isolated Se anions. Therefore, the two compounds are not isostructural due to different Wyckoff positions involved in the chalcogenide columns although they show the same symmetry, unit cell and framework (chains and Ba atoms). They can be considered as polymorphs. On another hand, Ba₉Fe₃S₁₅ is isostructural with the selenide phase with a similar sites distribution between column 1 and 2. We note however that the shortest/longest dichalcogenides pairs distances are found in column (1)/(2) in the Fe-compound while they are found in column (2)/(1) in the selenide phase.

***Figure 3***: *Comparison between the title phase and the selenide $Ba_9V_3Se_{15}$ highlighting the subtle difference of the arrangement within the (d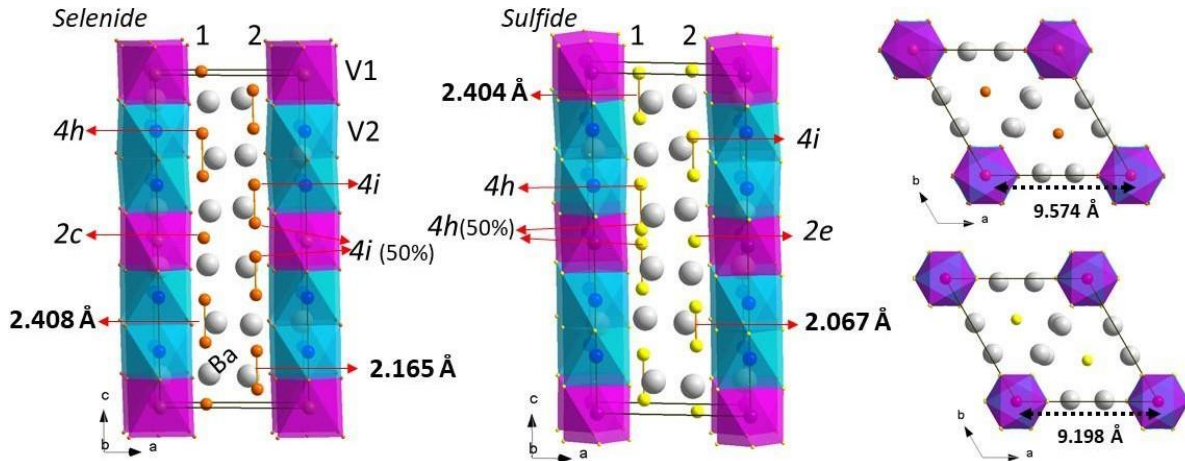i)chalcogenides columns. On the right, projections in the ab plan showing the distances between two adjacent chains in both phases*

## 4.3. DFT calculations

The electronic structure of the title phase was investigated using GGA+U calculations, the band structure and projected density of states are represented in **Figure 4**. The magnetic configurations considered in DFT+*U* here yield insulating states, we thus assume a magnetic insulator for the rest of the discussion. We have investigated several magnetic configurations including those studied by Zhang *et al.* for the selenide with similar $U_{eff}$= 5 value. Table 5 gathers the magnetic moments obtained for V1 and V2 for the different magnetic configurations. The FM gives 2.27 and 2.49 µB for V1 and V2, respectively, while the introduction of AFM interactions inverses the tendency and increases the difference between µ(V1) and µ(V2). For instance, the FIM configuration exhibits 2.74 and -2.20 µB for V1 and V2, respectively. For the selenide, 2.59 and -2.00 µB are reported for the FIM leading to a description of spin states for V1 and V2 being approximately $S_1$= 3/2 and $S_2$= 1. We can propose a similar scenario for all AFM-containing configurations but it doesn't hold for the FM. Regarding the band structure, its description is based on a lowered symmetry in *P*3*c*1 induced by the ordered structure that we built for the calculation (considering the split half occupied sulfur site). The structure was not relaxed to avoid slight geometrical changes in the spin chain especially in the lowered symmetry, that may affect

192

the magnetic exchanges. Focusing on the top of the valence band (VB) and bottom of the conduction band (CB), the bands are flat except in the $\Gamma \rightarrow A$ direction, *i.e.* the $k_z$ direction (of the chains) where they are more dispersed thus reflecting the quasi-1D structure. On another hand, the PDOS allow visualizing the contribution of the different anionic species if we consider separately the $S^{2-}$ of the $VS_6$ octahedra, the disulfide pairs ($S_2$) and the isolated sulfur within the interchain space. The $S_{(VS6)}$ states are hybridized with the vanadium states in the range of about -4.6 eV up to the Fermi level. The other anionic species have weak interactions with the framework. The two types of disulfide pairs with 2.0602(1) Å and 2.4404(1) Å S-S distances, show roughly similar DOS topologies but with different split in the major peaks and a higher dispersion for the shorter distance pair as expected from the stronger interaction within it.
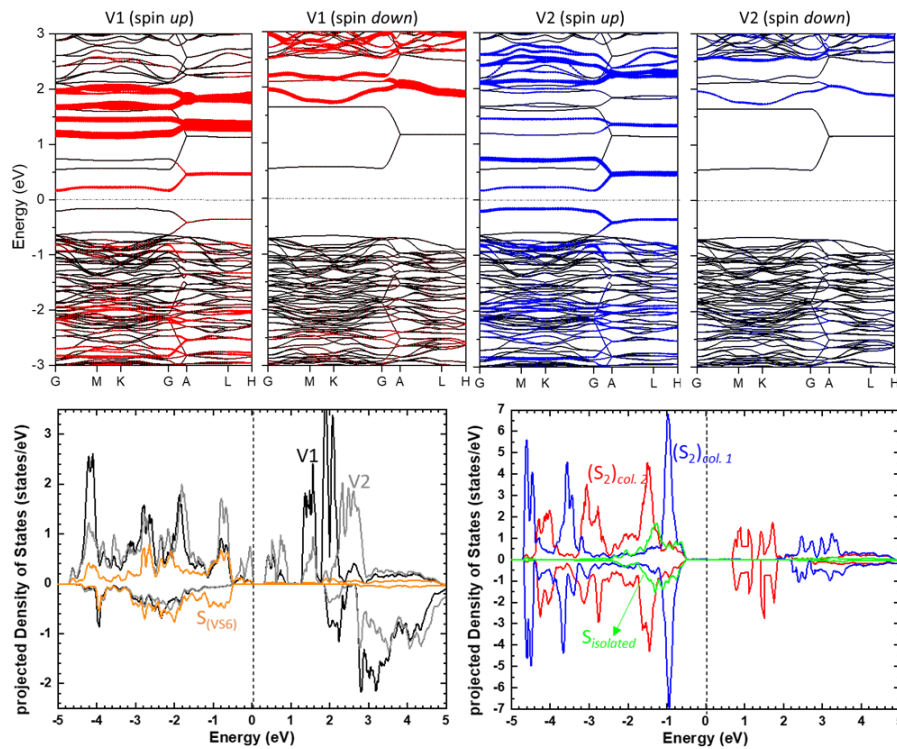


**Figure 4:** *Total band structure and fat bands (in red for V1 and blue for V2) (top). Projected density of states (PDOS) of $Ba_9V_3S_{15}$ (bottom)*

Using the procedure detailed in the supplementary information and the magnetic configurations represented in **Figure 5**, we extracted from our DFT+U calculations the magnetic interactions constants $J1$ = 77.66 meV and $J2$ = 2.15 meV, considering $U_{eff}$= 5 eV as used for the selenide (see

Table 6 for geometrical details of J1 and J2). We consider decoupled 1D spin chains with negligible interactions and estimate the intra-chain couplings. For the title phase, the calculated J and the relative energies of the magnetic configurations are dependent on the U choice, with J1 AFM below U= 3 eV and FM above. The ferromagnetic configuration becomes the most stable for U > 3eV and up to U= 8eV the same tendency is observed. For the later range, J1 is much stronger in magnitude than J2, which allow to use a similar *cluster* description $V(2)$-$V(1)$-$V(2)$ than for the selenide study[21] . Strong J1 interactions between V1 and V2 define the magnetic cluster while weak J2 (V2-V2 interactions) link those clusters (**see Figure 1. d**). Here, in absence of magnetic measurements it is difficult to draw conclusions on the expected behavior. Indeed, the reported magnetic systems in Ba-V-*X* (*X*= S, Se) show complex behaviors with multiple phenomena occurring upon temperature and pressure and their behaviors can be easily modified or suppressed upon slight chemical variations (doping, vacancies) as illustrated in the introduction. One more example is $Ba_{1-x}Sr_xVS_3$ that show an abrupt onset of ferromagnetic (FM) order at x=0.07[22].The magnetic cluster description should be a reasonable vision while further statements would need confrontation with experimental data.



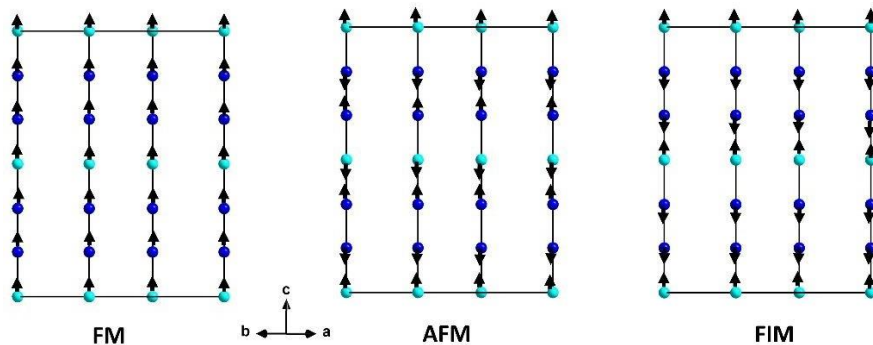**Figure 5:** *Different magnetic configurations of $Ba_9V_3S_{15}$ used in the DFT+U calculations. V1 is in light blue and V2 in dark blue, arrows represent spin up ( ↑) and spin down (↓).*

## 5. Conclusion

The new phase $Ba_9V_3S_{15}$ could be stabilized using high pressure and high temperature in the form of single crystals. It belongs to the one-dimensional magnetic system $Ba_9M_3X_{15}$ ($M=$ V, Fe and $X=$ S, Se) that exhibits chains made of face-sharing $MX_6$ octahedra as found in $BaVX_3$ (X= chalcogenide). Two major structural features differentiate those two structural types: two distinct $M$ sites are present in the former's chains while one site defines the chains in the later. Then, a higher separation between the magnetic chains with more complex interspace is found for $Ba_9M_3X_{15}$. It is made of columns of dichalcogenide pairs and chalcogenide anions alternating and surrounded by Barium cations. We show that the columns occupation by sulfur species is slightly different in the sulfide compared to the selenide, making them polymorphs and not isostructural. Within the $Ba_9M_3X_{15}$ ($M=$ V, Fe and $X=$ S, Se), $Ba_9V_3S_{15}$ was targeted in previous work, we show here its experimental realization in the form of single crystals within a complex mixture. Using first-principles calculations, we show the formation of magnetic clusters within the spin chains. Then, extensive synthetic efforts are required to reach a polycrystalline sample of this metastable phase to experimentally investigate this hypothesis.

CCDC Deposition Number 2051748 contains the **supplementary crystallographic data** for the compound $Ba_9V_3S_{11}(S_2)_2$. These data are provided free of charge by the joint Cambridge Crystallographic Data Centre and Fachinformationszentrum Karlsruhe Access Structures service www.ccdc.cam.ac.uk/structures.

**KEYWORDS:** high pressure chemistry, mixed-valent compounds, DFT, polychalcogenides, spin chains

***Table 1**. Data collection and refinement details*

| Formula | $Ba_9V_3S_{15}$ |
|---|---|
| Molecular weight (g. mol$^{-1}$) | 1869.8 |
| Symmetry | *Hexagonal* |
| Space group | P -6 c 2 (188) |
| Unit cell dimensions (Å) | a = 9.1979(4) |
| | c=18.0462(10) |
| Volume (Å$^3$) | 1322.19(11) |
| Z | 2 |
| Data Collection | |
| Equipment | Rigaku XtaLab P200 |
| Λ [Mo K$_\alpha$; Å] | 0.71073 |
| Calculated density (g cm$^{-3}$) | 4.6965 |
| Crystal shape | Needle |
| Crystal dimensions ($\mu$m) | 79×10×5 |
| Color | Black |
| Absorption correction | Analytical |
| Scan mode | ω, φ |
| θ (min–max) (°) | 2.26-30.74 |
| $\mu$ (mm$-1$ ; for λ Kα = 0.56087Å) | 15.343 |
| F(000) | 1626 |
| Reciprocal space recording | −8 ≤ h ≤ 13 |
| | −13 ≤ k ≤ 10 |
| | −25 ≤ l ≤ 24 |
| No. of measured reflections | 7128 |

| | |
|---|---|
| No. of independent reflections | 1315 |
| I > 3σ(I) (total) | 1222 |
| Refinement | |
| Number of refined parameters | 46 |
| Refinement method | Least-squares |
| Weighting scheme | Sigma |
| R1(F) [I > 3σ(I)]/R1(F$^2$) (all data, %) | 0.0298/0.0327 |
| wR2(F$^2$) [I > 3σ(I)]/wR2(F$^2$) (all data, %) | 0.0888/0.0909 |
| Goodness of Fit | 1.70 |
| Max/Min residual electronic density (e$^-$/Å$^3$) | 1.97/ -3.11 |

**Table 2.** *Atomic positions and isotropic thermal displacement for Ba$_9$V$_3$S$_{15}$*

| Atom | Wyck. | S.O.F | X | Y | Z | U$_{eq}$ |
|---|---|---|---|---|---|---|
| Ba1 | 12l | | 0.62727(8) | 0.01242(13) | 0.08393(2) | 0.0136(2) |
| Ba2 | 6k | | 0.02774(8) | 0.38827(9) | 1/4 | 0.0108(3) |
| V1 | 2a | | 0.00000 | 0.00000 | 0.00000 | 0.0101(7) |
| V2 | 4g | | 0.00000 | 0.00000 | 0.16808(12) | 0.0109(5) |
| S1 | 12l | | 0.2177(4) | -0.0039(8) | 0.08378(9) | 0.0122(9) |
| S2 | 6k | | 0.2262(4) | 0.2131(5) | 1/4 | 0.0117(11) |
| S3 | 4i | | 0.333333 | 0.666667 | 0.1539(2) | 0.0281(11) |
| S4 | 4h | 0.5 | 0.333333 | 0.666667 | 0.0207(3) | 0.0204(16) |
| S5 | 4g | | 0.666667 | 0.333333 | 0.19275(13) | 0.0015(5) |
| S6 | 2e | | 0.666667 | 0.3333333 | 0.00000 | 0.0043(8) |

**Table 3.** *ADP harmonic parameters Uij (Å²) for Ba₉V₃S₁₅*

| Atom | $U_{11}$ | $U_{22}$ | $U_{33}$ | $U_{12}$ | $U_{13}$ | $U_{23}$ |
|------|----------|----------|----------|----------|----------|----------|
| Ba1 | 0.0130(3) | 0.0133(3) | 0.0164(3) | 0.0079(3) | 0.00097(15) | 0.00170(12) |
| Ba2 | 0.0069(4) | 0.0105(3) | 0.0158(3) | 0.0050(3) | 0.00000 | 0.00000 |
| V1 | 0.0108(8) | 0.0108(8) | 0.0087(13) | 0.0054(4) | 0.00000 | 0.00000 |
| V2 | 0.0096(5) | 0.0096(5) | 0.0134(9) | 0.0048(3) | 0.00000 | 0.00000 |
| S1 | 0.0110(13) | 0.0107(8) | 0.0134(8) | 0.0044(13) | 0.0013(6) | 0.0008(4) |
| S2 | 0.0097(16) | 0.0117(15) | 0.0152(11) | 0.0064(10) | 0.00000 | 0.00000 |
| S3 | 0.0208(12) | 0.0208(12) | 0.043(2) | 0.0104(6) | 0.00000 | 0.00000 |
| S4 | 0.0221(18) | 0.0221(18) | 0.017(3) | 0.0111(9) | 0.00000 | 0.00000 |
| S6 | 0.0027(10) | 0.0027(10) | 0.0075(15) | 0.0013(5) | 0.00000 | 0.00000 |

**Table 4.** *Main distances (Å) for Ba₉V₃S₁₅*

| Atoms 1,2 | d 1,2 (Å) | Atoms 1,2 | d 1,2 (Å) |
|-----------|-----------|-----------|-----------|
| Ba1—S2 | 3.2672(11))×2 | Ba2—S4 | 3.059(7) |
| Ba1—S4 | 3.326(4)×2 | Ba2—S6 | 3.2283(18) |
| Ba1—S5 | 2.979(5) | Ba2—S1 | 3.182(2) |
| Ba1—S5 | 3.028(5) | V1—S1 | 2.5236(62) ×6 |
| Ba1—S6 | 3.204(2) ×2 | V2—S1 | 2.5292(63) ×3 |
| Ba2—S3 | 3.1731(11) | V2—S2 | 2.5056(27) ×3 |
| Ba2—S4 | 3.006(6) | S3—S3 | 3.4685(5) |
| S4—S4 | 0.7471(77) | S3—S4 | 2.4038(65) |
| S5—S5 | 2.0663(33) | S5—S6 | 3.4784(24) |

**Table 5.** *DFT+U calculated magnetic moments for V1 and V2 on different magnetic configurations*

| $U_{eff}$= 5 eV | $\mu_{FM}$ ($\mu B$) | $\mu_{AFM}$ ($\mu B$) | $\mu_{FIM}$ ($\mu B$) |
|---|---|---|---|
| V1 | 2.27 | 2.79 | 2.74 |
| V2 | 2.49 | 2.10 | 2.20 |

**Table 6**. *Description of the geometry around J1 and J2 interactions*

| | Atom1 | Atom2 | $d_{[1,2]}$ (Å) | V-S...S-V | V-S-V (°) |
|---|---|---|---|---|---|
| J1 | V1 | V2 | 3.033(2) | V1-S1=2.524(3) | V1-S1-V2= 73.78° |
| | | | | S1-V2=2.529(6) | |
| J2 | V2 | V2 | 2.957(3) | V2-S2= 2.506(4) | V2-S2-V2= 72.32° |
| | | | | S2-V2= 2.506(4) | |

## 6. REFERENCES

(1) Y.-Y. Li, H. Wang, B.-W. Sun, Q.-Q. Ruan, Y.-L. Geng, P.-F. Liu, L. Wang, L.-M. Wu, *Cryst. Growth Des.* **2019**, *19* (2), 1190–1197.

(2) L. Zhang, D. Mei, Y. Wu, C. Shen, W. Hu, L. Zhang, J. Li, Y. Wu, X. J. He, *Solid State Chem.* **2019**, *272*, 69–77.

(3) H. A. Katori, T. Adachi, H. Ohta, S. Nakamura, A. Fuwa, *Phys. Procedia* **2015**, *75*, 552–556.

(4) N. J. Poulsen, *Mater. Res. Bull.* **1998**, *33* (2), 313–322.

(5) K. Ishida, Y. Ikeuchi, C. Tassel, H. Takatsu, C. M. Brown, H. Kageyama, *Inorganics* **2019**, *7* (5), 63.

(6) Y.-Y. Li, P.-F. Liu, L.-M. Wu, *Chem. Mater.* **2017**, *29* (12), 5259–5266.

(7) F. Liang, L. Kang, Z. Lin, Y. Wu, *Cryst. Growth Des.* **2017**, *17* (4), 2254–2289.

(8) S. Fagot, P. Foury-Leylekian, S. Ravy, J. P. Pouget, M. Anne, G. Popov, M. V. Lobanov, M. Greenblatt, *Solid State Sci.* **2005**, *7* (6), 718–725.

(9) O. Fuentes, H. Wang, B. H. Ward, J. Zhang, D. M. Proserpio, F. Calvagna, C. E. Check, K. C. Lobring, C. Zheng, *Chem. Mater.* **2001**, *13* (9), 3051–3056.

(10) J. Zhang, M. Liu, X. Wang, K. Zhao, L. J. Duan, *Phys. Condens. Matter* **2018**, *4*, 1–10.

(11) A. B. Blake, *Acta Crystallogr. Sect. B Struct. Crystallogr. Cryst. Chem.* **1982**, *38* (1), 348–349.

(12) P. E. Blöchl, *Phys. Rev. B* **1994**, *50* (24), 17953–17979.

(13) G. Kresse, D. Joubert, *Phys. Rev. B* **1999**, *59* (3), 1758–1775.

(14) G. Kresse, D. Vogtenhuber, M. Marsman, M. Kaltak, F. Karsai, M. Schlipf, Vienna ab-initio simulation package (VASP) https://www.vasp.at.

(15) J. P. Perdew, K. Burke, M. Ernzerhof, *Phys. Rev. Lett.* **1996**, *77* (18), 3865–3868.

*(16)* S. L. Dudarev, G. A. Botton, S. Y. Savrasov, C. J. Humphreys, A. P. Sutton, *Phys. Rev. B* **1998**, *57* (3), 1505–1509.

(17) V. Petříček, M. Dušek, L. Palatinus, *Zeitschrift für Krist. - Cryst. Mater.* **2014**, *229* (5), 345–352.

*(18)* R. A. Gardner, M. Vlasse, A. Wold, *Acta Crystallogr. Sect. B Struct. Crystallogr. Cryst. Chem.* **1969**, *25* (4), 781–787.

(19) S. PETRICEK, H. BOLLER, K. KLEPP, *Solid State Ionics* **1995**, *81* (3–4), 183–188.

(20) H. Y. Hong, H. J. Steinfink, *Solid State Chem.* **1972**, *5* (1), 93–104.

(21) P. Foury-Leylekian, P. Leininger, V. Ilakovac, Y. Joly, S. Bernu, S. Fagot, J. Pouget, *Phys. B Condens. Matter* **2012**, *407* (11), 1692–1695.

*(22)* A. Gauzzi, N. Barišic, F. Licci, G. Calestani, F. Bolzoni, P. Fazekas, E. Gilioli, L. Forró, *cond-mat* **2006**, *1*, 2–5.
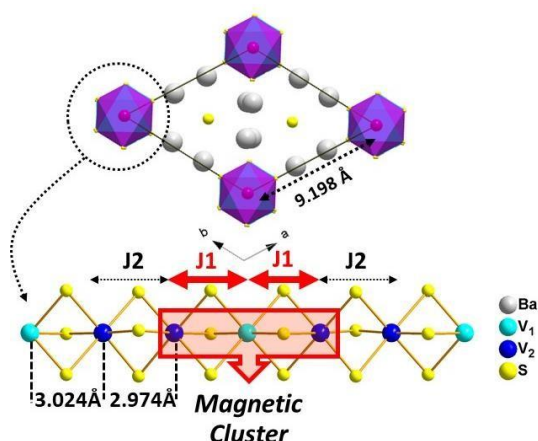
7.  Supplementary information

To estimate the relative energy scales of the spin chains, we have mapped the total energies of the magnetic configurations represented below into an effective 1D Heisenberg model:

$$H = E_0 - \sum_{i<j} J_{ij} \vec{S_i} \vec{S_j}$$

$E$0: sum of the nonmagnetic part

$Jij$: the exchange interactions between spin $Si$ and $Sj$ at sites $i$ and $j$, respectively.

The positive (negative) $Jij$ represents FM (AFM) coupling. Here, we only give the intra-chain exchange couplings $J$1 between the nearest neighboring $V$1–$V$2 and $J$2 for $V$2–$V$2 (next nearest neighbors), both are super-exchanges (SE) paths. The inter-chain exchange interactions are negligible because of the very long inter-chain distance. For one formula unit, the total energies associated with different magnetic orders can be written as:

1.  $E$ (FM) = $E_0 - 4\,J_1S_1S_2 - 2\,J_2S_2{}^2$

2. $E\,(\text{AFM}) = E_0 + 4\,J_1 S_1 S_2 + 2\,J_2 S_{\frac{2}{2}}$,

3. $E\,(\text{FIM}) = E_0 + 4\,J_1 S_1 S_2 - 2\,J_2 S_{\frac{2}{2}}$

Here, we use $S1 = 3/2$ and $S2 = 1$ for $V1$ and $V2$-ions, respectively, accordingly with the charge ordering assumed in this work ($V1^{2+}$ and $V2^{3+}$). The later allows the J calculations using defined spin state on each site. Then, from the above equations, we obtain the magnetic interactions $J1$ and $J2$.

**Table S1.** *Relative energies of the magnetic configurations (eV), the most stable one is set to 0.*

| U *eff* | $E_{FM}$ (eV) | $E_{AFM}$ (eV) | $E_{FIM}$ (eV) | J1 (meV) | J2 (meV) |
|---|---|---|---|---|---|
| $U_{eff}$= 5 eV | 0 | 0.48 | 0.47 | 77.66 | 2.15 |
| $U_{eff}$= 7 eV | 0 | 0.17 | 0.14 | 23.83 | 5.07 |
| $U_{eff}$= 8 eV | 0 | 0.12 | 0.10 | 16.93 | 2.925 |
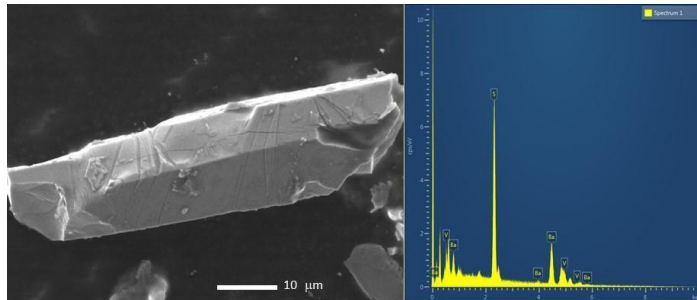


**Figure S1.** *Scanning Electron Microscope image of a typical single crystal of $Ba_9V_3S_{11}(S_2)_2$ and a spectrum of the EDX*

# Chapter V
# The first halide-thio-Apatites

# V. Chapter V: The first halide-thio-Apatites

## Introduction

The possibility of controlling the band gap and the optical properties by anionic manipulation is highlighted in chapter 2. By increasing the S/O ratio, the band gap decrease and consequently the absorption wavelength increase. In this thesis, all discovered optical compounds having thio-vanadate entities absorb in visible light range. This can be useful for many applications. For example, the photoelectric active material which absorb in the visible light range require less energy and are active under solar light.

Apatite $Ba_5(VO_4)_3X$ (X=Halide anion) with wide band gap are characterized by the disconnected tetrahedra $VO_4$ for which we managed the partial substitution of oxygen by sulfide anions. In the following chapter, a halide-thio-apatite series is reported for the first time. All synthesized powders absorb in the visible light range. The photoelectric measurement proves a photo-activated transport that depends on both O/S ratio and halide type.

The crystallographic comparison of three single crystal structures with X=Cl but, shows a correlation between different O/S ratio and degree of disorder. New perspectives are opened in the extended field of Apatite and their applications.

1. Abstract

The new thio-Apatite $Ba_5 (VO_{4-\alpha}S_\alpha)_3X$ (X: F, Cl, I) series of compounds was prepared and characterized. Compared to known Apatite phases having unconnected vanadate $VO_4$ groups separated by Ba cations delimiting halide-filled channels, their crystal structure is built from heteroleptic thiovanadates $VO_{4-\alpha}S_\alpha$. Here, the strategy consisting in incorporating a chalcogenide anion aims at raising the valence band to bring the band gap to the visible range in order to reach materials photoactive under visible light. Both the halide anion nature and S/O ratio impact the materials photoconductivity. While the photoconduction is comparable to that found in $Pb_5 (VO_4)_3I$, a short carrier lifetime is detected as well as a shift of the activity toward the visible-light. This Apatite series combining thiovanadates and halide-filled channels open new perspectives in the extended field of Apatite and their applications.

2. Introduction

Anionic species by their characteristic differentiation can afford unusual properties to mixed anion compounds. The large range of properties (superconductivity[1], non-linear optical[2], thermoelectric[3], magnetic[4],…) found among mixed anion compounds make them suitable for functional materials design. Theoretical calculations show that the valence band maximum is dictated mainly by hybridized orbital anions. A less electronegative anion will raise the valence band maximum. Therefore, they offer great possibilities to engineer the band gap by anionic manipulation. While oxynitrides[5] have been developed for decades now and are known to allow a photocatalytic activity for water-splitting in the visible range, a few oxysulfides have recently shown promising activities while being stable [5,6] like in $Y_2Ti_2O_5S_2$ [6] and $LaOInS_2$[7]. Dealing with oxychalcogenides, a few low-dimensional compounds are reported with thiovanadates. They constitute a great playground for band gap engineering based on the thiovanadate[8] species with all possible S/O ratios. For example, in $Ba_6V_4O_5S_{11}$ which formula can be decomposed as $Ba_6(VO_2S_2)_2(VS_3O)(VS_4)$, the density of states projected on the various thiovanadates units shows their tendency to contribute more in the top of the valence band when the sulfur content is increased (from $VO_3S \rightarrow VS_4$)[9]. This type of heteroleptic environment (at least two types of anions) around the active cation increase the local acentricity and the polarity in case of polar structures. In the later the increased built-in electrical field allow enhancing numerous properties

194

including photoelectric response by allowing a better charge carriers separation, however, mixed anion has been barely explored to that purpose. Apatites $M_{10}(AO_4)_6X_2$ (*M* and *A*: cationic sites with *A* in unconnected tetrahedral $AO_4$) and *X*: channel's anionic site such as a halide) are very common compounds which exhibit two anionic sites of different nature. They exhibit useful properties with various practical applications such as fertilizers, food additives, and bioceramics but also as catalysts and fluorescent host materials. On another hand, $Pb_5(VO_4)X$ (*X*= F, Cl, Br, I) apatites have been recently reported with light absorption properties which opens new perspectives in this family. Among those phases, the iodide-phase have its band gap of 2.7 eV in the visible range due to the contribution of the I $5p$ states at the top of the valence band. It shows a visible light response as a photoanode for photoelectric conversion. In this work, we adopt a strategy based on the insertion of sulfide anions in oxy-halide apatites in order to achieve band gaps in the visible light and so their photoactivity. It led to a new halide-thio-Apatites family $Ba_5(VO_{4-\delta}S_\delta)X$ (*X*= F, Cl, Br, I) which contain thiovanadate groups instead of vanadate groups. We present their structures, optical and photoelectric properties.

3. Experimental section

**Synthesis**: The powders were obtained from a stoichiometric mixture of BaO, $BaX_2$ ($BaCl_2$, BaI2 and $BaF_2$), $V_2O_5$, V and S pressed into pellets and heated in an evacuated sealed quartz tube. The heat treatment consisted in heating up to 450°C at the rate of 22°C/h for 5 hours, then heating up to 750°C at the rate of 30°C/h for 24 hours cooling down to 650°C at a 5°C/h rate, temperature at which the furnace was switched off.

**X-ray diffraction on single crystals** was performed on an X8 diffractometer equipped with a two-dimensional (2D) CCD 4K detector and an Ag $K_\alpha$ or Mo $K_\alpha$ source was used.

**The powder XRD** patterns were collected on a Bruker D8 diffractometer equipped with a Lynxeye linear detector (Cu Kα) in Bragg–Brentano geometry at room temperature.

**Scanning electron microscopy (SEM)** experiments and EDX analysis were carried out on a Hitachi S400N microscope.

**UV–Visible Measurements.** The reflectance of the sample was measured from 250 to 800 nm on a PerkinElmer Lambda 650 device.

**Photo-electrochemical Measurements.** The photocurrents and Mott-Schottky plots were measured by an electrochemical device (Autolab PGSTAT204, Metrohm) coupled to a LEDmodule (LED Driver kit, Metrohm). LEDs with low spectral dispersion are calibrated with the helpof a photodiode to determine the density of the luminous flux received by the sample. Three electrodes were used for the measurements, including Ag/AgCl and Pt wire acted as reference electrode and counter electrode, respectively. The working electrode was prepared using the drop-casting method. For this, 20 mg of sample is mixed with Polyvinylidene fluoride (PVDF) binder with 1:0.5 weight ratio. The homogeneous mixture is then coated on a Indium Tin Oxide (ITO) glass wafer. Finally, the photoelectrode is dried at 90°C for 30 min before being placed in a photoelectrochemical cell. The electrolyte was 0.1 M $Na_2SO_4$ aqueous solution (pH = 7). The Mott-Schottky curves were recorded at 1 kHz and the applied bias voltage was 0.2 V in the current-time curves.

4. Results and Discussion
## 4.1. Structures resolution and description

XRD data collections were carried out on selected orange or red single crystals found in the different preparations targeting compositions $Ba_5(VO_3S)X$ (*X*= F, Cl, I). Later, compositions with $(VO_2S_2)$ for the O/S ratio around vanadium will be discussed from powder data. Three single crystals from different preparations with *X*= Cl were studied and their structures solved in the hexagonal symmetry in space group P $6_3$/*mcm* (193). Surprisingly, they yield slightly different O/S ratio in the range of the targeted one. In comparison, the oxide analogue $Ba_5(V O_4)_3Cl$ crystallizes in the less symmetric P$6_3$/m space group. As we will see later, our structure is an average one because a modulation was suspected.. but it turns out that the additional spots are not due to modulations but to the crystal quality (additional crystals "stuck" on the main crystal). Here we see that the incorporation of sulfur impacts the symmetry although the Apatite type is preserved. The main differences between the Chlorine phases crystals are listed in Table 1. For clarity, those crystals are called c1, c2 and c3 respectively, the sulfur content is increased from c1 to c3. Their data collection and refinement details are given in Table 2 .The treatment of the data was

performed with Jana2006[10] and charge flipping[11] for structural solution and least squares method for refinement.

It is important to mention here the examination of the precession images constructed in the 0kl, h0l and hk0 planes (Figure 3). While they are consistent with our unit cell choice, they also allowed us to point weak additional reflections. At this stage, we present refinements on the average structures which are of good quality.

The common structure type of the three phases within the new family $Ba_5(VO_{4-\alpha}S_\alpha)_3Cl$, belongs to the well-known halide-apatite type with general formula $M_5(M'O_4)_3X$ ($M$ = divalent cation such as an alkaline earth, $Pb^{2+}$ etc…, $M'$ = pentavalent cation, and $X$ = F, Cl, Br or OH). The later is constituted by disconnected vanadate groups separated by $Ba^{2+}$ cations and delimiting channels occupied by halide anions. In the new series we present here, the vanadate groups are replaced by thiovanadates ($VO_{4-\alpha}S_\alpha$) which exhibit O/S environment around $V^{5+}$. The unit cell is shown in Figure 1.a. The $Ba^{2+}$ cations are located in two different crystallographic sites, while Vanadium atoms are defined with one site. There are two distinct anionic sites coordinating $V^{5+}$. O1(S1) is disordered with mixed O/S occupancy while O2 is fully occupied by oxygen. Depending on the O/S ratio, a possible splitting of Ba2 and Cl1 atoms into two positions is observed. When Sulfur content increase, the mean V1-(O1/S1), and Ba2-(O1/S1) distances slightly increases (as well as the volume of the unit cell) accordingly, as expected from the greater $S^{2-}$ ionic radii. During the refinement, the great anisotropic elongation of the thermal parameter of Cl within the channel was such that a split position (into two sites half occupied) was required to best describe the two compositions with less oxygen content. For the highest ratio O/S found ($\alpha$=0.966) both atoms Ba2 and Cl1 are split into two positions. Then for crystal c2, when O/S decrease, only Cl1 is split. For c3 with lowest O/S ratio, no split position was observed, but the reliability factor slightly increased.

Taking the case of $\alpha$=1.437 with greater sulfur incorporation (no split positions), Ba2 is coordinated to two Cl, two O1/S1 and two S2 atoms. In the case of $\alpha$=1.123, the split Cl lead to the $d_{Ba2-Cl1}$=3.09(2) Å (x2) distances with no Ba2 split. For $\alpha$=0.966, Cl is split into two positions as well as Ba2. The tendency is clearly that the more sulfur content, the more ordered the structure

197

is in the average structure within $P6_3/mcm$ space group. However, the reliability factors are slightly increasing indicating the limits of the description in the average structure. In C3, the most ordered case, the halide anions are coordinated by six Barium atoms (**Figure 1.b**) with $d_{Ba-Cl}$ =3.392(2) Å, This value is slightly longer than that found in $Ba_5(VO_4)_3Cl$[12] $d_{Ba-Cl}$ = 3.288(1) Å. Shorter distance is found in C2 where Cl is split into two positions $d_{Ba-Cl}$ =3.09(2)x2 Å. In the thiovanadate species $VO_{4-\alpha}S_\alpha$ (Figure 1.c) $d_{V-O}$ ranges from 1.688(7) to 1.696(112) Å. These values are in the range expected as found for other thiovanadate compounds (for instance $d_{V-O}$= 1.68 Å in $Ba_5 (VO_2S_2)_2(S$ )[8] and $d_{V-O}$ = 1.66 Å in $Ba_{15}V_{12}S_{34}O_3$[13]). For the disordered site O/S, $d_{V-(O/S)}$ was found between 2.001(3) and 2.046(7) Å. The distance is directly related to the O/S ratio and its value lying between the value expected for $V^{5+}$-O and the one expected for $V^{5+}$-S. Ba1 atom exclusively coordinated to oxygen atoms to form a regular $BaO_6$ octahedra with six Ba–O of 2.841(7) Å. Cell parameters and volume evolution with variation of sulfur percentage are plotted in Figure 2. Atomic Positions and Isotropic Thermal Displacement, Anisotropic Thermal Parameters Uij (Å2) and main distances for C1, C2 and C3 are listed in Table 3, Table 4 and Table5, respectively. In table 10, EDS analysis was carried out on different crystals of the Chlorine- crystals, C1 and C3 are reported and show good agreement between the theoretical ratios and EDS ratios.

For the fluorine-crystal, we index a unit cell which seems to correspond to a superstructure of the oxide $Ba_5(VO_4)_3F$ crystallizing in $P6_3/m$ (a= 10.333(5) Å, c= 7.697(7) Å). The structure could be solved and refined in a trigonal symmetry in space group $P$-$3m1$ (164) and is still related to the Apatite type. We note here that several space groups were tested with reasonable results found in $P6_3$ and $P6_3mc$, however, they were ruled out because of residual problems, higher reliability factors and no justification for the non-centrosymmetry. More into details of the structure, the only disorder within the structure is observed for some Ba atoms. Three of the five Ba locations (Ba1, Ba4 and Ba5) are disordered with an additional close position with complementary occupancy (Ba1a, Ba4a and Ba5a, respectively). Fluoride atoms occupy four different crystallographic sites into two types of channels. F1 and F2 are partially filled with complementary occupation to avoid their too short distance. the Ba-F distance found is in the range 2.554(6)-2.605(8) Å, those values are included in the range of distance found in

$Ba_5(VO_4)_3F^{14}$ with $d_{Ba-F}$ =2.489(16) and 2.768(68) Å. The heteroleptic $VO_3S$ tetrahedra are here fully ordered with no mixed O/S sites and with distances $d_{V-S}$ ranging from 2.081(8) to 2.198(7)Å and $d_{V-O}$ distances ranging from 1.694(15) to 1.909(10) Å.

A single crystal for with X= Iodide could be also collected. The same unit cell type than the Fluorine case just described is found and the structure could be solved in the same space group *P*-3*m*1 with a=18.4866(10) Å and c=8.6695(9) Å. However, at this stage a complex disorder has to be treated within the channels which requires improved crystal quality and data collection. This is under progress; thus, we will not present this phase in detail.
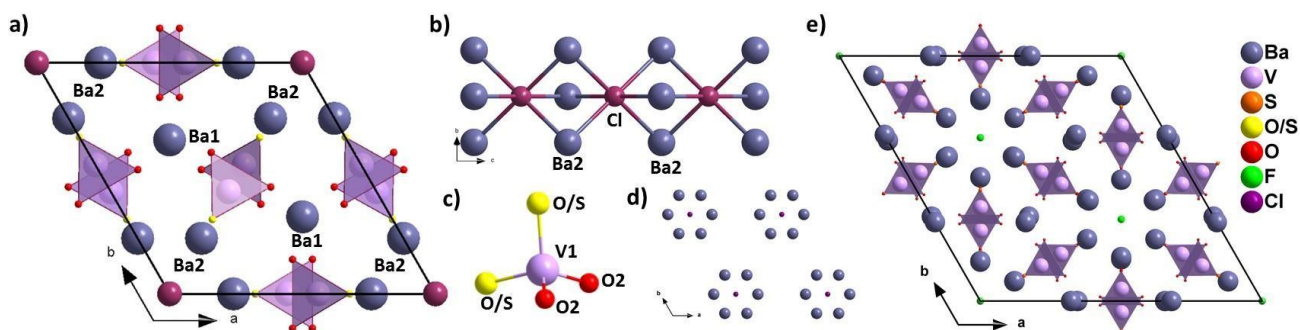


**Figure 1.** a) Simple thio-apatite unit cell projected along c-axis for the most ordered phase $Ba_5V_3O_{7.869}S_{4.131}Cl$. b) Chloride environment: $ClBa_6$ connected polyhedra. c) Disordered thio-vanadate tetrahedra $VO_2(O/S)_2$. d) View of channels occupied by chloride anion. e) unit-cell of $Ba_5V_3O_9S_3F$ projected along c-axis.

**Table 1.** Main refinement data for the reported phase $Ba_5V_3O_{12}Cl$ and the three single crystals of Chloro-thio-apatites C1, C2 and C3.

| | Formula | Cell parameters Å | Space group | $R_{obs}$ | Volume (Å) | Split positions |
|---|---|---|---|---|---|---|
| | $Ba_5V_3O_{12}Cl^{12}$ | a=10.5565 c= 7.7584 | $P6_3/m$ | | 749.03 | **none** |
| C1 | $Ba_5V_3O_{9.102}S_{2.898}Cl$ | a=10.6048 c= 8.6962 | $P6_3/mcm$ | **3.98** | 846.96(6) | **Ba2** **Cl1** |
| C2 | $Ba_5V_3O_{8.632}S_{3.368}Cl$ | a= 10.5913 c= 8.8891 | $P63/mcm$ | **5.75** | 863.55(19) | **Cl1** |
| C3 | $Ba_5V_3O_{7.869}S_{4.131}Cl$ | a= 10.5935 c= 8.9630 | $P6_3/mcm$ | **6.79** | 871.09(8) | **none** |

**Figure 2.** Cell parameters and volume evolution with O/S ratio variation for $Ba_5(VO_{4-\alpha} S_\alpha)Cl$.
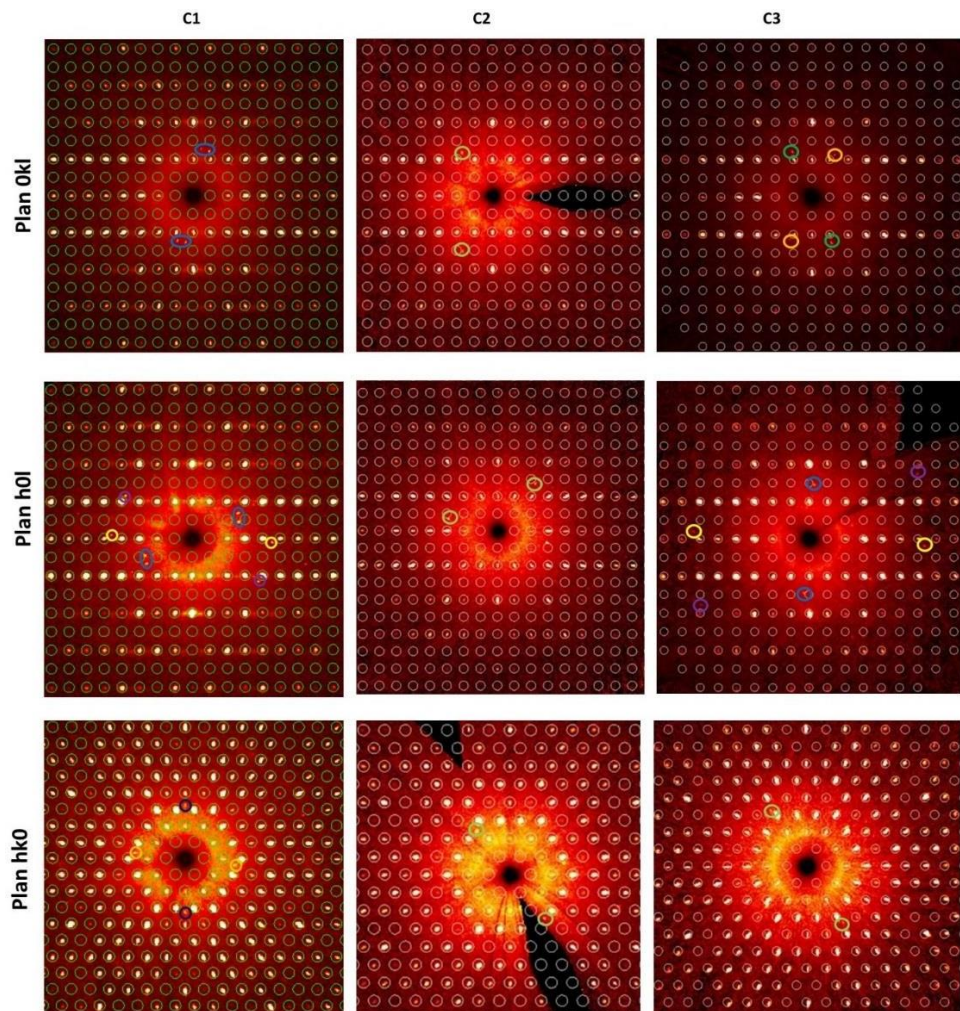
**Figure 3.** Precessions constructed in 0kl, h0l and hk0 planes from single-crystal XRD data collection for C1, C2 and C3 respectively.

**Table 2.** Data Collection and Refinement Details for crystals c1, c2 and c3 respectively.

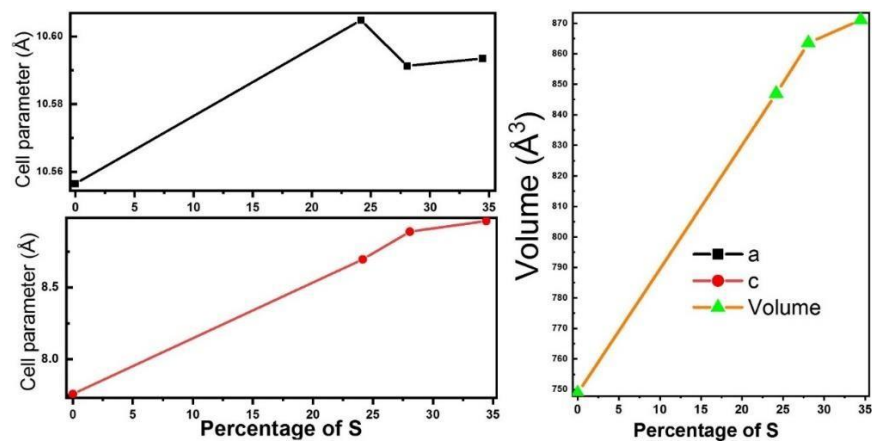| Crystal | C1 | C2 | C3 |
|---|---|---|---|
| **Formula** | $Ba_5V_3O_{9.102}S_{2.898}Cl$ | $Ba_5V_3O_{8.632}S_{3.368}Cl$ | $Ba_5V_3O_{7.869}S_{4.131}Cl$ |
| **Detailed formula** | $Ba_5(VO_{4-\delta}S_\delta)_3Cl$ | $Ba_5(VO_{4-\delta}S_\delta)_3Cl$ | $Ba_5(VO_{4-\delta}S_\delta)_3Cl$ |
| $\delta=$ | 0.966 | 1.123 | 1.437 |
| **Molecular weight (g. mol$^{-1}$)** | 1113.5 | 1121.1 | 1786.4 |
| **Symmetry** | *Hexagonal* | *hexagonal* | *Hexagonal* |
| **Space group** | P $6_3$/m c m (193) | P $6_3$/m c m (193) | P $6_3$/m c m (193) |
| **Unit cell dimensions (Å)** | a= 10.6048(3) | a=10.5913(9) | a= 10.5935(3) |
| | c= 8.6962(5) | c= 8.8891(16) | c= 8.9630(7) |
| **Volume (Å$^3$)** | 846.96(6) | 863.55(19) | 871.09(8) |
| **Z** | 2 | 2 | 2 |
| | | **Data Collection** | |
| **Equipment** | Bruker CCD (Ag Kα) | Bruker CCD (Ag Kα) | Bruker CCD (Ag Kα) |
| **Λ [Å]** | 0.56087 | 0.56087 | 0.56087 |
| **Calculated density (g cm$^{-3}$)** | 4.3662 | 4.3114 | 4.3208 |
| **Crystal shape** | Platelet | Platelet | Platelet |
| **Crystal dimensions (μm)** | 45×25×5 | 35×22×5 | 68×38×6 |
| **Color** | orange | orange | Orange |
| **Absorption correction** | analytical | analytical | Analytical |
| **Scan mode** | ω, φ | ω, φ | ω, φ |
| **θ (min–max) (°)** | 1.75- 24.4 | 1.75-18.31 | 1.75-22.5 |
| **μ (mm$^{-1}$)** | 7.129 | 7.019 | 7.002 |
| **F(000)** | 970 | 979 | 990 |
| **Reciprocal space recording** | $-15 \le h \le 14$ $-14 \le k \le 15$ $-12 \le l \le 12$ | $-11 \le h \le 11$ $-11 \le k \le 11$ $-9 \le l \le 9$ | $-14 \le h \le 14$ $-14 \le k \le 14$ $-12 \le l \le 12$ |
| **No. of measured reflections** | 42508 | 33181 | 45845 |
| **No. of independent reflections** | 545 | 256 | 451 |
| **I > 3σ(I) (total)** | 394 | 223 | 302 |
| | | **Refinement** | |
| **Number of refined parameters** | 29 | 27 | 26 |
| **Refinement method** | Least-squares | Least-squares | Least-squares |
| **Weighting scheme** | sigma | sigma | sigma |
| **R1(F) [I > 3σ(I)]/R1(F$^2$) (all data, %)** | 0.0398/0.0592 | 0.0575/0.0673 | 0.0679/0.0965 |

| | | | | | | |
|---|---|---|---|---|---|---|
| wR2(F²) [I > 3σ(I)]/wR2(F²) (all data, %) | 0.0452/0.0501 | | 0.0692/0.0708 | | 0.0794/0.0823 | |
| Goodness of Fit | 2.69 | | 4.25 | | 3.45 | |
| Max/Min residual electronic density (e⁻/Å³) | 1.34/-1.37 | | 2.61/-2.44 | | 5.36/-5.31 | |
| Tmin/tmax | 0.6916/0.7451 | | 0.6154/0.7442 | | 0.6118/0.7448 | |

**Table 3.** Atomic Positions and Isotropic Thermal Displacement for C1, C2 and C3 respectively.

| Atom | Wyck. | | x | y | z | $U_{eq}$ |
|---|---|---|---|---|---|---|
| C1-$Ba_5V_3O_{9.102}S_{2.898}$Cl | | | | | | |
| Ba1 | 4d | | 0.666667 | 0.333333 | 1 | 0.0435(3) |
| Ba2 | 12k | 0.5 | 0.24485(8) | 0.24485(8) | 0.70775(9) | 0.0336(3) |
| V1 | 6g | | 0.56277(17 | 0.56277(17) | 0.75 | 0.0460(8) |
| Cl1 | 4e | 0.5 | 0 | 0 | 0.5689(11) | 0.052(2) |
| O1 | 12k | 0.52(2) | 0.3180(3) | 0.3180(3) | 0.4283(4) | 0.0503(16) |
| S1 | 12k | 0.48(2) | 0.3180(3) | 0.3180(3) | 0.4283(4) | 0.0503(16) |
| O2 | 12j | | 0.5388(6) | 0.3930(6) | 0.75 | 0.051(3) |
| C2-$Ba_5V_3O_{8.632}S_{3.368}$Cl | | | | | | |
| Ba1 | 4d | | 0.666667 | 0.333333 | 0 | 0.0447(9) |
| Ba2 | 6g | | 0.7583(2) | 0.7583(2) | 0.25 | 0.0903(15) |
| V1 | 6g | | 0.4400(5) | 0.4400(5) | 0.25 | 0.050(2) |
| Cl1 | 4e | 0.5 | 0 | 0 | -1.444(4) | 0.10(2) |
| O1 | 12k | 0.43(5) | 0.3207(7) | 0.3207(7) | 0.4291(11) | 0.054(4) |
| S1 | 12k | 0.57(5) | 0.3207(7) | 0.3207(7) | 0.4291(11) | 0.054(4) |
| O2 | 12j | | 0.5388(6) | 0.3930(6) | 0.75 | 0.051(3) |
| C3-$Ba_5V_3O_{7.869}S_{4.131}$Cl | | | | | | |
| Ba1 | 4d | | 0.666667 | 0.333333 | 0 | 0.0396(7) |
| Ba2 | 6g | | 0.75966(17) | 0.75966(17) | 0.25 | 0.0777(11) |
| V1 | 6g | | 0.4420(4) | 0.4420(4) | 0.25 | 0.0465(19) |
| Cl1 | 2b | | 0 | 0 | 0 | 0.157(14) |
| O1 | 12k | 0.31(5) | 0.3220(6) | 0.3220(6) | 0.0712(9) | 0.057(3) |
| S1 | 12k | 0.69(5) | 0.3220(6) | 0.3220(6) | 0.0712(9) | 0.057(3) |
| O2 | 12j | | 0.6118(13) | 0.4640(13) | 0.25 | 0.049(6) |

**Table 4.** Anisotropic Thermal Parameters Uij (Å2) for c1, c2 and c3.

| Atom | $U_{11}$ | $U_{22}$ | $U_{33}$ | $U_{12}$ | $U_{13}$ | $U_{23}$ |
|---|---|---|---|---|---|---|
| | | | $C1-Ba_5V_3O_{9.102}S_{2.898}Cl$ | | | |
| Ba1 | 0.0521(4) | 0.0521(4) | 0.0265(4) | 0.0260(2) | 0 | 0 |
| Ba2 | 0.0233(3) | 0.0233(3) | 0.0448(7) | 0.0046(3) | -0.0027(3) | -0.0027(3) |
| V1 | 0.0203(6) | 0.0203(6) | 0.0927(17) | 0.0066(8) | 0 | 0 |
| Cl1 | 0.0298(19) | 0.0298(19) | 0.097(6) | 0.0149(10) | 0 | 0 |
| O1 | 0.0438(18) | 0.0438(18) | 0.049(2) | 0.0114(17) | 0.0127(13) | 0.0127(13) |
| S1 | 0.0438(18) | 0.0438(18) | 0.049(2) | 0.0114(17) | 0.0127(13) | 0.0127(13) |
| O2 | 0.025(3) | 0.030(3) | 0.103(5) | 0.016(3) | 0 | 0 |
| | | | $C2-Ba_5V_3O_{8.632}S_{3.368}Cl$ | | | |
| Ba1 | 0.0469(11) | 0.0469(11) | 0.0404(14) | 0.0234(6) | 0 | 0 |
| Ba2 | 0.0237(10) | 0.0237(10) | 0.217(4) | 0.0072(10) | 0 | 0 |
| V1 | 0.023(2) | 0.023(2) | 0.104(5) | 0.009(2) | 0 | 0 |
| Cl1 | 0.029(6) | 0.029(6) | 0.23(6) | 0.014(3) | 0 | 0 |
| O1 | 0.042(5) | 0.042(5) | 0.062(6) | 0.008(4) | 0.009(3) | 0.009(3) |
| S1 | 0.042(5) | 0.042(5) | 0.062(6) | 0.008(4) | 0.009(3) | 0.009(3) |
| O2 | 0.030(9) | 0.026(9) | 0.109(13) | 0.017(8 | 0 | 0 |
| | | | $C3-Ba_5V_3O_{7.869}S_{4.131}Cl$ | | | |
| Ba1 | 0.0431(8) | 0.0431(8) | 0.0325(10) | 0.0216(4) | 0 | 0 |
| Ba2 | 0.0279(8) | 0.0279(8) | 0.172(3) | 0.0098(8) | 0 | 0 |
| V1 | 0.0248(18) | 0.0248(18) | 0.089(4) | 0.012(2) | 0 | 0 |
| Cl1 | 0.037(5) | 0.037(5) | 0.40(4) | 0.018(3) | 0 | 0 |
| O1 | 0.048(4) | 0.048(4) | 0.064(5) | 0.016(4) | -0.017(3) | -0.017(3) |
| S1 | 0.048(4) | 0.048(4) | 0.064(5) | 0.016(4) | -0.017(3) | -0.017(3) |
| O2 | 0.030(7) | 0.027(7) | 0.092(10) | 0.015(6) | 0 | 0 |

**Table 5.** Main Distances (Å) for C1, C2 and C3.

| Atoms 1,2 | d 1,2 [Å] | Atoms 1,2 | d 1,2 [Å] |
|---|---|---|---|
| | $C1-Ba_5V_3O_{9.102}S_{2.898}Cl$ | | |
| Ba1-O2 | 2.797(5)x6 | Ba2-Cl1 | 3.242(5) |
| Ba2-O1/S1 | 2.551(3)x2 | Ba2-O2 | 2.725(5)x2 |
| Ba2-O1/S1 | 3.259(4) | V1-O1/S1 | 2.001(3)x2 |
| Ba2-O1/S1 | 3.280(5)x2 | V1-O2 | 1.688(7)x2 |
| Ba2-Cl1 | 2.863(4) | Cl1-Cl1 | 1.200(12) |
| | $C2-Ba_5V_3O_{8.632}S_{3.368}Cl$ | | |
| Ba1-O2 | 2.829(14)x6 | Ba2-O2 | 2.718(18)x2 |
| Ba2-O1/S1 | 2.974(9)x2 | V1-O1/S1 | 2.032(8)x2 |
| Ba2-O2 | 2.718(18)x2 | V1-O2 | 1.69(2)x2 |
| Ba2-Cl1 | 3.09(2)x2 | Cl1-Cl1 | 1.00(5) |
| | $C3-Ba_5V_3O_{7.869}S_{4.131}Cl$ | | |
| Ba1-O2 | 2.841(7)x6 | Ba2-O2 | 2.713(9)x2 |

| | | | |
|---|---|---|---|
| Ba2-O1/S1 | 3.006(8)x2 | V1-O1/S1 | 2.046(7)x2 |
| Ba2-O2 | 2.713(9)x2 | V1-O2 | 1.696(12)x2 |
| Ba2-Cl1 | 3.392(2)x2 | | |

**Table 6.** Data Collection and Refinement Details for C4, $Ba_5 (VO_3S)_3 F$

| Crystal | C4 |
|---|---|
| **Formula** | $Ba_5V_3O_9S_3 F$ |
| Detailed formula | $Ba_5 (VO_3S)_3 F$ |
| Molecular weight (g. mol$^{-1}$) | 1098.7 |
| Symmetry | *Trigonal* |
| Space group | P -3 m 1 (164) |
| Unit cell dimensions (Å) | a= 18.1597(8) |
| | c= 8.8299(5) |
| Volume (Å³) | 2521.8(2) |
| Z | 6 |
| | **Data Collection** |
| Equipment | Bruker CCD (Mo Kα) |
| Λ [Å] | 0.71075 |
| Calculated density (g cm$^{-3}$) | 4.3408 |
| Crystal shape | Platelet |
| Crystal dimensions ($\mu$m) | 50×40×5 |
| Color | orange |
| Absorption correction | analytical |
| Scan mode | ω, φ |
| θ (min–max) (°) | 2.24 - 26.01 |
| μ (mm$^{-1}$) | 13.512 |
| F(000) | 2868 |
| Reciprocal space recording | $-22 \leq h \leq 22$ |
| | $-22 \leq k \leq 22$ |
| | $-10 \leq l \leq 10$ |
| No. of measured reflections | 37203 |
| No. of independent reflections | 1828 |
| I > 3σ(I) (total) | 1370 |
| | **Refinement** |

| | | | | | | |
|---|---|---|---|---|---|---|
| **Number of refined parameters** | 98 | | | | | |
| **Refinement method** | Least-squares | | | | | |
| **Weighting scheme** | sigma | | | | | |
| **R1(F) [I > 3σ(I)]/R1(F²) (all data, %)** | 0.0588 /0.0781 | | | | | |
| **wR2(F²) [I > 3σ(I)]/wR2(F²) (all data, %)** | 0.0748 /0.0769 | | | | | |
| **Goodness of Fit** | 3.19 | | | | | |
| **Max/Min residual electronic density (e⁻/Å³)** | 4.09 / -2.78 | | | | | |
| **Tmin/tmax** | 0.6365/ 0.7453 | | | | | |

**Table 7.** Atomic Positions and Isotropic Thermal Displacement for C4, $Ba_5 (VO_3S)_3 F$

| | | | | | | |
|---|---|---|---|---|---|---|
| **C4-$Ba_5V_3O_9S_3F$** | | | | | | |
| **Atom** | **Wyck.** | | **x** | **y** | **z** | **$U_{eq}$** |
| Ba1 | 6i | 0.88(2) | 0.58523(6) | 0.41477(6) | 0.2059(7) | 0.0209(9) |
| Ba1a | 6i | 0.12(2) | 0.5897(5) | 0.4103(5) | 0.268(4) | 0.019(4) |
| Ba2 | 6g | | 0.67810(7) | 0.67810(7) | 0 | 0.0352(5) |
| Ba3 | 6h | | 0.65546(7) | 0.65546(7) | 0.5 | 0.0360(5) |
| Ba4 | 6i | 0.773(8) | 0.91881(4) | 0.83763(9) | 0.2900(4) | 0.0235(8) |
| Ba4a | 6i | 0.227(8) | 0.91975(16) | 0.8395(3) | 0.2047(12) | 0.0202(19) |
| Ba5 | 6i | 0.664(9) | 0.49536(10) | 0.74768(5) | 0.2930(5) | 0.0229(10) |
| Ba5a | 6i | 0.336(9) | 0.4950(2) | 0.74750(12) | 0.2120(9) | 0.0222(13) |
| V1 | 6i | | 0.47615(9) | 0.52385(9) | 0.2250(4) | 0.0242(12) |
| V2 | 6i | | 0.71386(19) | 0.85693(10) | 0.2708(4) | 0.0297(12) |
| V3 | 6i | | 0.80965(10) | 0.6193(2) | 0.2570(5) | 0.0425(15) |
| S1 | 6i | | 0.1226(3) | 0.56129(17) | 0.4352(6) | 0.0359(13) |
| S2 | 6i | | 0.10369(19) | 0.2074(4) | 0.0748(7) | 0.0437(14) |
| S3 | 6i | | 0.7735(2) | 0.5470(4) | 0.0596(8) | 0.0523(16) |
| O1 | 12j | | 0.5832(6) | 0.5662(6) | 0.2232(10) | 0.030(2) |
| O2 | 12j | | 0.7691(6) | 0.6853(7) | 0.2624(12) | 0.044(3) |
| O3 | 12j | | 0.6480(6) | 0.7500(6) | 0.2691(11) | 0.038(2) |
| O4 | 6i | | 0.7688(3) | 0.5375(6) | 0.4168(11) | 0.007(2) |
| O5 | 6i | | 0.7872(8) | 0.8936(4) | 0.4390(15) | 0.028(3) |
| O6 | 6i | | 0.4370(5) | 0.5630(5) | 0.0809(18) | 0.047(4) |
| F1 | 2c | 0.81(2) | 1 | 1 | 0.278(3) | 0.039(6) |
| F2 | 1b | 0.37(5) | 1 | 1 | 0.25 | 0.039(6) |
| F3 | 2d | | 0.666667 | 0.333333 | 0.218(4) | 0.077(12) |
| F4 | 2d | | 0.333333 | 0.666667 | 0.239(5) | 0.108(16) |

**Table 8.** Anisotropic Thermal Parameters Uij (Å$^2$) for C4 and C5.

| Atom | U$_{11}$ | U$_{22}$ | U$_{33}$ | U$_{12}$ | U$_{13}$ | U$_{23}$ |
|------|------|------|------|------|------|------|
| | | | C4-Ba$_5$V$_3$O$_9$S$_3$F | | | |
| Ba1 | 0.0200(6) | 0.0200(6) | 0.027(2) | 0.0135(6) | 0.0005(4) | -0.0005(4) |
| Ba2 | 0.0351(6) | 0.0351(6) | 0.0197(7) | 0.0058(6) | -0.0003(3) | 0.0003(3) |
| Ba3 | 0.0335(5) | 0.0335(5) | 0.0182(7) | -0.0004(6) | -0.0004(3) | 0.0004(3) |
| Ba4 | 0.0205(6) | 0.0149(8) | 0.0333(19) | 0.0075(4) | -0.0027(3) | -0.0054(6) |
| Ba5 | 0.0137(9) | 0.0195(8) | 0.034(2) | 0.0068(4) | 0.0058(8) | 0.0029(4) |
| V1 | 0.0202(12) | 0.0202(12) | 0.0353(19) | 0.0123(13) | 0.0016(7) | -0.0016(7) |
| V2 | 0.0142(16) | 0.0210(12) | 0.052(2) | 0.0071(8) | 0.0036(15) | 0.0018(7) |
| V3 | 0.0200(13) | 0.0142(17) | 0.091(3) | 0.0071(8) | -0.0023(9) | -0.0046(18) |
| F3 | 0.033(8) | 0.033(8) | 0.16(3) | 0.017(4) | 0 | 0 |
| F4 | 0.032(9) | 0.032(9) | 0.26(5) | 0.016(4) | 0 | 0 |

**Table 9.** Main Distances (Å) for C4.

| Atoms 1,2 | d 1,2 [Å] | Atoms 1,2 | d 1,2 [Å] |
|-----------|-----------|-----------|-----------|
| Ba1-S1 | 3.258(9) | Ba5-S3 | 3.218(8) |
| Ba1-S3 | 3.304(5)x2 | Ba5-O3 | 2.759(13)x2 |
| Ba1-O1 | 2.772(12)x2 | Ba5-O4 | 2.647(11) |
| Ba1-O6 | 2.627(17) | Ba5-F4 | 2.592(8) |
| Ba1-F3 | 2.564(2) | Ba5a-S3 | 2.534(10) |
| Ba2-O1 | 2.735(8)x2 | Ba5a-O3 | 2.802(13)x2 |
| Ba2-O2 | 2.810(11)x2 | Ba5a-F4 | 2.554(6) |
| Ba3-O1 | 2.863(9)x2 | V1—S1 | 2.198(7) |
| Ba3-O2 | 2.799(11)x2 | V1—O1 | 1.696(10)x2 |
| Ba3-O3 | 2.712(11)x2 | V1-O6 | 1.770(14) |
| Ba4-S2 | 3.299(7) | V2-S2 | 2.128(7) |
| Ba4-O2 | 2.754(8)x2 | V2-O3 | 1.697(9)x2 |
| Ba4-O5 | 2.521(13) | V2-O5 | 1.880(13) |
| Ba4-F1 | 2.5559(18) | V3-S3 | 2.081(8) |
| Ba4a-S2 | 3.177(10)x2 | V3-O2 | 1.694(15)x2 |
| Ba4a-S2 | 2.576(12) | V3-O4 | 1.909(10) |
| Ba4a-O2 | 2.815(9)x2 | | |
| Ba4a-F1 | 2.605(8) | | |
| Ba5-S1 | 3.257(7)x2 | | |
| Ba5-S3 | 3.218(8) | | |

**Table 10.** Comparison of atomic percentage calculated from empirical formula and EDS analysis, for crystals two types of Chlorine-crystals C1 and C3 (with good agreement between the theoretical ratios and EDS ratios) and crystals of the Iodide phase

| | Ba | V | S | X |
|---|---|---|---|---|
| $Ba_5V_3O_{9.102}S_{2.898}$ Cl **C1 (theoretical)** | 42 | 25.2 | 25.12 | 8.4 |
| $Ba_5V_3O_{9.102}S_{2.898}$ Cl- **C1-EDS** | 43 | 24 | 25 | 7.6 |
| $Ba_5V_3O_{7.869}S_{4.131}$Cl **C3 (theoretical)** | 38.078 | 22.847 | 31.46 | 7.62 |
| $Ba_5V_3O_{7.869}S_{4.131}$Cl **C3-EDS** | 39.3 | 21.4 | 33.1 | 6.2 |
| **EDS (Iodide phase)** | 40.59 | 25.23 | 29.88 | 4.3 |

## 4.2. Polycrystalline Phase Analysis

Here it is important to distinguish the compositions (ratio O/S in the thiovanadates) refined from single crystals and the one obtained in the case of powders. All initial synthesis (including in the preparations where single crystals were selected) were formulated considering simple O/S within thiovanadates toward $VO_3S$ and $VO_2S_2$ in a first step. ($VS_3O$ and higher sulfur content are under investigation)

The synthesis pure powder samples in those systems were carried out following the procedure described in the Experimental Section. For Fluorine, Chlorine and Iodide-phases, we attempted the synthesis starting from simple O/S ratio with either $VO_3S$ or $VO_2S_2$ tetrahedra. At this stage, we could not reach a powder sample of an iodide-phase as major phase (although clearly identified in the products) and thus we present results for F and Cl only, i.e. the compositions $Ba_5(VO_3S)_3F$, $Ba_5(VO_2S_2)_3F$, $Ba_5(VO_3S)Cl$ and $Ba_5(VO_2S_2)_3Cl$. For clarity, nomenclature phase 1, phase 2, phase 3 and phase 4 were attributed to them, respectively. Phases 1, 2 and 3 are obtained in high purity as shown in Figure 4, while for phase 4, the minor impurity $Ba_6(VO_2S_2)_2(VS_3O)(VS_4)$ was identified. Figure 4 shows the Le bail fit for the four powders obtained from the above-mentioned compositions using Jana2006. In the case of Fluorine-phase

1, the profile refinement of the XRD patterns suggests that the super-structure observed in the single crystal Fluorine-phase would be also relevant for those powder compositions to account for a few more weak intensity peaks; the refinements were thus done in the superstructure cell. For simplicity at this stage of the work, we present profile refinement only and we assume, regarding the unit cells refined and the purity, that the targeted composition were achieved. Meanwhile, for the precise structures, Rietveld refinements are under progress. They require to consider potential disorder as found on the single crystals, in particular for Chlorine-phases which shows different disorder features (positions splits …) depending on the O/S ratio (see the three single crystals compositions refined, C1 to C3). For phase 1, $Ba_5(VO_3S)_3F$, we found a=18.165 Å and c= 8.848 Å in $P$-3$m$1 which is very close to the unit cell parameters found in the single crystal refinement of the same composition. For phase 2 to 4, the unit cell in $P6_3/mcm$ was used as found from the Chlorine-single crystals. For phase 2, $Ba_5(VO_2S_2)_3F$, a=10.49 Å and c=9.497 Å. For phase 3, $Ba_5(VO_3S)Cl$, a= 10.659 Å and c= 8.6342 Å. For phase 4, $Ba_5(VO_2S_2)_3Cl$, a= 10.824 Å and c=8.753 Å. The evolution between the Cl-phases 3 and 4 is consistent as the unit cell parameters increase with sulfur content. On another hand, from the F-phase 2 and the Cl-phase 4 (with the same O/S ratio), the unit cell parameters increase from F to Cl consistently with their respective ionic radii.
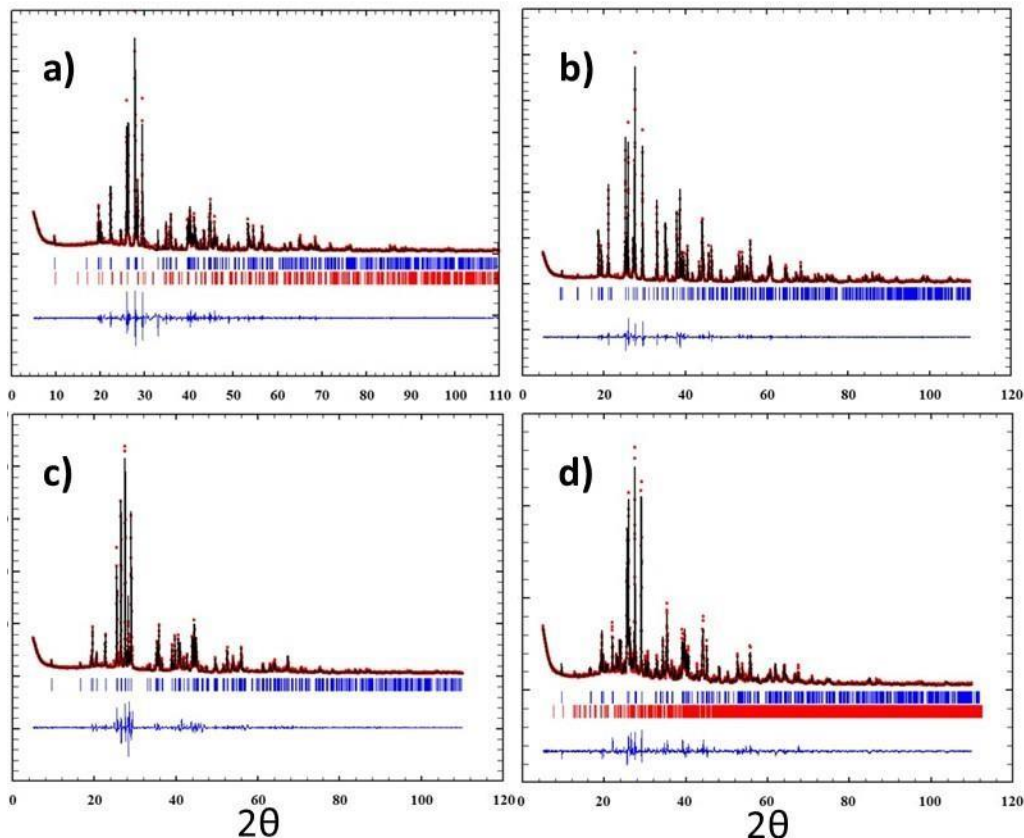
**Figure 4. a) to d)** Le Bail refinement for phases 1 → 4 respectively

### 4.3. Optical Measurements

The UV–visible diffuse-reflectance analysis of the polycrystalline phases is represented in Figure 5. A Kubelka–Munk[15] transformation was applied to the measured diffuse- reflectance (R) spectra using the function $F(R) = (1 – R)^2/2R$. Then a Tauc plot[16,17] was used to determine the optical band gap $E_g$, using the equation $[F(R)\ hv]^{1/n}= k(hv – E_g)$, where $hv$ is the photon energy, $k$ an energy-independent constant, $E_g$ the optical band gap, and $n$ is an exponent related to the type of transition. Assuming an indirect transition (exponent n = 2), the plot of $[F(R)\ hv]^2$ *versus* hv leads to $E_g$ in the range 2.11 − 2.48 eV, thus in the visible range. We note here however that the contribution of the impurity in the iodide-phase may hamper the exact determination of the band gap. Comparatively the oxyhalide based on vanadate groups $Ba_5(VO_4)_3F$ was reported with a band gap in the UV range ($E_g$= 3.85 eV). We confirm here the expected drastic shift of the band gap in

the visible range upon sulfur incorporation contained in the thiovanadate species. More into details, the band gaps are reduced from phase 1 to 2 and from phase 3 to 4 consistently with the greater sulfur content of lower electronegativity from $VO_3S$ to $VO_2S_2$ units. Then, considering similar O/S ratio, the band gap is reduced from phase 1 to 3 and from phase 2 to 4, when the halide is changed from F to Cl consistently with the lower electronegativity of Cl. Here we show how finely we can tune the band gap with such a versatile structure that can accommodate $O^{2-}$, $S^{2-}$, $F^-$ and $Cl^-$ (and $I^-$ not discussed here) with various O/S ratios.
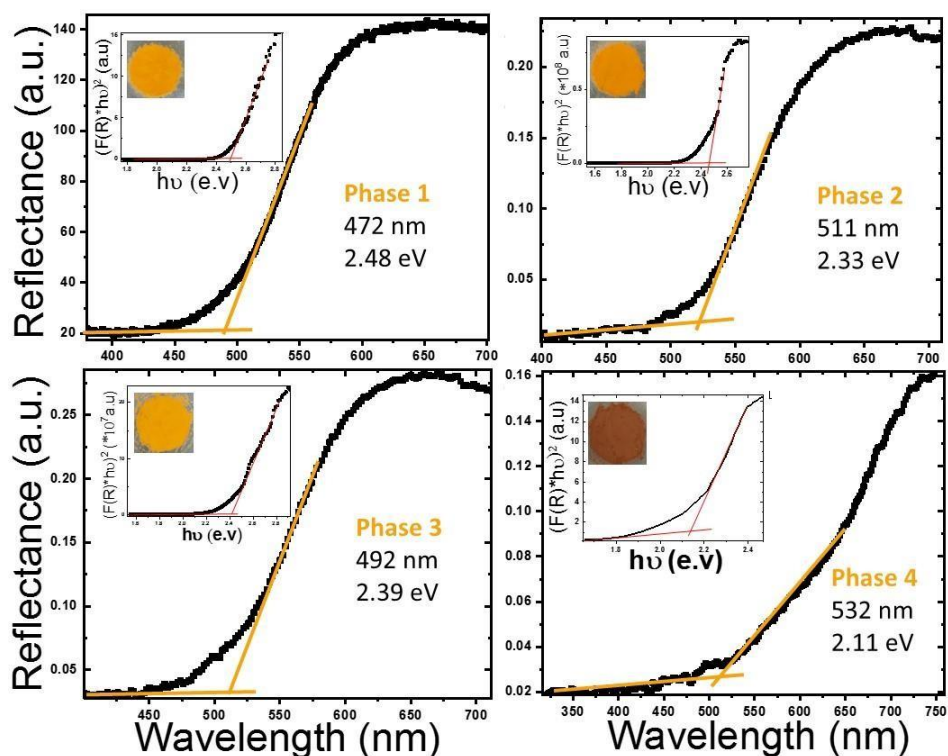


**Figure 5.** Diffuse-reflectance spectra for phases 1 →4 successively with a Tauc plot as insets to determine the experimental band gap.

## 4.4. Photoactivated Transport.

Mott-Schottky (MS) measurements ($1/C^2$ *vs.* V) were performed to elucidate the flat-band potential (Vfb) and to determine the type of semiconductor of all powder phases of $Ba_5 (VO_{4-\alpha}S_\alpha)_3X$. MS plots shows a positive slope (Figure 6.b) which indicate *n*-type semiconductors where the majority charge carriers are electrons. The flat-band potentials for powders 1, 2, 3 and 4 were

estimated to be approximately -0.62, -0.31, -0.55 and -0.27 V vs. Ag/AgCl, respectively. This potential allows locating the conduction band edge assuming that $V_{fb}$ is lower by 0.1–0.3 V from the conduction band for *n*-type semiconductors[18]. It is clear that the valence band maximum (VBM) shifts negatively from X= F to the less electronegative X=Cl  ($\chi_F$= 3.98 and $\chi_{Cl}$= 3.16) and by increasing S/O ratio ($\chi_O$= 3.44 and $\chi_S$= 2.58).

This is also consistent with the bands alignment shown in Figure 6.a We have calculated the later from empirical calculations based on Mulliken electronegativities as proposed by Butler and Ginley[19] and as further described by Xu and Schoonen[20] . Castelli *et al.*[21] have performed such calculations for a large set of materials including mixed anion oxynitrides and analysed how they align with the levels for hydrogen and oxygen evolution. In our case, the band edges positions encompass the redox potential of water which is required to evolve hydrogen and oxygen. Therefore, as shown from the comparison of the vanadate $Ba_5V_3O_{12}F$, the incorporation of thiovanadates preserve suitable band alignments for water-splitting reaction while it allows to shift the band gap in the visible range. Moreover, the samples having lower slopes indicate higher electron concentration in the crystal. However, the density of charge carriers cannot be estimated without knowing the effective dielectric constant of the mixture consisting of the phase analyzed and the polymer.
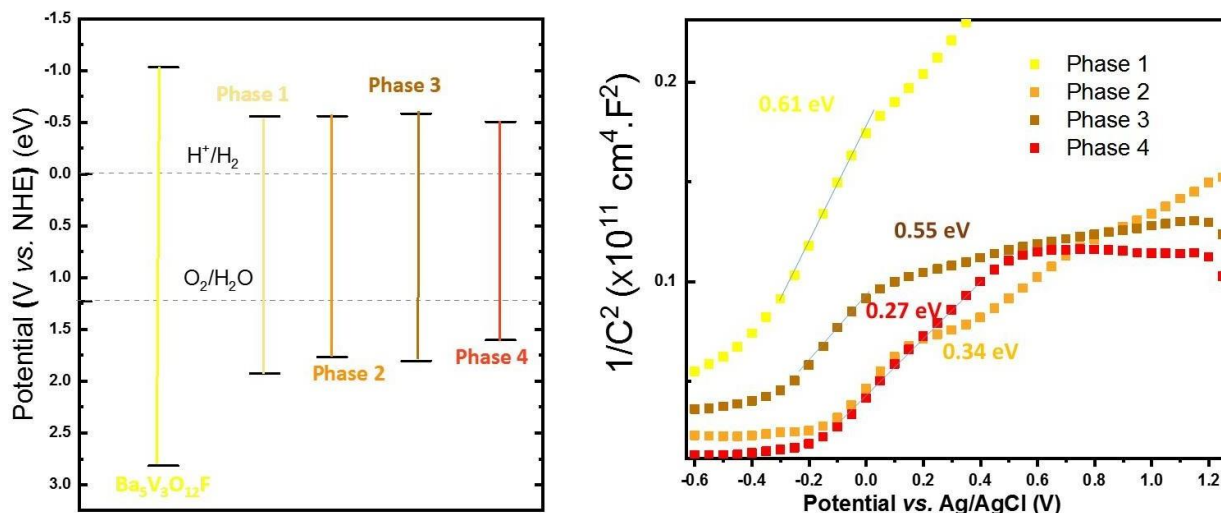


**Figure 6.** a) Calculated band edges positions obtained from empirical calculations for $Ba_5V_3O_{12}F$ and phases 1,2,3 and 4 respectively. The levels for hydrogen and oxygen evolution are indicated by dashed lines. b) Mott-Schottky plots carried out on the powders deposited on a slide of ITO/glass.
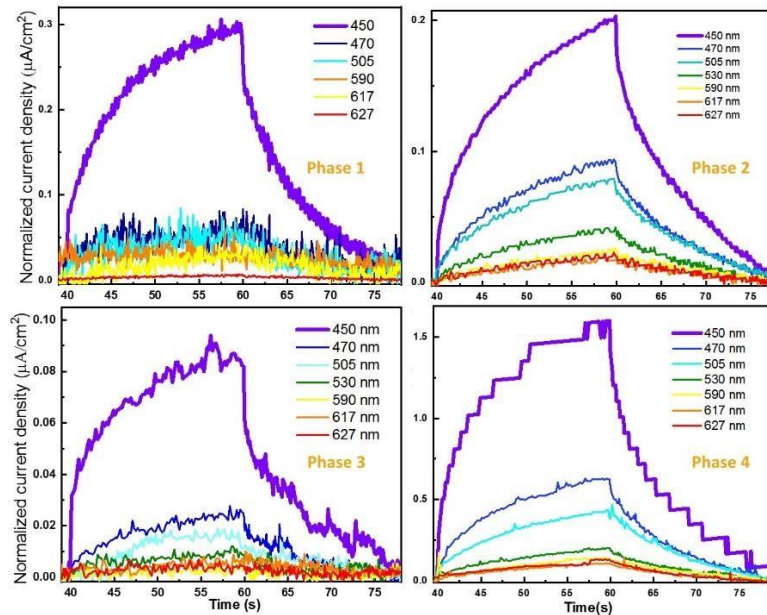
**Figure 7.** Evolution of the transient photo-current response for various wavelengths (performed under a constant luminous flux density of 42 mW.cm$^{-2}$ on a film deposited on a ITO/glass substrate.

**Figure 7** shows the influence of wavelengths on the transient photocurrent response. The photocurrent density (Δj) increases when the wavelength decreases for all samples. Samples 1 and 3 show a sharp drop between 450 and 470 nm showing an abrupt course in material absorption. While samples 2 and 4 show a gradual attenuation with increasing wavelength. Knowing that the photocurrent generated is proportional to the absorbance of the material. This change is also observed on the reflectance spectra.

**Figure 7** shows a maximum variation of the photo-current density occurring under an excitation of 450 nm and prove the generation of a photocurrent of about 0.1, 0.2 and 0.3 μA/cm$^2$ for phase 1 to 3; and 1.5 μA/cm$^2$ for phase 4 under 42 mW.cm$^{-2}$. The fact that phase 4 show a value one order of magnitude greater that the others has to be further investigated to the presence of an impurity that may contribute.

In **Figure 8**, a maximum variation of the photo-current density occurring under an excitation of 450 nm is observed and prove the generation of a photocurrent of about 0.1, 0.2, 0.3 and 1.5 μA/cm$^2$ for phase 1 to 4, respectively under 42 mW.cm$^{-2}$. The fact that phase 4 show a value one order of magnitude greater that the others has to be further investigated because there is probably a higher transfer rate compared to the recombination rate.
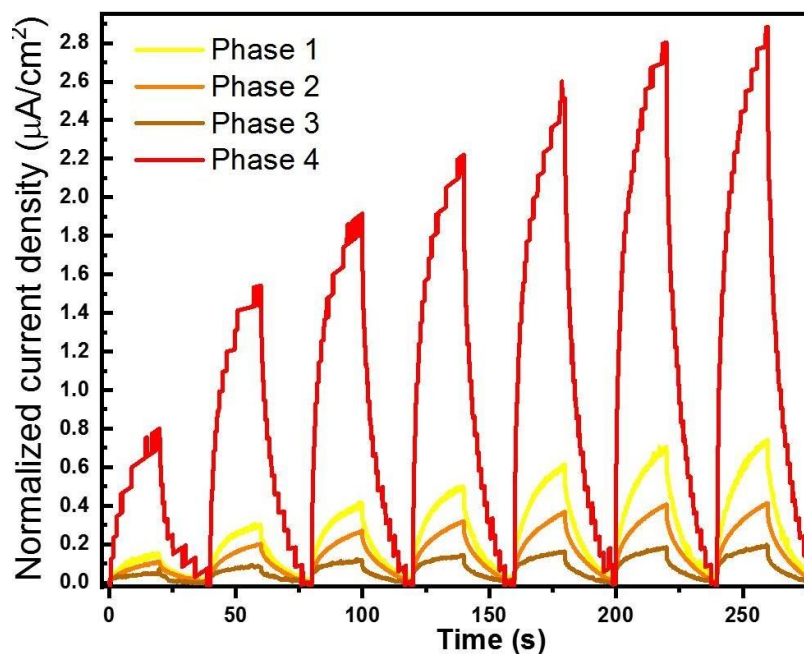
**Figure 8.** Variation of normalized current density *under increasing intensity illumination* (450 nm) or in the dark and with an applied potential of 0.2 V vs Ag/AgCl.

The on/off variation at 450 nm is maximal and present a photocurrent density of 0.8, 0.4, 0.2 and 2.8 $\mu A.cm^{-2}$ for phases 1, 2, 3 and 4, respectively with a bias potential of 0.2 V *vs* Ag/AgCl and under a light intensity ($\varphi_0$) of more $mW.cm^{-2}$. The evolution of the photocurrent $\Delta j$ with the intensity of the luminous flux ($\lambda$ = 450 nm; V = 0.2 V *vs* Ag/AgCl) is shown in Figure 8. the photocurrent density variation was plotted and in some cases it follows a power-type law whose model data are presented in Figure 9.

For phase 1, the evolution of the current density ($\Delta j = j_{light}-j_{dark}$) follows a quasi-linear evolution with $\gamma$ close to 1. For the other phases, the evolution is power law is clearly demonstrated. For low intensities, the photocurrent generated is directly proportional to the light intensity. The electron-hole pairs created are mainly transferred to the surface towards the electrode. Beyond a certain limit value of luminous intensity, the dependence is carried out in square root. This evolution of the exponent is probably not translated by a limitation of the charge transfer and a higher rate of recombination of the electron-hole pairs. This point is widely described in photocatalysis, in particular to explain a nonlinear evolution in the dyes photodegradation as a function of the luminous flux[22,23]. In this case, the limit between the two modes will depend on

214

the level of impurities compared to the density of the photoelectrons. This non-integer exponent can be regarded as a consequence of a complex process of electron–hole generation, trapping and recombination in the semiconductor[24]. Ullrich *et al.*[25] present a quantitative explanation to non-linearities phenomena. If we neglect the diffusion of carrier, the equilibrium between carrier generation and recombination is expressed by the following equation:

$$G = Bn\,(n+M) \propto \phi_0$$

Where G is the generation rate of photoelectrons by incident light (directly proportional to the luminous intensity); B is the recombination coefficient; n is the density of photoelectrons (whose value is proportional to the intensity of photocurrent) and M is number of impurity levels per $cm^3$.

At low intensities or for high impurity concentrations (n<<M), the previous expression becomes:

$$n = G/BM \propto i_{ph}$$

We can therefore observe a linear behavior between the photocurrent and the light intensity received by the sample (example of sample n°1 where the number of impurities must be important vis-à-vis the other phases). In addition, when the luminous flux increases, the value of $n_{pe}$ becomes greater than that of M and the expression takes the following form:

$$n = \sqrt{G/B} \quad a \quad \phi_0^{1/2}$$

The system gradually switches from a linear behavior to a square root behavior hence the evolution in power law (which is observed for samples n° 2, n°3 and n°4 where the density of the photoelectrons produced is higher than that of impurities). This model explains the experimental observations.

**Table 11.** Fit parameters of the power law applied on phases *1→4.*

| y = β*x^γ | Phase 1 | Phase 2 | Phase 3 | Phase 4 |
|---|---|---|---|---|
| β | 0.00952 ± 0.00121 | 0.0139 ± 0.0025 | 0.00427 ± 7.70304E-4 | 0.06952 ± 0.0226 |
| γ | 0.91517 ± 0.02798 | 0.71843 ± 0.04012 | 0.80475 ± 0.04003 | 0.74296 ± 0.07235 |
| R | 0.99735 | 0.99033 | 0.99271 | 0.97225 |

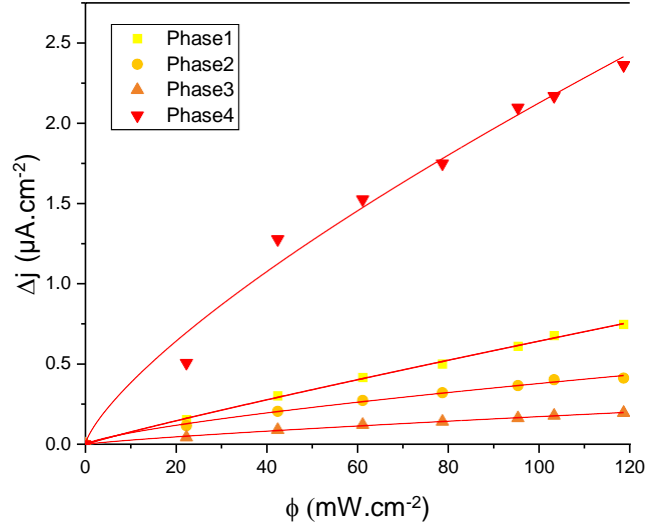**Figure 9.** The variation of current density (Δj) as a function of light intensity for phases 1→4.

5. Conclusion

The new $Ba_5 (VO_{4-\alpha}S_\alpha)_3X$ (X: F, Cl, I) series was designed by replacing vanadate groups by thiovanadate groups in the known Apatite series $Ba_5(VO_4)_3X$ (X: F, Cl, I). Compared to well-known Apatites, the presence of thiovanadates makes them the first halide-thio-Apatites. The light absorption characterizations show a visible light response for powders with X= F and Cl which make these materials promising for solar photoelectric and photocatalytic applications. For X= I, single crystals were identified but additional synthetic efforts are required to reach a high purity powder for photoelectric measurements. For the Cl-phases single crystals refinement, average structures have been refined. While the single crystal composition for $Ba_5(VO_4)_3F$ corresponds well to the pure powder, for the Cl-phases, the O/S ratios refined for single crystals diverge from the simple targeted powder compositions. Indeed, from one synthesis to the other, three different O/S ratios in three different crystals were refined. It shows both the versatility and the opportunity to easily modify the O/S ratio as well as the difficulty to control the stoichiometry of such crystals. Here the observation that crystal growth may occur with a slight divergence of the stoichiometry compared to the bulk is yet to understand.

The displacement of the light absorption range toward the visible compared to other apatite analogues is induced by the contribution of sulfur states at the top of the valence band which is raised. We show that those phases are suitable candidates as photocatalysts for solar water-

splitting reaction.  This study reveals the great versatility of this system for tuning finely the band gap by playing concomitantly with the vanadium O/S coordination ratio and the halide anion type within the channels. Multiple possibilities are opened knowing that the cationic sites might be also substituted. Substitution of the halide site by Br and higher O/S ratio in the thiovanadates are under investigation.

## 6. References

(1)     Al-Mamouri, M.; Edwards, P. P.; Greaves, C.; Slaski, M. *Nature* **1994**, *369* (6479), 382–384.

(2)     Li, Y.-Y.; Wang, W.-J.; Wang, H.; Lin, H.; Wu, L.-M. *Cryst. Growth Des.* **2019**, *19* (7), 4172–4192.

(3)     Palazzi, M.; Carcaly, C.; Laruelle, P.; Flahaut, J. In *The Rare Earths in Modern Science and Technology*; Springer US: Boston, MA, 1982; pp 347–350.

(4)     Valldor, M.; Adler, P.; Prots, Y.; Burkhardt, U.; Tjeng, L. H. *Eur. J. Inorg. Chem.* **2014**, *2014* (36), 6150–6155.

(5)     Miyoshi, A.; Maeda, K. *Sol. RRL* **2021**, *5* (6), 2000521.

(6)     Wang, Q.; Nakabayashi, M.; Hisatomi, T.; Sun, S.; Akiyama, S.; Wang, Z.; Pan, Z.; Xiao, X.; Watanabe, T.; Yamada, T.; Shibata, N.; Takata, T.; Domen, K. *Nat. Mater.* **2019**, *18* (8), 827–832.

(7)     Kabbour, H.; Sayede, A.; Saitzek, S.; Lefèvre, G.; Cario, L.; Trentesaux, M.; Roussel, P. *Chem. Commun.* **2020**, *56* (11), 1645–1648.

(8)     Almoussawi, B.; Huvé, M.; Dupray, V.; Clevers, S.; Duffort, V.; Mentré, O.; Roussel, P.; Arevalo-Lopez, A. M.; Kabbour, H. *Inorg. Chem.* **2020**, *59* (9), 5907–5917.

(9)     Nicoud, S.; Mentré, O.; Kabbour, H. *Inorg. Chem.* **2019**, *58* (2), 1349–1357.

(10)    Petříček, V.; Dušek, M.; Palatinus, L. *Zeitschrift für Krist. - Cryst. Mater.* **2014**, *229* (5), 345–352.

(11)    van der Lee, A. *J. Appl. Crystallogr.* **2013**, *46* (5), 1306–1315.

(12)    Roh, Y.-H.; Hong, S.-T. *Acta Crystallogr. Sect. E Struct. Reports Online* **2005**, *61* (8), i140–i142.

(13)    Wong, C. J.; Hopkins, E. J.; Prots, Y.; Hu, Z.; Kuo, C.-Y.; Pi, T.-W.; Valldor, M. *Chem. Mater.* **2016**, *28* (6), 1621–1624.

(14)    Kang, J.; Yang, Y.; Pan, S.; Yu, H.; Zhou, Z. *J. Mol. Struct.* **2014**, *1056–1057*, 79–83.

(15)    Tauc, J.; Grigorovici, R.; Vancu, A. *Phys. Status Solidi* **1966**, *15* (2), 627–637.

(16)    Kubelka, P. and Munk, F. *Techn. Phys.* **1931**, *12*, 593–601.

(17)    Wendlandt, W.; Hecht, H. G. *Reflectance Spectroscopy*; London Interscience: New York, 1966.

(18)    Matsumoto, Y. *J. Solid State Chem.* **1996**, *126* (2), 227–234.

(19)    Butler, M. A.; Ginley, D. S. *J. Electrochem. Soc.* **1978**, *125* (2), 228–232.

(20)     Xu, Y.; Schoonen, M. A. A. *Am. Mineral.* **2000**, *85* (3–4), 543–556.

(21)     Castelli, I. E.; Olsen, T.; Datta, S.; Landis, D. D.; Dahl, S.; Thygesen, K. S.; Jacobsen, K. W. *Energy Environ. Sci.* **2012**, *5* (2), 5814–5819.

(22)     Hussein, F. *Asian J. Chem.* **2012**, *24*, 5427–5434.

(23)     Herrmann, J.-M. *Catal. Today* **1999**, *53* (1), 115–129.

(24)     Jin, S. F.; Huang, Q.; Lin, Z. P.; Li, Z. L.; Wu, X. Z.; Ying, T. P.; Wang, G.; Chen, X. L. *Phys. Rev. B* **2015**, *91* (9), 094420.

(25)     Ullrich, B.; Xi, H. *Opt. Lett.* **2013**, *38* (22), 4698.

# General Conclusion and perspectives

# General conclusion and perspectives:

The research of innovative materials with functional properties is a requirement for technological progress. The anionic manipulation is a strategy much less explored than cationic manipulation. Regarding what a mixture of anionic species can induce, this strategy attracts a growing attention in the solid state chemistry community. Many reported mixed anion compounds have been compared to their single anion analogue, and proved their ability to arise some inaccessible properties, and enhance others.

In this work, we explored six new mixed anion systems with a wide range of properties. After introducing the thesis subject in the **first chapter**, we have presented in the **second chapter** five new oxysulfides: the fifth and sixth members in the quaternary system Ba-V-S-O, while we reported for the first time a phase in the Ba-V-Se-S-O system. $Ba_5(VO_2S_2)_2(S)_2$ exhibits the mixed anion building units $VO_2S_2$ and isolated disulfide pairs, it shows third-harmonic generation properties which is uncommon in oxychalcogenide or mixed anion crystalline solids. $Ba_7V_2S_{13}O_2$ and its three selenide-derivatives $Ba_7V_2O_2S_{6.787}Se_{6.213}$, $Ba_7V_2O_2S_{6.904}Se_{6.096}$ and $Ba_7V_2O_2S_{9.263}Se_{3.737}$ were elaborated and exhibit the mixed-anion building units $VOS_3$, isolated $Q^{2-}$ (Q= S, Se) sites (present in one layer) and isolated dichalcogenide pairs $Q_2$ (in the second layer). The selective substitution of sulfur by selenide in our synthetic conditions led to concomitant incorporation of Se in both the isolated Q and $Q_2$ pairs sites with mixed S/Se occupancy. Our meta-GGA DFT calculations, showed that the substitution in one layer only leads to some constraints which might explain the experimental disorder to avoid it.

This chapter highlights the rationalization of the structure with respect to the electronic structure which show all the interest of designing new phases using such mixed anion building blocks and/or dichalcogenide pairs. In particular, band gap engineering trough mastered approaches is important for a variety of properties.

**The third chapter** highlights the ability of anionic manipulation to change the symmetry. In the first part we showed the new polar oxychalcogenide obtained after the partial substitution of sulfide by selenide in $Ba_5(VO_2S_2)_2(S)_2$. It is the first polar one in the system Ba-V-O-S-Se. Non-

linear optical measurements show a strong SHG response which is still under investigation as well as NLO DFT calculations. Then, in the second part, the first Fresnoite-type oxysulfide, $Ba_2SnSSi_2O_7$ is presented. It exhibits the polar $SnO_4S$ square pyramids which is a scarce coordination polyhedra with tin. Our work opens the possibility of other Fresnoite-type oxychalcogenides. The bandgap of $Ba_2SnSSi_2O_7$ lies the visible range while those of most Fresnoite-type compounds fall into the UV or deep UV range. $Ba_2SnSSi_2O_7$ exhibits good SHG properties with an incident laser of 2.1 μm. These phases open new perspectives in the design of non-linear optical materials with greater performances.

**Then in Chapter IV,** Three new magnetic phases were presented. The original cubic non-centrosymmetric oxysulfide $Ba_{10}Fe_{7.75}Zn_{5.25}S_{18}Si_3O_{12}$ exhibits a 3D-structure made of large magnetic clusters, therefore standing apart from more commonly encountered layered oxychalcogenide. This partially charge-ordered phase presents strong AFM interactions with a spin-glass state arising from cluster geometry and disorder. It provides an exceptional new structure type and a rich playground for exotic physics.

In the second part, a new sulfide material $Ba_5Fe_2ZnIn_4S_{15}$ is presented and adopts a polar structure type isostructural with a family of wide band gap SHG materials. Preliminary magnetic measurements show a divergence of the ZFC/FC at very low temperature around 3 K and dominant antiferromagnetic interactions. DFT calculations suggest a stable antiferromagnetic state with strong AFM intrachain Fe-S-Fe super exchanges and very weak interchain Fe-S-S-Fe coupling (via $InS_4$). It thus represents an AFM S=5/2 spin chain system. A pure powder or magnetic measurements based on single crystals are required to further investigate this sample. It represents a promising playground to measure electric polarization and tune the magnetic interactions toward multiferroic systems.

The new phase $Ba_9V_3S_{15}$ could be stabilized using high pressure and high temperature in the form of single crystals. It belongs to the one-dimensional magnetic system $Ba_9M_3X_{15}$ ($M$= V, Fe and $X$= S, Se) that exhibits chains made of face-sharing $MX_6$ octahedra as found in BaV$X_3$ ($X$= chalcogenide). It is made of columns of dichalcogenide pairs and chalcogenide anions alternating and surrounded by Barium cations. We show that the columns occupation by sulfur species is slightly different in the sulfide compared to the selenide, making them polymorphs and not

isostructural. Within the $Ba_9M_3X_{15}$ ($M$= V, Fe and $X$= S, Se), $Ba_9V_3S_{15}$ was targeted in previous work, we show here its experimental realization in the form of single crystals within a complex mixture. Using first-principles calculations, we show the formation of magnetic clusters within the spin chains. Then, extensive synthetic efforts are required to reach a polycrystalline sample of this metastable phase to experimentally investigate this hypothesis.

Those magnetic phases described in this chapter open new perspectives in magnetic materials exploration.

In the **last chapter**, the new Apatite series $Ba_5$ $(VO_{4-\alpha}S_\alpha)_3X$ (X: F, Cl, I) was presented. It compares to well-known Apatites. They exhibit thiovanadates (instead of vanadate species in their known analogues), thus representing the first halide-thio-Apatites. The light absorption characterization shows a visible light response for powders with X= F and Cl. which make this material promising for solar photoelectric and photocatalytic applications.

# <span style="color:magenta">**Annexe 1**</span>

Théorie de la fonctionnelle de la densité

Dans le cas d'un système quantique comportant plus d'une particule (électrons ou noyaux), système dit à N corps, l'équation de Schrödinger n'a pas de solution analytique. Il est alors nécessaire de faire certaines approximations pour la résoudre numériquement et, en chimie quantique, deux approches distinctes sont couramment utilisées:

- la méthode Hartree-Fock et les méthodes dérivées post-Hartree-Fock (MPn, CI, CASSCF…) sont des méthodes auto-cohérentes basées sur la fonction d'onde électronique. La première est une approche monodéterminante dans laquelle la fonction d'onde globale est un produit de fonctions monoélectroniques. L'hamiltonien de la méthode Hartree-Fock traite l'échange électronique de façon exacte mais, en contre-partie, n'introduit aucun effet de corrélation. Dans les méthodes post-Hartree-Fock, un traitement de la corrélation électronique est rajouté soit via des développements perturbatifs, soit grâce à des approches multidéterminentales.

- la théorie de la fonctionnelle de la densité (DFT) est une approche basée uniquement sur la densité électronique ($\rho$). Elle exprime en effet l'énergie totale d'un système comme une fonctionnelle (fonction de fonction) de $\rho$. Comme il sera montré dans la suite, les contributions multiélectroniques sont représentées grâce à un potentiel d'échange et de corrélation, et les développements utilisés pour construire ce potentiel d'échange et de corrélation définissent la précision de la méthode DFT.

## I. L'hamiltonien électronique

L'objectif est de résoudre, pour un système quantique de N électrons et $M$ noyaux, l'équation de Schrödinger $H\Psi = E\Psi$, c'est-à-dire déterminer E et $\Psi$ avec H l'opérateur

hamiltonien, E étant l'énergie totale du système et $\Psi$ la fonction d'onde totale ; la connaissance de E et $\Psi$ permet d'accéder aux propriétés électroniques, chimiques et physiques du système.

L'expression exacte de l'hamiltonien est :

$$\hat{I} = \hat{T}_{él} + \hat{T}_{noy} + \hat{V}_{noy-él} + \hat{V}_{él-él} + \hat{V}_{noy-noy}$$

Cette expression comporte deux contributions : l'une cinétique $\hat{T}$ et l'autre potentielle $\hat{V}$. On trouve, dans le terme d'énergie potentielle, un terme attractif noyau-électron et deux termes répulsifs noyau-noyau et électron-électron, et, dans le terme d'énergie cinétique, une contribution électronique ainsi qu'une contribution nucléaire. Dans l'approximation de Born-Oppenheimer, les noyaux ayant une masse très supérieure à celle des électrons, on considère que leur énergie cinétique peut être négligée. Le terme de répulsion noyau-noyau devient donc une constante et la résolution de l'hamiltonien global se réduit à la seule détermination de l'hamiltonien électronique.

$$\hat{I} = \hat{H}_{él} + \hat{V}_{noy-noy}\left(= cste\right) \text{ avec } \hat{H}_{él} = \hat{T}_{él} + \hat{V}_{noy-él} + \hat{V}_{él-él}$$

soit

$$\hat{H}_{él} = -\sum_{i=1}^{N}\frac{\square^2}{2m}\nabla_i^2 - \sum_{i=1}^{N}\sum_{\alpha}\frac{Z_\alpha e^2}{r_{i\alpha}} + \sum_{i=1}^{N}\sum_{j\rangle i}\frac{e^2}{r_{ij}}$$

Les deux premiers termes sont monoélectroniques, tandis que le troisième est biélectronique.

## II. 1. La densité électronique

Un électron n'est pas une particule classique mais une particule quantique qui est décrite par sa probabilité de présence dans un élément de volume: c'est la densité électronique. L'ensemble des électrons forme le nuage électronique. La densité électronique $\rho(\mathbf{r})$ est une fonction positive qui dépend uniquement des trois coordonnées (x,y,z) de l'espace. Elle s'annule à l'infini $\rho(\mathbf{r} \rightarrow \infty)$=0 et s'intègre au nombre d'électrons $\int \rho(\mathbf{r}) d^3 r = N$. Contrairement à la fonction d'onde, la densité électronique est une observable qui, lorsqu'elle est connue, permet de décrire l'ensemble des propriétés physico-chimiques d'un système. Les premières tentatives de mise en place d'un formalisme reliant la densité électronique à l'énergie totale ont été proposées par Thomas et Fermi en 1927. Ce n'est cependant que 30 ans plus tard que Hohenberg et Kohn proposent le formalisme exact de la DFT, formalisme basé sur deux théorèmes.

## II. 2. Les théorèmes de Hohenberg et Kohn

Le premier théorème de Hohenberg et Kohn stipule que la densité électronique ρ(r) détermine le potentiel externe $v_{ext}$(r) (le potentiel externe $v_{ext}$(r) contient par exemple l'attraction électron-noyau et toute autre forme de potentiel extérieur : champ magnétique, champ électrique …). Ce potentiel extérieur $v_{ext}$(r) est en effet, à une constante près, une fonctionnelle unique de la densité électronique ρ(r) et comme $v_{ext}$(r) définit l'hamiltonien, le problème multiélectronique de l'état fondamental est donc complètement défini par la densité électronique ρ(r).

$$E[\rho(\mathbf{r})] = F_{HK}[\rho(\mathbf{r})] + \int \rho(\mathbf{r}) v_{ext}(\mathbf{r}) d^3\mathbf{r}$$

avec $F_{HK}[\rho(\mathbf{r})] = T_{él}[\rho(\mathbf{r})] + V_{él-él}[\rho(\mathbf{r})]$. C'est la fonctionnelle de Hohenberg et Kohn.

Le deuxième théorème stipule que $E[\rho(r)]$ suit une loi variationnelle. En d'autres termes, il est possible d'approcher (par valeurs supérieures) l'énergie totale exacte, et donc la densité électronique totale exacte, d'un système de N particules indépendantes, en utilisant un processus autocohérent. En résumé, si $F_{HK}[\rho(r)]$ est une fonction connue, la densité électronique de l'état fondamental d'un système constitué de N électrons en interaction est accessible variationnellement.

Toutefois, si ces deux théorèmes montrent que $\rho(r)$ et $E[\rho(r)]$ sont des quantités liées, ils ne précisent pas comment la seconde est calculée à partir de la première. Il faut, pour cela, procéder à de nouvelles approximations.

## II. 3. Les équations de Kohn et Sham

Kohn et Sham sont parvenus à développer un système d'équations qui permet de trouver la densité électronique exacte à l'aide d'un concept de particules fictives sans interactions de même densité électronique $\rho$. La fonctionnelle $F_{HK}[\rho(r)]$ s'écrit alors :

$$F_{HK}[\rho(\mathbf{r})] = \frac{1}{2}\iint \frac{\rho(\mathbf{r})\rho(\mathbf{r}')}{|\mathbf{r}-\mathbf{r}'|}d^3rd^3r' + T_{ref}[\rho(\mathbf{r})] + E_{xc}[\rho(\mathbf{r})]$$

et
$$E[\rho(\mathbf{r})] = T_{ref}[\rho(\mathbf{r})] + J[\rho(\mathbf{r})] + \int \rho(\mathbf{r})v_{ext}(\mathbf{r})d^3\mathbf{r} + E_{xc}[\rho(\mathbf{r})]$$

avec un terme classique d'interaction coulombienne : $J[\rho(\mathbf{r})] = \frac{1}{2}\iint \dfrac{\rho(\mathbf{r})\rho(\mathbf{r}')}{|\mathbf{r}-\mathbf{r}'|}d^3rd^3r'$

$T_{ref}[\rho(\mathbf{r})]$ est l'énergie cinétique du système de référence des particules sans interactions

$E_{xc}[\rho(\mathbf{r})]$ est l'énergie d'échange et de corrélation : $E_{xc} = T_{él} - T_{ref} + V_{él-él} - J$

$E_{xc[\rho]}$ représente la correction qu'il faut appliquer à l'énergie cinétique $T_{ref}[\rho]$ et à l'énergie de répulsion $J[\rho]$ afin d'obtenir l'énergie totale exacte. Le système de référence peut

être décrit par N équations monoélectroniques développées maintenant sur des spin-orbitales $\psi_i(\mathbf{r})$.

Les équations de Kohn et Sham s'obtiennent à partir du principe variationnel : $\left.\dfrac{\delta E[\rho(\mathbf{r})]}{\delta\rho(\mathbf{r})}\right|_{\rho_{GS}} = 0$.

$$\left\{ -\frac{1}{2}\nabla^2 + v_{eff}(\mathbf{r}) \right\}\psi_i(\mathbf{r}) = \varepsilon_i\psi_i(\mathbf{r})$$

Le potentiel $v_{eff}(r)$ est obtenu par dérivation fonctionnelle de l'expression de l'énergie totale.

$$v_{eff}(\mathbf{r}) = V_H(\mathbf{r}) + V_{xc}(\mathbf{r}) + v_{ext}(\mathbf{r})$$

avec $\quad V_H(\mathbf{r}) = \displaystyle\int \frac{\rho(\mathbf{r}')}{|\mathbf{r}-\mathbf{r}'|}d^3r'$ le potentiel classique de Hartree

et $\quad V_{xc}(\mathbf{r}) = \dfrac{\delta E_{xc}[\rho(\mathbf{r})]}{\delta\rho(\mathbf{r})}$ le potentiel d'échange et de corrélation

Comme on peut le voir plus haut, la seule approximation utilisée dans l'expression du potentiel effectif de Kohn et Sham concerne le potentiel d'échange et de corrélation. Aucune formulation exacte n'existe en effet pour cette quantité qui regroupe tous les effets multiélectroniques. La première approximation proposée est basée sur une approche locale de la densité (LDA, «local density approximation ») et considère que les effets d'échange et de corrélation sont des propriétés locales qui ne dépendent que de la densité électronique $\rho$(r) au point r. L'approche LDA, a été paramétrée à partir de calculs sur un gaz homogène d'électrons. Les fonctionnelles de type GGA (pour « generalized gradient approximation ») ont apporté ensuite des améliorations par rapport à la LDA car elles prennent en compte les fortes variations de la densité électronique autour du point r. Depuis, de nombreuses autres fonctionnelles ont été introduites et les plus performantes pour l'instant (mais non encore disponibles pour les codes de calculs sur les systèmes périodiques) sont des fonctionnelles hybrides type B3LYP où une partie d'échange exact est introduite dans le calcul de l'hamiltonien. Signalons finalement

que pour le traitement des systèmes à électrons fortement corrélés (éléments de la 1$^{ère}$ série de transition ou lanthanides), ces approches champ moyen sont peu performantes. Dans de tels cas,

des approches du type LDA+U ou LDA+DMFT améliorent grandement le traitement des états électroniques autour du niveau de Fermi. Ces fonctionnelles utilisent des équations dérivées de modèles de Hubard pour traiter spécifiquement l'échange et la corrélation des orbitales concernées. Dans nos calculs, nous avons utilisé la fonctionnelle d'échange et de corrélation de **type GGA PW91.**

III. Méthodes de calcul

Le code de calcul principalement utilisé au cours de ma thèse est VASP. Il est basé sur le formalisme DFT (Density Functional Theory) présenté auparavant, et permet d'accéder à une estimation quantitative de l'énergie totale des systèmes étudiés. Ce code utilise le formalisme de Bloch pour le traitement des systèmes périodiques. Il permet d'effectuer des optimisations de géométrie avec la possibilité de relaxer la maille et les positions atomiques, simultanément. Les bases des fonctions d'onde utilisées sont de type OP/PP (onde planes / pseudopotentiels). Toutes les méthodes de calcul basées sur ce formalisme ont pour point commun la résolution des équations de Kohn et Sham. Les orbitales de Kohn et Sham sont obtenues par combinaisons linéaires des orbitales monoélectroniques de la base et s'écrivent:

$$\left| \psi_i^{\mathbf{k}}(\mathbf{r}) \right\rangle = \sum_{j=1}^{N} c_j^{i,\mathbf{k}} \left| \varphi_j^{\mathbf{k}}(\mathbf{r}) \right\rangle$$

où $\left| \varphi_j^{\mathbf{k}}(\mathbf{r}) \right\rangle$ sont les fonctions de bases et $c_j^{i,\mathbf{k}}$ les coefficients de développement correspondants.

Du fait de l'approche de Bloch, **k** est un bon nombre quantique. L'hamiltonien est donc évalué pour un nombre discret de points **k** dans la zone de Brillouin (le plus petit possible mais suffisant pour obtenir une énergie totale convergente). Le problème aux valeurs propres/vecteurs propres est ensuite résolu par diagonalisation itérative, afin d'obtenir l'ensemble des coefficient $c_j^{i,\mathbf{k}}$.

**III. 1. Bases (onde plane / pseudopotentials)**

Les fonctions de base qui sont utilisées dans le code VASP sont des ondes planes (OP). D'un point de vue mathématique, ce type de base est idéal pour décrire les systèmes périodiques car parfaitement adapté au formalisme de Bloch. De plus, il permet d'évaluer à moindre coût nombre de quantités telles que l'énergie totale et ses dérivées grâce à l'utilisation d'algorithmes

performants comme les transformées de Fourier rapides (FFT). Les OP ne sont cependant pas adaptées pour décrire les fortes variations de densité électronique à proximité des noyaux et, pour rendre ces bases plus efficaces dans le traitement de la structure électronique des matériaux, on les couple à des pseudo potentiels (PP). On considère pour cela que seuls les électrons de valence contribuent à la liaison chimique et donc à la plupart des propriétés physico-chimiques des systèmes étudiés. Les électrons de cœur sont donc explicitement supprimés de la base. Un PP est alors utilisé pour reproduire les propriétés de diffusion de ces électrons de cœur sur les électrons de valence (cf. **Figure 1** ci-dessous). Ainsi, en dessous d'un certain rayon de coupure autour de chaque atome, les fonctions d'onde de valence sont remplacées par des pseudo-fonctions d'onde: plus lisses et sans nœuds, donc plus facile à décrire avec des OP. Pour nos calculs, nous avons utilisé des potentiels PAW (Projected Augmented Wave) qui, autorisant la reconstruction de la vraie fonction d'onde, permettent d'atteindre des précisions très semblables à celles de codes « tous » électrons.
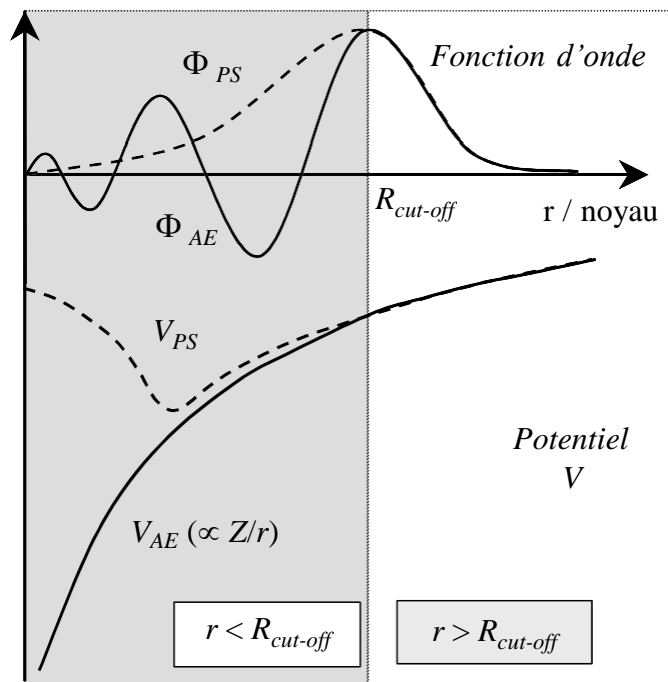


**Figure 1:** *Représentation des allures générales de la « vraie » fonction d'onde $\Phi_{AE}$ et de la pseudo-fonction d'onde $\Phi_{PS}$ (en haut), ainsi que du « tous électrons » $V_{AE}$ et du pseudo-potentiel $V_{PS}$ (en bas).*

### III. 2. Etapes d'un calcul de structure électronique périodique

Dans le cas des solides infinis périodiques, l'utilisation du théorème de Bloch permet de réduire l'étude à celle d'un système fini (la maille cristalline). On utilise pour cela un nombre discret, et assez faible, de points **k** et l'évaluation de la densité électronique se fait via des méthodes d'intégration assez sophistiquées sur cette grille de point **k**.

$$\rho(\mathbf{r}) = \sum_{\mathbf{k}=1}^{\mathbf{N_k}} \sum_{\varepsilon_i^\mathbf{k} < E_F} \omega_i^\mathbf{k} \, |\psi_i^\mathbf{k}(\mathbf{r})|^2$$

La densité électronique du système qui permet d'atteindre l'énergie totale minimale pour le système est obtenue variationnellement selon un processus itératif SCF (self-consistent-field). Une densité initiale est introduite par la superposition des densités atomiques:

$$\rho_{in} = \rho^{cristal} = \sum_{at} \rho^{at}$$

Cette densité électronique est utilisée dans l'équation de Poisson pour accéder au potentiel coulombien.

$$\nabla^2 V_C(r) = 4\pi\rho(r)$$

Le potentiel coulombien correspond à la somme du potentiel de Hartree (contribution $V_{él-él}$) et du potentiel nucléaire $V_{noy-noy}$. Pour obtenir le potentiel effectif, on ajoute alors le terme d'échange et de corrélation. Le potentiel effectif $V_{eff}$ et la densité électronique $\rho(r)$ permettent la construction de l'Hamiltonien électronique. Les équations de Kohn et Sham sont ensuite résolues pour accéder aux fonctions propres et aux valeurs propres de l'Hamiltonien électronique *($\phi_i$, $\varepsilon_i$)*. Une nouvelle densité électronique $\rho_{i+1}$ est alors obtenue en sommant le module du carré des fonctions d'ondes monoélectroniques sur l'ensemble des états occupés. Un mélange des densités $\rho_i$ et $\rho_{i+1}$ est réintroduit dans le cycle jusqu'à ce que le critère de convergence soit atteint, c'est-à-dire lorsque la densité électronique (ou l'énergie électronique qui lui correspond) est stable.

Le principe général d'un calcul DFT est résumé sur le schéma de la **Figure 2**.
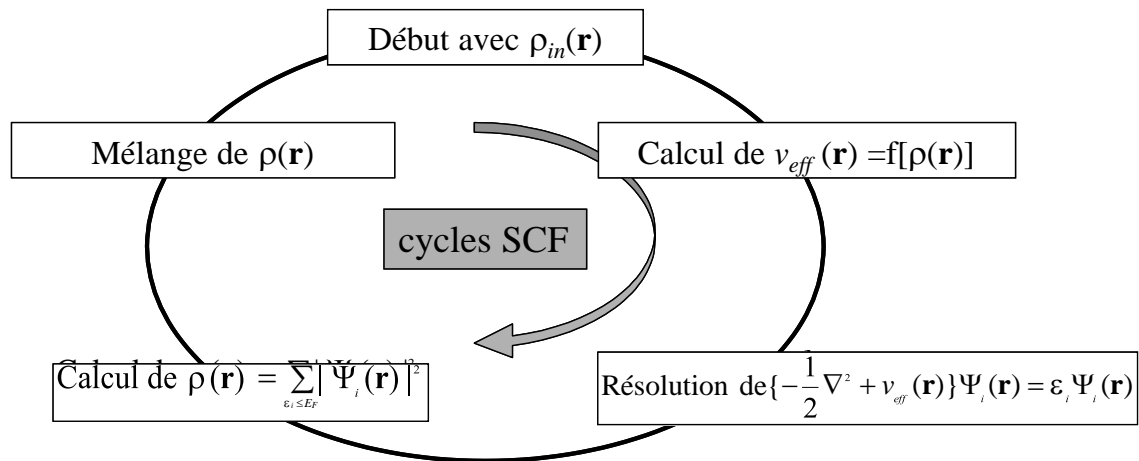
**Figure 2.** *Cycle autocohérent lors d'un calcul DFT*

### III. 3. Principe d'une optimisation de géométrie

Optimiser une structure cristalline revient à rechercher un minimum dans la surface d'énergie potentielle d'un système. Techniquement, dans l'approche que nous avons utilisé, cette exploration de surface consiste à faire varier les positions nucléaires dans des directions dictées par les forces atomiques. Pour chaque pas ionique, le calcul SCF d'énergie totale est effectué et les forces atomiques sont recalculées. C'est la dérivée de l'énergie totale par rapport aux coordonnées atomiques, qui permet d'accéder aux forces agissant sur les atomes.

Le théorème de Hellman-Feynman permet d'évaluer les forces sur les atomes. Pour l'état fondamental on a:

$$F_\alpha = -\frac{dE}{dR_\alpha} = -\frac{\partial E}{\partial R_\alpha}$$

Le critère de convergence est atteint lorsque les forces atomiques deviennent négligeables et que la structure cristalline obtenue ne peut plus évoluer.

L'énergie totale du système provient de la relation suivante:

$$E_{tot} = \frac{1}{2}\sum_{\alpha=1}^{N_z}\sum_{\beta\neq\alpha}\frac{Z_\alpha Z_\beta}{|R_\alpha - R_\beta|} + \sum_{i=1}^{N}\varepsilon_i + \int\left\{\varepsilon_{xc}[\rho(\mathbf{r})] - V_{xc}(\mathbf{r}) - \frac{1}{2}V_H(\mathbf{r})\right\}\rho(\mathbf{r})\,d\mathbf{r}$$

Et la dérivée partielle de l'expression de l'énergie totale par rapport aux déplacements atomiques conduit, dans le cas d'une base d'onde plane (base qui n'est pas liée aux postions atomiques) à l'expression simplifiée suivante pour les forces atomiques:

$$F^{IHF} = Z_I e \left. \frac{\partial}{\partial \mathbf{R}_I} \right| \left\{ - \sum_{\beta \neq I}^{maille} \sum_{\mathbf{R}} \frac{Z_\beta e}{\left| \mathbf{R}_I - \mathbf{R}_\beta + \mathbf{R} \right|} + \int \frac{\rho(\mathbf{r})}{\left| \mathbf{R}_I - \mathbf{r} \right|} d\mathbf{r} \right\}$$